HUMAN EXPOSURE TO NEW-EMERGING ELECTRIC, MAGNETIC AND ELECTROMAGNETIC FIELDS

EDITED BY: Tongning Wu, Ruiyun Peng, Lei Zhang and Kun Li

PUBLISHED IN: Frontiers in Public Health

frontiers Research Topics

frontiers

ISSN 1664-8714
ISBN 978-2-88976-194-4
DOI 10.3389/978-2-88976-194-4

About Frontiers

Frontiers is more than just an open-access publisher of scholarly articles: it is a pioneering approach to the world of academia, radically improving the way scholarly research is managed. The grand vision of Frontiers is a world where all people have an equal opportunity to seek, share and generate knowledge. Frontiers provides immediate and permanent online open access to all its publications, but this alone is not enough to realize our grand goals.

Frontiers Journal Series

The Frontiers Journal Series is a multi-tier and interdisciplinary set of open-access, online journals, promising a paradigm shift from the current review, selection and dissemination processes in academic publishing. All Frontiers journals are driven by researchers for researchers; therefore, they constitute a service to the scholarly community. At the same time, the Frontiers Journal Series operates on a revolutionary invention, the tiered publishing system, initially addressing specific communities of scholars, and gradually climbing up to broader public understanding, thus serving the interests of the lay society, too.

Dedication to Quality

Each Frontiers article is a landmark of the highest quality, thanks to genuinely collaborative interactions between authors and review editors, who include some of the world's best academicians. Research must be certified by peers before entering a stream of knowledge that may eventually reach the public - and shape society; therefore, Frontiers only applies the most rigorous and unbiased reviews.
Frontiers revolutionizes research publishing by freely delivering the most outstanding research, evaluated with no bias from both the academic and social point of view. By applying the most advanced information technologies, Frontiers is catapulting scholarly publishing into a new generation.

What are Frontiers Research Topics?

Frontiers Research Topics are very popular trademarks of the Frontiers Journals Series: they are collections of at least ten articles, all centered on a particular subject. With their unique mix of varied contributions from Original Research to Review Articles, Frontiers Research Topics unify the most influential researchers, the latest key findings and historical advances in a hot research area! Find out more on how to host your own Frontiers Research Topic or contribute to one as an author by contacting the Frontiers Editorial Office: frontiersin.org/about/contact

HUMAN EXPOSURE TO NEW-EMERGING ELECTRIC, MAGNETIC AND ELECTROMAGNETIC FIELDS

Topic Editors:
Tongning Wu, China Academy of Information and Communications Technology, China
Ruiyun Peng, Beijing Institute of Radiation Medicine, Academy of Military Medical Sciences (AMMS), China
Lei Zhang, Third Military Medical University, China
Kun Li, Kagawa University, Japan

Citation: Wu, T., Peng, R., Zhang, L., Li, K., eds. (2022). Human Exposure to New-Emerging Electric, Magnetic and Electromagnetic Fields. Lausanne: Frontiers Media SA. doi: 10.3389/978-2-88976-194-4

Table of Contents

frontiers | Frontiers in Public Health

EDITORIAL
published: 28 April 2022
doi: 10.3389/fpubh.2022.894624

Editorial: Human Exposure to New-Emerging Electric, Magnetic and Electromagnetic Fields

Tongning Wu[1]*, *Ruiyun Peng*[2], *Lei Zhang*[3] and *Kun Li*[4]

[1] China Academy of Information and Communications Technology, Beijing, China, [2] Beijing Institute of Radiation Medicine, Academy of Military Medical Sciences, Beijing, China, [3] Department of Occupational Health, Third Military Medical University, Chongqing, China, [4] Faculty of Engineering and Design, Kagawa University, Takamatsu, Japan

Keywords: terahertz, millimeter wave, microwave, radiofrequency, low-frequency

Editorial on the Research Topic

Human Exposure to New-Emerging Electric, Magnetic and Electromagnetic Fields

With the advancement of wireless technologies and electronic/electrical devices, humans are exposed to more complicated electric, magnetic, and electromagnetic fields (EMF), which has raised public concerns on potential health effects. Researchers have recently conducted a series of studies on diverse exposure scenarios. In addition, international standard organizations have revised safety guidelines and standards (1). These recent results and practices can enhance our knowledge in assessing health risks from the exposure to EMF (2). This Research Topic consists of 14 articles (one review article, two brief research report articles, and 11 original research articles) published in the Radiation and Health section of Frontiers in Public Health.

There have been immense concerns over the neurological effect of EMF exposure. Hu et al. reviewed the effects on metabolism and receptors of neurotransmitters in the brain and found them to be important, while the mechanisms have not yet been clarified. The authors advocated the application of novel techniques, such as neuroviral tracers, neuroimaging, and neuroelectrophysiology. Li et al. investigated the effects of 1,800 MHz EMF exposure for 48 h on neurite outgrowth in neuronal cells and explored the associated role of the Rap1 signaling pathway, using primary hippocampal neurons from C57BL/6 mice and Neuro2a cells. They found that the neurite length, primary and secondary neurite numbers, and branch points of primary mouse hippocampal neurons were significantly impaired by 48-h RF-EMF exposure. The neurite-bearing cell percentage and neurite length of Neuro2a cells were inhibited by 48-h RF-EMF exposure. Rap1 activity was inhibited by 48-h RF-EMF with no detectable alteration in either gene or protein expression of Rap1. The protein expression of Rap1GAP increased after 48-h exposure, while the expression of p-MEK1/2 protein decreased. Concerning human studies, Yang et al. conducted functional magnetic resonance imaging for 17 adults. No alteration was found before and after exposure to a 30-min time-division long-term evolution (LTE) signal (2.573 GHz) with an intensity similar to the maximum emission of a mobile phone. The authors generated intrinsic connectivity networks and conducted static and dynamic functional network connectivity analysis. There exists very few human studies using functional magnetic resonance imaging. The results were generally consistent (3) but the scarce number of the subjects may be a limitation of these articles. These pilot publications shed light on defining the exposure protocol and selecting the appropriate neurophysiological/dosimetric metrics for future human studies.

There is a revival in the interest of revisiting the exposure that people experience every day. A pulsed low-frequency magnetic field is widely generated by household appliances and the potential biological effect on fetuses has attracted public concerns. Sun et al. investigated the effect of 10 Hz

Edited by:
Micaela Liberti,
Sapienza University of Rome, Italy

Reviewed by:
Olga Zeni,
National Research Council (CNR), Italy
Theodoros Samaras,
Aristotle University of Thessaloniki, Greece

***Correspondence:**
Tongning Wu
wutongning@caict.ac.cn

Specialty section:
This article was submitted to Radiation and Health, a section of the journal Frontiers in Public Health

Received: *11 March 2022*
Accepted: *31 March 2022*
Published: *28 April 2022*

Citation:
Wu T, Peng R, Zhang L and Li K (2022) Editorial: Human Exposure to New-Emerging Electric, Magnetic and Electromagnetic Fields. Front. Public Health 10:894624. doi: 10.3389/fpubh.2022.894624

pulsed magnetic field exposure on cellular senescence in a 2BS cell line, isolated from human fetal lung fibroblasts, and found that 1 day on/1 day off exposure to the magnetic field of 1.0 mT for 2 weeks induced DNA damage, but no other significant phenotype of cellular senescence in the cells. Xie et al. found the exposure to low-dose 900 MHz signals increased the level of reactive oxygen species and activated a mitochondrial unfolded protein response in mouse bone marrow stromal cells. The increased HSP10/HSP60/ClpP protein level lasted up to 4 h, while mitochondrial homeostasis was restored 24 h after exposure. However, the molecular mechanism was unclear.

New exposure scenarios posed challenges to quantify the EMF distribution which would make the result reproducible. Wang et al. assessed the dosimetric variability of the free rats in exposure experiments of 1.8 GHz. Chakarothai et al. proposed a frequency-dependent finite-difference time-domain method for human exposure to pulsed EMF at microwave bands. The use of a four-term Cole-Cole model for complex permittivity functions, applying the fast inverse Laplace transform and Prony method, improved the accuracy when calculating the specific energy absorption for biological tissues. To characterize exposure by 4G signals, Mazloum et al. conducted measurement campaigns in a multi-floor indoor environment using a drive test solution to record both downlink (DL) and uplink (UL) connection parameters for LTE networks. Several typical usage services were involved and investigated. They proposed an artificial neural network model to accurately estimate UL TX power with a mean absolute error of 1.487 dB. Concerning 5G, Xu et al. reported the computational results of actual maximum EMF exposure and the corresponding power reduction factors (PRFs) for millimeter-wave (28 GHz) base station antennas. They clarified the effectiveness of using this far-field approach, which can also guarantee the conservativeness of the PRFs for the assessment of the actual maximum exposure close to the antenna. A 60 GHz frequency point could also be deployed by 5G. Hikage et al. developed an exposure setup for the experiment of biological effects of local exposure to millimeter waves on the human body. The designed system enabled the researchers to achieve high-intensity 60 GHz irradiation to the target area of the human body by a spatial synthetic beam-type exposure setup with two dielectric lens antennas. Interference fringes can be generated in the exposed area by applying an orthogonalizing polarized feeding structure, where the expected local temperature changes at the target area of the human forearm skin were confirmed. Li et al. reported a formula-based analysis of cloth effects on human skin exposure to obliquely incident electromagnetic waves at 60 GHz by the Monte Carlo method. The analyzed absorbed power density (APD) within the skin surface covered by different cloth materials increased up to 40% compared with that of bare skin, but all the results of the APD did not exceed the basic restriction for local exposure specified in the exposure guidelines and standards. In particular, occupational exposure in a military scenario was accessed by Colella et al. The obtained E-field values radiated in the free space by a HF vehicular antenna may exceed the safety guideline reference levels. However, SAR and E-field values induced inside the body remained well below safety limits.

There were also two studies dedicated to exposure of medical devices. RF-induced heating in implantable devices during magnetic resonance imaging is a complex function of many different clinical factors. To reduce implant heating and maintain good image quality at the same time, Yao et al. developed an exposure optimization trail that allowed for comprehensive optimization in an efficient and traceable manner. Major clinical factors were decoupled from the redundant dataset using principal component analysis. Exposure optimization for a 40-cm cardio implant was demonstrated with the proposed workflow. Lu et al. optimized the position of a transcranial magnetic stimulation coil to maximize the E-field distribution in the target brain region and also reduced unnecessary exposure to the other regions. A genetic algorithm was applied in this practice relating to stroke.

The editors of this Research Topic are grateful to all distinguished authors for their invaluable contributions and are indebted to the expert reviewers for their time, dedication, and constructive comments. We wish to acknowledge the Radiation and Health section of Frontiers in Public Health for the opportunity to guest edit this Research Topic.

AUTHOR CONTRIBUTIONS

TW and KL drafted the editorial and RP and LZ commented on it. All authors contributed to the guest editing of the Research Topic.

REFERENCES

1. ICNIRP. Guidelines for limiting exposure to electromagnetic fields (100 kHz to 300 GHz). *Health Phys.* (2020) 118:483–524. doi: 10.1097/HP.0000000000001210
2. Hirata A, Diao Y, Onishi T, Sasaki K, Ahn S, Colombi D, et al. Assessment of human exposure to electromagnetic fields: review and future directions. *IEEE Trans Electromagn Compat.* (2021) 63:1619–30. doi: 10.1109/TEMC.2021.3109249
3. Yang L, Zhang C, Chen Z, Li C, Wu T. Functional and network analyses of human exposure to long-term evolution signal. *Environ Sci Pollut Res.* (2021) 28:5755–73. doi: 10.1007/s11356-020-10728-w

Conflict of Interest: The authors declare that the research was conducted in the absence of any commercial or financial relationships that could be construed as a potential conflict of interest.

frontiers in Public Health

ORIGINAL RESEARCH
published: 13 August 2021
doi: 10.3389/fpubh.2021.725310

Dosimetry of Various Human Bodies Exposed to Microwave Broadband Electromagnetic Pulses

Jerdvisanop Chakarothai, Kanako Wake and Katsumi Fujii*

Electromagnetic Compatibility Laboratory, Electromagnetic Standards Research Center, Radio Research Institute, National Institute of Information and Communications Technology, Koganei, Japan

In this paper, human exposures to ultra-wideband (UWB) electromagnetic (EM) pulses in the microwave region are assessed using a frequency-dependent FDTD scheme previously proposed by the authors. Complex permittivity functions of all biological tissues used in the numerical analyses are accurately expressed by the four-term Cole–Cole model. In our method, we apply the fast inverse Laplace transform to determine the time-domain impulse response, utilize the Prony method to find the Z-domain representation, and extract residues and poles for use in the FDTD formulation. Update equations for the electric field are then derived via the Z-transformation. Firstly, we perform reflection and transmission analyses of a multilayer composed of six different biological tissues and then confirm the validity of the proposed method by comparison with analytical results. Finally, numerical dosimetry of various human bodies exposed to EM pulses from the front in the microwave frequency range is performed, and the specific energy absorption is evaluated and compared with that prescribed in international guidelines.

Keywords: electromagnetic pulses, finite-difference time-domain method, fast inverse Laplace transform, Prony method, exposure assessment

OPEN ACCESS

Edited by:
Tongning Wu,
China Academy of Information and Communications Technology, China

Reviewed by:
Yinliang Diao,
Nagoya Institute of Technology, Japan
Congsheng Li,
China Academy of Information and Communications Technology, China

****Correspondence:***
Jerdvisanop Chakarothai
jerd@nict.go.jp

Specialty section:
This article was submitted to Radiation and Health, a section of the journal Frontiers in Public Health

Received: *15 June 2021*
Accepted: *21 July 2021*
Published: *13 August 2021*

Citation:
Chakarothai J, Wake K and Fujii K (2021) Dosimetry of Various Human Bodies Exposed to Microwave Broadband Electromagnetic Pulses. Front. Public Health 9:725310. doi: 10.3389/fpubh.2021.725310

INTRODUCTION

In 2002, the Federal Communications Commission of the United States of America issued a ruling allowing the use of ultra-wideband (UWB) electromagnetic (EM) pulses in the frequency range between 3.1 and 10.6 GHz (1). Since then, numerous applications of UWB pulses have emerged as a result of the regulation, such as vital signal detection and locating moving human bodies, as well as ground-penetrating radar, remote sensing, non-destructive inspection, and so forth (2). Owing to many advantages of UWB pulses such as low power consumption and immunity to multipath of EM propagations and EM interferences, the widespread use of EM pulses is expected to continue. Some of these applications use UWB pulses in the vicinity of human bodies, such as wireless capsule endoscopy using broadband EM pulses for on/in-body communications (3, 4). These applications have led to public concern about the effect on the broadband EM pulses to human body.

Meanwhile, biological effects due to EM pulses have been numerically and experimentally investigated. The effects include the microwave hearing effect, microwave heating effect, and electroporation (5–9). Consequently, international organizations have prescribed exposure limits for the temporal peak of specific energy absorption (SA) in published guidelines to prevent adverse effects, particularly of microwave hearing, which is considered an acute biological effect (10, 11). The International Commission on Non-ionizing Radio Protection (ICNIRP) provided an SA limit

of 2 mJ/kg in an arbitrary 10 g-averaged tissue for a single pulse illumination (10), while the SA limit is up to 576 J/kg for continuous exposure of 6 min in the regulation defined by the Institute of Electrical and Electronics Engineers (IEEE) (11). Recently, the ICNIRP has revised the Guidelines based on the relevant scientific knowledge and published them in 2020. In the guidelines, it is mentioned that there is no evidence that microwave hearing in any realistic exposure scenarios causes adverse health consequence and the microwave hearing effect is not considered in the guideline but it is still mandate to consider the heating effect from the pulse exposures (12). Although many biological effects due to EM pulses have been experimentally confirmed, there are few studies providing detailed exposure levels or showing the distribution of SA inside a human body.

To derive SA inside the human body, calculation of the interactions between EM pulses and biological bodies is necessary. In the earliest studies, most of the biological targets were objects having simple shapes such as a multilayer or a dielectric sphere, inside which SA or the induced electric field was derived theoretically (13, 14). However, there has been no detailed dosimetric information of the detailed human body exposed to EM pulses due to difficulties in the calculation of SA or the induced electric field inside biological bodies. These problems are mainly attributed to the frequency dependence of the dielectric properties of biological tissues, which are expressed by the four-term Cole-Cole model (15).

To perform numerical dosimetry of EM pulses, we need to consider the frequency dependence of the permittivity and conductivity of biological tissues over a broad frequency range. Many frequency-dependent finite-difference time-domain [$(FD)^2TD$] approaches have been proposed, such as recursive convolution method (16), piecewise linear recursive convolution method (17), trapezoidal recursive convolution method (18), auxiliary differential equation method (19–21), and Z-transform method (22). However, these approaches have only been applied to materials having complex permittivity expressed by relatively simple models such as the Debye and Lorentz models. These approaches are not applicable to the Cole–Cole function, due to difficulties in finding the exact time-domain solution of a fractional-order differential equation. Nevertheless, many attempts have been made to address this problem, including those using the Riemann–Liouville theory to find the time-domain solution of the model (23, 24). Recently, our research group has proposed an FDTD formulation for analyses of arbitrary frequency-dependent materials via the use of the fast inverse Laplace transform (FILT) and the Prony method (25). The proposed method has also been extended to three-dimensional analyses of UWB antennas in the vicinity of the human body and the dosimetry of EM pulses incident to a human head (26, 27).

In this study, we extend our numerical models to whole-body human models which are exposed to broadband EM pulses. To the best of our knowledge, this is the first ever numerical dosimetry of EM pulses, and detailed information of SA inside the human body is provided for compliance with the SA limit prescribed in international guidelines. The proposed method involves two steps; firstly, we apply the FILT to permittivity functions in the complex frequency domain to transform them into time-domain impulse responses. Then, the Prony method is used to extract the model parameters and to determine expressions for the infinite impulse response (IIR) expressions in the Z-domain. The update equations of electric field are derived via the Z-transform.

This paper is outlined as follows. The proposed $(FD)^2TD$ formulation and the calculation of the update coefficients for the electric field are described in section $(FD)^2TD$ Formulation Using FILT and Prony Method. The validity of the method in calculating SA and internal electric field strength (IEFS) inside a multilayer model of biological tissues is demonstrated via comparison with the theoretical results in section Transmission Characteristics of EM Pulses Into Biological Bodies. Numerical dosimetry of anatomically detailed human body models exposed to UWB EM pulses is performed and physical quantities such as SA and IEFS are quantitatively derived and compared with those prescribed in the guidelines in section Transmission Characteristics of EM Pulses Into Biological Bodies. Finally, conclusions are drawn in section Conclusion.

$(FD)^2TD$ FORMULATION USING FILT AND PRONY METHOD

Methodology

In this study, all media used in the numerical analyses are biological tissues having complex relative permittivity expressed by the four-term Cole–Cole function as

$$\varepsilon_m(\omega) = \varepsilon_\infty + \frac{\sigma}{j\omega\varepsilon_0} + \sum_{q=1}^{4} \frac{\Delta\chi_q}{1 + \left(j\omega\tau_q\right)^{1-\alpha_q}}, \tag{1}$$

where, ω, ε_∞, and σ are the angular frequency [rad/s], relative permittivity and conductivity [S/m] of a biological medium at infinite frequency, respectively. ε_0 is the free-space permittivity and $\Delta\chi_q$ represents the change in relative permittivity in the qth relaxation term. τ_q and α_q are the relaxation time and a parameter determining the broadness of the qth term, respectively. All parameters in (1) can be found in Gabriel's database of dielectric properties for biological tissues (15). Although Gabriel's permittivity data are de facto, it is noteworthy that different Cole–Cole parameters may be derived, depending on the method used in fitting the measurement data of the dielectric properties. By limiting the frequency range to between 1 MHz and 20 GHz, the number of Cole–Cole terms may be reduced from four terms to two terms while providing the best fit to the measurement data (28). The average deviations from the measurement results over a frequency range between 1 MHz and 20 GHz are higher than 20% for both relative permittivity and loss factor of some biological tissues but they are shown to be $<$15% for the two Cole-Cole terms used in Kensuke et al. (28).

Since the $(FD)^2TD$ formulation for biological bodies has been described in the literature (26), we hereby only show the numerical procedures of the proposed method and the derived update equation for electric fields. Firstly, we apply the FILT to electric susceptibility represented by the Cole–Cole model, with

the relaxation time normalized by the time step interval used in the FDTD simulations and obtain impulse responses for each susceptibility term in the time domain. Then, we use the Prony method to transform the time-domain impulse response into that in the Z-domain. The permittivity is now expressed in the Z-domain as

$$\varepsilon_m(z) = \varepsilon_\infty + \frac{1+z^{-1}}{1-z^{-1}}\frac{\sigma\Delta t}{2\varepsilon_0} + \sum_{q=1}^{4}\sum_{l=1}^{L_q}\frac{A_l^{(q)}}{1-p_l^{(q)}z^{-1}}, \quad (2)$$

where Δt and L_q are the time step interval and number of poles for the qth Cole–Cole term, respectively. $A_l^{(q)}$ and $p_l^{(q)}$ are residues and poles, respectively. Note that the second term of the right hand side is obtained by applying the bilinear approximation, i.e., $j\omega \approx s = 2\left(1-z^{-1}\right)/\left(1+z^{-1}\right)/(\Delta t)$. Since the nested summation in the third term of the right-hand side of (2) can be merged into a single summation, (2) can simply be expressed as

$$\varepsilon_m(z) = \varepsilon_\infty + \frac{1+z^{-1}}{1-z^{-1}}\frac{\sigma\Delta t}{2\varepsilon_0} + \sum_{k=1}^{N}\frac{A_k}{1-p_k z^{-1}}, \quad (3)$$

where N is the total number of Debye terms, i.e., $N = L_1 + L_2 + L_3 + L_4$. Procedures for determining N, A_k, and p_k using the Prony method will be described in subsection Calculation of Specific Energy Absorption and Internal Electric Field Strength and can also be found in the literature (25). Substituting (3) into the discrete constitutional relation of Maxwell's equations, we obtain the update equation for the electric field as

$$\boldsymbol{E}^n = \frac{1}{L_0}\left[\frac{\boldsymbol{D}^n}{\varepsilon_0} - \frac{\sigma\Delta t}{2\varepsilon_0}\boldsymbol{E}^{n-1} - \boldsymbol{I}^{n-1} - \sum_{k=1}^{N}p_k\boldsymbol{P}_k^{n-1}\right], \quad (4)$$

where,

$$L_0 = \varepsilon_\infty + \frac{\sigma\Delta t}{2\varepsilon_0} + \sum_{k=1}^{N}A_k \quad (5)$$

$$\boldsymbol{I}^n = \boldsymbol{I}^{n-1} + \frac{\sigma\Delta t}{2\varepsilon_0}\left(\boldsymbol{E}^n + \boldsymbol{E}^{n-1}\right) \quad (6)$$

$$\boldsymbol{P}_k^n = p_k\boldsymbol{P}_k^{n-1} + A_k\boldsymbol{E}^n, \quad (7)$$

$\mathbf{I}^n$ and $\mathbf{P}_k^n$ are the auxiliary variables which are initialized by setting $\mathbf{I}^0 = 0$ and $\mathbf{P}_k^0 = 0$, respectively. Equations (4), (6), and (7) are the update equations for the electric field, the auxiliary field used for considering the conductivity term, and the auxiliary field used for considering the Cole–Cole terms, respectively. The update equations for the electric flux density and magnetic field can be obtained by applying the central difference to Maxwell's equations similarly to those in conventional FDTD procedures (20).

The main advantages of the proposed method are that we can avoid the formulation of fractional-order differential equations by using the FILT and the Prony method and it is straightforward to implement the proposed method into the conventional FDTD code.

Calculation of Specific Energy Absorption and Internal Electric Field Strength

The exposure level inside biological bodies illuminated by broadband EM pulses can be evaluated using SA, which has been used as a metric in the guidelines. In the FDTD simulations, SA can be calculated using the following equation:

$$\begin{aligned}\mathrm{SA}^{n-\frac{1}{2}} &= \Delta t\sum_{m=1}^{n}\left(\frac{\mathbf{E}(t)}{\rho}\cdot\frac{\partial\mathbf{D}(t)}{\partial t}\right)\Big|_{t=\left(m-\frac{1}{2}\right)\Delta t},\\ &= \frac{1}{2\rho}\sum_{m=1}^{n}\left(\mathbf{E}^m+\mathbf{E}^{m-1}\right)\cdot\left(\mathbf{D}^m-\mathbf{D}^{m-1}\right), \quad (8)\end{aligned}$$

where ρ is the density of the biological tissue. The electric flux density in Equation (7) at the nth time step ($\mathbf{D}^n$) is updated using the magnetic field at the (n+1/2)$^{\text{th}}$ time step ($\mathbf{H}^{n+1/2}$) and $\mathbf{E}^n$ is updated using (4).

Since a broadband pulse is utilized in our simulations, we can also obtain numerical solutions of the electric and magnetic fields at each frequency component within a single run. The electric field at a frequency is determined via Fourier transform of the waveform obtained at an observation location as

$$\mathbf{E}(\omega) = \int_0^T\mathbf{E}(t)\,e^{-j\omega t}dt = \sum_{n=0}^{N^T}\mathbf{E}^n e^{-j\omega n\Delta t}\Delta t, \quad (9)$$

where N^T is the total number of time steps. After the electric field at each frequency is obtained, the specific absorption rate (SAR) is then calculated as follows:

$$SAR(\omega) = \frac{\sigma\,|\mathbf{E}(\omega)|^2}{2\rho}. \quad (10)$$

Calculation of Update Coefficients for Electric Field

The procedures for determining coefficients A_k and p_k in the update equation for the electric field are described as follows. First, we transform relative permittivity represented in the frequency domain into that in the complex frequency domain by replacing $j\omega$ with the complex frequency s and apply the FILT to find impulse response of the permittivity in the time domain. Then, the Prony method is used to extract the residues A_k and poles p_k from the expression for the IIR in the Z-domain.

As an example, we apply the FILT and the Prony method to the permittivity functions of biological tissues "Fat" and "Gray Matter." Each Cole–Cole parameter is taken from the Gabriel's database and listed in **Table 1**. The time step interval Δt used to normalize the relaxation time in the Cole–Cole function before applying the FILT is set to 1.668 ps.

Table 2 shows the update coefficients A_k and p_k used in the FDTD calculations for "Fat" and "Gray Matter." These values are directly obtained from the Prony method and the number of coefficients for each Cole–Cole term is truncated when the ratio of $\{|A_k|/\max|A_k|\}$ for $k = 1, 2, \ldots, N$ is less than a tolerance value of 10^{-3}. The update coefficients A_k and p_k physically correspond to the initial amplitude and the decreasing ratio of

TABLE 1 | Cole–Cole parameters for "Fat" and "Gray Matter" from Gabriel's database.

Tissue name	ε_∞	σ (S/m)	1st term	2nd term	3rd term	4th term
Fat	2.5	0.035	$\Delta\chi_1 = 9$ $\tau_1 = 7.958$ ps $\alpha_1 = 0.2$	$\Delta\chi_2 = 35$ $\tau_2 = 15.915$ ns $\alpha_2 = 0.1$	$\Delta\chi_3 = 3.3 \times 10^4$ $\tau_3 = 159.155$ ms $\alpha_3 = 0.05$	$\Delta\chi_4 = 10^7$ $\tau_4 = 15.915$ ms $\alpha_4 = 0.01$
Gray Matter	4	0.02	$\Delta\chi_1 = 45$ $\tau_1 = 7.958$ ps $\alpha_1 = 0.1$	$\Delta\chi_2 = 400$ $\tau_2 = 15.915$ ns $\alpha_2 = 0.15$	$\Delta\chi_3 = 2.0 \times 10^5$ $\tau_3 = 106.103$ ms $\alpha_3 = 0.22$	$\Delta\chi_4 = 4.5 \times 10^7$ $\tau_4 = 5.305$ ms $\alpha_4 = 0$

TABLE 2 | Update coefficients for "Fat" and "Gray Matter."

Cole-Cole terms	Fat		Gray Matter	
	A_k	p_k	A_k	p_k
1st	$A_1 = 0.51370$	$p_1 = 0.82495$	$A_1 = 3.94634$	$p_1 = 0.80579$
	$A_2 = 0.44668$	$p_2 = 0.71195$	$A_2 = 2.27434$	$p_2 = 0.69670$
	$A_3 = 0.38560$	$p_3 = 0.54623$	$A_3 = 1.16025$	$p_3 = 0.88246$
	$A_4 = 0.27620$	$p_4 = 0.90559$	$A_4 = 1.01923$	$p_4 = 0.51558$
	$A_5 = 0.18682$	$p_5 = 0.33125$	$A_5 = 0.57702$	$p_5 = 0.29143$
	$A_6 = 0.16287$	$p_6 = 0.96186$	$A_6 = 0.12362$	$p_6 = 0.95064$
	$A_7 = 0.02939$	$p_7 = 0.11328$	$A_7 = 0.32517$	$p_7 = 0.09047$
	$A_8 = 0.00263$	$p_8 = 0.99134$	$A_8 = 0.00886$	$p_8 = 0.98824$
2nd	$A_9 = 0.00456$	$p_9 = 0.99981$	$A_9 = 0.05766$	$p_9 = 0.99977$
	$A_{10} = 0.00137$	$p_{10} = 0.99470$	$A_{10} = 0.02718$	$p_{10} = 0.99451$
	$A_{11} = 0.00090$	$p_{11} = 0.96716$	$A_{11} = 0.01975$	$p_{11} = 0.96773$
	$A_{12} = 0.00067$	$p_{12} = 0.89813$	$A_{12} = 0.01582$	$p_{12} = 0.90147$
	$A_{13} = 0.00054$	$p_{13} = 0.77398$	$A_{13} = 0.01333$	$p_{13} = 0.78223$
			$A_{14} = 0.01158$	$p_{14} = 0.60236$
			$A_{15} = 0.00997$	$p_{15} = 0.36732$
			$A_{16} = 0.00762$	$p_{16} = 0.12557$
3rd	$A_{14} = 0.00060$	$p_{14} = 0.99998$	$A_{17} = 0.03134$	$p_{17} = 0.99991$
			$A_{18} = 0.01880$	$p_{18} = 0.99735$
			$A_{19} = 0.01668$	$p_{19} = 0.98646$
			$A_{20} = 0.01495$	$p_{20} = 0.96009$
			$A_{21} = 0.01353$	$p_{21} = 0.91205$
			$A_{22} = 0.01233$	$p_{22} = 0.83801$
			$A_{23} = 0.01125$	$p_{23} = 0.73622$
			$A_{24} = 0.01025$	$p_{24} = 0.60828$
			$A_{25} = 0.00926$	$p_{25} = 0.46002$
			$A_{26} = 0.00820$	$p_{26} = 0.30292$
			$A_{27} = 0.00694$	$p_{27} = 0.15589$
			$A_{28} = 0.00533$	$p_{28} = 0.04538$
4th	$A_{15} = 0.00122$	$p_{15} = 1.00000$	$A_{29} = 0.01415$	$P_{29} = 1.00000$

the time-domain impulse response, respectively. From **Table 2**, the total numbers of coefficients are 15 and 29 for "Fat" and "Gray Matter," respectively.

To demonstrate the validity of the update coefficients, we calculate the reflection coefficients from each biological medium by one-dimensional FDTD simulation using the model shown as Figure 4 in Chakarothai et al. (26) and compare their values with those obtained from the EM theory. The analysis model is half filled with biological tissues and truncated with perfectly matched layers in order to absorb the outgoing wave. Numerical results using a time step interval of 1.668 ps and a resolution of 0.5 mm are shown in **Figure 1**. The reflection coefficients are analytically calculated using $\Gamma = \left|1 - \sqrt{\varepsilon_m}\right| / \left|1 + \sqrt{\varepsilon_m}\right|$, where ε_m is the complex relative permittivity expressed by Equation (1).

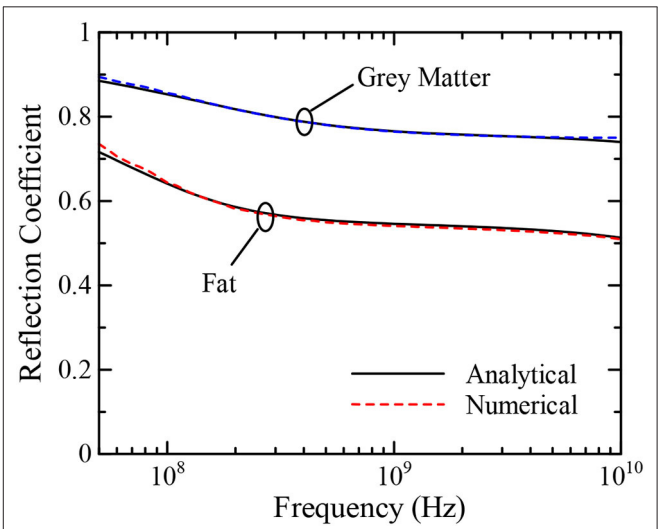

FIGURE 1 | Reflection coefficients of "Fat" and "Gray Matter".

As shown in **Figure 1**, the reflection coefficients of "Fat" and "Gray Matter" obtained via numerical simulations are within 2% of those obtained by the analytical method over a broad frequency range between 50 MHz and 10 GHz, demonstrating the validity of the update coefficients and our numerical approach. Update coefficients for the other type of biological tissues can also be calculated straightforwardly using the procedures described above. Note that when we change the time step interval, we also need to recalculate the update coefficients.

TRANSMISSION CHARACTERISTICS OF EM PULSES INTO BIOLOGICAL BODIES

Multilayer Model

Figure 2 shows a multilayer model mimicking a human head, which comprises six biological tissues, similar to those used in the literature (29, 30). **Table 3** indicates the thicknesses of biological tissues used in the analysis model and the number of the update coefficients for each biological tissue. The total size of the multilayer model is 180 mm. These coefficients are obtained by applying the FILT and the Prony method with a time step interval of $\Delta t = 1.668$ ps. The resolution and the total number of cells used in our analysis model are 0.5 mm and 5,000, respectively. CPMLs with eight layers are utilized on both sides

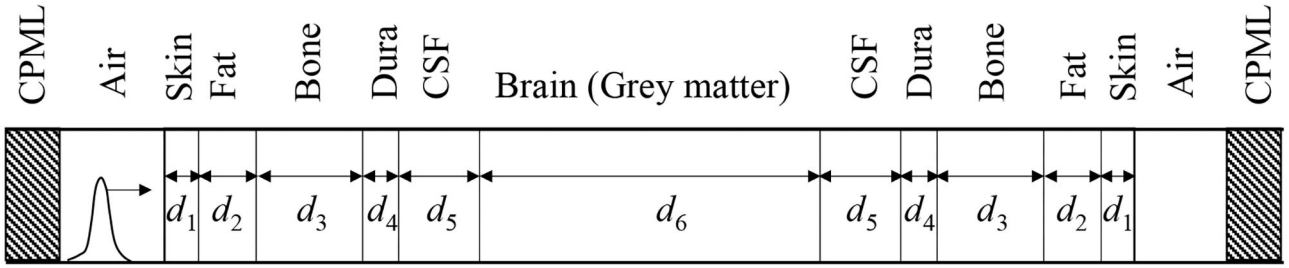

FIGURE 2 | Multilayer model consisting of six biological tissues.

TABLE 3 | Tissue density and thickness of each tissue layer.

Tissue name	Thickness (mm)	Number of coefficients
Skin (Wet)	$d_1 = 1.0$	21
Fat	$d_2 = 1.5$	15
Bone	$d_3 = 4.0$	14
Dura	$d_4 = 1.0$	16
CSF	$d_5 = 3.0$	9
Brain (Gray Matter)	$d_6 = 159$	29

of the analysis domain to absorb the outgoing EM waves. The total number of time steps is 100,000. The incident electric field is given by a Gaussian pulse expressed as

$$E^{inc}(t) = \exp\left(-\left(\frac{t - T_0}{a_0}\right)^2\right) u(t), \tag{11}$$

where $T_0 = 0.250$ ns, $a_0 = 0.0633$ ns, and $u(t)$ is the unit step function, which is applied from the air region on the left side as shown in **Figure 2**. The applied Gaussian pulse contains frequency components from dc to approximately 9.3 GHz, where the power of the pulse decreases 1,000-fold from its maximum value. Number of sampling points used in fast Fourier transform to obtain the reflection coefficients and transmission characteristics is 120,000. Zero padding is used after 100,000 sampling data.

Figure 3 indicates the reflection coefficient and the transmission of the multilayer model as a percentage obtained by the FDTD and analytical methods from 50 MHz to 10 GHz. The transmission, indicating the power transmitting into a biological tissue layer, is calculated using the following equation:

$$P^t(\omega) = \left(1 - |\Gamma|^2\right) \times 100\ [\%], \tag{12}$$

where Γ is the reflection coefficient. It is shown that the numerical and analytical results are in good agreement, demonstrating the validity of our proposed FDTD method again. Note also that the broadband results are numerically obtained in the time domain by a single FDTD run and transformed to those in the frequency domain via the fast Fourier transform. From the results, it can be seen that the reflection coefficient decreases

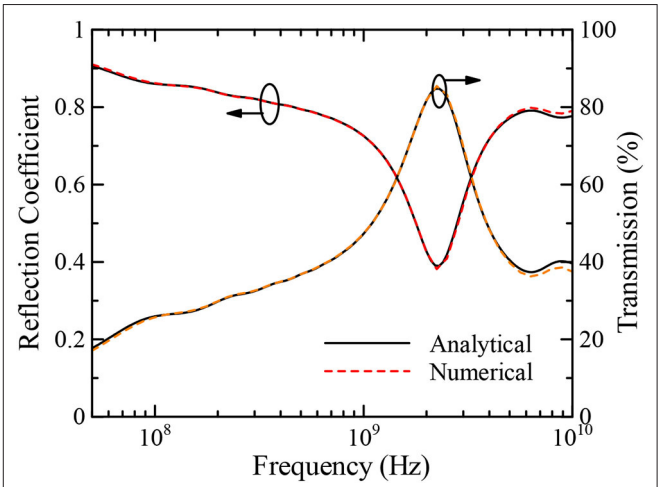

FIGURE 3 | Reflection coefficient and transmission of multilayer mimicking a human head model.

with increasing frequency and reaches a minimum value of 0.38 at ∼2 GHz, while the transmission exhibits peak at 2 GHz. From **Figure 3**, more than 80% of the incident power penetrates into the multilayer model at the maximum transmission frequency of around 2 GHz. Note that the maximum transmission frequency depends on the thicknesses of the biological tissues in the model; thus, using a different model will yield different results from those shown in this study. Next, the transmission characteristics of the EM pulse are obtained from the ratio between the receiving power at an observation point inside a biological tissue layer and the power penetrating into the model from the leftmost boundary of the skin layer.

Figure 4 indicates the transmission characteristics at the center of each layer in the left half of the analysis model as a percentage. From the figure, we observe a peak of the transmitted power in the skin at around 2.5 GHz. This peak shifts to a higher frequency with decreasing maximum value when the power penetrates into the subsequent layer, which is the "Bone" layer in this case. It is also shown that when the observation point is located inside the CSF layer, the transmission characteristics of this multilayer model are almost flat in the range between 300 and 800 MHz, having a maximum at ∼500 MHz. In addition,

when the frequency is larger than 1 GHz, most of the power is absorbed at the superficial layers before reaching the CSF layer and, therefore, the transmitted power monotonically decreases with increasing frequency in this region, except between 5 and 8 GHz, where the transmissions in the "Fat" layer is greater than that in the "Skin" layer. This may be due to a small loss in the "Bone," compared to that of "Skin," and multiple reflections occurring between the Skin–Fat and Fat–Bone boundaries that create a local maximum. Note that only a small proportion of the power reaches the other side of the analysis region. For example, as shown in **Figure 4**, the transmission power that reaches the CSF layer on the right side of the analysis model is <2% of the total transmission power and is concentrated at lower frequencies of below 100 MHz.

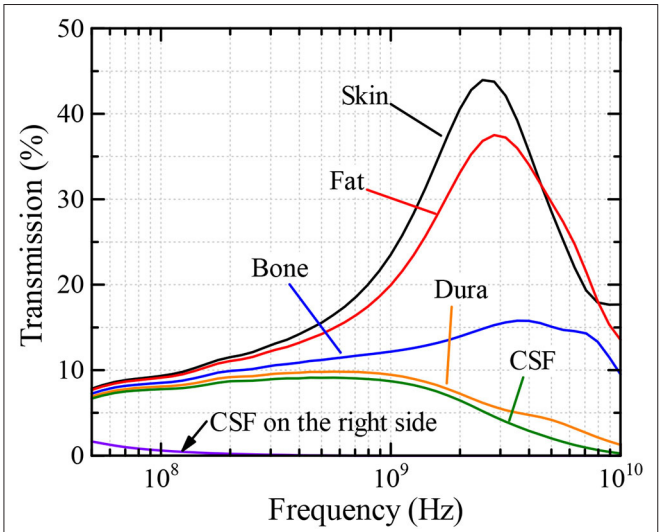

FIGURE 4 | Transmission characteristics at observation points inside biological tissue layers.

Dosimetry of Various Human Bodies Exposed to EM Pulses

As discussed in the previous subsection, the transmission into the multilayer mimicking a human head model shows a high value in the frequency range between 300 and 800 MHz at the deep tissues such as "Dura" and "CSF" and decreases above a frequency of 1 GHz due to the superficial absorption of EM energy. Therefore, our target for numerical dosimetry is an EM pulse having broad frequency components below 1 GHz. As shown in **Figure 5**, numerical human models of anatomical adult male (TARO), adult female (HANAKO), 7-, 5-, and 3-year child models, which were developed by National Institute of Information and Communications Technology, Japan, are chosen as our targets for numerical dosimetry (31, 32). They contain 51

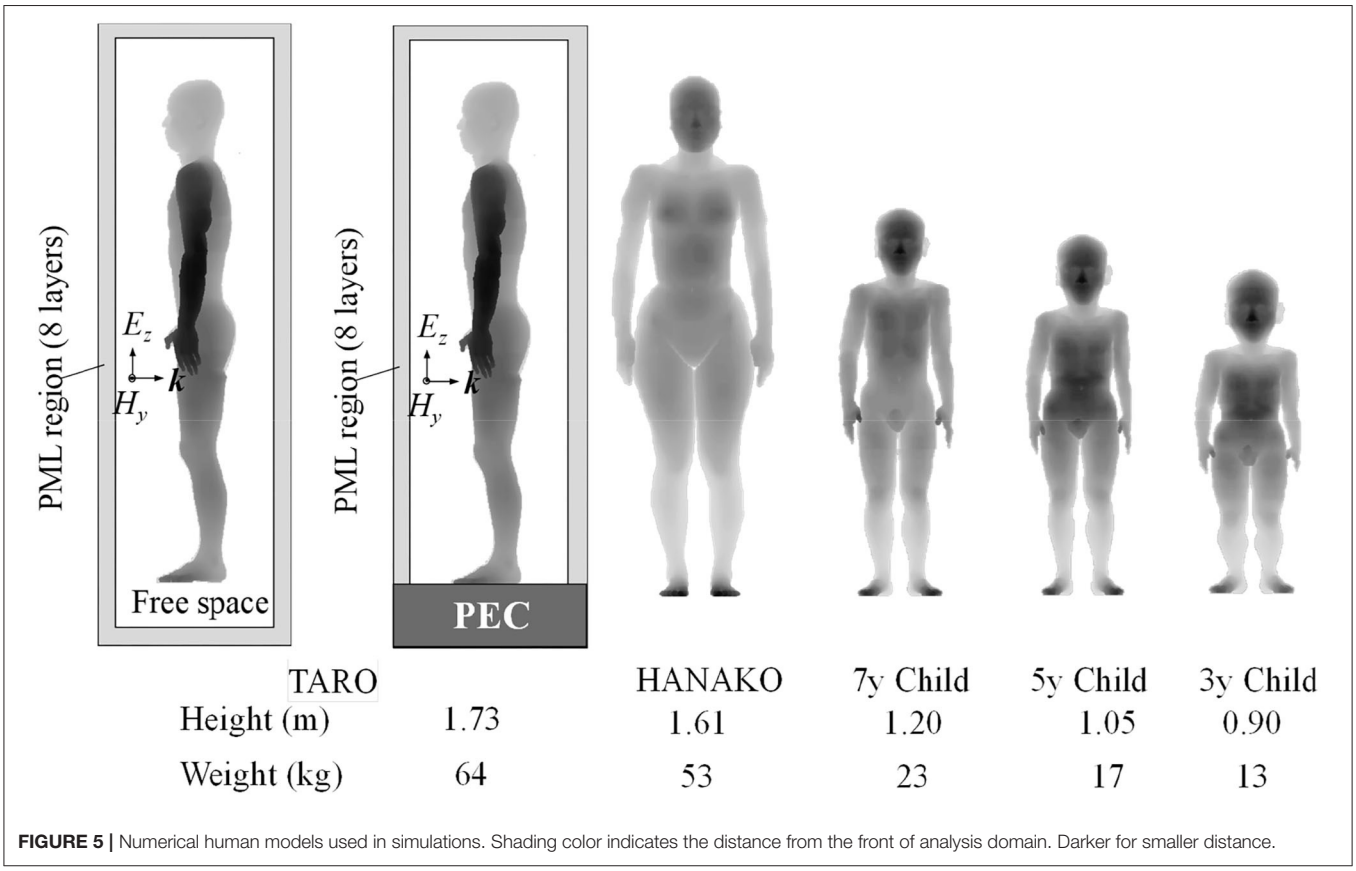

FIGURE 5 | Numerical human models used in simulations. Shading color indicates the distance from the front of analysis domain. Darker for smaller distance.

TABLE 4 | Calculation time and memory usage for each model.

Model	Memory usage (GBytes)	Size of analysis region (cells)	Calculation time (s)	Calculation time with constant permittivity at a frequency (s)
Male (TARO)	88.6	200 × 360 × 906	45,090 (12 h 31 min)	14,767 (4 h 6 min)
Female (HANAKO)	81.7	200 × 360 × 844	34,124 (9 h 29 min)	13,547 (3 h 46 min)
7-year child	29.2	146 × 225 × 645	11,598 (3 h 13 min)	4,677 (1 h 18 min)
5-year child	20.8	136 × 196 × 560	11,067 (3 h 4 min)	2,942 (49 min)
3-year child	16.6	132 × 187 × 481	9,126 (2 h 32 min)	2,795 (47 min)

different biological tissues and have a spatial resolution of 2 mm. **Figure 5** also shows exposure situations with an ungrounded model (free-space model) and a grounded model standing on a ground plane made of the perfectly electric conductor (PEC). The height and weight for each numerical human model are also indicated in **Figure 5**. In accordance with the Courant condition, the time step interval is determined as 3.85 ps. The time step interval used here is different from that used in subsection Multilayer Model; thus, we need to recalculate the update coefficients for all biological tissues used in the numerical simulations.

The update coefficients are derived by applying the FILT and the Prony method as described above. The time step interval used to normalize the relaxation time in the Cole–Cole function is then set to 3.85 ps, the same as that used in the numerical simulations. After calculating the update coefficients, we validate them by performing one-dimensional simulations and computing the reflection coefficients. We have found that the reflection coefficients of all biological media having a permittivity function characterized by the Cole–Cole model match those obtained from the EM theory with a small difference of <2% in the frequency range between 10 MHz and 2 GHz, demonstrating the validity of the determined update coefficients used in FDTD simulations (33). The required number of terms of the update coefficients is different for each tissue, with the maximum number of $N = 50$ for "Infiltrated Cancellous Bone Barrow." The reflection coefficients show values ranging from 0.70 to 0.90 at 10 MHz, which decrease to 0.40–0.80 at 2 GHz. The biological tissue with the lowest and highest reflection coefficients are "Non-infiltrated Bone Marrow" and "Cerebro-Spinal Fluid (CSF)," respectively. This is attributed to the fact that CSF has a higher conductivity than other tissues.

An incident electric field polarized in the z-direction, having the same Gaussian waveform with $T_0 = 0.385$ ns and $a_0 = 0.146$ ns impinges on each model from the front. The power of the incident EM pulse decreases by half at ∼1.3 GHz. An EM plane wave has a polarization axis parallel with the human body axis. The amplitude of the incident electric field is 1 V/m. The calculation of SA can be carried out until the pulse strength decreased to almost zero at a specific time step. The calculation time and memory usage for each model are tabulated in **Table 4**. The calculation time also includes the computation time for an on-the-fly Fourier transform to obtain the electric field distributions inside the human models for use in deriving the whole-body average SAR at 24 different frequencies from 10 MHz to 1 GHz within a single FDTD run. Numerical simulations involving human models are carried out on a single calculation node (Intel Xeon E5-2680v4 @ 2.4 GHz, 256 GB memory) of TSUBAME3.0 supercomputer at Tokyo Institute of Technology, Japan, with 28 parallel threads. The total number of time steps is 10,000 steps. For our cases, total electric energy inside the human

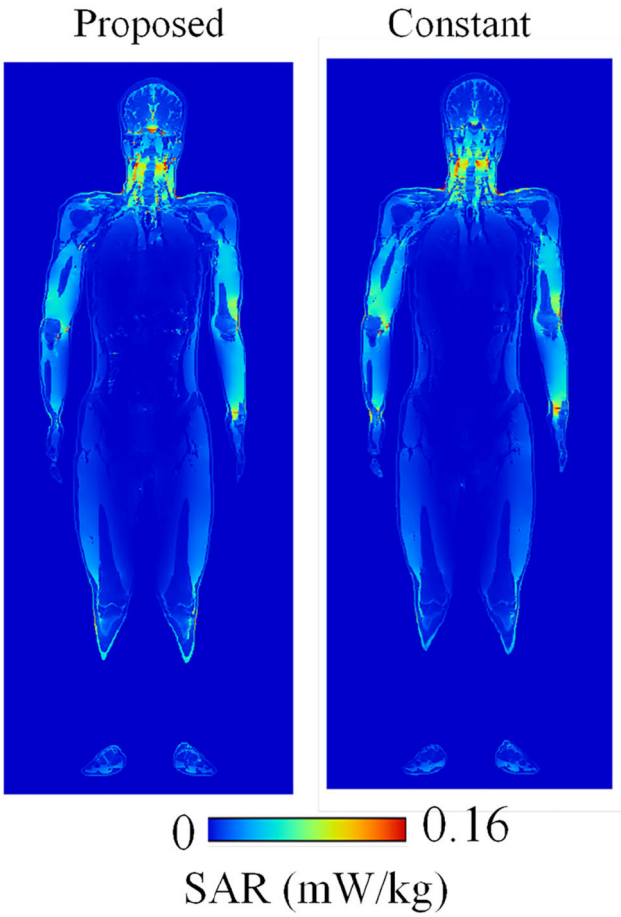

FIGURE 6 | SAR distribution at 500 MHz calculated using the proposed FDTD method and that using the conventional FDTD method with constant dielectric properties.

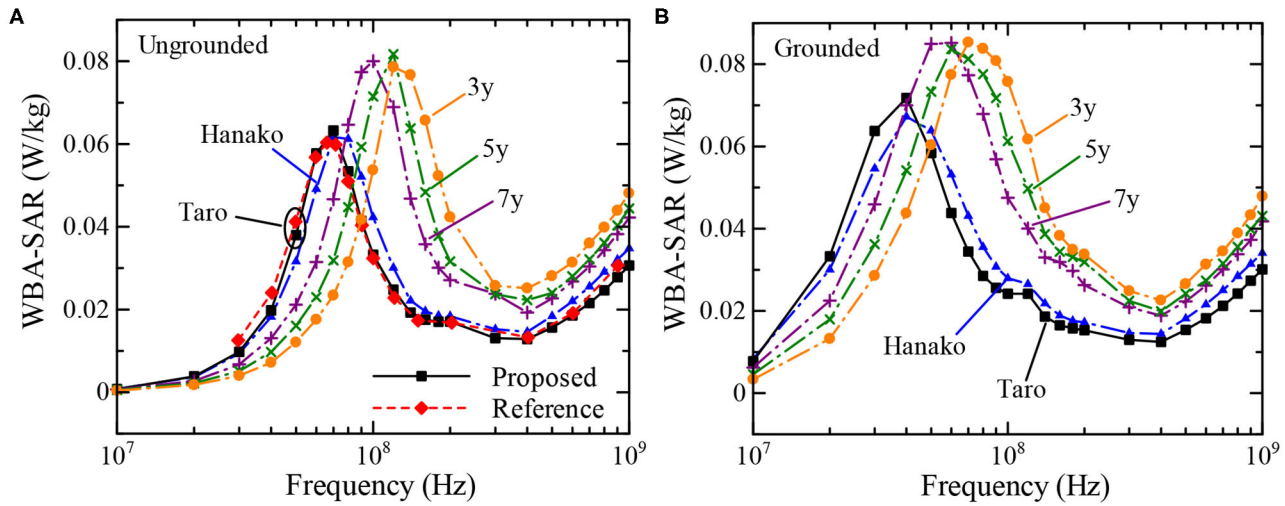

FIGURE 7 | Whole-body average SAR over a frequency range between 10 MHz to 1 GHz, calculated using the proposed FDTD method for the ungrounded and grounded cases. **(A)** Ungrounded cases. **(B)** Grounded cases.

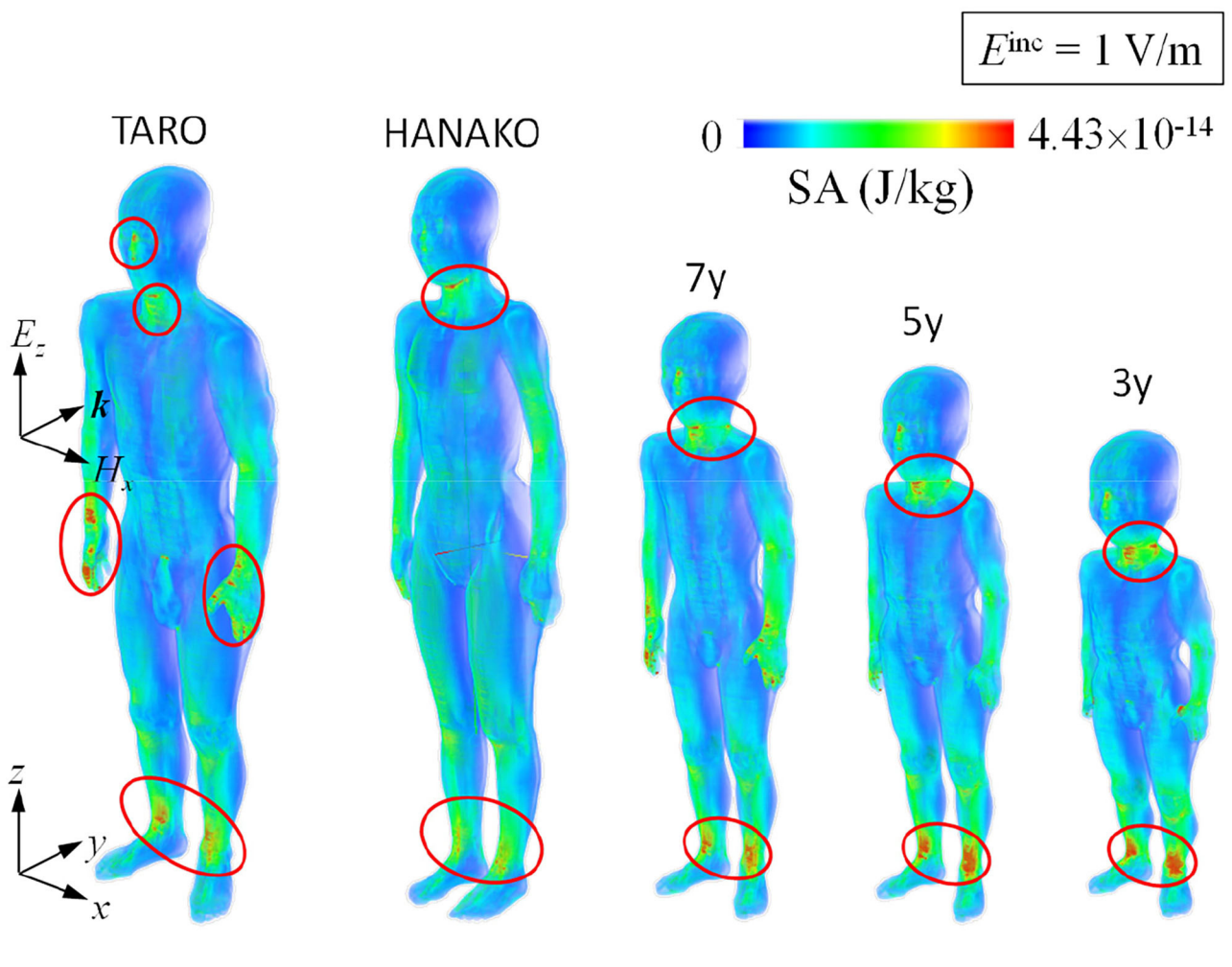

FIGURE 8 | SA distribution for one pulse illumination for various ungrounded human models.

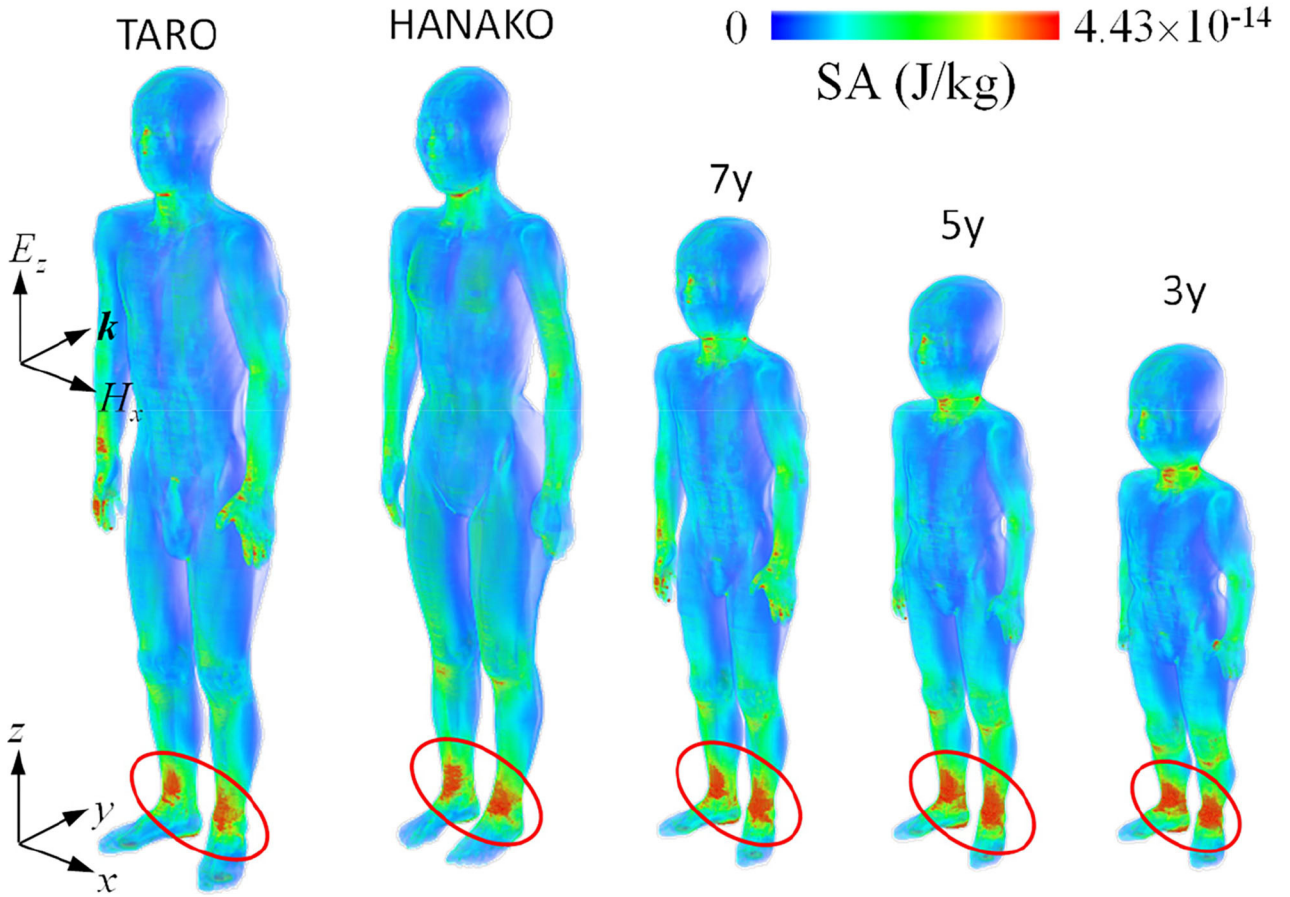

FIGURE 9 | SA distribution for one pulse illumination for various grounded human models.

model was <-50 dB after 10,000 step, compared to its maximum during numerical simulations. The total size of the analysis region including perfectly matched layers (PMLs) are also indicated in the table.

Figure 6 shows the SAR distribution inside the TARO model illuminated by a planewave with a 1 V/m electric field at 200 MHz. The results are obtained by using the proposed $(FD)^2TD$ approach and using constant dielectric properties for comparison. Both distributions are well-matched, demonstrating the validity of the $(FD)^2TD$ method. **Figures 7A,B** indicate the whole-body-average specific absorption rate (WBA-SAR) of various numerical human models for the ungrounded and grounded conditions, respectively. Note that our numerical results are obtained by a single run of FDTD computation for each model. The WBA-SAR at each frequency is calculated using an on-the-fly Fourier transform during the FDTD run. It is shown that the results obtained by the proposed method are in good agreement with those derived in the literature, which are also shown as a red dashed line in the figure (34), again demonstrating the validity of our proposed method. Note that the results in **Figure 7** are normalized by the limits of the incident power density prescribed by the ICNIRP guidelines at each frequency. As indicated in **Table 4**, our proposed method requires almost three time longer than the conventional one using constant permittivity at a frequency, however, the conventional method can only provide WBA-SAR at only one frequency per FDTD computation and number of time steps required to obtain the converged solution is different for each frequency (35). Meanwhile, the proposed method requires only a single FDTD run to determine the solutions at 24 analysis frequencies. Although the proposed method requires more memory usage, in consequence, it is shown to be very computationally efficient. As number of frequency points increases, efficiency of the proposed method increases at the

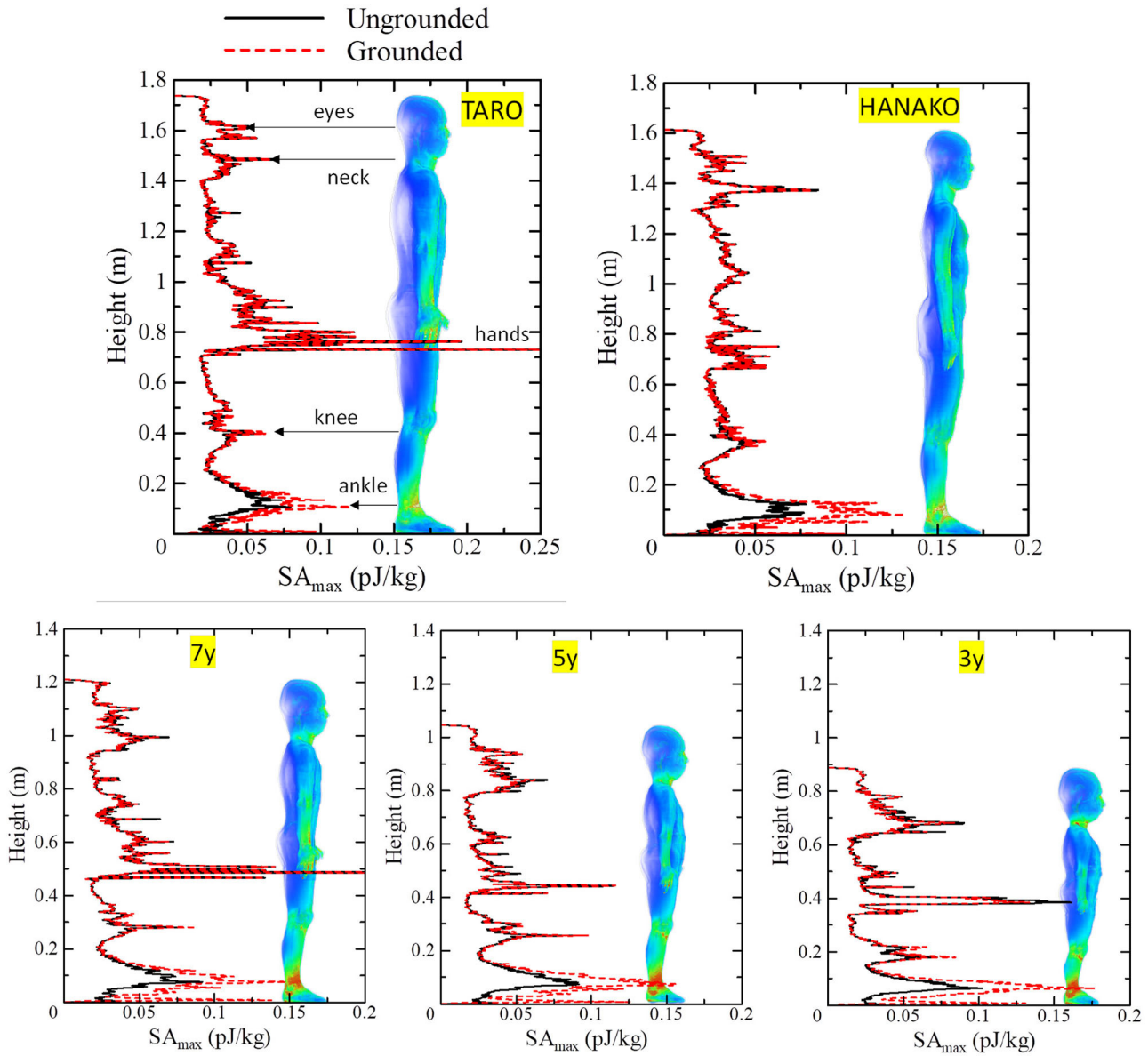

FIGURE 10 | Maximum SA at each height for various human models for 1 V/m electric field strength.

expense of using more memory. From **Figure 7**, the SAR peak is found at around 70 MHz for the ungrounded TARO model, which corresponds to the whole-body resonance and the peak frequency increases for the shorter HANAKO, 7-, 5-, and 3-y-child models. For grounded conditions, the SAR peaks occur at 40 and 70 MHz for the adult and 3-y-child models, respectively. These results are in good agreement with those indicated in the literature (32, 34).

Figures 8, **9** show SA distributions on the human surface for ungrounded and grounded cases, respectively. For the ungrounded cases, SA peaks appear at the ankles, wrists (hand), forearm, and neck; SA increases by 53% (adult male) to 74% (3-y-child) at the ankle, whereas SA at the other parts remain almost the same in the ungrounded cases. **Figure 10** shows the layer maximum SA at each height of various human bodies when exposed to an EM pulse of 1 V/m, polarized in the z-direction. The peak SA and the SA at the ankle for various human models, which are normalized to the ICNIRP-prescribed power density limit of 2 W/m^2, are summarized in **Table 5** (10). Note that the power density limit is constant for 10–400 MHz and increases with respect to the frequency over 400 MHz. Therefore, there is no prescribed limit value of the power density for a wideband

TABLE 5 | Maximum specific energy absorption normalized by an ICNIRP-prescribed power density limit of 2 W/m^2 for general exposures to various human model.

Model	Ungrounded case		Grounded case	
	Maximum SA (nJ/kg)	SA at the ankle (nJ/kg)	Maximum SA (nJ/kg)	SA at the ankle (nJ/kg)
Male (TARO)	0.401 (hand)	0.119	0.401 (hand)	0.182
Female (HANAKO)	0.127 (neck)	0.117	0.199 (ankle)	0.199
7-year child	0.437 (hand)	0.139	0.436 (hand)	0.223
5-year child	0.173 (hand)	0.138	0.237 (ankle)	0.237
3-year child	0.243 (hand)	0.154	0.267 (ankle)	0.267

TABLE 6 | Peak 1 g-averaged and 10 g-averaged SA normalized by an ICNIRP-prescribed power density limit of 2 W/m^2 for general exposures to various human model.

Model	Ungrounded case		Grounded case	
	1 g-averaged SA (pJ/kg)	10 g-averaged SA (pJ/kg)	1 g-averaged SA (pJ/kg)	10 g-averaged SA (pJ/kg)
Male (TARO)	0.0846	0.0536	0.1019	0.0616
Female (HANAKO)	0.0737	0.0433	0.1234	0.0632
7-year child	0.0821	0.0457	0.1310	0.0710
5-year child	0.0947	0.0507	0.1543	0.0839
3-year child	0.1013	0.0512	0.1691	0.0900

pulse such as one used in our study. However, we hereby use 2 W/m^2 for the normalization of SA in **Table 5** as it should provide conservative evaluations. The maximum SA appears at the hands for the adult male, 7-, 5-, and 3-y-child models for the ungrounded case, while it appears at the neck for the adult female model. This may be attributed to the proportion of biological tissues in the male and female human models is different since the female model contains more fat in each body part. Note that 7-, 5-, and 3-y-child models are proportionally morphed using a morphing algorithm (32). The maximum SA among five human models is 0.437 pJ/kg. Note that this SA value also depends on the waveform (which is the Gaussian pulse in our study). To reach a dose of 2 mJ/kg, as prescribed in the ICNIRP guidelines, we need to increase the field strength from 1 V/m to more than 83 kV/m or 9.14 MW/m^2, which does not seem realistic in real life. Note that SA is obtained from the value at a voxel and it should be smaller for an average over 10 g tissues. Hence, the SA values shown in **Table 5** assume a worst-case scenario. For compliance with the IEEE standards, the repetition rate of an incident pulse having a field strength of 87 kV/m must be $<$800 Hz or 800 pulses per second in order not to exceed the SA limit. In the grounded case, the maximum SA occurs at the ankle for the adult female, 5-, and 3-y-child while they are found at the same location (hands) in the ungrounded case for the adult male and 7-y-child. It is found that energy absorption at the ankle increases when the human body is grounded, while that at the other parts remains almost unchanged for all the models used in this study. **Table 6** shows the peak 1 g-averaged and 10 g-averaged SAs normalized by a power density limit of 2 W/m^2. It is shown that the peak 1 g-averaged and 10 g-averaged SAs are higher in the grounded cases than those in the ungrounded cases for all models. The increases in the SAs are significant in a smaller model, e.g., for the grounded 3-y-child model, the peak 1 g-averaged and 10 g-averaged SAs are $\sim$1.67 and 1.76 than those of the ungrounded cases. These results provide the first ever demonstration that the SA distribution due to broadband EM pulse illumination can be quantitatively evaluated in detail and compared with the SA limit prescribed in international guidelines or standards. Further detailed exposure levels for different incident angles, different pulse shapes, and postures will be investigated in the future.

CONCLUSION

We have performed numerical dosimetry on human bodies illuminated by an EM pulse from the front by using the (FD)^{2}TD method, previously proposed by the authors. The method fully considers broadband characteristics of the complex relative permittivity of the biological media used in the analysis model via the application of the FILT and the Prony method. Firstly, we demonstrated the validity of the update coefficients, i.e., the residues and poles of the expression for the IIR in the z-domain, by comparing the numerical reflection coefficients with those derived from the EM theory. It was clarified that the numerical results within 2% of those obtained theoretically over a broad frequency range from 50 MHz to 10 GHz, demonstrating the validity of the proposed approach. It was also found that the transmission characteristics of the EM pulse into the CSF layer of a multilayer mimicking a human head are almost flat over a frequency range between 300 and 800 MHz and that the transmission decreases with increasing EM traveling distance from the skin boundary due to higher energy absorption at superficial biological tissues such as "Skin" and "Fat" when the frequency is higher than 1 GHz. Therefore, most of the pulse energy that penetrates into the biological body has a frequency below 1 GHz. Then, numerical dosimetry of various human models exposed to an EM pulse having a frequency component of up to $\sim$1.3 GHz was performed. The whole-body average SAR at 24 frequencies was determined by a single run of broadband FDTD simulations. The results matched those published in the literature, demonstrating the validity and availability of the proposed FDTD method. Then the SA distribution of each numerical model was determined, and it was found that the maximum SA occurs at the hands and neck for the ungrounded model, while they appear at the hands and ankle when the model is grounded. The maximum SA value was 0.290 pJ/kg for an incident electric field strength of 1 V/m or 0.437 nJ/kg for an incident power density of 2 W/m^2. It has been shown for the first time that, by using our proposed FDTD approach with the FILT and the Prony method, we can obtain quantitatively detailed information on SA that can be compared with the limits prescribed in international guidelines or standards.

DATA AVAILABILITY STATEMENT

The original contributions presented in the study are included in the article, further inquiries can be directed to the corresponding author.

AUTHOR CONTRIBUTIONS

JC designed and performed all the simulations, analyzed the data, and wrote the paper. KW and KF gave advices and revised the paper. All authors have read and agreed to the published version of the manuscript.

FUNDING

This study was financially supported by a JSPS Grant-in-Aid for Scientific Research (JP18K18376), Japan, parts of the numerical calculations were carried out on the TSUBAME3.0 supercomputer at Tokyo Institute of Technology.

REFERENCES

1. FCC. *Revision of Part 15 of the Commission's Rules Regarding Ultra-Wideband Transmission Systems* (2002).
2. Allen B, Dohler M, Okon E, Malik W, Brown A, Edwards D. *Ultra-Wideband Antennas and Propagation for Communications, Radar and Imaging*. West Sussex: John Wiley & Sons, Ltd. (2007).
3. Thotahewa KMS, Redout JM, Yuce MR. Propagation, power absorption, and temperature analysis of UWB wireless capsule endoscopy devices operating in the human body. *IEEE Trans Microwave Theory Tech.* (2015) 63:3823–33. doi: 10.1109/TMTT.2015.2482492
4. Hall PS. *Antennas and Propagation for Body-Centric Wireless Communications*. Norwood, MA: Artech House, Inc. (2006).
5. Gandhi OP, Furse CM. Currents induced in the human body for exposure to ultrawideband electromagnetic pulses. *IEEE Trans Electromagn Compat.* (1997) 39:174–80. doi: 10.1109/15.584941
6. Chou CK, Guy AW. Microwave-induced auditory responses in guinea pigs: relationship of threshold and microwave-pulse duration. *Radio Sci.* (1979) 14:193–7. doi: 10.1029/RS014i06Sp00193
7. Weaver JC, Smith KC, Esser AT, Son RS, Gowrishankar TR. A brief overview of electroporation pulse strength-duration space: a region where additional intracellular effects are expected. *Bioelectrochemistry.* (2012) 87:236–43. doi: 10.1016/j.bioelechem.2012.02.007
8. Lin JC. The microwave auditory effect. *IEEE J Electromagn RF Microwaves Med Biol.* (2021). doi: 10.1109/JERM.2021.3062826
9. Weil CM. Absorption characteristics of multilayered sphere models exposed to UHF/microwave radiation. *IEEE Trans Biomed Eng.* (1975) 22:468–76. doi: 10.1109/TBME.1975.324467
10. ICNIRP. Guidelines for limiting exposure to time-varying electric, magnetic, and electromagnetic fields (up to 300 GHz). International Commission on Non-Ionizing Radiation Protection. *Health Phys.* (1998) 74:494–522.
11. IEEE-C95.1. *IEEE Standard for Safety Levels With Respect to Human Exposure to Radio Frequency Electromagnetic Fields, 3 kHz to 300 GHz*. IEEE Std C951-2005 (Revision of IEEE Std C951-1991) (2006). p. 1–238.
12. ICNIRP. Guidelines for limiting exposure to electromagnetic fields (100 kHz to 300 GHz). *Health Phys.* (2020) 118:483–524. doi: 10.1097/HP.0000000000001210
13. Lin JC, Chuan-Lin W, Lam CK. Transmission of electromagnetic pulse into the head. *Proc IEEE.* (1975) 63:1726–7. doi: 10.1109/PROC.1975.10043
14. Lin JC. Interaction of electromagnetic transient radiation with biological materials. *IEEE Trans Electromagn Compat.* (1975) 17:93–7.
15. Gabriel S, Lau RW, Gabriel C. The dielectric properties of biological tissues: III. Parametric models for the dielectric spectrum of tissues. *Phys Med Biol.* (1996) 41:2271. doi: 10.1088/0031-9155/41/11/003
16. Luebbers R, Hunsberger FP, Kunz KS, Standler RB, Schneider M. A frequency-dependent finite-difference time-domain formulation for dispersive materials. *IEEE Trans Electromagn Compat.* (1990) 32:222–7. doi: 10.1109/15.57116
17. Kelley DF, Luebbers RJ. Piecewise linear recursive convolution for dispersive media using FDTD. *IEEE Trans Antennas Propag.* (1996) 44:792–7. doi: 10.1109/8.509882
18. Shibayama J, Ando R, Nomura A, Yamauchi J, Nakano H. Simple trapezoidal recursive convolution technique for the frequency-dependent FDTD analysis of a Drude–Lorentz model. *IEEE Photon Technol Lett.* (2009) 21:100–2. doi: 10.1109/LPT.2008.2009003
19. Goorjian PM, Taflove A. Direct time integration of Maxwell's equations in nonlinear dispersive media for propagation and scattering of femtosecond electromagnetic solitons. *Opt Lett.* (1992) 17:180–2. doi: 10.1364/OL.17.000180
20. Taflove A, Hagness SC. *Computational Electrodynamics: The Finite-Difference Time-Domain Method*. Artech House (2005).
21. Kashiwa T, Fukai I. A treatment by the FD-TD method of the dispersive characteristics associated with electronic polarization. *Microwave Opt Technol Lett.* (1990) 3:203–5. doi: 10.1002/mop.4650030606
22. Sullivan DM. Frequency-dependent FDTD methods using Z transforms. *IEEE Trans Antennas Propag.* (1992) 40:1223–30. doi: 10.1109/8.182455
23. Rekanos IT, Papadopoulos TG. FDTD modeling of wave propagation in Cole-Cole media with multiple relaxation times. *IEEE Antennas Wireless Propag Lett.* (2010) 9:67–9. doi: 10.1109/LAWP.2010.2043410
24. Mescia L, Bia P, Caratelli D. Fractional derivative based FDTD modeling of transient wave propagation in Havriliak-Negami media. *IEEE Trans Microwave Theory Tech.* (2014) 62:1920–9. doi: 10.1109/TMTT.2014.2327202
25. Chakarothai J. Novel FDTD scheme for analysis of frequency-dependent medium using fast inverse Laplace transform and Prony's method. *IEEE Trans Antennas Propag.* (2019) 67:6076–89. doi: 10.1109/TAP.2018.2878077
26. Chakarothai J, Watanabe S, Wake K. Numerical dosimetry of electromagnetic pulse exposures Using FDTD Method. *IEEE Trans Antennas Propag.* (2018) 66:5397–408. doi: 10.1109/TAP.2018.2862344
27. Chakarothai J, Wake K, Watanabe S, Chen Q, Sawaya K. Frequency dependent FDTD method for ultra-wideband electromagnetic analyses. *IEICE Trans Electr.* (2019) J102-C:102–13.
28. Kensuke S, Kanako W, Soichi W. Development of best fit Cole-Cole parameters for measurement data from biological tissues and organs between 1 MHz and 20 GHz. *Radio Sci.* (2014) 49:459–72. doi: 10.1002/2013RS005345
29. Abdalla A, Teoh A. A multi layered model of human head irradiated by electromagnetic plane wave of 100MHz–300 GHz. *Int J Sci Res.* (2005) 15:1–7.
30. Sabbah AI, Dib N, Al-Nimr M. Evaluation of specific absorption rate and temperature elevation in a multi-layered human head model exposed to radio frequency radiation using the finite-difference time domain method. *Microwaves Antennas Propag IET.* (2011) 5:1073–80. doi: 10.1049/iet-map.2010.0172
31. Nagaoka T, Watanabe S, Sakurai K, Kunieda E, Watanabe S, Taki M, et al. Development of realistic high-resolution whole-body voxel models of Japanese adult males and females of average height and

weight, and application of models to radio-frequency electromagnetic-field dosimetry. *Phys Med Biol.* (2004) 49:1–15. doi: 10.1088/0031-9155/49/1/001
32. Nagaoka T, Kunieda E, Watanabe S. Proportion-corrected scaled voxel models for Japanese children and their application to the numerical dosimetry of specific absorption rate for frequencies from 30 MHz to 3 GHz. *Phys Med Biol.* (2008) 53:6695. doi: 10.1088/0031-9155/53/23/004
33. Chakarothai J, Fujii K, editors. A Unified approach for treatment of frequencydependent materials in FDTD method. In: *2019 International Symposium on Antennas and Propagation (ISAP)*. Xi'an (2019).
34. Wang J, Fujiwara O, Kodera S, Watanabe S. FDTD calculation of whole-body average SAR in adult and child models for frequencies from 30 MHz to 3 GHz. *Phys Med Biol.* (2006) 51:4119. doi: 10.1088/0031-9155/51/17/001
35. Chakarothai J, Wake K, Watanabe S. Convergence of a Single-Frequency FDTD Solution in Numerical Dosimetry. *IEEE Trans Microwave Theory Tech.* (2016) 64:707–14. doi: 10.1109/TMTT.2016.2518661

Conflict of Interest: The authors declare that the research was conducted in the absence of any commercial or financial relationships that could be construed as a potential conflict of interest.

frontiers in Public Health

REVIEW
published: 17 August 2021
doi: 10.3389/fpubh.2021.691880

Effects of Radiofrequency Electromagnetic Radiation on Neurotransmitters in the Brain

Cuicui Hu[1,2], *Hongyan Zuo*[2*] *and Yang Li*[1,2*]

[1] *Anhui Medical University, Academy of Life Sciences, Hefei, China,* [2] *Department of Experimental Pathology, Beijing Institute of Radiation Medicine, Beijing, China*

With the rapid development of electronic information in the past 30 years, technical achievements based on electromagnetism have been widely used in various fields pertaining to human production and life. Consequently, electromagnetic radiation (EMR) has become a substantial new pollution source in modern civilization. The biological effects of EMR have attracted considerable attention worldwide. The possible interaction of EMR with human organs, especially the brain, is currently where the most attention is focused. Many studies have shown that the nervous system is an important target organ system sensitive to EMR. In recent years, an increasing number of studies have focused on the neurobiological effects of EMR, including the metabolism and transport of neurotransmitters. As messengers of synaptic transmission, neurotransmitters play critical roles in cognitive and emotional behavior. Here, the effects of EMR on the metabolism and receptors of neurotransmitters in the brain are summarized.

Keywords: EMR, brain, neurotransmitter, metabolism, transmission, receptor

OPEN ACCESS

Edited by:
Lei Zhang,
Third Military Medical University, China

Reviewed by:
Yael Stein,
Hadassah Medical Center, Israel
Sareesh Naduvil Narayanan,
Ras al-Khaimah Medical and Health Sciences University, United Arab Emirates
Gui Rong Ding,
Fourth Military Medical University, China

***Correspondence:**
Hongyan Zuo
zuohy2005@126.com
Yang Li
leeyoung109@hotmail.com

Specialty section:
This article was submitted to Radiation and Health, a section of the journal Frontiers in Public Health

Received: *07 April 2021*
Accepted: *13 July 2021*
Published: *17 August 2021*

Citation:
Hu C, Zuo H and Li Y (2021) Effects of Radiofrequency Electromagnetic Radiation on Neurotransmitters in the Brain. Front. Public Health 9:691880. doi: 10.3389/fpubh.2021.691880

BACKGROUND

Electromagnetic radiation (EMR) is closely related to human life and originates from various electrical systems, such as mobile phones, microwave ovens, communication base stations, high-voltage lines, electronic instruments and other electromagnetic equipment. EMR produces various electromagnetic waves of different frequencies, resulting in the increasing EMR intensity in human living spaces. The high-frequency waves such as cosmic, gamma and X-rays, have enough energy to cause ionization. Non-ionizing electromagnetic waves, including ultraviolet, visible region, infrared, microwave, and radio waves are frequently used in daily life, especially radiofrequency electromagnetic fields (RF-EMFs, 30 kHz-300 GHz) for communications, and extremely low-frequency EMFs (ELF-EMFs, 3 Hz-3 kHz) generated by electricity. RF is also commonly referred to as microwave (MW) radiation. The impact of EMR on human health has also gradually attracted attention, and the modulation of brain functional connectivity was observed in human body (1–3). This review summarizes the effects of RF-EMF on neurotransmitters in the brain.

The effects of EMR on body systems might depend on the frequency, intensity and power of radiation, so the parameters of EMR provide a challenge for a literature review. Specific absorption rate (SAR) measures the rate of energy absorbed by the human body when exposed to electromagnetic fields between 100 kHz and 10 GHz. With the unit of watt per kilogram (W/kg), SAR reflects the power absorbed per mass of tissue. The SAR value depends on the frequency, incident direction, E-polarization direction, and the structure of different tissues.So far, the SAR values range from 10^{-4} to 35 W/kg in those reported studies on the bioeffects of microwave radiation.

Numerous studies have shown that the nervous system is an important target organ system sensitive to EMR. Exposure to electromagnetic fields can cause structural and functional changes in the nervous system (4–7). Neurotransmitters are specific chemicals that act as messengers during synaptic transmission within the nervous system. Many studies have shown that EMR affects the metabolism and transport of neurotransmitters (8). It is well understood that neural circuit is the structural basis of brain function, and the brain works by the interplay of various brain regions and many neurotransmitters. Consequently, the modulatory effect of EMR on neurotransmitter levels in various brain regions may play a critical role in the brain functioning. According to many studies, RF-EMR exposure can induce the imbalance of amino acid neurotransmitters in various parts of the brain (9, 10).

Neurotransmitters are synthesized by nerve cells and transported into the synaptic vesicles of presynaptic cells. Through action potentials, transmitter release at synaptic endings is mediated by calcium ion channels; transmitters are then diffused through the synaptic cleft and act on specific receptors on postsynaptic neurons or effector cells, thus transferring information from presynapses to postsynapses (11). The action of neurotransmitters can be discontinued by recycling; that is, excess neurotransmitters in the synaptic cleft are recycled to presynaptic neurons by the action of presynaptic vectors and are stored in vesicles. Neurotransmitter activity can also be aborted by enzymatic hydrolysis; for instance, dopamine (DA), is metabolically inactivated by the actions of monoamine oxidase located in mitochondria and catechol-O-methyltransferase (COMT) located in the cytoplasm (12). Neurotransmitters are involved in the processes of brain development, including neurotransmission, differentiation, and the formation of neural circuitry. They enable neurons to communicate with each other, and alterations in the levels of specific neurotransmitters are related to various neurological disorders, such as depression, schizophrenia, Alzheimer disease, and Parkinson disease (13). Neurotransmitters in the central nervous system are usually divided into four categories based on their chemical constitution. Biogenic amines include DA, norepinephrine (NE), epinephrine (E), 5-hydroxytryptamine (5-HT), etc. Amino acids include γ-aminobutyric acid (GABA), glycine, glutamate, acetylcholine (Ach), etc. Peptide neurotransmitters include endogenous opioid peptides and other varieties. The remaining category of transmitters includes other types, such as nitric oxide (NO) and substance P. Pertinently, the current review discusses the pivotal studies that shed light on the neurotransmitters in the brain in the above mentioned four categories when they encountered EMR exposure, thus providing an overview of the metabolism and receptor changes of these neurotransmitters.

For the literature retrieval, we searched all the articles in the NCBI PubMed database, with the keywords of each "neurotransmitter" and "electromagnetic field" or "radiofrequency electromagnetic field," and selected the published articles written in English and referring to neurotransmitter measurement in the brain encounter with RF-EMF exposure. Overall, 21 articles related to neurotransmitters with short-term EMR exposure were discussed in the text and summarized in **Table 1**, and 19 articles related to neurotransmitters with long-term EMR exposure were discussed in the text and summarized in **Table 2**.

EFFECTS OF EMR ON BIOLOGICAL AMINE NEUROTRANSMITTERS

Effects of EMR on Dopamine (DA)

As a precursor of norepinephrine, DA is a key neurotransmitter in the hypothalamus and pituitary gland. It is mainly responsible for activity in the brain associated with reward, learning, emotion, motor control, and executive functions. DA also correlates to psychiatric and neurological disorders, including Parkinson disease, multiple sclerosis, and Huntington disease (13). It has been suggested that DA inhibits the secretion of gonadotropin-releasing hormone, and there is an axonal connection and interaction between gonadotropin-releasing hormone and DA in nerve endings (49). Deficiency of DA in the basal ganglia is seen in patients with Parkinsonism (50). DA also has some role in Schizophrenia—striatal DA is increased, and cortical DA transmission is altered (51, 52).

Several studies reported the effects of EMR on DA. For example, adult rats undergoing daily EMR exposure for 1 h, with an EMR frequency of 1,800 MHz, a specific absorption rate (SAR) value of 0.843 W/kg, power density of 0.02 mW/cm^2, induced a significant decrease in DA in the hippocampus after 2 months of exposure and 1 month after cessation of exposure. This study indicated that EMR exposure may reduce DA production in the hippocampus, affect rat arousal, and contribute to decreased learning and memory ability after exposure to EMR (14). Maaroufi et al. exposed rats to 900 MHz EMF, 1 h/day during 21 consecutive days, with the minimum SAR 0.05 W/kg and the maximum SAR 0.18 W/kg, depending on the position of the rat in the field. A decrease in DA was observed in the hippocampus of the EMR exposed group. Moreover, there is a significant difference of DA and dihydroxyphenyl acetic acid (DOPAC) between hippocampus and striatum in the EMR exposed group (34). Furthermore, exposure to a RF-EMR of 835 MHz, SAR value of 4.0 W/kg, for 5 h/day for 12 weeks, led to a reduction in DA concentration in the striatum of C57BL/6 mice (33). The above studies suggest that a certain intensity of microwave radiation can lead to abnormal metabolism of monoamine neurotransmitters in the hippocampus and striatum.

Inaba et al. exposed adult rats to microwave radiation for 1 h, with the frequency of 2,450 MHz, and at power densities of 5 and 10 mW/cm^2 respectively. The DOPAC content in the pons and medulla oblongata, the DA turnover rates and the DOPAC:DA ratio increased significantly in the striatum and cerebral cortex only at a power density of 10 mW/cm^2, but no significance was observed in the DA content of any region of the brain at a power density of 5 mW/cm^2 (15). In addition, 32 pregnant Wistar rats were divided into control group, low-dose group (receiving mobile phone radiation for 10-min periods), middle-dose group (receiving mobile phone radiation for 30-min periods), and high-dose group (receiving mobile phone radiation for 60-min periods). Rats underwent

TABLE 1 | The influence of short-term EMR exposure on neurotransmitters in the brain.

Neurotransmitter	Reference	Sample/Model	Exposure condition	Results
DA	Aboul Ezz et al. (14)	Adult rats	1800 MHz, 0.843 W/kg, 0.02 mW/cm^2, 1 h	DA decrease in the hippocampus
	Inaba et al. (15)	Rats	2450 MHz, 5 and 10 mW/cm^2, 1 h	DOPAC increase in the pons and medulla oblongata at 10 mW/cm^2
5-HT	Inaba et al. (15)	Rats	2450 MHz, 5 and 10 mW/cm^2, 1 h	5-HIAA increase in the cerebral cortex at 5 and 10 mW/cm^2. 5-HIAA:5-HT ratio increase in the cerebral cortex at 5 mW/cm^2. 5-HT turnover rate increase in the pons and medulla oblongata
	Ishikawa et al. (16)	Male Wistar rats	2450 MHz, 5 kW; 0.5 or 1.5 s	5-HIAA decrease at 0.5 s; 5-HIAA increase at 1.5 s
Glutamate & aspartic acid	Karri et al. (17)	Wistar rats	30 mW/cm^2, 10 min	Glutamate and aspartic acid decrease 1 day after radiation
	Wei et al. (1)	Male Wistar rats	5,10,30, and 100 mW/cm^2; 5 min	Glutamate and aspartic acid decrease in the hippocampus within 7 days after radiation, especially in the 10 mW/cm^2 group
	Mausset-Bonnefont et al. (18)	Rats	900 MHz, 6 W/kg, 15 min	NR1 decrease in the cortex; NR2A decrease in the cortex and hippocampus; NR2B decrease in the striatum
	Zhang et al. (19)	Rats	12.0 W/kg, 65 mW/cm^2, 20 min	NR1 decrease at 3 h, 24 h, and 3 days; NR2A decrease at 0 h, 3 h, and 12 h; NR2C decrease at 0 h and 24 h; NR2D increase at 0 h, 12 h, 24 h, and 3 days in the hippocampus after radiation
	Wang et al. (20)	Rats	65 mW/cm^2, 12.0 W/kg, 20 min	NR1, NR2A, NR2C decrease; NR2D increased in the hippocampus
	Xiong et al. (21)	Male Wistar rats	2.856 GHz, 30 mW/cm^2, for 10 min every other day three times	NR2A increase at 7 days; NR2B increase at 1 day in the hippocampus
GABA	Qiao et al. (22)	Wistar rats	30 mW/cm^2, 5 min	GABA decrease in the hippocampus
	Wang et al. (23)	Wistar rats	2.856 GHz, 50 mW/cm^2, 6 min	GABA decrease at 6 months
	Noor et al. (9)	Male albino rats	900 MHz, 1.165 W/kg, 0.02 mW/cm^2, 1 h/day	Glycine increase in the midbrain after 1 month
	Wang et al. (24)	Rats	900 MHz, 2.23 W/kg, 6 mW/cm^2	GABA receptor upregulation in cultured neurons
ACh	Fujiwara et al. (25)	Mice	2.45 GHz	Transient elevated ACh content in the brain
	Lai et al. (26)	Rats	2.45 GHz, 0.6 W/kg, 20 min	Choline uptake activity increase in the frontal cortex, hippocampus, and hypothalamus
	Krylova et al. (27)	Rats	2.35 GHz, 1 mW/cm^2	Decreased mAChR activity; increased number of mAChR receptors in the cerebral cortex
	Testylier et al. (28)	Rats	2.45 GHz, 4 mW/cm^2, 1 h	ACh decrease in the hippocampal CA1 area
	Lai et al. (29)	Rats	Pulsed (2 μs, 500 pps) or continuous wave 2450 MHz microwaves, 45 min	Choline uptake decreased in the frontal cortex
Peptides	Lai et al. (30)	Rats	2450 MHz, 0.6 W/kg, 1 mW/cm^2, 45 min	Three subtypes of opioid receptor blocked cholinergic activity decrease in the hippocampus induced by microwave radiation
	Lai et al. (31)	Rats	2450 MHz, 0.6 W/kg, 1 mW/cm^2, 45 min	Pretreatment with opioid antagonists naltrexone or cholinergic agonists inhibited microwave-induced radial arm maze learning disorders
NO	Burlaka et al. (32)	Wistar rats	0.465 GHz, 1.0-6.0 mW/cm^2 pulse duration 2 ms, 17.5 min	NO synthesis increase in mitochondria of neural cells, NO synthase increase in the brain

periods of radiation three times daily from the day of pregnancy continuously for 20 days. Then, the effects of mobile phone radiation on monoamine neurotransmitters in the brain tissue of fetal mice were studied, with a center frequency of 900 MHz, and a SAR value of 0.9 W/kg. The results showed that the DA content in the brain tissue of fetal mice increased

TABLE 2 | The influence of long-term EMR exposure on neurotransmitters in the brain.

Neurotransmitter	Reference	Sample/Model	Exposure condition	Results
DA	Kim et al. (33)	C57BL/6 mice	835 MHz, 4.0 W/kg, 5 h/day for 12 weeks	DA decrease in the striatum
	Maaroufi et al. (34)	Rats	900 MHz, 1 h/day for 21 days, 0.05 W/kg< SAR< 0.18 W/kg	DA decrease in in the hippocampus
	Ji et al. (35)	Pregnant Wistar rats	900 MHz, 3 times daily for 20 days; 10, 30, or 60 min each time	DA increases in brain tissue of both pregnant and fetal mice in the 10 min group; DA decrease in the 60 min group
NE and E	Megha et al. (36)	Male Fischer 344 rats	1800 MHz, 1 mW/cm^2, 2 h/day, 5 days/week for 30 days	NE and E decrease in the hippocampus
	Cao et al. (37)	Male LACA mice	900 MHz, 0, 1, 2 and 5 mW/cm^2; 0, 0.22, 0.44 or 1.1 W/kg; 1 h/day for 35 days	NE increase at 1 mW/cm^2
	Ji et al. (35)	Pregnant rats	900 MHz,0.9W/kg, m 3 times daily for 20 days; 10, 30, or 60 min each time	NE increase in the 10 min group; NE decrease in the 60 min group
5-HT	Li et al. (38)	Wistar rats	2.856 GHz, 5, 10, 20, 30 mW/cm^2; 3 times per week for up to 6 weeks	5-HT increase in the hippocampus from 28 days to 2 months at 30 mW/cm^2
	Aboul Ezz et al. (14)	Adult rats	1800 MHz, 1 h/day for 1, 2 and 4 months, 0.843 W/kg,0.02 mW/cm^2	5-HT increase in the hippocampus, hypothalamus and midbrain
	Maaroufi et al. (34)	rats	900 MHz, 1 h/day for 21 days, 0.05 W/kg< SAR< 0.18 W/kg	5-HIAA decrease, the 5-HIAA/5-HT ratio decrease in the cerebellum
Glutamate & aspartic acid	Ahmed et al. (39)	Rats	1800 MHz, 0.843 W/kg, 0.02 mW/cm^2; 1 h/day for 1, 2, or 4 months	Glutamate and glutamine decrease in the hippocampus after 1 month
	Wang et al. (20)	Wistar rats	30 mW/cm^2 for 5 min/day, 5 days/week, 2 months	Glutamate increase and NR2B decrease in the hippocampus and cerebrospinal fluid
	Zhao et al. (40)	Male Wistar rats	2.5, 5 and 10 mW/cm^2, 6 min/day, 1 months	Glutamate and aspartic acid, increase in the 2.5 and 5 mW/cm^2 groups and decrease in the 10 mW/cm^2 group in the hippocampus
	Wang et al. (41)	Male Wistar rats	2.856 GHz; 0, 2.5, 5 and 10 mW/cm^2 for 5 min/day, 5 days/week and up to 6 weeks	NR2B and p-NR2B decrease in the 10 mW/cm^2 group; NR2A decrease in the 10 mW/cm^2 group at 1 day and 6 months
	Huang et al. (42)	Female Wistar rats	1800 MHz, 0.5 mW/cm^2 and 1.0 mW/cm^2, 12 h/day for 21 days	For the 0.5 mW/cm^2 group, NR2A decrease in the CA3 region, NR2B decrease in the CA1 and CA3 regions. For the 1.0 mW/cm^2 group, NR2A decrease in the CA1 and CA3 regions and an NR2B decrease in the CA1 region, CA3 region, and DG
GABA	Zhang et al. (43)	Male mice	1.8 GHz, 4 weeks	GABA and aspartic acid decrease in the cortex and hippocampus
ACh	Kumar et al. (44)	Mice	2.45 GHz, 2 h/day, 1 months	M1 AChRs upregulated; AChE activity increased in the hippocampus
	Gökçek-Saraç et al. (45)	Wistar rats	2.1 GHz, 45 V/m and 65 V/m, 1 week	AChE, ChAT, and VAChT decrease in rat hippocampus after exposure to 65 V/m
	Gupta et al. (46)	Rats	2.45 GHz, 1 h/day for 28 consecutive days	ACh decrease, AChE activity increased in the hippocampus
	Kunjilwar and Behari (47)	Rats	147 MHz, subharmonics of 73.5 MHz and amplitude of 36.75 MHz modulated at 16 Hz and 76 Hz, 3 h/day, for 30-35 consecutive days	AChE decrease in the brain
NO	Qin et al. (48)	Mice	0.9 V/m, 6 h/day, 12 h/day, and 18 h/day, 30 days	NO increase in the brain

in the low-dose group but decreased in the high-dose group, and no significant changes were observed in the middle-dose group, which suggested that long-term mobile phone radiation could cause abnormal DA content in the central nervous system in fetal mice and might affect the brain development of mice (35). In summary, these studies indicate that EMR can lead to metabolic disorders of monoamine neurotransmitters in the brain, depending on the intensity of radiation exposure, and might in theory result in abnormal emotional behavior.

Effects of EMR on Norepinephrine and Epinephrine

As a neurotransmitter, norepinephrine is mainly synthesized and secreted by sympathetic postganglionic neurons and adrenergic nerve endings in the brain. A small number of norepinephrine is produced in adrenal medulla as a hormone (53). It can bind to two types of adrenergic receptors, α and β, but it mainly binds to α receptors (including $\alpha 1$ and $\alpha 2$). Norepinephrine can be converted to epinephrine through N-methylation (54). The release of norepinephrine in the brain plays a role in various processes, such as stress, attention, sleep, inflammation, and the responses of the autonomic nervous system (13). Megha et al. found that after 30 days (2 h/day, 5 days/week) of continuous 1,800 MHz, 1 mW/cm^2 microwave radiation, the levels of norepinephrine and epinephrine in rat hippocampal tissue were significantly decreased, indicating that certain conditions of microwave radiation could lead to a decrease in norepinephrine and epinephrine contents in the brain (36). Cao et al. applied 900 MHz microwave radiation to male LACA mice. The radiation intensity used was 0, 1, 2, and 5 mW/cm^2; the SAR values were 0, 0.22, 0.44, and 1.1 W/kg, respectively; mice were exposed for 1 h/day for 35 consecutive days. The results showed that the brain norepinephrine content increased significantly when EMR intensity was 1 mW/cm^2, but no obvious changes in norepinephrine content were observed when exposure intensity was 2 or 5 mW/cm^2 (37). This further suggests that low-intensity EMR exposure can cause an increase in norepinephrine content in the brain, which might in theory affect epinephrine content, leading to neurotransmitter production disorders.

Moreover, Ji et al. performed experiments on pregnant rats by exposing them to microwave radiation from 900 MHz cellular phones with the SAR value of 0.9W/kg. The control, low, middle and high dose group received 0, 10, 30, and 60 min radiation each time respectively. The radiation was applied three times a day from the first day of pregnancy for 20 consecutive days. The results showed that the norepinephrine content in the fetal rats of the low dose group increased, and the norepinephrine content in the fetal rats of the high dose group decreased significantly, compared with that in the control group (35). Together, these results suggest that long-term exposure to EMR may lead to abnormal norepinephrine and epinephrine contents in the brain, depending on the dose of radiation.

Effects of EMR on 5-Hydroxytryptamine "Serotonin"

5-hydroxytryptamine (5-HT) is massively synthesized in the gastrointestinal tract (mainly in enterochromafin cells), whereas only a small percentage is produced within the nervous system. In the brain, 5-HT cell bodies, mainly localized in the raphe nuclei, and send axons to almost every brain region (55). As an inhibitory neurotransmitter, 5-HT is mainly distributed in the pineal gland and hypothalamus, especially in the cerebral cortex and neural synapses. 5-HT contributes to the regulation of physiological functions such as mood, feeding, cognition, memory, pain, sleep, and body temperature maintenance (56), and these physiological functions have been reported as indicators of brain injury induced by electromagnetic radiation (57). Consequently, 5-HT might play an important role in the neurobiological effects of EMR. Few studies have reported the effect of microwave radiation on 5-HT. It was reported that rats were exposed to microwave radiation for 1 h, with a frequency of 2,450 MHz, at power densities of 5 and 10 mW/cm^2. The 5-hydroxyindoleacetic acid (5-HIAA) content in the cerebral cortex was significantly increased after microwave exposure at power densities of 5 and 10 mW/cm^2. The 5-HT turnover rates and the 5-HIAA:5-HT ratio in the cerebral cortex increased significantly at a power density of 5 mW/cm^2. However, there were no obvious changes in 5-HT content in the brain of microwave-exposed rats. Consistently, the 5-HT turnover rate was significantly increased in the pons, medulla oblongata and hypothalamus at a power density of 10 mW/cm^2 (15).

Li et al. exposed Wistar rats to 2.856 GHz microwave radiation, with mean power densities of 5, 10, 20, and 30 mW/cm^2, separately, three times per week for up to 6 weeks. Spatial learning and memory function, the hippocampal morphological structure, electroencephalogram (EEG) data and neurotransmitter content of rats were tested after the last exposure. The results showed that the content of 5-HT in the hippocampus and cerebrospinal fluid of rats in each radiation group increased significantly from 28 days to 2 months after exposure, and these changes were related to the decrease in learning and memory ability, abnormal hippocampal morphology and abnormal EEG results induced by microwave radiation (38). Maaroufi et al. reported the 5-HT increase, the 5-HIAA decrease and the 5-HIAA/5-HT ratio decrease in the cerebellum of rats, exposed to 900 MHz EMF, 1 h/day for 21 consecutive days, with the minimum SAR 0.05 W/kg and the maximum SAR 0.18 W/kg (34). Moreover, the 5-HT increase was found in the hippocampus, hypothalamus and midbrain of adult rats, after 1,800 MHz, 1 h/day for 1, 2, and 4 months EMR exposure respectively, with SAR value of 0.843 W/kg, and power density of 0.02 mW/cm^2 (14). These studies suggest that long-term exposure to microwave radiation can lead to an increase in 5-HT in the brain, indicating a disorder in the metabolism of the neurotransmitter.

Additionally, the effect of microwave radiation on monoamine metabolism was investigated in the cortex, striatum and hippocampus of the rat brain, with the maximum power level of 5 kW at 2,450 MHz, and the radiation durations of 0.5 and 1.5 s. High-performance liquid chromatography (HPLC) with electrochemical detection was used to determine the concentrations of intracerebral monoamines and their metabolites. The concentrations of norepinephrine, DA and 5-HIAA were reduced by 0.5 s radiation. While the levels of these monoamines were increased by 1.5 s radiation (16). Whereas, another study on pregnant rats exposing to 900 MHz cellular phones, showed no significant difference in the content of 5-HT of fetal rats, in different intensities of microwave radiation groups (35). Altogether, further studies are necessary to illuminate the role of 5-HT in EMR-induced learning and memory dysfunction and morphological changes in the brain.

EFFECTS OF EMR ON AMINO ACID NEUROTRANSMITTERS

Effects of EMR on Excitatory Amino Acid Neurotransmitters

Glutamate is the major excitatory neurotransmitter in the nervous system. Glutamate receptors distribute in neurons and glia of the brain and spinal cord. The C-terminus and carbon backbone of glutamate derive from glucose. After crossing the blood-brain barrier through astrocytic end feet, glucose is broken down to pyruvic acid *via* glycolysis in the cytosol. Then pyruvic acid enters the tricarboxylic acid (TCA) cycle, and α-ketoglutarate is generated. Pyruvic acid is finally transmitted to receive an amino group donated by leucine, isoleucine and valine, aspartate, γ-aminobutyric acid (GABA) and alanine etc. (58). In addition, glutamate also acts as a metabolic precursor to GABA and a component of various amino acid-based derivatives, such as the antioxidant glutathione. Metabolic studies have shown that all of the glucose is eventually converted to glutamate in the CNS, which indicating the key role of glutamate in multiple aspects of brain physiology (59, 60).

In addition to glutamate, aspartate is another excitatory neurotransmitter with high concentrations in the CNS. The synthetic and metabolic enzymes for both glutamate and aspartate are localized to neurons and glial cells, especially in the mitochondria of neurons involved in the TCA cycle of glucose metabolism. Using oxaloacetic acid as raw materials, catalyzed by aminotransferase, aspartate is synthesized and stored in axon terminals. When nerve impulses are transmitted to axonal terminals, glutamate and aspartate are released by the presynaptic membrane and rapidly diffuse into the postsynaptic membrane; here, they bind to their corresponding receptors and prompt the opening of sodium and potassium channel gates to produce excitatory effects. The presynaptic membrane and glial cells reuptake a small amount of glutamate and aspartate.

Wistar rats were exposed to 30 mW/cm^2 for 10 min of microwave radiation, and HPLC was used to detect changes in the levels of neurotransmitters, such as aspartate and glutamate, in the hippocampus 1, 7, 14, and 28 days after radiation. The results showed that the contents of aspartate and glutamate decreased 1 day after radiation, suggesting that acute EMR exposure could reduce the amount of excitatory amino acids in the hippocampus (17). Consistently, Ahmed et al. investigated the effect of EMR on the concentrations of amino acid neurotransmitters in the hippocampus, striatum, and hypothalamus of juvenile and young adult rats. The animals were divided into the control group and the exposure group, and the exposure group was subjected to 1,800MHz EMR, with SAR value of 0.843 W/kg, power density of 0.02 mW/cm^2, 1 h daily for 1, 2, and 4 months. The results showed EMR induced significant decreases in glutamate and glutamine levels in hippocampal after 1 month (39). These data suggest that EMR can lead to a decrease in excitatory amino acid neurotransmitters in the hippocampus, which may affect the excitatory-inhibitory balance of neurons, thus causing a decline in learning and memory ability.

On the other hand, some studies have reported an increase in glutamate in the brain after radiation. Wang et al. exposed 160 Wistar rats to microwave radiation at 30 mW/cm^2 for 5 min/day, 5 days/week, over a period of 2 months. The learning and memory ability, amino acid contents in the hippocampus and cerebrospinal fluid, and N-methyl D-aspartate receptor (NMDAR) subtype 2B (NR2B) expression were then investigated. Following microwave exposure, rats exhibited a significant decrease in learning and memory ability at 7 days and the glutamate contents in their hippocampus and cerebrospinal fluid increased, whereas the expression of NR2B protein decreased (20). Zhao et al. performed microwave exposure on 184 male Wistar rats for 6 min/day, over one month, at average power densities of 2.5, 5, and 10 mW/cm^2. Morris water maze was applied to examine the learning and memory abilities. The concentrations of neurotransmitter in the hippocampus was detected by HPLC. The learning and memory ability of rats showed a significant decrease at 7, 14, and 1 month, following all three long-term microwave exposures. The concentrations of glutamate, aspartic acid, glycine, and GABA in the hippocampus were all increased for both 2.5 and 5 mW/cm^2 groups, but these four amino acids were decreased in the 10 mW/cm^2 group (40). These data further suggest the neurotransmitter disruption in the hippocampus might result in impairment of cognitive function caused by long-term microwave exposure.

Glutamate receptors are mainly constitutive of two types. The first type comprises ionic receptors, including NMDAR, kainate receptors (KARs) and α-amino-3-hydroxy-5-methyl-4-isoxazole receptors (AMPARs), which are conjugated with ion channels to form receptor channel complexes and mediate fast signal transmission. The second type encompasses metabolic receptors (mGluRs), which are conjugated to G proteins in the membrane. After being activated, these receptors act through a signal transduction system composed of a G-protein effector enzyme and a second messenger in the brain and produce a slow physiological response. Each NMDAR contains two binding recognition sites for glutamate and glycine, both of which are specific activators of the receptor (61). NMDARs are most often composed of two NR1 subunits and two NR2 subunits, and are highly permeable to Ca^{2+}. NR1 is the basic subunit of NMDAR. For NR2 subunit, there are four subtypes including NR2A, NR2B, NR2C and NR2D. Glutamate binds to the NR2 subunits, while glycine binds to the NR1 subunit. The function of NMDARs is mainly dependent on the N-terminal domain of NR2 subunits (61, 62). Some studies have investigated the influence of EMRs on NMDAR expression in the brain.

Wang et al. exposed 220 male Wistar rats to microwave radiation, with frequency of 2.856 GHz, for 5 min/day, 5 days/week, over 6 weeks, at average power densities of 0, 2.5, 5, and 10 mW/cm^2 respectively. For the 10 mW/cm^2 group, the escape latency of rats significantly prolonged in the navigation tests of the Morris water maze, at 7 days, 1, 3, and 9 months after radiation. At 3 days after radiation, a significant impairment of rats in the probe trials was found in the 10 mW/cm^2 group. Additionally, the protein levels of NR2A, NR2B and p-NR2B significantly decreased, and no significant change was observed for NR1 expression in the 10 mW/cm^2 group from 1 day to 12

months after radiation. This suggests that decreases in NR2A, 2B and p-NR2B might contribute to the impairment of cognitive functions induced by microwave radiation (41).

Mausset et al. using a head-only exposure device in rats, found that a 15 min exposure to 900 MHz pulsed microwaves at a SAR value of 6 W/kg induced a strong glial reaction in the brain, a significant reduction in NR1 subunits in the cortex, a reduction in NR2A in the cortex and hippocampus, and a reduction in NR2B in the striatum. This suggests that exposure to high-power 900 MHz pulsed microwave radiation promotes specific NMDAR degradation processes (18). Moreover, Huang et al. exposed four-week-old female Wistar rats to 1800 MHz microwaves, at power densities of 0.5 mW/cm^2 or 1.0 mW/cm^2, for 21 days and 12 h each day. The expression of NR2A and NR2B in the hippocampal CA1, CA3 and dentate gyrus (DG) was determined by immunohistochemistry. For NR2A, the expression in the 0.5 mW/cm^2 group was significantly lower than that in the 0 mW/cm^2 group in CA3, but no significant changes were noted in CA1 and the DG. The expression in the 1.0 mW/cm^2 group was significantly lower in CA1 and CA3, but no significant changes were found in the DG. For NR2B, the expression in the 0.5 mW/cm^2 group was significantly lower than that in the 0 mW/cm^2 group in CA1 and CA3. The expression in the 1.0 mW/cm^2 group was significantly lower in CA1, CA3 and the DG (42). This further suggests that the decrease of NR2A and NR2B induced by microwave exposure depends on the dose of radiation and the district of hippocampus.

In addition, after microwave radiation exposure of 65 mW/cm^2 for 20 min (SAR value 12.0 W/kg), the mRNA expression of the NR1 subunit in the hippocampus decreased at 3, 24 h, and 3 days, and the expression of the NR2A subunit decreased at 0 h, 3 h, and 12 h after microwave exposure. The mRNA expression of the NR2C subunit decreased at 0 and 24 h, but the expression of the NR2D subunit increased at 0, 12, 24 h, and 3 days after radiation. No significant changes in NR2B mRNA expression were observed (19). However, Xiong et al. exposed 48 male Wistar rats to 2.856 GHz, 30 mW/cm^2 microwave radiation, for 10 min every other day three times. The mRNA expression of the NR2A subunit notably increased at 7 days, and the mRNA expression of the NR2B subunit in the rat hippocampus increased at 1 day after microwave exposure (21). Together, these results indicate that the composition of subunits comprising NMDARs can be altered and that the autoregulation of NMDARs can be destroyed in the rat hippocampus after exposure to microwave radiation. Furthermore, microwave radiation may affect the expression of excitatory amino acids.

Effects of EMR on Inhibitory Amino Acid Neurotransmitters

GABA and glycine are the main inhibitory neurotransmitters in the brain, and GABA is an important neurotransmitter for approximately 50% of the synaptic sites in the central nervous system. GABA plays a critical role in the cerebral cortex, hippocampus, thalamus, basal ganglia and cerebellum, and has a regulatory role in various functions of the body, such as the regulation of emotion, memory and sleep, antihypertension, antifatigue, analgesia, etc. (63). GABA is produced in nerve endings catalyzed by glutamate decarboxylase. After release from the presynaptic membrane, most GABA diffuses to the postsynaptic membrane, causing an inhibitory effect in the postsynaptic membrane. The presynaptic membrane and glial cells reuptake a few GABA molecules, which are converted into succinic semi formaldehyde in mitochondria and then converted into succinic acid, which participates in the tricarboxylic acid cycle and provides a small part of the energy for glial cells and neural terminals (64, 65). Qiao et al. exposed Wistar rats to microwave radiation, with an average power density of 30 mW/cm^2 for 5 min; then, HPLC was used to determine the GABA content released by hippocampal synaptosomes 6 h after exposure. The results showed that the amount of GABA released by hippocampal synaptosomes significantly decreased after radiation exposure (22). Zhang et al. investigated the effects of EMR exposure on the emotional behavior and spatial memory of adolescent male mice, with frequency of 1.8 GHz, and time duration of 4 weeks. The authors found that the levels of GABA and aspartic acid in the cortex and hippocampus significantly decreased after EMR exposure (66). These results suggest that EMR can reduce GABA neurotransmission.

Wang et al. exposed 80 Wistar rats to a 2.856 GHz pulsed microwave radiation, at a power density of 50 mW/cm^2 for 6 min. The contents of amino acid neurotransmitters in the hippocampus were detected at 1, 3, 6, 9, 12, and 18 months after microwave exposure. The results showed that the glutamate to GABA ratio significantly decreased at 6 months after exposure (23). Noor et al. investigated the effect of 1 h of daily exposure to EMR, with a frequency of 900 Mz, SAR value 1.165 W/kg, power density 0.02 mW/cm^2, on the levels of amino acid neurotransmitters in the midbrain, cerebellum, and medulla of adult male albino rats. The assessment of amino acid levels was applied after 1 h, 1, 2, and 4 months of radiation exposure. A significant glycine increase in the midbrain was observed after 1 month, followed by a significant increase in GABA after 4 months (9). These results further suggest that microwave radiation may affect the neuroregulatory function of GABA, resulting in an imbalance in excitation and inhibition in the central nervous system.

In the central nervous system, GABA acts as an inhibitory transmitter. GABA receptors include ligand-gated GABA (A) channels and G-protein-coupled GABA (B) receptors, which mediate inhibitory postsynaptic transmission throughout the nervous system (67). In one study, primary cultured rat cortical neurons were exposed to 900 MHz microwave radiation, with an average power density of 6 mW/cm^2 and SAR value of 2.23 W/kg. As a result, the expression of neuronal GABA receptor proteins was significantly upregulated (24). Few studies have reported the effects of EMR on GABA receptors. Further investigation to clarify the role of GABA and its receptors during EMR exposure is necessary in the future. Overall, the above studies suggest that EMR can cause metabolic disorders of the inhibitory neurotransmitters GABA and glycine, which may lead to neuronal dysfunction by affecting the neuronal excitation-inhibition balance.

Effects of EMR on Acetylcholine (Ach)

Cholinergic fiber projection from the basal forebrain to the cortex and hippocampus is the most important cholinergic system in the brain, and the cholinergic system plays a critical role in behavioral cognition. Ach is released from cholinergic nerve endings, and it was the first neurotransmitter to be measured in the brain. Changes in Ach in the extracellular fluid of the brain are closely related to functional changes in the central nervous system. Ach is synthesized by choline and acetyl-CoA under the catalysis of choline acetyltransferase (ChAT) and then taken up and stored by vesicles. When the neuronal presynaptic membrane is excited, Ach in synaptic vesicles is released into the synaptic cleft and acts on G-protein-coupled muscarinic acetylcholine receptors (mAChRs) or ligand-gated nicotinic acetylcholine receptors (nAChRs). Synaptic transmission efficacy can be changed by receptor-mediated membrane depolarization and downstream signal transduction, thus affecting learning and memory. Post-acting Ach is hydrolyzed to choline and acetic acid by acetylcholine esterase (AChE) and inactivated (68). The mode of action of Ach in learning and memory depends on the type of receptor it activates (69).

Few studies have been reported on the metabolism of Ach in brains exposed to EMR. Fujiwara et al. found that 2.45 GHz high-power microwave radiation caused transiently elevated Ach content in the mouse brain (25). Lai et al. found that acute exposure to 2.45 GHz, 0.6 W/kg microwave radiation for 20 min caused increased choline uptake activity in the frontal cortex, hippocampus, and hypothalamus of rats (26). Meanwhile, 2.45 GHz, 0.6 W/kg microwave radiation for 20 min/day for 10 consecutive days resulted in a decrease in the mAChR concentration in the rat frontal cortex and hippocampus, whereas radiation exposure of 45 min/day for 10 consecutive days resulted in an increase in the mAChR concentration in the rat hippocampus, both coinciding with a decrease in learning and memory ability. In addition, Krylova et al. found that 2.35 GHz, 1 mW/cm^2 microwave radiation could induce a decrease in the functional activity of mAChRs in the rat cerebral cortex, though the number of mAChR receptors increase (27). We found an increase in Ach, ChAT and AChE in the rat hippocampus at 6 h and 3 days after microwave radiation, with a frequency of 2.856 GHz, and an average power density of 30 mW/cm^2 for 15 min but no significant effect on the activity of ChAT and AChE. Moreover, we found that the expression of M1-, M3- and β2-type AChR mRNA was downregulated, whereas the expression of α4- and α7-type AChR mRNA was upregulated after radiation exposure. This indicates that the increased synthesis and metabolism of Ach and the disordered expression of Ach receptors may result in cholinergic system dysfunction and a decrease in cognitive function in the early period of acute microwave radiation exposure.

Furthermore, Testylier et al. found that the Ach released in the hippocampal CA1 area decreased after 1 h of microwave radiation exposure with 2.45 GHz and 4 mW/cm^2, and the extracellular Ach concentration reached the lowest level of approximately 60% pre-exposure at 6 h after radiation (28). Other studies have shown that the M1 type of AChR is upregulated, the activity of AChE is increased, and the intracellular calcium concentration is increased in the hippocampus after long-term and low-dose microwave radiation at 2.45 GHz (44, 70). Derin et al. arranged Wistar rats into a sham-exposed group and 45 and 65 V/m exposed groups; the exposure group experienced 1 week of exposure at a frequency of 2.1 GHz. The protein and mRNA expression levels of AChE, ChAT, and VAChT in the hippocampus were examined using western blot and real-time PCR. The levels of AChE, ChAT, and VAChT were significantly lower in the rat hippocampus exposed to 65 V/m than in other regions (45). Additionally, sodium-dependent high-affinity choline uptake was measured in the striatum, frontal cortex, hippocampus, and hypothalamus of rats, after 45 min of short-term exposure to pulsed (2 μs, 500 pulses per second) or continuous 2,450 MHz microwaves in cylindrical waveguides. The average whole-body SAR value was 0.6 W/kg in all exposure conditions. The choline uptake was decreased in the frontal cortex after microwave exposure in all the radiation conditions (29). Gupta et al. reported a decrease in Ach content and an increase in AChE activity in the rat hippocampus caused by microwave radiation with 2.45 GHz, 1 h/day, for 28 consecutive days (46). Kunjilwar and Behari examined the effect of long-term exposure to RF-EMF on cholinergic systems in the developing rat brain, with a frequency of 147 MHz, subharmonics of 73.5 MHz and an amplitude of 36.75 MHz modulated at 16 and 76 Hz, 3 h/day, for 30–35 consecutive days. A significant decrease in AChE activity was found in exposed rats compared to control rats (71). These studies further suggested that disorders of Ach synthesis and metabolism are an important part of the cognitive dysfunction caused by EMR.

EFFECTS OF EMR ON PEPTIDES AND OTHER NEUROTRANSMITTERS

Opioid peptides include β-endorphins, enkephalins and dynorphins, which are peptides with morphine-like activity in the brain. The Opioid receptors are G-protein-coupled receptors. Endogenous opioid receptors are able to inhibit adenosine cyclase, reduce voltage-dependent calcium channel currents or activate potassium channels, resulting in a decrease in membrane excitability and transmitter release, thus participating in the regulation of learning and memory processes (72). Lai et al. investigated subtypes of opioid receptors in the brain exposed to a 45 min of short-term exposure to pulsed microwaves (2,450 MHz, 1 mW/cm^2, SAR value 0.6 W/kg) on cholinergic activity in the rat brain. The results showed that 3 opioid receptor subtypes blocked the decrease in cholinergic activity in the hippocampus induced by microwave radiation, suggesting that the opioid system is involved in microwave-induced hippocampal cholinergic activity decrease (30). There are few reports on the effect of EMR on peptide neurotransmitters. Lai et al. reported that after 45 min of exposure to pulsed 2,450 MHz microwaves (1 mW/cm^2, SAR value 0.6 W/kg), rats showed learning impairment while performing in the radial arm maze to obtain food rewards. This indicated a deficit in spatial working memory function after EMR exposure. The

microwave-induced learning deficit in the radial arm maze was blocked by pretreatment with the opiate antagonist naltrexone or a cholinergic agonist. This further suggests that both endogenous opioid neurotransmitter and cholinergic systems in the brain are involved in microwave-induced spatial memory deficits (31).

Nitric Oxide (NO) acts as a retrograde messenger in synaptic plasticity changes and long-term potentiation effects (48). Mice were exposed to computer electromagnetic radiation (30 x 10^{14}-715 x 10^{14} Hz) with an intensity of 0.9 V/m (power density 0.22 μw/cm^2) for either 6, 12, and 18 h/day for 30 continuous days. The results showed that the level of NO in the mouse brain gradually increased with prolonged radiation time (73). NO can pass through cell membranes by lipophilicity but is not released in the form of exocytosis; it acts through chemical reactions before becoming inactivated. In addition, NO can react with other free radicals and d-orbitals of transition metals. The most common for the latter is the interaction of NO with iron, because iron acts as a key component of abundant proteins, especially hemeproteins, involved in numerous physiological processes. Burlaka et al. exposed animals to ultrahigh frequency EMR of the non-thermal spectrum using the generator "Volna" (Ukraine) with impulse modulation and the following parameters: pulse duration 2 ms, pulse separation 10 ms, carrier frequency 0.465 GHz, and exposure duration 17.5 min. The energy flux density in the exposure area was 1.0–6.0 mW/cm^2. Ultrahigh frequency EMR resulted in a significant increase in the level of NO synthesis in the mitochondria of neural cells in animal brain tissue and a significant increase in the activity of mitochondrial NO synthase (32). Considering the toxic effect of high NO concentrations on cells, the increase in NO may cause neuronal damage, which in turn leads to a decrease in learning and memory ability in mice.

POSSIBLE MECHANISMS UNDERLYING NEUROTRANSMITTER CHANGES CAUSED BY EMR

Electrophysiological Changes

Neurophysiological mechanisms especially electrophysiological changes would lead to better understanding the neurotransmitter changes associated with EMR exposure. Several neuroimaging methods are used to illuminate the interference between brain electrical activity and EMR. For example, the changes of extracellular electrical potential in the cortex can be measured by EEG techniques, the regional changes of blood oxygen utilization can be detected with functional magnetic resonance imaging (fMRI) method during neuropsychological performance, and positron emission tomography (PET) reflects the cerebral metabolism (43, 74–76). Brain electrical activity originates from the fluctuation of membrane potential in the neuron. The transduction of a nerve impulse results in the postsynaptic potential and the following synaptic transmission, which could reflect the modulation of neurotransmission.

Many studies indicate an increase of cortical excitability and/or efficiency during EMR exposure, and this electrical activity changes may persist for several minutes post-exposure. In addition, an increase of cerebral metabolism (PET), a decrease of alpha activity, an increase of high beta and gamma frequency activity, increased reaction time, and disrupted sleep EEG were also induced by EMR exposure (77–82). Based on several methodologies, such as fMRI, PET, EMF-elicited event-related potentials (ERPs) (83, 84), and event-related desynchronization (ERD), and interhemispheric synchronization, frontal and temporal regions appear to be more susceptible (76, 81, 82, 85–87). In terms of the EMF-induced effects on cortical excitability and efficiency, several factors have been proposed, including alteration of dependent Na-K trans-membrane ionic channels, changes of cellular calcium homeostasis, increased cellular excitability, and modulation of cellular response to stress (86, 87). However, several inconsistent findings exist, and the heterogeneity of results may be due to methodological differences, statistical power, and interpretation criteria (88). Altogether, the abnormal brain electrical activity may reflect the modulation of neurotransmission induced by EMR, and result in the changes of neurotransmitters.

Cell Membrane Damage

It is known that membrane is the first and an important target of EMF in cells. Cell membrane damage might result in neurotransmitter changes in the brain. Understanding the effects of EMR on neurotransmitters is critical for further determining the targets of EMR in cells. EMR can alter cell membrane permeability such as changes in calcium, ionic distribution and ion permeability (89). Calcium is one of the important signaling substances, and an imbalance of calcium homeostasis can alter many functions of the cell. Previous studies have showed that EMR exposure can alter the calcium channels and receptors on the cell membrane, and influence transport of calcium ions over the cell membrane, which play an important role in cell signaling pathways, and in turn may affect the response of neurotransmitters (90, 91). It was reported that the number of opened calcium channel increased with the presence of EMFs, which might resulting in the increased intracellular calcium concentration under EMR exposure (92). In addition, the changes of intracellular calcium levels can trigger unusual synaptic action or cause neuronal apoptosis. This in turn can exert an influence on the neurotransmission of learning and memory process (93).

Additionally, the enhanced activity of voltage-gated calcium channels (VGCCs) have been delineated, after exposure to EMR in many cell types (94–96). Previous studies used the activity of VGCCs as an indicator of microwave radiation induced changes in ion channels (96, 97). The level of neurotransmitters can indicate the membrane properties, such as the expression level of synaptic vesicular-associated proteins, can indicate the function of the synaptic vesicular membrane (22, 98). It was reported that, EMR activation of VGCCs causes a rapid increase in intracellular calcium, nitric oxide, and peroxynitrite (99). However, a recent study on the effects of 2.856 GHz pulsed microwave radiation in the primary hippocampal neurons, reported that the total cellular calcium, the levels of calcium in endoplasmic reticulum and mitochondria all decreased after microwave exposure, suggesting calcium efflux during microwave radiation (100). Although many animal studies have suggested about the effects of EMR on

the calcium efflux and influx in the neurons (101–103), the results regarding the effects of EMR on the membrane integrity and permeability are still unclear. The changes of membrane permeability may result in the damage of membrane integrity, and lead to the changes in brain neurotransmitter imbalance. In this regard, further studies by various duration and dose of EMR are needed to investigate the effects of EMR on the relationship of neurotransmitters and cell membrane permeability.

Abnormal Signal Transduction

It is known that neurotransmitter and its receptors are involved in various signaling related to cell proliferation, apoptosis, differentiation and inflammation. The crosstalk between neurotransmission and cell signaling may in turn affect the metabolism and transport of neurotransmitters. EMR exposures produce the main pathophysiological effects via excessive calcium signaling and the peroxynitrite pathway, and the diverse non-thermal effects of EMR are produced via VGCC activation (104). As the energy source of the cell, the mitochondrial calcium reaction was influenced by the alterations in calcium signaling pathways in response to the effects of EMR exposure (90). In addition to calcium signaling changes, EMR can cause activation of free radical processes and overproduction of reactive oxygen species (ROS) in neurons (53, 104–108). Due to the dependent on oxidative phosphorylation for energy, neurons are vulnerable for oxidative stress compared to other cells. During EMR exposure, the occurrence of oxidant-antioxidant imbalance in the brain leads to oxidative stress (109). Both NO and superoxide (O_2^-) are elevated by increased calcium, resulting in the increase of peroxynitrite ($ONOO^-$) levels. The various oxidants act to produce greatly elevated NF-kappa B (NF-κB) activity, leading to inflammation (110). In addition, NF-κB signaling is reported to be involved in neural immune response, synaptic plasticity, learning and memory, neuroprotection and neurodegeneration (111, 112). It has been shown that EMR exposure leads to up-regulated elements belonging to apoptotic pathways, which results in neuronal apoptosis (113, 114). The probable mechanisms are mainly attributed to increased ROS generation following EMR exposure.

The energy of non-ionizing radiation is not enough to directly break chemical bonds, and therefore the occurrence of DNA damage with non-ionizing EMR exposures is primarily a consequence of generation of ROS, followed by oxidative stress. Numerous animal experiments have clearly demonstrated that non-thermal EMR can cause oxidative stress (115, 116), particularly in the brain (3, 117–119). It has been documented that non-thermal EMR exposure of 900 MHz or 2.45 GHz in rats, either short-term or long-term, can trigger neuronal dysfunction and apoptosis of hippocampal pyramidal cells (117, 120) and cerebellum Purkinje cells (121) through induction of oxidative stress. In addition, the mitogen-activated phosphokinase (MAPK) pathway plays a key role in cell proliferation and metabolism. The phosphorylation of transcription factors in the downstream occurs after activation of the MAPK cascades pathway (89, 122). The proliferation and survival of different cell types can be stimulated by low concentrations of free radicals. The effects of ROS on cell proliferation, is an important secondary messenger in the physiological process, and ROS plays a key role in the regulation of cytosolic calcium homeostasis. The protein phosphorylation and activation of the AP-1 family factors and nuclear factor kappa B (NF-κB) is regulated by the level of cytosolic calcium (123). Activation of the protein kinases pathways regulates the physiological response to EMR exposure including neurotransmitter imbalance, but the detailed mechanisms are still unclear.

DISCUSSION

According to the time duration of EMR exposure, we divided all the references including neurotransmitter measurement in the brain into two groups: short-term (within one week) exposure and long-term (more than one week) exposure groups. It is apparent from the listed reference in **Tables 1**, **2** that, no obvious difference was observed for neurotransmitter changes between the short-term (**Table 1**) and long-term (**Table 2**) EMR exposure. It is known that the response to non-thermal EMR depends on both power density and duration of exposure. Some studies show no effect under fixed short-term EMR exposures, but this does not imply no effects under longer-term exposures (5, 124). In a recent review, Leach et al. analyzed 2,653 papers captured in the database examine the bioeffect outcomes in the 300 MHz−3 GHz range. The results showed three times more biological "Effect" than "No Effect" papers (125). Although some studies report no effect on the tested indicators, there are studies find the significant effect in many cases. This inconsistency might due to the lack of replication between studies. It is challenging for undertaking a literature review or comparing findings between relevant scientific papers, due to the subject, various experimental methodology and changing exposure parameters in the available studies. Notwithstanding animal models can only provide a strong indication of risks to humans, and the exchange formula or conversion rules between animal studies and human biological effects are far from clarified. The development of reliable safety standards has analyzed such parameters as power density, dose, and duration of exposure, and this would protect against the detrimental health effects of EMR exposure at non-thermal intensities.

Many evidences indicate that EMR alter several aspects of calcium function in cells. In spite of numerous studies reporting altered calcium metabolism upon exposure to radiofrequency electromagnetic fields, the underlying mechanisms of these effects are still not clear. However, some studies have suggested that the calcium activation could be the initial event leading to alteration in protein configuration, followed by generation of ROS and ultimately activation of the molecular apoptosis pathways (101). Lushchak et al. reported that EMR exposure may firstly produce the free radicals in the brain and later they are converted to ROS (126). The elevation of ROS level can attack various biomolecules in the cell. The raised ROS can also in turn trigger calcium release, and then activate the genetic factors leading to DNA damage (110). Any alteration in gene and enzyme levels, may result in the activation of

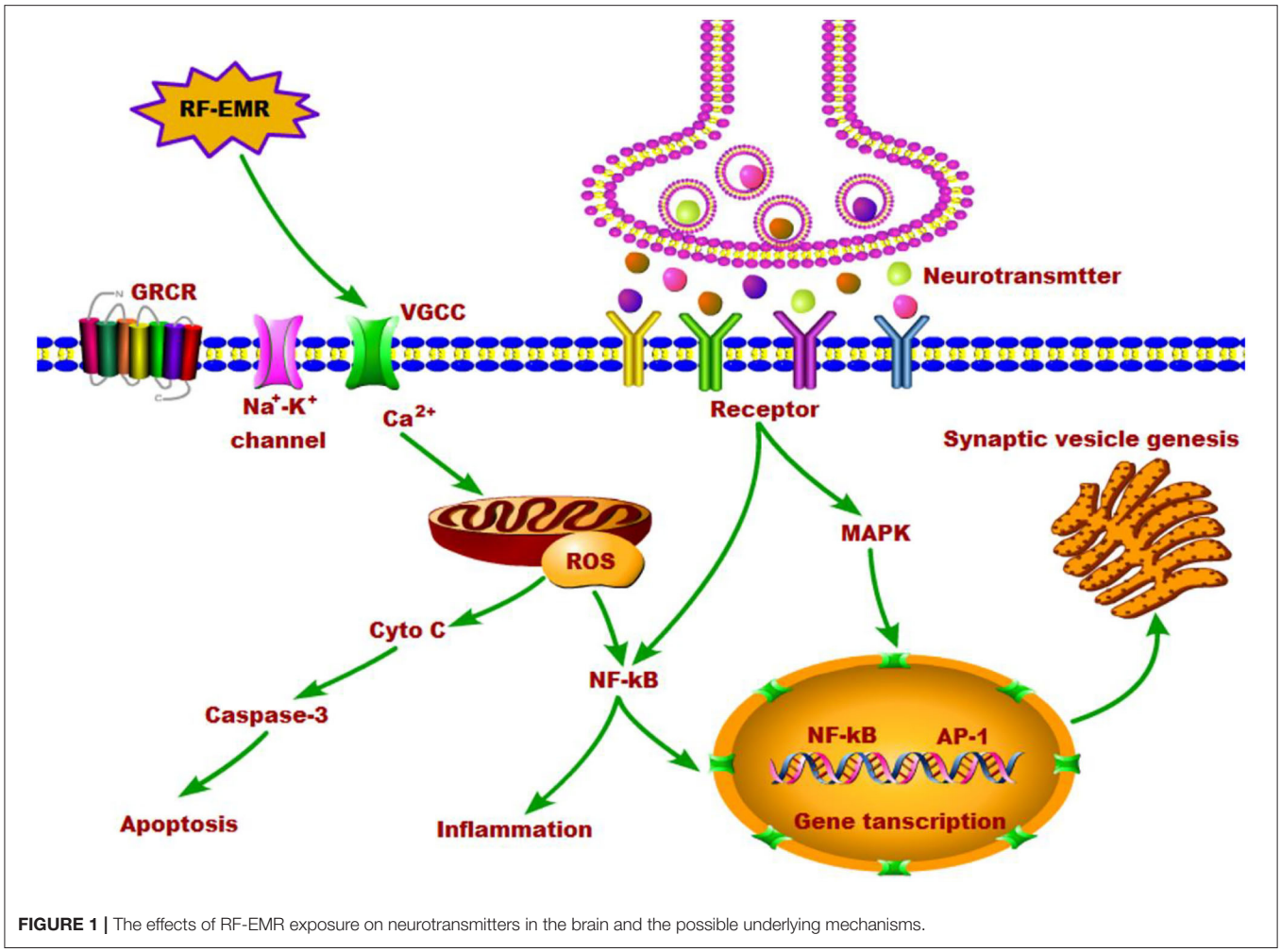

FIGURE 1 | The effects of RF-EMR exposure on neurotransmitters in the brain and the possible underlying mechanisms.

downstream signaling (114), particularly the mitochondria-dependent caspase-3 pathway can cause the apoptosis of neurons (113, 127), which would lead to altered behavioral manifestations and pathophysiological changes in the brain. In a word, EMR exposure does increases the intracellular calcium and the formation of ROS, which would alter the cellular function eventually and lead to numerous biological effects including neurotransmitter imbalance. We summarized the effects of EMR on neurotransmitters in the brain and the possible underlying mechanisms in **Figure 1**.

Though we narrow down to biochemical imbalance to simplify explanation for changes of each neurotransmitter, the combined effects of neurotransmitters still deserves attention. It is also possible that the various neurotransmission effects following EMR exposure in animals might be due to combined effects in various brain regions, such as neurophysiological changes, increase of calcium and ROS, and thereby cell membrane damage and the downstream signaling changes. An imbalance in the excitation-inhibition imbalance of neurons resulting from neurotransmitter changes, would alter behavior, and it might do so without evident structural changes. Currently, the neurochemical mechanisms of EMR exposure are still unclear. Further study in this regard is needed and will reveal much clearer picture of brain mechanisms caused by EMR.

CONCLUSION

In summary, research on the synthesis, metabolism and transport of neurotransmitters in the brain by EMR is increasing gradually, but due to the different parameters of EMR, experimental objects and conditions, the experimental results are not very consistent and comparative. Therefore, the effects of EMR on the metabolism and transport of neurotransmitters have not been clarified. Moreover, the role of neurotransmitters and their mechanism in the neurobehavioral dysfunction induced by EMR have not been revealed. Further detailed studies are needed. On the other hand, because of the complex diversity of neurotransmitters in the brain, the interaction, cotransmission and coregulation of neurotransmitters make it difficult to distinguish the primary and secondary changes of each neurotransmitter. Furthermore, the interaction of different neural nuclei in the brain constitutes sophisticated neural circuits, which is the fundamental basis of how the brain performs functions. Consequently, the regulation of neural

circuits may be involved in the neurotransmitter disorder of the brain induced by EMR.

FUTURE PERSPECTIVES

Recently, novel techniques in brain science, such as neuroviral tracers, neuroimaging and neuroelectrophysiology, have been rapidly developed. These techniques were devised especially for the development and wide application of brain intervention techniques, including optogenetics and chemical genetics. Moreover, these advances have provided new methods to study the neurobiological effects of EMR at the neural circuit level. Notably, the G-protein-coupled receptor activation-based (GRAB) sensor can directly measure neurotransmitter release and monitor the activity of neurotransmission *in vivo* (128). Combined with fiber photometry recording, the GRAB sensor enables sensitive detection of single-trial neurotransmitter dynamics in multiple brain regions in mice performing a variety of behaviors (82). With these new techniques in neuroscience, studying the effects of EMR on neurotransmitter metabolism and the transport of neurotransmitters at the neural circuit level is expected to overcome the challenges inherent in investigating the neurobiological effect of EMR and its mechanisms and open novel pathways for the exploration of preventive targets and interventions.

AUTHOR CONTRIBUTIONS

CH wrote the paper and outlined this manuscript. HZ and YL provided a detailed guidance throughout the article. All the authors read and approved the final manuscript.

FUNDING

This work was supported by the National Natural Science Foundation of China (81472951).

REFERENCES

1. Wei YW, Yang JY, Chen ZY, Wu TN, Lv B. Modulation of resting-state brain functional connectivity by exposure to acute fourth-generation long-term evolution electromagnetic field: An fMRI study. *Bioelectromagnetics.* (2019) 40:42–51. doi: 10.1002/bem.22165
2. Yang L, Zhang C, Chen ZY Li CS, Wu TN. Functional and network analyses of human exposure to long-term evolution signal. *Environ Sci Pollut Res Int.* (2021) 28:5755–73. doi: 10.1007/s11356-020-10728-w
3. Megha K, Deshmukh PS, Banerjee BD, Tripathi AK, Ahmed R, Abegaonkar MP. Low intensity microwave radiation induced oxidative stress, inflammatory response and DNA damage in rat brain. *Neurotoxicology.* (2015) 51:158–65. doi: 10.1016/j.neuro.2015.10.009
4. Saikhedkar N, Bhatnagar M, Jain A, Sukhwal P, Sharma C, Jaiswal N. Effects of mobile phone radiation (900 MHz radiofrequency) on structure and functions of rat brain. *Neurol Res.* (2014) 36:1072–9. doi: 10.1179/1743132814Y.0000000392
5. Belpomme D, Hardell L, Belyaev I, Burgio E, Carpenter DO. Thermal and non-thermal health effects of low intensity non-ionizing radiation: An international perspective. *Environ Pollut.* (2018) 242:643–58. doi: 10.1016/j.envpol.2018.07.019
6. Zhi WJ, Wang LF, Hu XJ. Recent advances in the effects of microwave radiation on brains. *Mil Med Res.* (2017) 4:29. doi: 10.1186/s40779-017-0139-0
7. Comelekoglu U, Aktas S, Demirbag B, Karagul MI, Yalin S, Yildirim M, et al. Effect of low-level 1800 MHz radiofrequency radiation on the rat sciatic nerve and the protective role of paricalcitol. *Bioelectromagnetics.* (2018) 39:631–43. doi: 10.1002/bem.22149
8. Eris AH, Kiziltan HS, Meral I, Genc H, Trabzon M, Seyithanoglu H, et al. Effect of Short-term 900 MHz low level electromagnetic radiation exposure on blood serotonin and glutamate levels. *Bratisl Lek Listy.* (2015) 116:101–3. doi: 10.4149/BLL_2015_019
9. Noor NA, Mohammed HS, Ahmed NA, Radwan NM. Variations in amino acid neurotransmitters in some brain areas of adult and young male albino rats due to exposure to mobile phone radiation. *Eur Rev Med Pharmacol Sci.* (2011) 15:729–42.
10. Ferreri F, Curcio G, Pasqualetti P, De Gennaro L, Fini R, Rossini PM. Mobile phone emissions and human brain excitability. *Ann Neurol.* (2006) 60:188–96. doi: 10.1002/ana.20906
11. Tuszynski J, Tilli TM, Levin M. Ion Channel and Neurotransmitter Modulators as Electroceutical Approaches to the Control of Cancer. *Curr Pharm Des.* (2017) 23:4827–41. doi: 10.2174/1381612823666170530105837
12. Ng J, Heales SJ, Kurian MA. Clinical features and pharmacotherapy of childhood monoamine neurotransmitter disorders. *Paediatr Drugs.* (2014) 16:275–91. doi: 10.1007/s40272-014-0079-z
13. Sheffler ZM, Reddy V, Pillarisetty LS. *Physiology, Neurotransmitters*. Treasure Island, FL: StatPearls Publishing (2021).
14. Aboul Ezz HS, Khadrawy YA, Ahmed NA, Radwan NM, El Bakry MM. The effect of pulsed electromagnetic radiation from mobile phone on the levels of monoamine neurotransmitters in four different areas of rat brain. *Eur Rev Med Pharmacol Sci.* (2013) 17:1782–8.
15. Inaba R, Shishido K, Okada A, Moroji T. Effects of whole body microwave exposure on the rat brain contents of biogenic amines. *Eur J Appl Physiol Occup Physiol.* (1992) 65:124–8. doi: 10.1007/BF00705068
16. Ishikawa K, Shibanoki S, Saito S, McGaugh JL. Effect of microwave irradiation on monoamine metabolism in dissected rat brain. *Brain Res.* (1982) 240:158–61. doi: 10.1016/0006-8993(82)90655-2
17. Karri V, Schuhmacher M, Kumar V. Heavy metals (Pb, Cd, As and MeHg) as risk factors for cognitive dysfunction: A general review of metal mixture mechanism in brain. *Environ Toxicol Pharmacol.* (2016) 48:203–13. doi: 10.1016/j.etap.2016.09.016
18. Mausset-Bonnefont AL, Hirbec H, Bonnefont X, Privat A, Vignon J, de Sèze R. Acute exposure to GSM 900-MHz electromagnetic fields induces glial reactivity and biochemical modifications in the rat brain. *Neurobiol Dis.* (2004) 17:445–54. doi: 10.1016/j.nbd.2004.07.004
19. Zhang YW Yu ZP, Xie Y, Fang Q. Effects of microwave irradiation on NMDA receptor subunits mRNA expressions in rat hippocampus. *J Hygiene Res.* (2008) 37:25–8.
20. Wang LF, Tian DW Li HJ, Gao YB, Wang CZ, Zhao L, Zuo HY, et al. Identification of a novel rat NR2B subunit gene promoter region variant and its association with microwave-induced neuron impairment. *Mol Neurobiol.* (2016) 53:2100–11. doi: 10.1007/s12035-015-9169-3
21. Xiong L, Sun CF, Zhang J, Gao YB, Wang LF, Zuo HY, et al. Microwave exposure impairs synaptic plasticity in the rat hippocampus and PC12 cells through over-activation of the NMDA receptor signaling pathway. *Biomed Environ Sci.* (2015) 28:13–24. doi: 10.3967/bes2015.002
22. Qiao SM, Peng RY, Yan HT, Gao YB, Wang CZ, Wang SM, et al. Reduction of phosphorylated synapsin I (ser-553) leads to spatial memory impairment by attenuating GABA release after microwave exposure in Wistar rats. *PLoS ONE.* (2014) 9:e95503. doi: 10.1371/journal.pone.0095503
23. Wang H, Peng RY, Zhao L, Wang SM, Gao YB, Wang LF, et al. The relationship between NMDA receptors and microwave-induced learning and memory impairment: a long-term observation on Wistar rats. *Int J Radiat Biol.* (2015) 91:262–9. doi: 10.3109/09553002.2014.988893

24. Wang Q, Cao ZJ, Bai XT. Effect of 900 MHz electromagnetic fields on the expression of GABA receptor of cerebral cortical neurons in postnatal rats. *J Hygiene Res.* (2005) 34:546–68.
25. Fujiwara M, Watanabe Y, Katayama Y, Shirakabe Y. Application of high-powered microwave irradiation for acetylcholine analysis in mouse brain. *Eur J Pharmacol.* (1978) 51:299–301. doi: 10.1016/0014-2999(78)90416-8
26. Lai H, Carino MA, Horita A, Guy AW. Low-level microwave irradiation and central cholinergic systems. *Pharmacol Biochem Behav.* (1989) 33:131–8. doi: 10.1016/0091-3057(89)90442-5
27. Krylova IN, Dukhanin AS. Il'in AB, Kuznetsova EIu, Balaeva NV, Shimanovskii NL, Pal'tsev IuP, Iasnetsov VV. The effect of ultrahigh-frequency electromagnetic radiation on learning and memory processes. *Biull Eksp Biol Med.* (1992) 114:483–4. doi: 10.1007/BF00837653
28. Testylier G, Tonduli L, Malabiau R, Debouzy JC. Effects of exposure to low level radiofrequency fields on acetylcholine release in hippocampus of freely moving rats. *Bioelectromagnetics.* (2002) 23:249–55. doi: 10.1002/bem.10008
29. Lai H, Horita A, Guy AW. Acute low-level microwave exposure and central cholinergic activity: studies on irradiation parameters. *Bioelectromagnetics.* (1988) 9:355–62. doi: 10.1002/bem.2250090405
30. Lai H, Carino MA, Horita A, Guy AW. Opioid receptor subtypes that mediate a microwave-induced decrease in central cholinergic activity in the rat. *Bioelectromagnetics.* (1992) 13:237–46. doi: 10.1002/bem.2250130308
31. Lai H, Horita A, Guy AW. Microwave irradiation affects radial-arm maze performance in the rat. *Bioelectromagnetics.* (1994) 15:95–104. doi: 10.1002/bem.2250150202
32. Burlaka AP, Druzhyna MO, Vovk AV. Lukin SM. Disordered redox metabolism of brain cells in rats exposed to low doses of ionizing radiation or UHF electromagnetic radiation. *Exp Oncol.* (2016) 38:238–41. doi: 10.31768/2312-8852.2016.38(4):238-241
33. Kim JH, Lee CH, Kim HG, Kim HR. Decreased dopamine in striatum and difficult locomotor recovery from MPTP insult after exposure to radiofrequency electromagnetic fields. *Sci Rep.* (2019) 9:1201. doi: 10.1038/s41598-018-37874-z
34. Maaroufi K, Had-Aissouni L, Melon C, Sakly M, Abdelmelek H, Poucet B, et al. Spatial learning, monoamines and oxidative stress in rats exposed to 900 MHz electromagnetic field in combination with iron overload. *Behav Brain Res.* (2014) 258:80–9. doi: 10.1016/j.bbr.2013.10.016
35. Ji J, Zhang YH, Yang XQ, Jiang RP, Guo DM, Cui X. The influence of microwave radiation from cellular phone on fetal rat brain. *Electromagn Biol Med*. (2012) 31:57–66. doi: 10.3109/15368378.2011.624652
36. Megha K, Deshmukh PS, Ravi AK, Tripathi AK, Abegaonkar MP, Banerjee BD. Effect of low-intensity microwave radiation on monoamine neurotransmitters and their key regulating enzymes in rat brain. *Cell Biochem Biophys*. (2015) 73:93–100. doi: 10.1007/s12013-015-0576-x
37. Cao Z, Zhang H, Tao Y, Liu J. Effects of microwave radiation on lipid peroxidation and the content of neurotransmitters in mice. *J Hygiene Res.* (2000) 30:28–9.
38. Li HJ, Peng RY, Wang CZ, Qiao SM, Yong Z, Gao YB, et al. Alterations of cognitive function and 5-HT system in rats after long term microwave exposure. *Physiol Behav.* (2015) 140:236–46. doi: 10.1016/j.physbeh.2014.12.039
39. Ahmed NA, Radwan NM, Aboul Ezz HS, Khadrawy YA, Salama NA. The chronic effect of pulsed 1800 MHz electromagnetic radiation on amino acid neurotransmitters in three different areas of juvenile and young adult rat brain. *Toxicol Ind Health.* (2018) 34:860–72. doi: 10.1177/0748233718798975
40. Zhao L, Peng RY, Wang SM, Wang LF, Gao YB, Dong J, et al. Relationship between cognition function and hippocampus structure after long-term microwave exposure. *Biomed Environ Sci.* (2012) 25:182–8. doi: 10.3967/0895-3988.2012.02.009
41. Wang H, Tan SZ, Xu XP, Zhao L, Zhang J, Yao BW, et al. Long term impairment of cognitive functions and alterations of NMDAR subunits after continuous microwave exposure. *Physiol Behav.* (2017) 181:1–9. doi: 10.1016/j.physbeh.2017.08.022
42. Huang CT, Liu P, Wu HX, Wang JL, Wu XN. Effects of NMDA receptor expression in rat's hippocampus after exposure to 1800 MHz radiofrequency field. *Zhonghua Yu Fang Yi Xue Za Zhi.* (2006) 40:21–4.
43. Zhang J, Sumich A, Wang GY. Acute effects of radiofrequency electromagnetic field emitted by mobile phone on brain function. *Bioelectromagnetics.* (2017) 38:329–38. doi: 10.1002/bem.22052
44. Kumar M, Singh SP, Chaturvedi CM. Chronic nonmodulated microwave radiations in mice produce anxiety-like and depression-like behaviours and calcium- and NO-related biochemical changes in the brain. *Exp Neurobiol.* (2016) 25:318–27. doi: 10.5607/en.2016.25.6.318
45. Gökçek-Saraç Ç, Akçay G, Karakurt S, Ateş K, Özen S, Derin N. Possible effects of different doses of 2. 1 GHz electromagnetic radiation on learning, and hippocampal levels of cholinergic biomarkers in Wistar rats. *Electromagn Biol Med.* (2021) 40:179–90. doi: 10.1080/15368378.2020.1851251
46. Gupta SK, Mesharam MK, Krishnamurthy S. Electromagnetic radiation 2450 MHz exposure causes cognition deficit with mitochondrial dysfunction and activation of intrinsic pathway of apoptosis in rats. *J Biosci.* (2018) 43:263–76. doi: 10.1007/s12038-018-9744-7
47. Kunjilwar KK, Behari J. Effect of amplitude-modulated radio frequency radiation on cholinergic system of developing rats. *Brain Res.* (1993) 601:321–4. doi: 10.1016/0006-8993(93)91729-c
48. Qin FJ, Nie JH, Cao Y, Li JX, Tong J. Influence of computer electromagnetic radiation on learning and memory ability as well as cerebra neuron transmitter of mice. *J Radiat Res.* (2010) 28:185–9. Available online at: https://kns.cnki.net/kcms/detail/detail.aspx?
49. Kasture AS, Hummel T, Sucic S, Freissmuth M. Big Lessons from tiny flies: drosophila melanogaster as a model to explore dysfunction of dopaminergic and serotonergic neurotransmitter systems. *Int J Mol Sci.* (2018) 19:1788. doi: 10.3390/ijms19061788
50. Gilman AG, Goodman LS, Gilman A. Goodman and Gilman's The Pharmacological Basis of Therapeutics. 6th ed. New York: Macmillan Publishing Co. Inc. 1980; 476.
51. Davis KL, Kahn RS, Ko G, Davidson M. Dopamine in schizophrenia: a review and reconceptualization. *Am J Psychiatry.* (1991) 148:1474–86. doi: 10.1176/ajp.148.11.1474
52. Abi-Dargham A. From "bedside" to "bench" and back: A translational approach to studying dopamine dysfunction in schizophrenia. *Neurosci Biobehav Rev.* (2020) 110:174–9. doi: 10.1016/j.neubiorev.2018.12.003
53. Silverberg AB, Shah SD, Haymond MW, Cryer PE. Norepinephrine: hormone and neurotransmitter in man. *Am J Physiol.* (1978) 234:252–56. doi: 10.1152/ajpendo.1978.234.3.E252
54. Zhu ZJ, Cheng CC, Chang C, Ren GH, Zhang JB, Peng Y, et al. Characteristic fingerprint spectrum of neurotransmitter norepinephrine with broadband terahertz time-domain spectroscopy. *Analyst.* (2019) 144:2504–10. doi: 10.1039/C8AN02079E
55. Charnay Y, Léger L. Brain serotonergic circuitries. *Dialogues Clin Neurosci.* (2010) 12:471–87. doi: 10.31887/DCNS.2010.12.4/ycharnay
56. Petkov VD, Konstantinova E. Effects of the ergot alkaloid elymoclavine on the level and turnover of biogenic monoamines in the rat brain. *Arch Int Pharmacodyn Ther.* (1986) 281:22–34.
57. Lai YF, Wang HY, Peng RY. Establishment of injury models in studies of biological effects induced by microwave radiation. *Mil Med Res.* (2021) 8:12. doi: 10.1186/s40779-021-00303-w
58. Pellerin L, Magistretti PJ. Neuroenergetics: calling upon astrocytes to satisfy hungry neurons. *Neuroscientist.* (2004) 10:53–62. doi: 10.1177/1073858403260159
59. Shen J, Petersen KF, Behar KL, Brown P, Nixon TW, Mason GF, et al. Determination of the rate of the glutamate/glutamine cycle in the human brain by in vivo 13C NMR. *Proc Natl Acad Sci U S A.* (1999) 96:8235–40. doi: 10.1073/pnas.96.14.8235
60. Niciu MJ, Kelmendi B, Sanacora G. Overview of glutamatergic neurotransmission in the nervous system. *Pharmacol Biochem Behav.* (2012) 100:656–64. doi: 10.1016/j.pbb.2011.08.008
61. Rebola N, Srikumar BN, Mulle C. Activity-dependent synaptic plasticity of NMDA receptors. *J Physiol.* (2010) 588:93–9. doi: 10.1113/jphysiol.2009.179382
62. Chater TE, Goda Y. The role of AMPA receptors in postsynaptic mechanisms of synaptic plasticity. *Front Cell Neurosci.* (2014) 27:401. doi: 10.3389/fncel.2014.00401
63. Stone E, Haario H, Lawrence JJ, A. kinetic model for the frequency dependence of cholinergic modulation at hippocampal GABAergic

synapses. *Math Biosci.* (2014) 258:162–75. doi: 10.1016/j.mbs.2014.09.013
64. Lawrence JJ. Cholinergic control of GABA release: emerging parallels between neocortex and hippocampus. *Trends Neurosci.* (2008) 31:317–27. doi: 10.1016/j.tins.2008.03.008
65. Fedotcheva NI, Sokolov AP, Kondrashova MN. Nonezymatic formation of succinate in mitochondria under oxidative stress. *Free Radic Biol Med.* (2006) 41:56–64. doi: 10.1016/j.freeradbiomed.2006.02.012
66. Zhang JP, Zhang KY, Guo L, Chen QL, Gao P, Wang T, et al. Effects of 1. 8 GHz Radiofrequency Fields on the Emotional Behavior and Spatial Memory of Adolescent Mice. *Int J Environ Res Public Health.* (2017) 14:1344. doi: 10.3390/ijerph14111344
67. Stein V, Nicoll RA, GABA. generates excitement. *Neuron.* (2003) 37:375–8. doi: 10.1016/S0896-6273(03)00056-4
68. Li XN Yu B, Sun QT, Zhang YL, Ren M, Zhang XY, et al. Generation of a whole-brain atlas for the cholinergic system and mesoscopic projectome analysis of basal forebrain cholinergic neurons. *Proc Natl Acad Sci U S A.* (2018) 115:415–20. doi: 10.1073/pnas.1703601115
69. Dannenberg H, Young K, Hasselmo M. Modulation of hippocampal circuits by muscarinic and nicotinic receptors. *Front Neural Circuits.* (2017) 13:102. doi: 10.3389/fncir.2017.00102
70. Hassanshahi A, Shafeie SA, Fatemi I, Hassanshahi E, Allahtavakoli M, Shabani M, et al. The effect of Wi-Fi electromagnetic waves in unimodal and multimodal object recognition tasks in male rats. *Neurol Sci.* (2017) 38:1069–76. doi: 10.1007/s10072-017-2920-y
71. Shang Y, Filizola M. Opioid receptors: Structural and mechanistic insights into pharmacology and signaling. *Eur J Pharmacol.* (2015) 763:206–13. doi: 10.1016/j.ejphar.2015.05.012
72. Kirichuk VF, Ivanov AN, Kirijazi TS. Correction of microcirculatory disturbances with terahertz electromagnetic radiation at nitric oxide frequencies in albino rats under conditions of acute stress. *Bull Exp Biol Med.* (2011) 151:288–91. doi: 10.1007/s10517-011-1311-2
73. Curcio G, Nardo D, Perrucci MG, Pasqualetti P, Chen TL, Del Gratta C, et al. Effects of mobile phone signals over BOLD response while performing a cognitive task. *Clin Neurophysiol.* (2012) 123:129–36. doi: 10.1016/j.clinph.2011.06.007
74. Berger A. How does it work? Positron emission tomography. *BMJ.* (2003) 326:1449. doi: 10.1136/bmj.326.7404.1449
75. Wang GY, Kydd R, Russell BR. Auditory event-related potentials in methadone substituted opiate users. *J Psychopharmacol.* (2015) 29:983–95. doi: 10.1177/0269881115587929
76. Volkow ND, Tomasi D, Wang GJ, Vaska P, Fowler JS, Telang F, et al. Effects of cell phone radiofrequency signal exposure on brain glucose metabolism. *JAMA.* (2011) 305:808–13. doi: 10.1001/jama.2011.186
77. Lowden A, Akerstedt T, Ingre M, Wiholm C, Hillert L, Kuster N, et al. Sleep after mobile phone exposure in subjects with mobile phone-related symptoms. *Bioelectromagnetics.* (2011) 32:4–14. doi: 10.1002/bem.20609
78. Schmid MR, Loughran SP, Regel SJ, Murbach M, Bratic Grunauer A, Rusterholz T, et al. Sleep EEG alterations: effects of different pulse-modulated radio frequency electromagnetic fields. *J Sleep Res.* (2012) 21:50–8. doi: 10.1111/j.1365-2869.2011.00918.x
79. Schmid MR, Murbach M, Lustenberger C, Maire M, Kuster N, Achermann P, et al. Sleep EEG alterations: effects of pulsed magnetic fields versus pulse-modulated radio frequency electromagnetic fields. *J Sleep Res.* (2012) 21:620–9. doi: 10.1111/j.1365-2869.2012.01025.x
80. Ghosn R, Yahia-Cherif L, Hugueville L, Ducorps A, Lemaréchal JD, Thuróczy G, et al. Radiofrequency signal affects alpha band in resting electroencephalogram. *J Neurophysiol.* (2015) 113:2753–9. doi: 10.1152/jn.00765.2014
81. Roggeveen S, van Os J, Viechtbauer W, Lousberg R, EEG. Changes due to experimentally induced 3g mobile phone radiation. *PLoS ONE.* (2015) 10:e0129496. doi: 10.1371/journal.pone.0129496
82. Carrubba S, Frilot C. 2nd, Chesson AL Jr, Marino AA. Mobile-phone pulse triggers evoked potentials. *Neurosci Lett.* (2010) 469:164–8. doi: 10.1016/j.neulet.2009.11.068
83. Carrubba S, Marino AA. The effects of low-frequency environmental-strength electromagnetic fields on brain electrical activity: a critical review of the literature. *Electromagn Biol Med.* (2008) 27:83–101. doi: 10.1080/15368370802088758
84. Roggeveen S, van Os J, Lousberg R. Does the brain detect 3G mobile phone radiation peaks? An explorative in-depth analysis of an experimental study. *PLoS ONE.* (2015) 10:e0125390. doi: 10.1371/journal.pone.0125390
85. Vecchio F, Buffo P, Sergio S, Iacoviello D, Rossini PM, Babiloni C. Mobile phone emission modulates event-related desynchronization of α rhythms and cognitive-motor performance in healthy humans. *Clin Neurophysiol.* (2012) 123:121–8. doi: 10.1016/j.clinph.2011.06.019
86. Vecchio F, Tombini M, Buffo P, Assenza G, Pellegrino G, Benvenga A, et al. Mobile phone emission increases inter-hemispheric functional coupling of electroencephalographic α rhythms in epileptic patients. *Int J Psychophysiol.* (2012) 84:164–71. doi: 10.1016/j.ijpsycho.2012.02.002
87. Valentini E, Ferrara M, Presaghi F, De Gennaro L, Curcio G. Systematic review and meta-analysis of psychomotor effects of mobile phone electromagnetic fields. *Occup Environ Med.* (2010) 67:708–16. doi: 10.1136/oem.2009.047027
88. Warille AA, Altun G, Elamin AA, Kaplan AA, Mohamed H, Yurt KK, et al. Skeptical approaches concerning the effect of exposure to electromagnetic fields on brain hormones and enzyme activities. *J Microsc Ultrastruct.* (2017) 5:177–84. doi: 10.1016/j.jmau.2017.09.002
89. Walleczek J. Electromagnetic field effects on cells of the immune system: the role of calcium signaling. *FASEB J.* (1992) 6:3177–85. doi: 10.1096/fasebj.6.13.1397839
90. Bauréus Koch CL, Sommarin M, Persson BR, Salford LG, Eberhardt JL. Interaction between weak low frequency magnetic fields and cell membranes. *Bioelectromagnetics.* (2003) 24:395–402. doi: 10.1002/bem.10136
91. Narayanan SN, Mohapatra N, John P. K N, Kumar RS, Nayak SB, Bhat PG. Radiofrequency electromagnetic radiation exposure effects on amygdala morphology, place preference behavior and brain caspase-3 activity in rats. *Environ Toxicol Pharmacol.* (2018) 58:220–9. doi: 10.1016/j.etap.2018.01.009
92. Zhang YH, Zhan Y, Zhao TJ, Han YR, Liu H. Mechanism of permeation in calcium channels activation by applied magnetic fields. *Annu Int Conf IEEE Eng Med Biol Soc.* (2007) 2007:1391–3. doi: 10.1109/IEMBS.2007.4352558
93. Maskey D, Pradhan J, Aryal B, Lee CM, Choi IY, Park KS, et al. Chronic 835-MHz radiofrequency exposure to mice hippocampus alters the distribution of calbindin and GFAP immunoreactivity. *Brain Res.* (2010) 1346:237–46. doi: 10.1016/j.brainres.2010.05.045
94. Papatheofanis FJ. Use of calcium channel antagonists as magnetoprotective agents. *Radiat Res.* (1990) 122:24–8. doi: 10.2307/3577578
95. Catterall WA. Structure and regulation of voltage-gated Ca2+ channels. *Annu Rev Cell Dev Biol.* (2000) 16:521–55. doi: 10.1146/annurev.cellbio.16.1.521
96. Pall ML. Electromagnetic fields act via activation of voltage-gated calcium channels to produce beneficial or adverse effects. *J Cell Mol Med.* (2013) 17:958–65. doi: 10.1111/jcmm.12088
97. Olgar Y, Hidisoglu E, Celen MC, Yamasan BE, Yargicoglu P, Ozdemir S. 2.1 GHz electromagnetic field does not change contractility and intracellular Ca2+ transients but decreases β-adrenergic responsiveness through nitric oxide signaling in rat ventricular myocytes. *Int J Radiat Biol.* (2015) 91:851–7. doi: 10.3109/09553002.2015.1068462
98. Wang LF, Peng RY, Hu XJ, Gao YB, Wang SM, Zhao L, et al. Abnormality of synaptic vesicular associated proteins in cerebral cortex and hippocampus after microwave exposure. *Synapse.* (2009) 63:1010–6. doi: 10.1002/syn.20684
99. Ledoigt G, Belpomme D. Cancer induction pathways and HF-EMF irradiation. *Adv Biol Chem.* (2013) 03:177–86. doi: 10.4236/abc.2013.32023
100. Wang H, Zhang J, Hu SH, Tan SZ, Zhang B, Zhou HM, et al. Real-time microwave exposure induces calcium efflux in primary hippocampal neurons and primary cardiomyocytes. *Biomed Environ Sci.* (2018) 31:561–71. doi: 10.3967/bes2018.077
101. Adey WR, Bawin SM, Lawrence AF. Effects of weak amplitude-modulated microwave fields on calcium efflux from awake cat cerebral cortex. *Bioelectromagnetics.* (1982) 3:295–307. doi: 10.1002/bem.2250030302
102. Dutta SK, Ghosh B, Blackman CF. Radiofrequency radiation-induced calcium ion efflux enhancement from human and other

neuroblastoma cells in culture. *Bioelectromagnetics.* (1989) 10:197–202. doi: 10.1002/bem.2250100208
103. Dutta SK, Subramoniam A, Ghosh B, Parshad R. Microwave radiation-induced calcium ion efflux from human neuroblastoma cells in culture. *Bioelectromagnetics.* (1984) 5:71–8. doi: 10.1002/bem.2250050108
104. Pall ML, Wi-Fi. is an important threat to human health. *Environ Res.* (2018) 164:405–16. doi: 10.1016/j.envres.2018.01.035
105. Friedman J, Kraus S, Hauptman Y, Schiff Y, Seger R. Mechanism of short-term ERK activation by electromagnetic fields at mobile phone frequencies. *Biochem J.* (2007) 405:559–68. doi: 10.1042/BJ20061653
106. Blank M, Goodman R. Electromagnetic fields stress living cells. *Pathophysiology.* (2009) 16:71–8. doi: 10.1016/j.pathophys.2009.01.006
107. Bilgici B, Akar A, Avci B, Tuncel OK. Effect of 900 MHz radiofrequency radiation on oxidative stress in rat brain and serum. *Electromagn Biol Med.* (2013) 32:20–9. doi: 10.3109/15368378.2012.699012
108. Stein Y, Udasin IG. Electromagnetic hypersensitivity (EHS, microwave syndrome) - Review of mechanisms. *Environ Res.* (2020) 186:109445. doi: 10.1016/j.envres.2020.109445
109. Narayanan SN, Jetti R, Kesari KK, Kumar RS, Nayak SB, Bhat PG. Radiofrequency electromagnetic radiation-induced behavioral changes and their possible basis. *Environ Sci Pollut Res Int.* (2019) 26:30693–710. doi: 10.1007/s11356-019-06278-5
110. Görlach A, Bertram K, Hudecova S, Krizanova O. Calcium and ROS: A mutual interplay. *Redox Biol.* (2015) 6:260–71. doi: 10.1016/j.redox.2015.08.010
111. Kaltschmidt B, Widera D, Kaltschmidt C. Signaling via NF-kappaB in the nervous system. *Biochim Biophys Acta.* (2005) 1745:287–99. doi: 10.1016/j.bbamcr.2005.05.009
112. Kopitar-Jerala N. Innate Immune Response in Brain, NF-Kappa B Signaling and Cystatins. *Front Mol Neurosci.* (2015) 8:73. doi: 10.3389/fnmol.2015.00073
113. Zuo HY, Lin T, Wang DW, Peng RY, Wang SM, Gao YB, et al. Neural cell apoptosis induced by microwave exposure through mitochondria-dependent caspase-3 pathway. *Int J Med Sci.* (2014) 11:426–35. doi: 10.7150/ijms.6540
114. Zuo HY, Lin T, Wang DW, Peng RY, Wang SM, Gao YB, et al. RKIP regulates neural cell apoptosis induced by exposure to microwave radiation partly through the MEK/ERK/CREB pathway. *Mol Neurobiol.* (2015) 51:1520–9. doi: 10.1007/s12035-014-8831-5
115. Esmekaya MA, Ozer C, Seyhan N. 900 MHz pulse-modulated radiofrequency radiation induces oxidative stress on heart, lung, testis and liver tissues. *Gen Physiol Biophys.* (2011) 30:84–9. doi: 10.4149/gpb_2011_01_84
116. Burlaka A, Tsybulin O, Sidorik E, Lukin S, Polishuk V, Tsehmistrenko S, et al. Overproduction of free radical species in embryonal cells exposed to low intensity radiofrequency radiation. *Exp Oncol.* (2013) 35:219–25.
117. Shahin S, Banerjee S, Swarup V, Singh SP, Chaturvedi CM. From the Cover: 2. 45-GHz Microwave Radiation Impairs Hippocampal Learning and Spatial Memory: Involvement of Local Stress Mechanism-Induced Suppression of iGluR/ERK/CREB Signaling. *Toxicol Sci.* (2018) 161:349–74. doi: 10.1093/toxsci/kfx221
118. Dasdag S, Akdag MZ, Kizil G, Kizil M, Cakir DU, Yokus B. Effect of 900 MHz radio frequency radiation on beta amyloid protein, protein carbonyl, and malondialdehyde in the brain. *Electromagn Biol Med.* (2012) 31:67–74. doi: 10.3109/15368378.2011.624654
119. Furtado-Filho OV, Borba JB, Maraschin T, Souza LM, Henriques JA, Moreira JC, et al. Effects of chronic exposure to 950 MHz ultra-high-frequency electromagnetic radiation on reactive oxygen species metabolism in the right and left cerebral cortex of young rats of different ages. *Int J Radiat Biol.* (2015) 91:891–7. doi: 10.3109/09553002.2015.1083629
120. Bas O, Odaci E, Kaplan S, Acer N, Ucok K, Colakoglu S. 900 MHz electromagnetic field exposure affects qualitative and quantitative features of hippocampal pyramidal cells in the adult female rat. *Brain Res.* (2009) 1265:178–85. doi: 10.1016/j.brainres.2009.02.011
121. Sonmez OF, Odaci E, Bas O, Kaplan S. Purkinje cell number decreases in the adult female rat cerebellum following exposure to 900 MHz electromagnetic field. *Brain Res.* (2010) 1356:95–101. doi: 10.1016/j.brainres.2010.07.103
122. Ding GR, Yaguchi H, Yoshida M, Miyakoshi J. Increase in X-ray-induced mutations by exposure to magnetic field (60 Hz, 5 mT) in NF-kappaB-inhibited cells. *Biochem Biophys Res Commun.* (2000) 276:238–43. doi: 10.1006/bbrc.2000.3455
123. Storz P. Reactive oxygen species in tumor progression. *Front Biosci.* (2005) 10:1881–96. doi: 10.2741/1667
124. Choi SB, Kwon MK, Chung JW, Park JS, Chung K, Kim DW. Effects of short-term radiation emitted by WCDMA mobile phones on teenagers and adults. *BMC Public Health.* (2014) 14:438. doi: 10.1186/1471-2458-14-438
125. Leach V, Weller S, Redmayne M, A. novel database of bio-effects from non-ionizing radiation. *Rev Environ Health.* (2018) 33:273–80. doi: 10.1515/reveh-2018-0017
126. Lushchak VI. Free radicals, reactive oxygen species, oxidative stress and its classification. *Chem Biol Interact.* (2014) 224:164–75. doi: 10.1016/j.cbi.2014.10.016
127. Liu B, Jian Z, Li Q, Li K, Wang Z, Liu L, et al. Baicalein protects human melanocytes from H_2O_2-induced apoptosis via inhibiting mitochondria-dependent caspase activation and the p38 MAPK pathway. *Free Radic Biol Med.* (2012) 53:183–93. doi: 10.1016/j.freeradbiomed.2012.04.015
128. Jing M, Li YX, Zeng JZ, Huang PC, Skirzewski M, Kljakic O, et al. An optimized acetylcholine sensor for monitoring in vivo cholinergic activity. *Nat Methods.* (2020) 17:1139–46. doi: 10.1038/s41592-020-0953-2

Conflict of Interest: The authors declare that the research was conducted in the absence of any commercial or financial relationships that could be construed as a potential conflict of interest.

Publisher's Note: All claims expressed in this article are solely those of the authors and do not necessarily represent those of their affiliated organizations, or those of the publisher, the editors and the reviewers. Any product that may be evaluated in this article, or claim that may be made by its manufacturer, is not guaranteed or endorsed by the publisher.

frontiers in Public Health

BRIEF RESEARCH REPORT
published: 26 August 2021
doi: 10.3389/fpubh.2021.724239

900 MHz Radiofrequency Field Induces Mitochondrial Unfolded Protein Response in Mouse Bone Marrow Stem Cells

Wen Xie[1,2†], *Rui Xu*[1,2†], *Caiyun Fan*[1,2], *Chunyu Yang*[1,2], *Haiyan Chen*[1,2] *and Yi Cao*[1,2*]

[1] *Department of Toxicology, School of Public Health, Medical College of Soochow University, Suzhou, China,* [2] *Jiangsu Key Laboratory of Preventive and Translational Medicine for Geriatric Diseases, Suzhou, China*

OPEN ACCESS

Edited by:
Tongning Wu,
China Academy of Information and Communications Technology, China

Reviewed by:
Mindi He,
Army Medical University, China
Guangdi Chen,
Zhejiang University, China

****Correspondence:***
Yi Cao
yicao@suda.edu.cn

†These authors have contributed equally to this work and share first authorship

Specialty section:
This article was submitted to Radiation and Health, a section of the journal Frontiers in Public Health

Received: *12 June 2021*
Accepted: *04 August 2021*
Published: *26 August 2021*

Citation:
Xie W, Xu R, Fan C, Yang C, Chen H and Cao Y (2021) 900 MHz Radiofrequency Field Induces Mitochondrial Unfolded Protein Response in Mouse Bone Marrow Stem Cells. Front. Public Health 9:724239. doi: 10.3389/fpubh.2021.724239

Objective: To examine whether exposure of mouse bone marrow stromal cells (BMSC) to 900 MHz radiofrequency fields used in mobile communication devices can induce mitochondrial unfolded protein response (UPR^{mt}).

Methods: BMSCs were exposed to continuous wave 900 MHz radiofrequency fields (RF) at 120 $\mu W/cm^2$ power intensity for 4 h/d for 5 consecutive days. Cells in sham group (SH) were cultured in RF exposure system, but without RF radiation. The positive control cells were irradiated with 6 Gy X-ray at a dose rate of 1.103 Gy/min (XR). To inhibit the upstream molecular JNK2 of UPR^{mt}, cells in siRNA + RF, and siRNA + XR group were also pretreated with 100 nM siRNA-JNK2 for 48 h before RF/XR exposure. Thirty minutes, 4 h, and 24 h post-RF/XR exposure, cells were collected, the level of ROS was measured with flow cytometry, the expression levels of UPR^{mt}-related proteins were detected using western blot analysis.

Results: Compared with Sham group, the level of ROS in RF and XR group was significantly increased 30 min and 4 h post-RF/XR exposure ($P < 0.05$), however, the RF/XR-induced increase of ROS level reversed 24 h post-RF/XR exposure. Compared with Sham group, the expression levels of HSP10/HSP60/ClpP proteins in cells of RF and XR group increased significantly 30 min and 4 h post-RF/XR exposure ($P < 0.05$), however, the RF/XR-induced increase of HSP10/HSP60/ClpP protein levels reversed 24 h post-RF exposure. After interfering with siRNA-JNK2, the RF/XR exposures could not induce the increase of HSP10/HSP60/ClpP protein levels any more.

Conclusions: The exposure of 900 MHz RF at 120 $\mu W/cm^2$ power flux density could increase ROS level and activate a transient UPR^{mt} in BMSC cells. Mitochondrial homeostasis in term of protein folding ability is restored 24 h post-RF exposure. Exposure to RF in our experimental condition did not cause permanent and severe mitochondrial dysfunctions. However, the detailed underlying molecular mechanism of RF-induced UPR^{mt} remains to be further studied.

Keywords: mitochondria, radiofrequency fields, unfolded protein response, reactive oxygen species, microwave, heat shock protein

INTRODUCTION

Non-ionizing radiofrequency fields (RF) are ubiquitous in the environment. They are used in military, radio, and television broadcasting, wireless communications systems, industry, and medicine. The number of people exposed to RF increased exponentially with the introduction of wireless communication devices which transmit voice, data and images. The scientific information on the biological and health effects of exposure to RF is more extensive now than ever before (1). Nonetheless, the unfolded protein response (UPR) in mitochondria in cells exposed to RF received little attention of researchers. Mitochondria is the organelle with the closed bilayer membranes structure, which play a key role in cellular biosynthetic, intracellular oxidative phosphorylation and the regulation of calcium levels. Mitochondria contain specific heat shock proteins (HSP) and protease, which help to fold, unfold, or degrade other proteins for the protein equilibrium inside. When a large number of unfolded or misfolded proteins are accumulated in cells due to external stimulus, the reverse signaling pathway from mitochondria to nucleus will be activated to increase the expression of nuclear genes encoding mitochondrial proteins (2). The newly-synthesized mitochondrial proteins include chaperones HSP10 and HSP60 which facilitate the import and correct folding of unfolded proteins, and proteases ClpP and ClpX which help to degrade the unfolded and misfolded proteins. This process is called mitochondrial unfolded protein response (UPR^{mt}) (3–7).

Mitochondria are the main source and one of the targets of RF-induced reactive oxygen species (ROS) (8). Electromagnetic field (EMF) directly targets the electron transport chain, which leads to mitochondrial dysfunction and overproduction of ROS. EMF can cause a disturbance of mitochondrial proton motive force, which then disrupts the balance between ROS production and ROS clearance. The severe and long-lasting oxidative stress may play a key role in mitochondrial damage that leads to some human health problems (9). However, mild ROS increase could lead to cellular defense mechanisms, including unfolded protein response (10). Studies showed that during mild mitochondrial dysfunction, UPR^{mt} activation promotes development and prolonging longevity, suggesting that UPR^{mt} activation may be a useful therapeutic approach for some mitochondria-related diseases. However, prolonged or dysregulation of UPR^{mt} activation can exacerbate mitochondrial dysfunction caused by external stimuli (11–13).

Currently, there are few reports on the effect of RF-induced ROS on UPR^{mt}. In view of the paucity of RF investigations on UPR in mitochondria, we have conducted the present study to investigate whether 900 MHz RF can induce UPR^{mt} in BMSCs. Mouse bone marrow stem cells (BMSCs) were exposed to 900 MHz RF for 4 h/d for 5 d to examine if RF exposure can induce UPR in mitochondria. Sham-exposed (SH) control cells as well as those exposed to an acute dose of ionizing/X-rays radiation (XR) as positive control cells were included in the experiment. The expression levels of HSP10/HSP60/ClpP proteins involved in UPR^{mt} were examined. To verify the induction of UPR in BMSCs, siRNA-JNK2 was used to inhibit the known signal molecular JNK2 of UPR^{mt} in the study.

MATERIALS AND METHODS

Bone Marrow Stromal Cells

The collection and culture of BMSCs were described in detail in our earlier paper (14). Single cell suspensions were prepared in complete IMDM medium (Iscove's modified Dulbecco's medium, Hyclone, Suzhou, China) containing 10% fetal bovine serum (FBS, Gibco, Shanghai, China), 100 units/ml penicillin and 100 μg/ml streptomycin (Bio Basic, Hangzhou, China). From each mouse, aliquots of 4×10^5 cells in 10 ml medium were placed in 100 mm petri dishes cultured in an incubator (Heal Force Bio-Meditech, Hong Kong, China) maintaining $37 \pm 0.5^{\circ}C$ with humidified atmosphere of 95% air and 5% carbon dioxide (CO_2). Cells in 3–6 passages from a single mouse were used for different exposures described below.

Radiofrequency Fields/Sham Exposed Exposure

The exposure system was built in-house and consists of a signal generator (SN2130J6030, PMM, Cisano sul Neva, Italy), a power amplifier (SN1020, HD Communication, Ronkonkoma, NY), and a Gigahertz Transverse Electro-Magnetic (GTEM) chamber. The RF signal was generated, amplified and fed through an antenna (Southeast University, Nanjing, Jiangsu, China) and detected by a field strength meter (PMM, Cisano sul Neva, Italy). The specific operation principle and exposure protocols has been discussed in detail by the previous studies of our lab (14–16). The same GTEM without RF transmission, was used for SH-exposure of cells. During the RF/SH exposure, the culture medium was changed once and the external environment was maintained 37 $\pm$ 0.5°C with 87% relative humidity (without CO_2). The peak and average SARs could be computed by either frequency or time domain method (17), and the estimated values were extremely low: they were 4.1×10^{-4} and 2.5×10^{-4} W/kg, respectively.

X-Ray Radiation

Irradiations were performed with an X-ray apparatus (Rad Source Technologies Inc., USA) operating at a dose rate of 1.103 Gy/min.

Group Design

Several 100 mm petri dishes, each containing $\sim 4 \times 10^5$ cells/ml (total 10 ml medium), were used for the following exposure conditions: (a) kept in GTEM without RF (Sham, SH); (b) 900 MHz RF, 120 $\mu W/cm^2$ power intensity for 4 h/d for 5 d (RF); (c) acute 6 Gy X-ray radiation (XR); (d) kept in GTEM without RF for 4 h/d for 5 d after siRNA transfection (si + SH); (e) 900 MHz RF for 4 h/d for 5 d after siRNA transfection (si + RF); (f) acute 6 Gy X-ray radiation after siRNA transfection (si + XR). Cells in each group were collected at 30 min, 4 h, and 24 h post treatment for subsequent experiments. The entire investigation was repeated 3 times.

Measurement of Reactive Oxygen Species

ROS level was measured with reactive oxygen detection kit (Beyotime, Shanghai, China). After different treatments, the cells were gently washed twice with neutral phosphate buffer after digestion and centrifugation. Serum-free IMDM medium (Hyclone, USA) was used to prepare DCFH-DA solution with a final concentration of 10 μM. One mL of DCFH-DA solution was added into the centrifuge tubes of each group and thoroughly mixed. Centrifuge tube was incubated at 37°C for 20 min, mixed upside down every 3 min to promote maximum contact between the cells and the probe. At the end of incubation, supernatant was discarded, and the cells were washed with serum-free IMDM medium for 3 times. Then, the intracellular fluorescence intensity was measured at excitation wavelength of 488 nm and the emission wavelength of 525 nm.

siRNA Transfection

Transfection with siRNA was used to inhibit JNK2 expression, in a separate series of experiments, prior to sham, RF and X-rays exposure, cells grown to 60–70% confluence were transfected with 100 nM siRNA (ribo FECT^{TM} CP, Guangzhou, China) for 48 h, the target sequence used for JNK siRNA were GGCATCAAGCATCTGCATT. Subsequently, siRNA was washed out three times followed by the different exposure conditions. Transfection was performed for 48 h, and then the cells were collected. Quantitative real-time PCR was used to verify the transfection efficiency.

Western-Blot Analysis

In this study, HSP60/HSP10/ClpP protein, known UPR^{mt} markers, were chosen as the indicators to verify whether UPR^{mt} occurred (18–20). The expression levels of the heat shock protein HSP60/HSP10 and mitochondrial protease ClpP were detected with Western-Blot Analysis. Protein extracts were prepared by lysing the cells in lysis buffer containing 50 mM Tris (pH 7.4), 150 mM sodium chloride, 1%Triton X-100, 1% sodium deoxycholate, 0.1% sodium dodecyl sulfate, and 1 mM phenyl-methyl-sulfonyl fluoride (all obtained from Beyotime, Shanghai, China). The cell lysates were centrifuged at 14,000 × g for 5 min at 4°C and the supernatant containing solubilized proteins was collected. The protein concentration in all samples was determined using the BCA protein assay kit (Beyotime, Shanghai, China). From each sample, equal amount of protein (40 μg per lane) was loaded, separated by 10% sodium dodecyl sulfate polyacrylamide gel (SDS–PAGE) and then transferred to polyvinylidene difluoride (PVDF) membranes (Millipore Corporation, Billerica, MA, USA). The membranes were blocked for 2 h in 5% fat-free dry milk (Yili Industrial, Inner Mongolia, China) containing Tris Buffered Saline with Tween (TBST). The membranes were then incubated with primary antibodies (rabbit monoclonal anti-HSP10 antibody, rabbit monoclonal anti-HSP60 antibody, rabbit monoclonal anti-ClpP antibody, and rabbit monoclonal anti-GADPH, Abcam, Cambridge, USA) overnight at 4°C. They were washed three times in TBST and incubated further with horseradish peroxidase-conjugated antibodies (Beyotime, Shanghai, China) for 1.5 h at room temperature. This was followed by washing the membranes three times with TBST. The immunoreactive proteins on the membranes were detected using enhanced chemiluminescence reagents (Millipore Corporation) and G-BOX Chemi XRQ (Syngene, UK). The blots were quantified and normalized with the level of GADPH to correct the differences in loading of the proteins in different treatment cells.

Statistical Analyses

The results from three independent experiments were pooled and analyzed using GraphPad Prism 8.0 (GraphPad Software, San Diego, CA, USA). The results were subjected to One-way analysis of variance (ANOVA) to test differences between groups. A $P < 0.05$ was considered as significance difference between groups.

RESULTS

Reactive Oxygen Species

The expression levels of ROS in different groups were shown in **Figure 1**. The level of ROS in the RF group and XR group was significantly increased at 30 min and 4 h post-exposure ($P < 0.05$). The ROS level decreased to nearly those in SH cells 24 h post-RF and XR exposure. Compared with the cells exposed to RF, those exposed to XR showed significant increase in ROS at 30 min, 4 h ($P < 0.05$). These results indicated that both RF and X-ray could induce the production of ROS in BMSCs for a certain period of time. The increase of ROS induced by X-ray was much higher than that induced by RF.

siRNA Transfection Efficiency

After siRNA transfection for 48 h, the expression level of JNK2 mRNA was shown in **Figure 2**. The expression level of JNK2 mRNA decreased significantly compared to sham group ($P < 0.05$). The knockdown efficiency of siRNA transfection is 50%.

HSP10, HSP60, and ClpP Proteins (Western Blot Analysis)

The expression levels of HSP10, HSP60, ClpP proteins in different groups at 30min, 4 h, and 24 h were shown in **Figure 3**. Compared to the cells in SH group, the expression levels of HSP10, HSP60, ClpP proteins in the RF group increased significantly at 30 min and 4 h ($P < 0.05$), then decreased gradually and returned to nearly those in SH cells at 24 h. These results indicate that low-dose Radio-frequency could induce UPR^{mt} in BMSCs. After the interference of the upstream molecular JNK2 of UPR^{mt} with siRNA, the expression levels of HSP10, HSP60, ClpP proteins in si + RF group were significantly decreased compared to the RF group ($P < 0.05$), indicated that RF activates UPR^{mt} through the JNK2 signaling pathway.

DISCUSSION

Mitochondria are organelles that play important functions in cells and participate in a variety of physiological functions and

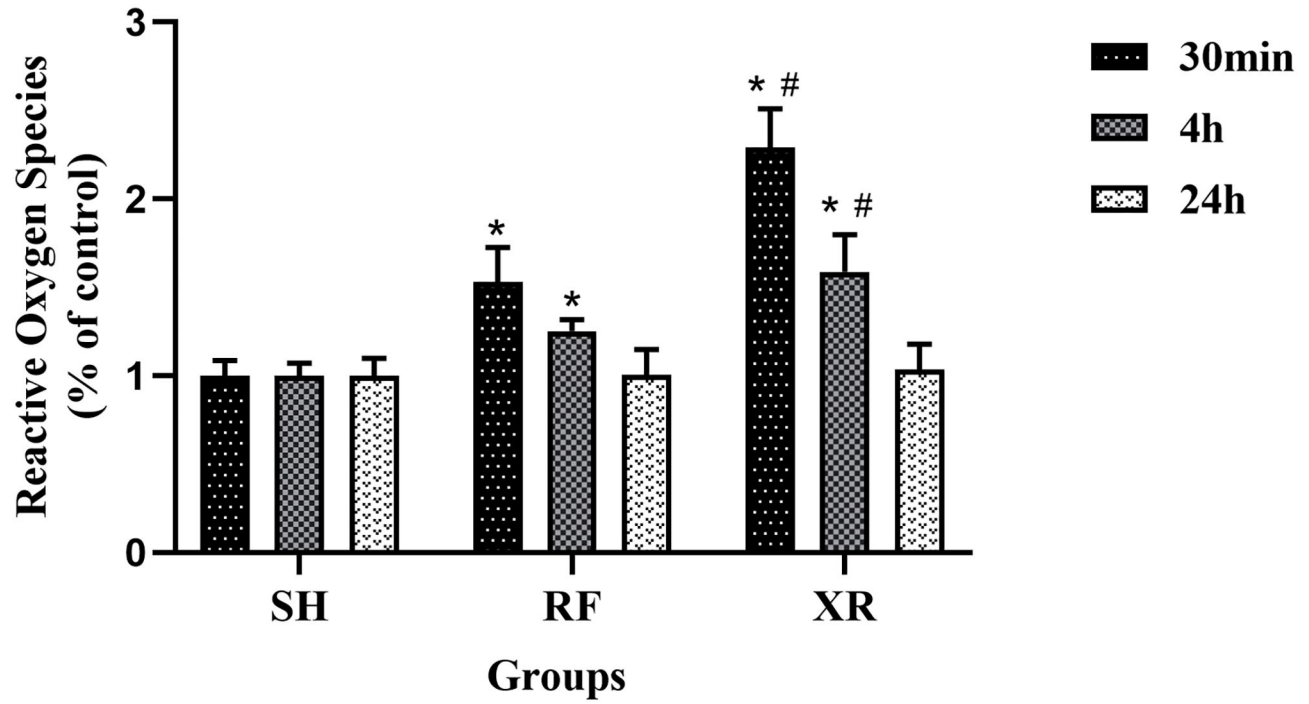

FIGURE 1 | ROS levels in BMSCs at 30 min, 4 h, and 24 h post exposure. SH, Sham; RF, RF-exposed; XR, X-rays irradiated. RF and XR vs. SH: $^{*}P < 0.05$; XR vs. RF: $^{\#}P < 0.05$.

biochemical reactions, including ATP production, iron-sulfur cluster biosynthesis, nucleotide and amino acid metabolism, and cell apoptosis (21–24). In order to maintain normal cellular physiological activities and functions, mitochondria have a complete set of molecular chaperone systems and quality control proteases, which promote the correct folding of proteins and degradation of misfolded/unfolded proteins (25, 26). Upon environmental stress, the accumulation of unfolded protein in the mitochondria could reach a certain threshold or severely damaged mitochondria appear in the cell, hence UPR^{mt} can enhance the overall function of cellular mitochondria by upregulating protective molecular chaperones and proteases that promote protein folding or clearance of defective proteins within stressed mitochondria, restore and maintain mitochondria steady state, and ultimately prevent and/or reduce the damage of environmental factors to the cells.

Non-ionizing radiofrequency fields (RF, 300 MHz to 300 GHz) are ubiquitous in environment (27). 900 MHz RF is one of the frequencies commonly used in mobile communication. High doses or long duration of radiofrequency radiation will exert harmful health effects on living organisms. The power density of 120 $\mu W/cm^2$ used in this study is below the exposure limit stipulated by the International Commission on Non-Ionizing Radiation Protection (ICNIRP), which is generally considered as low dose radiation. The biological effects and health impacts of long-term exposure to low-dose RF are a matter of widespread concern, and also a scientific issue that needs to be studied (28). In this study, we found that exposure to RF in our experimental condition did not cause permanent and severe mitochondrial dysfunctions. Our findings may shed light on dark areas of health effects of human exposure to radiofrequency radiation.

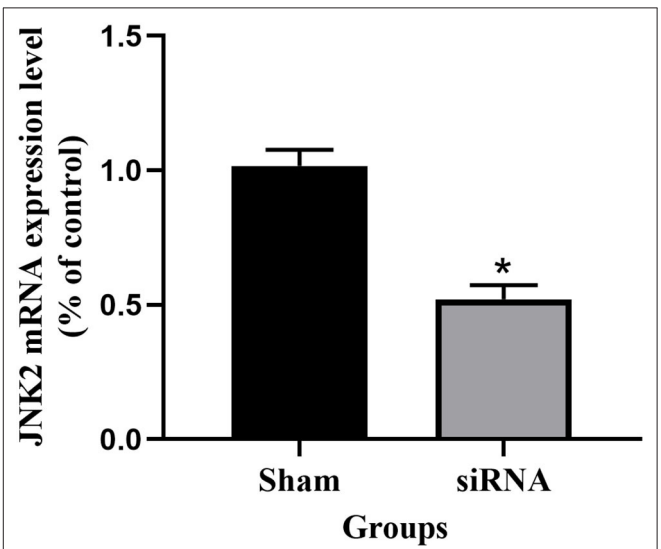

FIGURE 2 | The expression level of JNK2 mRNA after siRNA transfection for 48 h. siRNA vs. Sham: $^{*}P < 0.05$.

To the best of our knowledge, there have been very few peer-reviewed scientific publications in which ROS and mitochondrial UPR were examined in cells exposed to RF. Studies have shown that RF radiation can induce oxidative

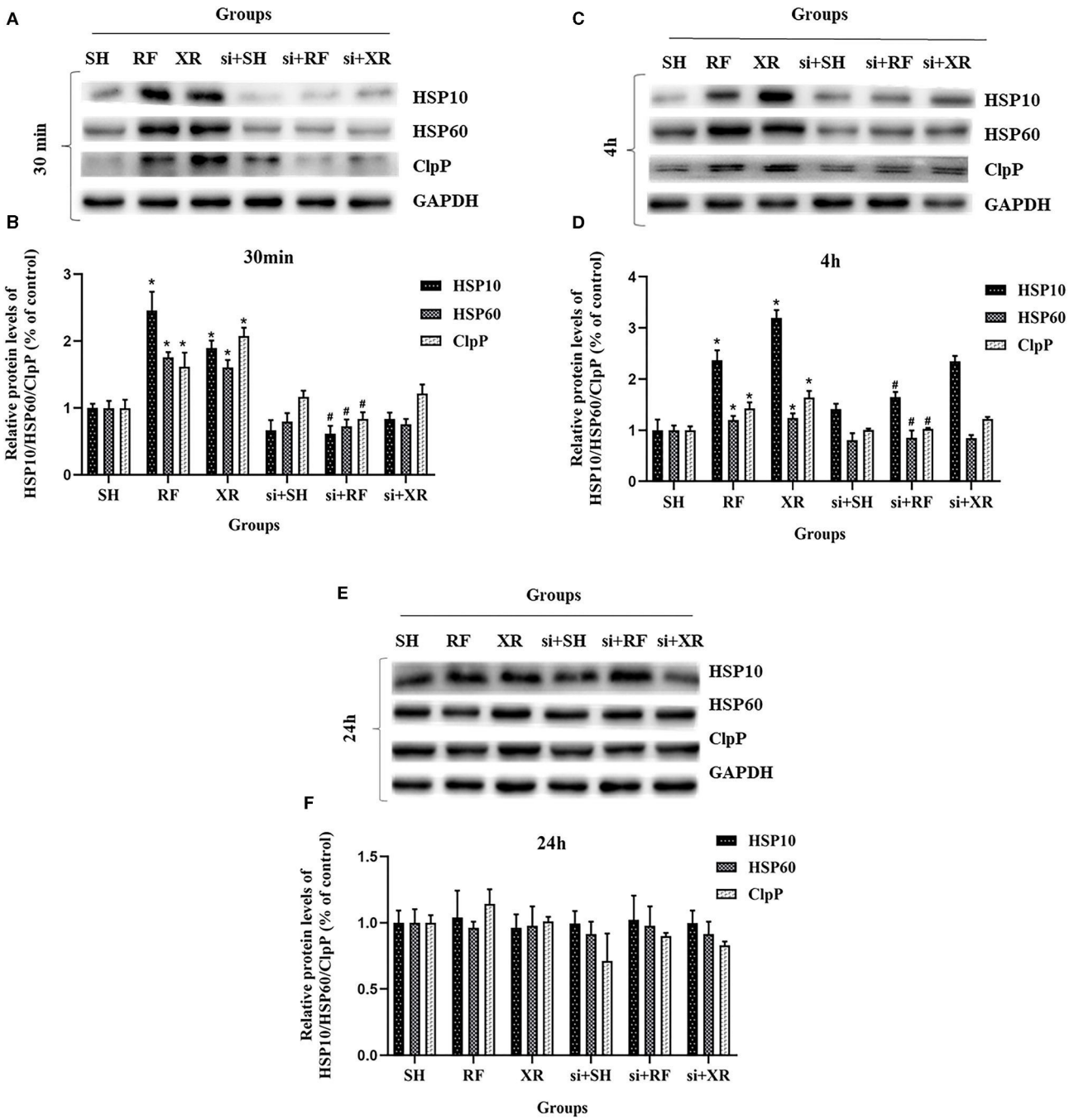

FIGURE 3 | Protein levels of HSP10, HSP60, ClpP in BMSCs after exposure. **(A)** Western blot analysis of HSP10, HSP60, ClpP in BMSCs at 30 min post exposure. **(B)** Relative expression on level of HSP10, HSP60, ClpP protein at 30 min post exposure. **(C)** Western blot analysis of HSP10, HSP60, ClpP in BMSCs at 4 h post exposure. **(D)** Relative expression on level of HSP10, HSP60, ClpP protein at 4 h post exposure. **(E)** Western blot analysis of HSP10, HSP60, ClpP in BMSCs at 24 h post exposure. **(F)** Relative expression on level of HSP10, HSP60, ClpP protein at 24 h post exposure. SH, Sham; RF, RF-exposed; XR, X-rays irradiated; si + SH, siRNA + Sham; si + RF, siRNA + RF-exposed; si + XR, siRNA + X-rays irradiated. RF and XR vs. SH: $^{*}P < 0.05$; si + RF vs. RF: $^{\#}P < 0.05$.

damage of mtDNA in cerebral cortical neurons of SD rats (29). It is reported that mitochondrial UPR could inhibit oxidative phosphorylation and ROS production (30). Increased protein level of chaperones HSP10, HSP60, and protease ClpP are considered to be the hallmark of UPR^{mt} activation (2, 3). As a mitochondrial chaperone protein encoded by the nuclear genome, HSP60 mainly promotes the folding of relatively small soluble monomeric proteins (31, 32), and plays an important role

in protein transport and folding in the mitochondria. HSP10 is widely present in a variety of mammalian tissues and can bind to unfolded proteins, effectively reducing energy barriers that occur during protein folding (33, 34). Mitochondrial ClpP is a serine protease located in the mitochondrial matrix. ClpP forms a proteolytic complex with AAA+ partner ClpX called ATP-dependent unfolding enzyme (ClpXP), which degrades misfolded or denatured proteins to participate in the quality control of mitochondrial proteins and maintain normal metabolic function (35). In this study, the expression levels of HSP10, HSP60, and ClpP in BMSCs were all upregulated within a certain period of time upon radio-frequency and X-rays exposure, indicating that both RF and X-rays could induce UPR^{mt} in BMSCs, however, the level of unfolded protein response induced by ionizing X-rays radiation was much greater than non-ionizing radio frequency. This phenomenon possibly be explained by the more severe mitochondria damage and more misfolded protein aggregation caused by X-rays radiation.

Many literatures have reported that ionizing radiation and non-ionizing radiation could activate the JNK signaling pathway (36–39). The activation of JNK2 is closely related to the induction of UPR. Activation of JNK2 could trigger c-Jun binding to AP-1 elements to up-regulate CHOP and C/EBPβ transcription. Dimer of CHOP and C/EBPβ transcription factors binds to specific UPR^{mt} promoter element and activates the target genes (40, 41). In this study, after interfering with siRNA-JNK2, the RF/XR exposures could not induce the increase of HSP10/HSP60/ClpP protein level, suggesting that JNK2 is involved in 900 MHz RF-induced UPR^{mt}. Our results are in agreement with reported investigations (36–41).

To further investigate an association between RF exposure and activation of UPR^{mt}, the level of ROS after RF and X-rays exposure were measured. The rationale for the study is that RF-induced ROS possibly causes mitochondrial damage, and hence the accumulation of misfolded/unfolded proteins which in turn activate UPR^{mt} in BMSCs (2). One of the main sources of cellular ROS is the mitochondrial respiratory chain, when affected by external stimuli, ETC produces excessive ROS, disturbing the mitochondrial environment homeostasis (42, 43). When moderate ROS exists, it will play a beneficial physiological role, but when excessive ROS content increases, it will cause severe cell stress damage and even lead to cell death (44). For decades, people have been focused on the RF effect on the health of human body, many studies have tried to assess whether or not the RF can affect the production of ROS in cells. However, due to the differences in cell types, RF parameters and exposure time, etc., the effects of RF exposure on ROS levels are inconsistent (45). Some studies have shown that radio-frequency radiation could induce the increase of intracellular ROS content (46, 47). In this study, the increased ROS level are in line with the increased level of UPR^{mt}-associated mitochondrial chaperone and protease. To date, very little is known about the mechanism underlying RF-induced UPR^{mt}. Some investigations found that ROS increase is closely related to the induction of UPR^{mt}, and UPR^{mt} is in turn an indispensable and complex response that allows cells to buffer ROS (48, 49), suggesting that RF exposure could induce the occurrence of UPR^{mt} via ROS production (50). The results of this research is consistent with the above reports.

Mitochondrial homeostasis determined the fate of cells. The functioning of the mitochondria are in turn tightly aligned to energy transduction and to the control of calcium and redox stress homeostasis (51). The observations obtained in our current study in BMSCs indicated that non-ionizing 900 MHz RF exposure at 120 $\mu W/cm^2$ power density was capable of inducing UPR^{mt} in response to mitochondria stress, increasing the expression of HSP10/HSP60/ClpP proteins, restoring mitochondrial homeostasis. Although RF exposure has already been demonstrated to activate UPR^{mt} in this study, the detailed underlying mechanism remains to be further studied.

DATA AVAILABILITY STATEMENT

The original contributions presented in the study are included in the article/supplementary material, further inquiries can be directed to the corresponding author/s.

AUTHOR CONTRIBUTIONS

WX and RX conceived the manuscript, did the experiments, and wrote the draft of the manuscript. CF, CY, and HC reviewed the manuscript. YC designed the experiment and critically revised the manuscript. All authors listed have made a substantial, direct and intellectual contribution to the work, and approved it for publication.

FUNDING

This research was provided by the National Natural Science Foundation of China (Grant# 81373025) and Chinese Ministry of Science.

REFERENCES

1. Yang L, Zhang C, Chen Z, Li C, Wu T. Functional and network analyses of human exposure to long-term evolution signal. *Environ Sci Pollut Res Int.* (2021) 28:5755–73. doi: 10.1007/s11356-020-10728-w
2. Haynes CM, Fiorese CJ, Lin YF. Evaluating and responding to mitochondrial dysfunction: the mitochondrial unfolded-protein response and beyond. *Trends Cell Biol.* (2013) 23:311–8. doi: 10.1016/j.tcb.2013.02.002
3. Haynes CM, Ron D. The mitochondrial UPR - protecting organelle protein homeostasis. *J Cell Sci.* (2010) 123:3849–55. doi: 10.1242/jcs.075119
4. Medinas DB, Hetz C. Protein homeostasis: modeling UPR adaptive responses. *Nat Chem Biol.* (2014) 10:879–80. doi: 10.1038/nchembio.1653
5. Quiros PM, Mottis A, Auwerx J. Mitonuclear communication in homeostasis and stress. *Nat Rev Mol Cell Bio.* (2016) 17:213–26. doi: 10.1038/nrm.2016.23
6. Yoneda T, Benedetti C, Urano F, Clark SG, Harding HP, Ron D. Compartment-specific perturbation of protein handling activates genes encoding mitochondrial chaperones. *J Cell Sci.* (2004) 117:4055–66. doi: 10.1242/jcs.01275
7. Pickles S, Vigie P, Youle RJ. Mitophagy and quality control mechanisms in mitochondrial maintenance. *Curr Biol.* (2018) 28:R170–85. doi: 10.1016/j.cub.2018.01.004

8. Sun Y, Zong L, Gao Z, Zhu S, Tong J, Cao Y. Mitochondrial DNA damage and oxidative damage in HL-60 cells exposed to 900MHz radiofrequency fields. *Mutat Res.* (2017) 797–9:7–14. doi: 10.1016/j.mrfmmm.2017.03.001
9. Santini SJ, Cordone V, Falone S, Mijit M, Tatone C, Amicarelli F. Role of mitochondria in the oxidative stress induced by electromagnetic fields: focus on reproductive systems. *Oxid Med Cell Longev.* (2018) :5076271. doi: 10.1155/2018/5076271
10. Tauffenberger A, Fiumelli H, Almustafa S, Magistretti PJ. Lactate and pyruvate promote oxidative stress resistance through hormetic ROS signaling. *Cell Death Dis.* (2019) 10:653. doi: 10.1038/s41419-019-1877-6
11. Melber A, Haynes CM. UPR^{mt} regulation and output: a stress response mediated by mitochondrial-nuclear communication. *Cell Res.* (2018) 28:281–95. doi: 10.1038/cr.2018.16
12. Lin YF, Schulz AM, Pellegrino MW, Lu Y, Shaham S, Haynes CM. Maintenance and propagation of a deleterious mitochondrial genome by the mitochondrial unfolded protein response. *Nature.* (2016) 533:416–9. doi: 10.1038/nature17989
13. Gitschlag BL, Kirby CS, Samuels DC, Gangula RD, Mallal SA, Patel MR. Homeostatic responses regulate selfish mitochondrial genome dynamics in *C. elegans*. *Cell Metab.* (2016) 24:91–103. doi: 10.1016/j.cmet.2016.06.008
14. Ji Y, He Q, Sun Y, Tong J, Cao Y. Adaptive response in mouse bone-marrow stromal cells exposed to 900-MHz radiofrequency fields: Gamma-radiation-induced DNA strand breaks and repair. *J Toxicol Environ Health A.* (2016) 79:419–26. doi: 10.1080/15287394.2016.1176618
15. He Q, Zong L, Sun Y, Vijayalaxmi, Prihoda TJ, Tong J, et al. Adaptive response in mouse bone marrow stromal cells exposed to 900MHz radiofrequency fields: impact of poly (ADP-ribose) polymerase (PARP). *Mutat Res.* (2017) 820:19–25. doi: 10.1016/j.mrgentox.2017.05.007
16. Zong L, Gao Z, Xie W, Tong J, Cao Y. Role of NF-κB activation in mouse bone marrow stromal cells exposed to 900-MHz radiofrequency fields (RF). *J Toxicol Environ Health A.* (2019) 82:46–51. doi: 10.1080/15287394.2018.1553372
17. Li C, Yang L, Li CH, Xie Y, Wu T. Dosimetric variability of the rats' exposure to electromagnetic pulses. *Electromagn Biol Med.* (2015) 34:334–43. doi: 10.3109/15368378.2014.925472
18. Papa L, Germain D. Estrogen receptor mediates a distinct mitochondrial unfolded protein response. *J Cell Sci.* (2011) 124(Pt 9):1396–402. doi: 10.1242/jcs.078220
19. Papa L, Germain D. SirT3 regulates the mitochondrial unfolded protein response. *Mol Cell Biol.* (2014) 34:699–710. doi: 10.1128/MCB.01337-13
20. Zhao Q, Wang J, Levichkin IV, Stasinopoulos S, Ryan MT, Hoogenraad NJ. A mitochondrial specific stress response in mammalian cells. *EMBO J.* (2002) 21:4411–9. doi: 10.1093/emboj/cdf445
21. Mayevsky A, Rogatsky GG. Mitochondrial function in vivo evaluated by NADH fluorescence: from animal models to human studies. *Am J Physiol Cell Physiol.* (2007) 292:C615–40. doi: 10.1152/ajpcell.00249.2006
22. Yin F, Sancheti H, Liu Z, Cadenas E. Mitochondrial function in ageing: coordination with signalling and transcriptional pathways. *J Physiol.* (2016) 594:2025–42. doi: 10.1113/JP270541
23. Midzak AS, Chen H, Aon MA, Papadopoulos V, Zirkin BRJBoR. ATP synthesis, mitochondrial function, and steroid biosynthesis in rodent primary and tumor leydig cells. *Biol Reprod.* (2014) 84:976–85. doi: 10.1095/biolreprod.110.087460
24. Yang PM, Chen HC, Tsai JS, Lin LYJCRiT. Cadmium induces Ca^{2+}-dependent necrotic cell death through calpain-triggered mitochondrial depolarization and reactive oxygen species-mediated inhibition of nuclear factor-kappaB activity. *Chem Res Toxicol.* (2014) 20:406–15. doi: 10.1021/tx060144c
25. Bukau B, Weissman J, Horwich A. Molecular chaperones and protein quality control. *Cell.* (2006) 125:443–51. doi: 10.1016/j.cell.2006.04.014
26. Pagliarini DJ, Calvo SE, Chang B, Sheth SA, Vafai SB, Ong SE, et al. A mitochondrial protein compendium elucidates complex I disease biology. *Cell.* (2008) 134:112–23. doi: 10.1016/j.cell.2008.06.016
27. Li CS, Xu CY, Wang RX, Yang L, Wu TN. Numerical evaluation of human exposure to 3.5-GHz electromagnetic field by considering the 3GPP-like channel features. *Ann Telecommun.* (2019) 74:25–33. doi: 10.1007/s12243-018-0682-z
28. Sarika S, Neeru K. Health implications of electromagnetic fields, mechanisms of action, and research needs. *Adv Biol.* (2014) 2014: 198609. doi: 10.1155/2014/198609
29. Xu S, Zhou Z, Zhang L, Yu Z, Zhang W, Wang Y, et al. Exposure to 1800 MHz radiofrequency radiation induces oxidative damage to mitochondrial DNA in primary cultured neurons. *Brain Res.* (2010) 1311:189–96. doi: 10.1016/j.brainres.2009.10.062
30. Zhu L, Luo X, Fu N, Chen L. Mitochondrial unfolded protein response: a novel pathway in metabolism and immunity. *Pharmacol Res.* (2021) 168:105603. doi: 10.1016/j.phrs.2021.105603
31. Cheng MY, Hartl FU, Martin J, Pollock RA, Kalousek F, Neupert W, et al. Mitochondrial heat-shock protein Hsp60 is essential for assembly of proteins imported into yeast mitochondria. *Nature.* (1989) 337:620–5. doi: 10.1038/337620a0
32. Yamano K, Kuroyanagi-Hasegawa M, Esaki M, Yokota M, Endo T. Step-size analyses of the mitochondrial Hsp70 import motor reveal the Brownian ratchet in operation. *J Biol Chem.* (2008) 283:27325–32. doi: 10.1074/jbc.M805249200
33. Höhfeld J, Hartl FU. Role of the chaperonin cofactor Hsp10 in protein folding and sorting in yeast mitochondria. *J Cell Biol.* (1994) 126:305–15. doi: 10.1083/jcb.126.2.305
34. Shan YX, Yang TL, Mestril R, Wang PH. Hsp10 and Hsp60 suppress ubiquitination of insulin-like growth factor-1 receptor and augment insulin-like growth factor-1 receptor signaling in cardiac muscle: implications on decreased myocardial protection in diabetic cardiomyopathy. *J Biol Chem.* (2003) 278:45492–8. doi: 10.1074/jbc.M304498200
35. Nouri K, Feng Y, Schimmer AD. Mitochondrial ClpP serine protease-biological function and emerging target for cancer therapy. *Cell Death Dis.* (2020) 11:841. doi: 10.1038/s41419-020-03062-z
36. Chen YR, Wang X, Templeton D, Davis RJ, Tan TH. The role of c-Jun N-terminal kinase (JNK) in apoptosis induced by ultraviolet C and gamma radiation. Duration of JNK activation may determine cell death and proliferation. *J Biol Chem.* (1996) 271:31929–36. doi: 10.1074/jbc.271.50.31929
37. Wong WY, Allie S, Limesand KH. PKCζ and JNK signaling regulate radiation-induced compensatory proliferation in parotid salivary glands. *PLoS ONE.* (2019) 14:e0219572. doi: 10.1371/journal.pone.0219572
38. Li F, Zheng X, Liu Y, Li P, Liu X, Ye F, et al. Different roles of CHOP and JNK in mediating radiation-induced autophagy and apoptosis in breast cancer cells. *Radiat Res.* (2016) 185:539–48. doi: 10.1667/RR14344.1
39. Buttiglione M, Roca L, Montemurno E, Vitiello F, Capozzi V, Cibelli G. Radiofrequency radiation (900 MHz) induces Egr-1 gene expression and affects cell-cycle control in human neuroblastoma cells. *J Cell Physiol.* (2007) 213:759–67. doi: 10.1002/jcp.21146
40. Mottis A, Jovaisaite V, Auwerx J. The mitochondrial unfolded protein response in mammalian physiology. *Mamm Genome.* (2014) 25:424–33. doi: 10.1007/s00335-014-9525-z
41. Barbour JA, Turner N. Mitochondrial stress signaling promotes cellular adaptations. *Int J Cell Biol.* (2014) 156020. doi: 10.1155/2014/156020
42. Yang S, Lian G. ROS and diseases: role in metabolism and energy supply. *Mol Cell Biochem.* (2020) 467:1–12. doi: 10.1007/s11010-019-03667-9
43. Castello PR, Drechsel DA, Patel M. Mitochondria are a major source of paraquat-induced reactive oxygen species production in the brain. *J Biol Chem.* (2007) 282:14186–93. doi: 10.1074/jbc.M700827200
44. Bertero E, Maack C. Calcium signaling and reactive oxygen species in mitochondria. *Circ Res.* (2018) 122:1460–78. doi: 10.1161/CIRCRESAHA.118.310082
45. Wang H, Zhang X. Magnetic fields and reactive oxygen species. *Int J Mol Sci.* (2017) 18:2175. doi: 10.3390/ijms18102175
46. Zhao L, Yang YF, Gao YB, Wang SM, Wang LF, Zuo HY, et al. Upregulation of HIF-1α via activation of ERK and PI3K pathway mediated protective

response to microwave-induced mitochondrial injury in neuron-like cells. *Mol Neurobiol.* (2014) 50:1024–34. doi: 10.1007/s12035-014-8667-z

47. Houston BJ, Nixon B, King BV, Aitken RJ, De Iuliis GN. Probing the origins of 1,800 MHz radio frequency electromagnetic radiation induced damage in mouse immortalized germ cells and spermatozoa *in vitro*. *Front Public Health.* (2018) 6:270. doi: 10.3389/fpubh.2018.00270
48. Runkel ED, Liu S, Baumeister R, Schulze E. Surveillance-activated defenses block the ROS-induced mitochondrial unfolded protein response. *PLoS Genet.* (2013) 9:e1003346. doi: 10.1371/journal.pgen.1003346
49. Shao LW, Niu R, Liu Y. Neuropeptide signals cell non-autonomous mitochondrial unfolded protein response. *Cell Res.* (2016) 26:1182–96. doi: 10.1038/cr.2016.118
50. Runkel ED, Baumeister R, Schulze E. Mitochondrial stress: balancing friend and foe. *Exp Gerontol.* (2014) 56:194–201. doi: 10.1016/j.exger.2014.02.013
51. Sack MN. The role of SIRT3 in mitochondrial homeostasis and cardiac adaptation to hypertrophy and aging. *J Mol Cell Cardiol.* (2012) 52:520–5. doi: 10.1016/j.yjmcc.2011.11.004

Conflict of Interest: The authors declare that the research was conducted in the absence of any commercial or financial relationships that could be construed as a potential conflict of interest.

frontiers in Public Health

ORIGINAL RESEARCH
published: 30 September 2021
doi: 10.3389/fpubh.2021.721166

Electromagnetic Exposure Dosimetry Study on Two Free Rats at 1.8 GHz via Numerical Simulation

*Xianghui Wang, Chengjie Xia, Lu Lu, Hongxin Qi and Jie Zhang**

Shanghai Key Laboratory of Magnetic Resonance & Biophysics Lab, School of Physics and Electronic Sciences, East China Normal University, Shanghai, China

Normally, the impact of electromagnetic exposure on human health is evaluated by animal study. The biological effect caused by electromagnetic exposure on such experimental animals as rats has been proven to be dose-dependent. However, though the dose of radio frequency (RF) electromagnetic exposure described by the specific absorbing rate (SAR) on fixed rats has been relatively well-studied utilizing the numerical simulations, the dosimetry study of exposure on free rat is insufficient, especially in the cases of two or more free rats. Therefore, the present work focuses on the variation of SAR caused by the existence of neighboring free rat in the same cage. Here, infrared thermography was used to record the activity of the two free rats who lived in the same cage that mounted at the far-field region in the microwave darkroom for a duration of 48 h. Then, using image processing techniques, the relative positions and orientations of the two rats are identified, which are defined by three parameters, such as the relative distance (d), relative direction angle (α), and relative orientation angle (β). Using the simulation software XFdtd 7.3, the influence of d, α, and β on the whole-body average SAR (WB-avgSAR) of the rats exposed to 1.8 GHz electromagnetic wave was calculated and analyzed. Then, the average variation of WB-avgSAR of the two rats compared with that of a single rat within 48 h was calculated. The numerical simulation results showed that the relative posture position described by (d, α, and β) of the two rats affects their WB-avgSAR and leads to fluctuations at different positions. However, the variation rate of the 48-h-average WB-avgSAR was only 10.3%, which implied that the over-time average SAR of two or more rats can be roughly described by the WB-avgSAR of a single free rat, except when a real-time precise control of exposure dose is necessary.

Keywords: electromagnetics, exposure dose, free rats, relative posture position, numerical simulation

OPEN ACCESS

Edited by:
Tongning Wu,
China Academy of Information and Communications Technology, China

Reviewed by:
Xi Cheng,
Xinjiang Agricultural University, China
Chang Wang,
Shanghai Institute of Microsystem and Information Technology (CAS), China

****Correspondence:***
Jie Zhang
jzhang@phy.ecnu.edu.cn

Specialty section:
This article was submitted to Radiation and Health, a section of the journal Frontiers in Public Health

Received: *06 June 2021*
Accepted: *27 August 2021*
Published: *30 September 2021*

Citation:
Wang XH, Xia CJ, Lu L, Qi HX and Zhang J (2021) Electromagnetic Exposure Dosimetry Study on Two Free Rats at 1.8 GHz via Numerical Simulation. Front. Public Health 9:721166. doi: 10.3389/fpubh.2021.721166

INTRODUCTION

Public concerns about the potential effects on human health of non-ionizing electromagnetic radiation in the environment require studies on the bioeffect caused by electromagnetic exposure. Normally, experimental animals, such as mice or rats are used to perform biological studies instead of humans. It has been proven that the bioeffect caused by electromagnetic exposure is dose-dependent (1–4), which implies that monitoring the exposure dose in both experimental animals and humans is important. According to IEEE Std C95.1^{TM}-2019, the specific energy absorption rate (SAR) is a controlling criterion in the frequency range from 10 kHz to 6 GHz

(5). International Commission on Non-Ionizing Radiation Protection (ICNIRP) guidelines for limiting exposure to electromagnetic fields (EMFs) (100 kHz−300 GHz) also indicated that from a health risk perspective, how much EMF power absorbed by the biological tissues was generally interested. Below about 6 GHz, where EMFs penetrate deep into the tissue, SAR, which is the power absorbed per unit mass (W/kg), is useful to describe the dosimetric quantity (6). Since the frequencies of electromagnetic radiation from our daily-used wireless devices, such as mobile phones, radar, and WIFI signals all lie in this range, the bioeffects caused by 10 kHz ∼ 6 GHz microwave attract interest. Thus, the studies on exposure dose characterized by SAR under different exposure conditions were carried out through numerical simulation. Besides humans, the exposure doses of various experimental animals, such as mice, rats, rabbits, and monkeys have been studied. In this study, we take rats into account.

The present dosimetry studies indicated that the SAR value of one rat is influenced by both the irradiation manners (e.g., the frequency and the polarization direction of the wave) and the situation of the rat (e.g., the weight, the posture, and the size of the rat). For example, Mason reported that when the RF microwave incident from the back to the abdomen, and the electric component of the microwave polarized along the long axis of the rat, the whole-body average SAR first increased and then decreased with increasing wave frequency within 300–2,060 MHz, and the resonance absorption appeared at a frequency of 600 MHz (7). This implies that the frequency of the electromagnetic wave is a key factor for SAR value. Chen calculated the SAR value under 12 different kinds of irradiation manners of a 220 g rat, whose body size was 244.8 mm in length and 46.8 mm in width. Their results demonstrated that both the incident direction of the wave and the polarization direction of its electric component affect the SAR value of the rat (8). The permittivity of tissues is another major determinant of the SAR value. According to the measurement data from Gabriel, the permittivity values of different organs are different, which also varies with the weight, age, and size of the rat (9–12). Therefore, the weight, age, and size of the rat are also regarded as the influence factors of the SAR value (13).

Meanwhile, it is worth noting that most of the previous studies on electromagnetic exposure dose are based on fixed rats. However, in most real-life events, rats are in a free state rather than in a fixed state, and different postures, such as straight, curling, sleeping, or drinking should affect the SAR value because the polarization direction of the incident microwave changes with rats postures. Therefore, further research on the exposure dose of free rats is necessary to assess accurate exposure dose. One preliminary research work has been carried out concerning a single free rat, and a rough estimation of SAR value was obtained according to the statistical results of rat postures (14). Yet, rats prefer a social living, and the presence of neighboring rats might also inevitably cause variation of the SAR value (15). Thus, it would be meaningful to further study the exposure dose of

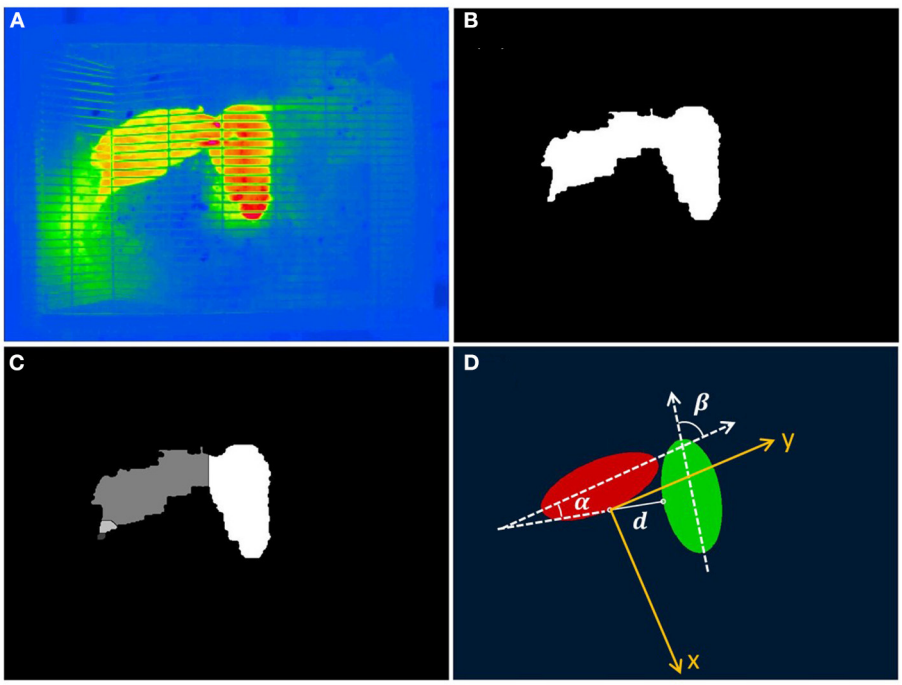

FIGURE 1 | Image processing procedure of identifying images of the two rats. **(A)** A raw thermography. **(B)** The binarized image of **(A)**. **(C)** A segmented image of the two rats with pixels belonging to the different rats shown in different grayscale. **(D)** Representing the positions and orientations of the two rats using two ellipses. The coordinate system and definitions of the relative distances, directions, and orientations are superimposed.

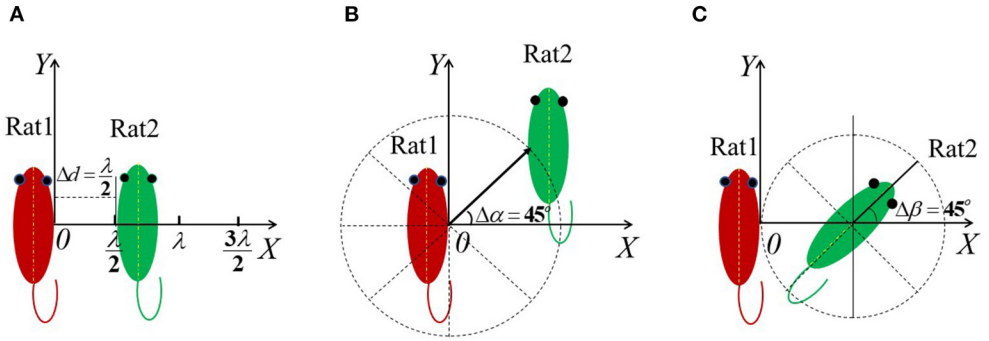

FIGURE 2 | Illustration of the variation manner of *d*, α, and β used for numerical simulation. **(A)** The variation manner of d; **(B)** The variation manner of α; **(C)** The variation manner of β.

multiple free rats within a group. To investigate the influence of multiple rats on their whole-body average SAR (WB-avgSAR), Shi et al. separately calculated the average SAR of one, two, and four rats located at a fixed position in a reverberation room. The result showed that the number of rats has no significant influence on the WB-avgSAR of rats, which was 0.0510, 0.0507, and 0.0506 mW/kg, respectively, with 1 V/m spatial electric field intensity and 6 GHz microwave (16). To investigate the whole-body SAR (WBSAR) of newborn and young rats at 2.45 GHz, Wu and coworkers have taken the habit and behavior of the newborn and young rats into consideration. The calculation results showed that the three typical configurations (rats close to the mother, group without mother, and single mother rat) affect the WBSAR of the young rats, with a maximum reduction of 30.0% (17).

To assess the electromagnetic exposure dose closer to the real situation, more and more interest focused on multiple free rats. Though a lot of works have been reported on either single or multiple rats with fixed posture positions, the work on free rat or rats is still insufficient. The present work aimed to study the exposure dose of two free rats. A real-time tracking technique was developed to record the behavior of the two rats and recognize their relative position. The influence of the relative position of the two rats on their WB-avgSAR and the average SAR variation within 48 h was calculated and discussed.

METHODS

Identification of the Relative Gesture Position of the Two Free Rats

The two rats were feed in a cage (0.46 m × 0.30 m × 0.18 m) with a food and water supply system. The cage was mounted on the sample stage in a microwave darkroom, and the distance between the sample stage and the antenna was 1 m, where the power density was 1.0 ± 0.2 W/m^2. The microwave was turned on and off every 12 h. An infrared thermography camera (804RC2, Manfrotto Company, Italy) was placed at 1.5 m above the cage to automatically record the behavior of the two rats without disturbing them. Before the 48-h video recording, the rats had adapted to the environment for 3 days. Using an in-house image processing algorithm (18), we distinguished the rough positions and directions of the two rats. The image processing steps were introduced as followed. First, the thermography (**Figure 1A**) was converted into a gray-scale image by calculating the difference of pixel values of the red channel and the blue channel to obtain a high-contrast image. This gray scale image was then binarized with a properly chosen grayscale threshold (**Figure 1B**). Next, a watershed method (19, 20) was used to segment and label the images of the two rats, even when they were slightly connected (**Figure 1C**). Finally, by calculating the secondary moment of the positions of the pixels belonging to each rat, their postures, centroids, and directions can be roughly represented by two ellipses (**Figure 1D**).

By comparing the results of a series of frames in a row when one of the rats is at rest, we estimate that the uncertainty caused by the above image processing alone is about 3 mm for centroid position and 1.5° for rat direction, respectively. In addition, through visual inspection, we estimate the error caused by different postures of the rats on centroid positions and directions to be <10% of rat length and 10°.

Characterization of the Relative Gesture Position of the Two Free Rats

The cage was put in the far-field region of the EMF. Therefore, the electric field in the cage area was considered uniform so that the coordinate position of the rat has little influence on its SAR value. Thus, we used three parameters to characterize the relative gesture position of the two free rats. That is, the relative distance d, the relative direction angle α, and the relative orientation angle β.

Through image processing, the two rats were substituted by the two ellipsoid models. Here, we defined the red ellipsoid as rat 1, and the blue one as rat 2. Thus, the two dash lines in **Figure 1D** show the respective long axes of the two rats. The angle between the two long axes was defined as the relative orientation angle β. Taken the midpoint of the right contour of rat 1 as the coordinate origin O, a plane rectangular coordinates system OXY was established, with its *Y-axis* parallels to the long axis of rat 1. In such a coordinate, the relative distance between

TABLE 1 | Case ID corresponding to the 125 relative posture positions of the two rats.

Case ID	Value of d, α and β	Case ID	Value of d, α and β	Case ID	Value of d, α and β
1	$d = 0$, $\alpha = 0°$, $\beta = 0°$	43	$d = 0.5\lambda$, $\alpha = 67.5°$, $\beta = 45°$	85	$d = 1.5\lambda$, $\alpha = 22.5°$, $\beta = 90°$
2	$d = 0$, $\alpha = 0°$, $\beta = 22.5°$	44	$d = 0.5\lambda$, $\alpha = 67.5°$, $\beta = 67.5°$	86	$d = 1.5\lambda$, $\alpha = 45°$, $\beta = 0°$
3	$d = 0$, $\alpha = 0°$, $\beta = 45°$	45	$d = 0.5\lambda$, $\alpha = 67.5°$, $\beta = 90°$	87	$d = 1.5\lambda$, $\alpha = 45°$, $\beta = 22.5°$
4	$d = 0$, $\alpha = 0°$, $\beta = 67.5°$	46	$d = 0.5\lambda$, $\alpha = 90°$, $\beta = 0°$	88	$d = 1.5\lambda$, $\alpha = 45°$, $\beta = 45°$
5	$d = 0$, $\alpha = 0°$, $\beta = 90°$	47	$d = 0.5\lambda$, $\alpha = 90°$, $\beta = 22.5°$	89	$d = 1.5\lambda$, $\alpha = 45°$, $\beta = 67.5°$
6	$d = 0$, $\alpha = 22.5°$, $\beta = 0°$	48	$d = 0.5\lambda$, $\alpha = 90°$, $\beta = 45°$	90	$d = 1.5\lambda$, $\alpha = 45°$, $\beta = 90°$
7	$d = 0$, $\alpha = 22.5°$, $\beta = 22.5°$	49	$d = 0.5\lambda$, $\alpha = 90°$, $\beta = 67.5°$	91	$d = 1.5\lambda$, $\alpha = 67.5°$, $\beta = 0°$
8	$d = 0$, $\alpha = 22.5°$, $\beta = 45°$	50	$d = 0.5\lambda$, $\alpha = 90°$, $\beta = 90°$	92	$d = 1.5\lambda$, $\alpha = 67.5°$, $\beta = 22.5°$
9	$d = 0$, $\alpha = 22.5°$, $\beta = 67.5°$	51	$d = \lambda$, $\alpha = 0°$, $\beta = 0°$	93	$d = 1.5\lambda$, $\alpha = 67.5°$, $\beta = 45°$
10	$d = 0$, $\alpha = 22.5°$, $\beta = 90°$	52	$d = \lambda$, $\alpha = 0°$, $\beta = 22.5°$	94	$d = 1.5\lambda$, $\alpha = 67.5°$, $\beta = 67.5°$
11	$d = 0$, $\alpha = 45°$, $\beta = 0°$	53	$d = \lambda$, $\alpha = 0°$, $\beta = 45°$	95	$d = 1.5\lambda$, $\alpha = 67.5°$, $\beta = 90°$
12	$d = 0$, $\alpha = 45°$, $\beta = 22.5°$	54	$d = \lambda$, $\alpha = 0°$, $\beta = 67.5°$	96	$d = 1.5\lambda$, $\alpha = 90°$, $\beta = 0°$
13	$d = 0$, $\alpha = 45°$, $\beta = 45°$	55	$d = \lambda$, $\alpha = 0°$, $\beta = 90°$	97	$d = 1.5\lambda$, $\alpha = 90°$, $\beta = 22.5°$
14	$d = 0$, $\alpha = 45°$, $\beta = 67.5°$	56	$d = \lambda$, $\alpha = 22.5°$, $\beta = 0°$	98	$d = 1.5\lambda$, $\alpha = 90°$, $\beta = 45°$
15	$d = 0$, $\alpha = 45°$, $\beta = 90°$	57	$d = \lambda$, $\alpha = 22.5°$, $\beta = 22.5°$	99	$d = 1.5\lambda$, $\alpha = 90°$, $\beta = 67.5°$
16	$d = 0$, $\alpha = 67.5°$, $\beta = 0°$	58	$d = \lambda$, $\alpha = 22.5°$, $\beta = 45°$	100	$d = 1.5\lambda$, $\alpha = 90°$, $\beta = 90°$
17	$d = 0$, $\alpha = 67.5°$, $\beta = 22.5°$	59	$d = \lambda$, $\alpha = 22.5°$, $\beta = 67.5°$	101	$d = 2\lambda$, $\alpha = 0°$, $\beta = 0°$
18	$d = 0$, $\alpha = 67.5°$, $\beta = 45°$	60	$d = \lambda$, $\alpha = 22.5°$, $\beta = 90°$	102	$d = 2\lambda$, $\alpha = 0°$, $\beta = 22.5°$
19	$d = 0$, $\alpha = 67.5°$, $\beta = 67.5°$	61	$d = \lambda$, $\alpha = 45°$, $\beta = 0°$	103	$d = 2\lambda$, $\alpha = 0°$, $\beta = 45°$
20	$d = 0$, $\alpha = 67.5°$, $\beta = 90°$	62	$d = \lambda$, $\alpha = 45°$, $\beta = 22.5°$	104	$d = 2\lambda$, $\alpha = 0°$, $\beta = 67.5°$
21	$d = 0$, $\alpha = 90°$, $\beta = 0°$	63	$d = \lambda$, $\alpha = 45°$, $\beta = 45°$	105	$d = 2\lambda$, $\alpha = 0°$, $\beta = 90°$
22	$d = 0$, $\alpha = 90°$, $\beta = 22.5°$	64	$d = \lambda$, $\alpha = 45°$, $\beta = 67.5°$	106	$d = 2\lambda$, $\alpha = 22.5°$, $\beta = 0°$
23	$d = 0$, $\alpha = 90°$, $\beta = 45°$	65	$d = \lambda$, $\alpha = 45°$, $\beta = 90°$	107	$d = 2\lambda$, $\alpha = 22.5°$, $\beta = 22.5°$
24	$d = 0$, $\alpha = 90°$, $\beta = 67.5°$	66	$d = \lambda$, $\alpha = 67.5°$, $\beta = 0°$	108	$d = 2\lambda$, $\alpha = 22.5°$, $\beta = 45°$
25	$d = 0$, $\alpha = 90°$, $\beta = 90°$	67	$d = \lambda$, $\alpha = 67.5°$, $\beta = 22.5°$	109	$d = 2\lambda$, $\alpha = 22.5°$, $\beta = 67.5°$
26	$d = 0.5\lambda$, $\alpha = 0°$, $\beta = 0°$	68	$d = \lambda$, $\alpha = 67.5°$, $\beta = 45°$	110	$d = 2\lambda$, $\alpha = 22.5°$, $\beta = 90°$
27	$d = 0.5\lambda$, $\alpha = 0°$, $\beta = 22.5°$	69	$d = \lambda$, $\alpha = 67.5°$, $\beta = 67.5°$	111	$d = 2\lambda$, $\alpha = 45°$, $\beta = 0°$
28	$d = 0.5\lambda$, $\alpha = 0°$, $\beta = 45°$	70	$d = \lambda$, $\alpha = 67.5°$, $\beta = 90°$	112	$d = 2\lambda$, $\alpha = 45°$, $\beta = 22.5°$
29	$d = 0.5\lambda$, $\alpha = 0°$, $\beta = 67.5°$	71	$d = \lambda$, $\alpha = 90°$, $\beta = 0°$	113	$d = 2\lambda$, $\alpha = 45°$, $\beta = 45°$
30	$d = 0.5\lambda$, $\alpha = 0°$, $\beta = 90°$	72	$d = \lambda$, $\alpha = 90°$, $\beta = 22.5°$	114	$d = 2\lambda$, $\alpha = 45°$, $\beta = 67.5°$
31	$d = 0.5\lambda$, $\alpha = 22.5°$, $\beta = 0°$	73	$d = \lambda$, $\alpha = 90°$, $\beta = 45°$	115	$d = 2\lambda$, $\alpha = 45°$, $\beta = 90°$
32	$d = 0.5\lambda$, $\alpha = 22.5°$, $\beta = 22.5°$	74	$d = \lambda$, $\alpha = 90°$, $\beta = 67.5°$	116	$d = 2\lambda$, $\alpha = 67.5°$, $\beta = 0°$
33	$d = 0.5\lambda$, $\alpha = 22.5°$, $\beta = 45°$	75	$d = \lambda$, $\alpha = 90°$, $\beta = 90°$	117	$d = 2\lambda$, $\alpha = 67.5°$, $\beta = 22.5°$
34	$d = 0.5\lambda$, $\alpha = 22.5°$, $\beta = 67.5°$	76	$d = 1.5\lambda$, $\alpha = 0°$, $\beta = 0°$	118	$d = 2\lambda$, $\alpha = 67.5°$, $\beta = 45°$
35	$d = 0.5\lambda$, $\alpha = 22.5°$, $\beta = 90°$	77	$d = 1.5\lambda$, $\alpha = 0°$, $\beta = 22.5°$	119	$d = 2\lambda$, $\alpha = 67.5°$, $\beta = 67.5°$
36	$d = 0.5\lambda$, $\alpha = 45°$, $\beta = 0°$	78	$d = 1.5\lambda$, $\alpha = 0°$, $\beta = 45°$	120	$d = 2\lambda$, $\alpha = 67.5°$, $\beta = 90°$
37	$d = 0.5\lambda$, $\alpha = 45°$, $\beta = 22.5°$	79	$d = 1.5\lambda$, $\alpha = 0°$, $\beta = 67.5°$	121	$d = 2\lambda$, $\alpha = 90°$, $\beta = 0°$
38	$d = 0.5\lambda$, $\alpha = 45°$, $\beta = 45°$	80	$d = 1.5\lambda$, $\alpha = 0°$, $\beta = 90°$	122	$d = 2\lambda$, $\alpha = 90°$, $\beta = 22.5°$
39	$d = 0.5\lambda$, $\alpha = 45°$, $\beta = 67.5°$	81	$d = 1.5\lambda$, $\alpha = 22.5°$, $\beta = 0°$	123	$d = 2\lambda$, $\alpha = 90°$, $\beta = 45°$
40	$d = 0.5\lambda$, $\alpha = 45°$, $\beta = 90°$	82	$d = 1.5\lambda$, $\alpha = 22.5°$, $\beta = 22.5°$	124	$d = 2\lambda$, $\alpha = 90°$, $\beta = 67.5°$
41	$d = 0.5\lambda$, $\alpha = 67.5°$, $\beta = 0°$	83	$d = 1.5\lambda$, $\alpha = 22.5°$, $\beta = 45°$	125	$d = 2\lambda$, $\alpha = 90°$, $\beta = 90°$
42	$d = 0.5\lambda$, $\alpha = 67.5°$, $\beta = 22.5°$	84	$d = 1.5\lambda$, $\alpha = 22.5°$, $\beta = 67.5°$	–	–

the two rats was determined by the length of the connection line between the two midpoints of the two rats, which was marked as d. The angle between this connection line and the *X-axis* was defined as the relative direction angle α. With (d, α), the relative position of the two rats is determined. By fixing the position of rat 1 at the origin of the OXY coordinate, the posture position of rat 2 relative to rat 1 can be expressed by (d, α, β).

Statistic Analysis of the Relative Gesture Position of the Two Free Rats

Taking rat 1 as the reference, the variation of the relative position caused by the motion of rat 2 was statistically analyzed. Because of the symmetry between the two rats, only the first quadrant of the coordinate system is necessary to represent the relative position of rat 2 referring to rat 1. The quadrant region is partitioned into

16 small regions, with a span of $\Delta d = 0.5\lambda$ (λ is the wavelength of the incident microwave, which is 166.7 mm for 1.8 GHz) and $\Delta\alpha = 22.5^\circ$. Here, we use $d = 0$ to represent the statistic distance interval of $d\epsilon(0, 0.5\lambda)$, and $\alpha = 0$ to represent the statistic angle interval of $\alpha\epsilon(0, 22.5^\circ)$. Accordingly, the values of d are chosen to be 0, 0.5, 1, 1.5, and 2, respectively, and α were valued as 0, 22.5, 45, 67.5, and 90. Similarly, the relative orientation angle β is categorized into five different numerical ranges marked as $\beta = 0$, 22.5, 45, 66.7, and 90° considering the symmetry between rat head and tail which cannot be strictly identified in this work. Therefore, there are 125 combinations of d, α, and β in total, and the frequency of each case was calculated based on the 48-h video.

Numerical Simulation

The rat anatomical model (220 g weight, 244.8 mm long) used here is the same as our previous work (8). XFDTD 7.3 (Remcom, PA, USA) was used to calculate the WB-avgSAR of the rat. The incident power density of the 1.8 GHz microwave was 1 W/m^2. The boundary condition was set as the perfectly matched layer with a seven-layered absorbance boundary. The grid size was set to 0.4 mm × 0.4 mm × 0.4 mm to guarantee convergent results and accurate SAR values in specific tissues.

To investigate the effect of the relative distance on the WB-avgSAR of the two rats, α and β was set as 0° (in this case, the two long axes are parallel), and the variation span of d was set as $\Delta d = 0.5\lambda$. To investigate the effect of relative position on the WB-avgSAR, d was set as the half-length of the rat body (i.e., $d =$ 122.4 mm in this work) and $\beta = 0^\circ$, and α varied from 0 to 360° with a span of $\Delta\alpha = 45^\circ$. To investigate the effect of the relative orientation on the WB-avgSAR, the d was set as 122.4 mm (to avoid the overlapping of two rats) and $\alpha = 0^\circ$. Rat 1 located at the coordinate origin and rat 2 laid flatly and spun clockwise with a span of $\Delta\beta = 22.5^\circ$. The illustration is shown in **Figure 2**.

Based on the 48-h video, there are 125 combinations of d, α, and β in total. Different values of d, α, and β were corresponded to the Case ID, as shown in **Table 1**.

In the 25 cases of $d = 0$ (α and β varied from 0 to 90°), the two rats tightly closed to each other or even overlapped. In such cases, it is difficult to separate the gesture of the two rats in XFDTD software. Therefore, we took the 25 cases into 1 case consideration that valued as $d = 0$, $\alpha = 0$, and $\beta = 0$ in the numerically simulated. The WB-avgSAR of rat 1 in each case was recorded as S_{1i}, where i varied from 1 to 125. Then, η_i was calculated with Equation (1)

$$\eta_i = \frac{S_{1i} - S_1}{S_1} \times 100\% \quad (1)$$

where S_1 is the WB-avgSAR of rat 1 fixed on the coordinate origin with the irradiation manner of EHK, which takes the value of 0.043 W/kg here. η_i reflects the influence of the relative gesture position of rat 2 on the WB-avgSAR of rat 1.

Two irradiation methods, EHK (the microwave incident from the back to the abdomen of the rat, and its electric field polarization direction was along the long axis of rat 1) and HEK (the microwave incident from the same direction, but its electric field polarization direction was along the short axis of rat 1), were considered in this study.

The average variation of the WB-avgSAR (η_{avg}) of rat 1 within 48 h was subsequently calculated by Equation (2) to see the overall impact of the existence of rat 2:

$$\eta_{avg} = \sum_i W_i \times \eta_i \quad (2)$$

where, W_i is the statistical probability of each relative posture position obtained from the 48-h-video.

RESULTS

The Effect of the Relative Position on the WB-AvgSAR of the Two Rats

The influence of the relative distance between the two rats on the WB-avgSAR is shown in **Figure 3**. The dashed line indicates the WB-avgSAR of a single rat, which has been calculated as 0.043 W/kg for EHK and 0.0245 W/kg for HEK. The WB-avgSAR of both rats is the same because they two are plane symmetry. The distance between the two paralleled rats does influence their WB-avgSAR in a form of fluctuation. In both irradiation manners EHK and HEK, the maximum values appeared at d $= \frac{2k-1}{2}\lambda$, while the minimum values appeared at $d = k\lambda$. The amplitude of the fluctuation decreased with the relative distance increasing. This might result from the disturbance of the spatial distribution of the microwave due to the existence of the neighboring rat. Compared with HEK, the results of the EHK method showed a higher WB-avgSAR and a larger fluctuation amplitude, this might be since EHK contributes to a long-axis polarization direction of its electric field.

The influence of relative direction angle α on the WB-avgSAR is shown in **Figure 4**. Similar to the effect of d, the WB-avgSAR of EHK irradiation was higher than that of HEK due to electric field polarization direction. The effect of α exhibited an orientation symmetry pattern in the case of EHK, and the maximum value appeared at the two rats in alignment that correspond to $\alpha = 90^\circ$ and 270°.

The influence of relative orientation angle β on the WB-avgSAR was shown in **Figure 5**. Since rat 1 was in a fixed position, the relative orientation of rat 2 leads to the asymmetric fluctuation of the WB-avgSAR on rat 1. The WB-avgSAR of rat 2 varied with the orientation angle β because its long-axis changed with β. When its long-axis was aligned with the electric field polarization direction under the $\beta = 90^\circ$ and 270°, the WB-avgSAR value of rat 2 is maximized.

The Statistical Result on the Relative Gesture Position of the Two Rats Within 48 h

The statistical result on the relative gesture position of the two rats within 48 h was shown in **Figure 6**. It gives the value of W_i in Equation (2).

For most of the time, the two rats laid closely, and the total probability of $d = 0$ (corresponded to case 1 to case 25) is about

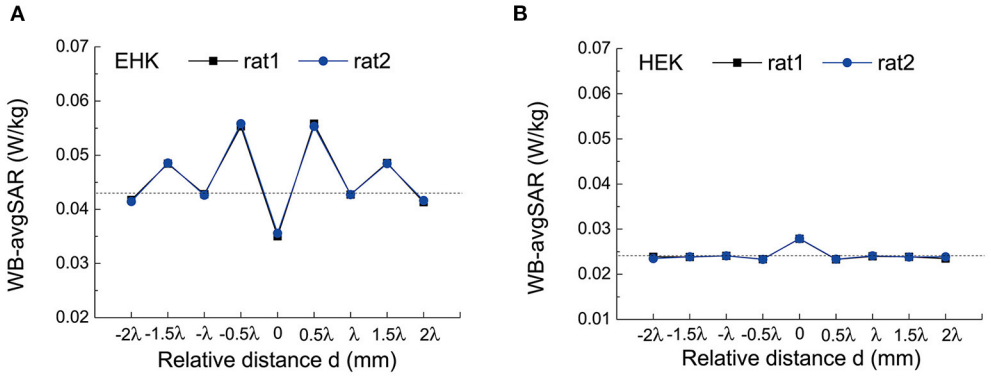

FIGURE 3 | The whole-body average SAR (WB-avgSAR) of two rats in different horizontal distance *d*. **(A)** The simulation results under EHK; **(B)** The simulation results under HEK.

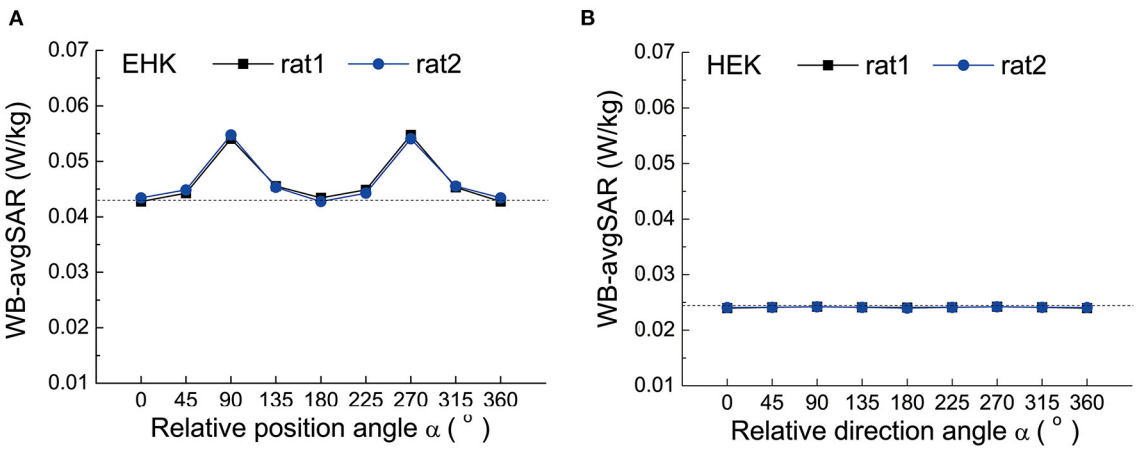

FIGURE 4 | The WB-avgSAR of two rats in different relative direction angles α **(A)** The simulation results under EHK; **(B)** The simulation results under HEK.

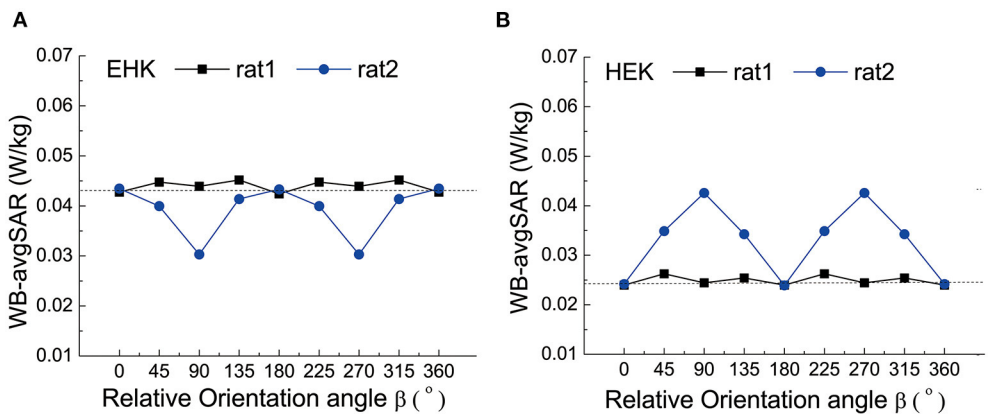

FIGURE 5 | The WB-avgSAR of two rats in different relative orientation angles β. **(A)** the simulation results of rat 1 laid flatly and in EHK radiation mode; **(B)** The simulation results of rat 1 laid flatly and in HEK radiation mode.

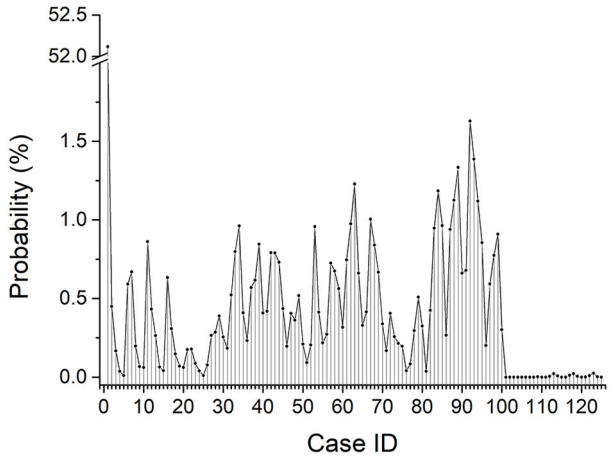

FIGURE 6 | Time probability distribution of two free rats in 125 relative posture positions (total time duration was 48 h).

57.74%. For the rest of the time, the two rats moved freely in the cage, and the distance between them mostly ranged from 0.5λ to 1.5λ. The probability of each relative gesture position fluctuated between 0 and 1.63%.

The Effect of the Existence of Rat 2 on the WB-AvgSAR of Rat 1

The variation rate of the WB-avgSAR of rat 1 under each relative gesture position case that was calculated from Equation (1) is shown in **Figure 7**. The existence of rat 2 affects the WB-avgSAR of rat 1 to a certain degree, and the effect would be either positive or negative. In most cases, the variation rate is lower than 10%. The average variation rate of the WB-avgSAR of rat 1 given by Equation (2) is about −10.3% within 48 h. When there are two free rats in the cage, the WB-avgSAR of each rat reduced about 10.3% when compared with the case of only one rat in the cage. However, it is worth noting that the calculation error caused by theoretical simulation is normally larger than 10%. So that, the variation of the WB-avgSAR of the rat that caused by the existence of another rat is too small to be considered unless the real-time SAR is required to be precisely controlled.

DISCUSSION

Wu et al. reported that the exposure of multiple rats led to significantly different dosimetric results at the microwave frequency (17), and they further indicated that the variation of the WB-avgSAR of the rat due to the existence of the adjacent rats differed from their intervals (21). Our study on the effect of the relative positive of the two rats showed similar results.

At a certain moment, the relative gesture position of two free rats is definable and can be treated as the two fixed rats. Thus, in the case of two free rats, the real-time dosimetric variation depends on their relative gesture position at that moment. Since the real-time dosimetric variation could be both positive and negative, the time-weighted average dosimetric variation within 48 h was only 10.3%.

Most of the time, the two rats stayed closely or even overlap. In such cases, the two rats might absorb the irradiation power together with a minimum reflection area, which led to a negative effect on the WB-avgSAR. Therefore, though in

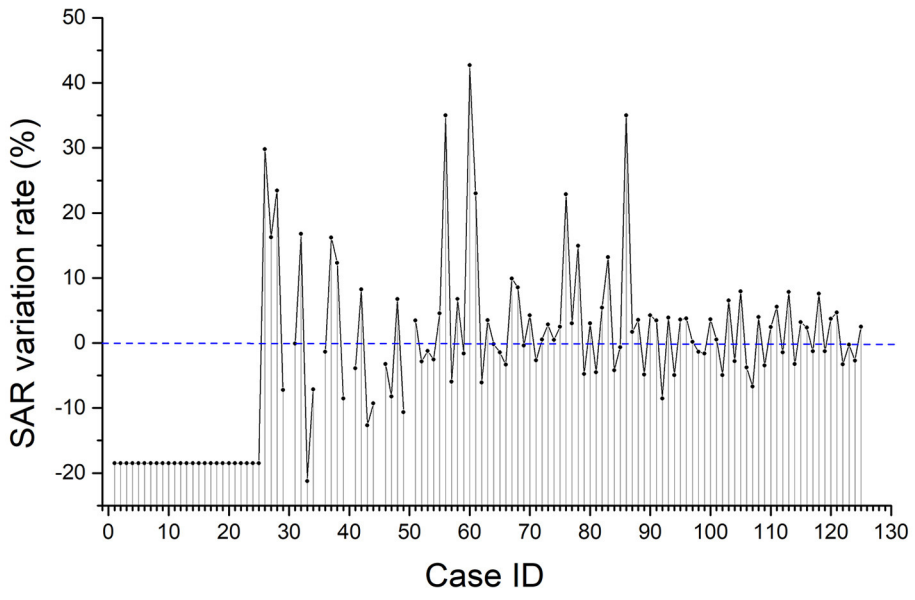

FIGURE 7 | The variation rate of the WB-avgSAR of rat 1 under each relative gesture position.

some cases, the positive effect could exceed 40%, the overall effect of the existence of rat 2 is to reduce the WB-avgSAR of rat 1.

In the present study, we only considered the average dosimetric variation on the WB-avgSAR of the rat. The dosimetric variation within the different organs might be further studied.

SUMMARY

Infrared thermography was used to record the activity of the two free rats who lived in the same cage that mounted at the far-field region in the microwave darkroom. Using an in-house image processing algorithm, we distinguish the rough positions and directions of the two rats. Three parameters as the relative distance (d), relative direction angle (α), and relative orientation angle (β) were defined to describe the relative posture position of the two rats. The existence of rat 2 leads to a fluctuation on the WB-avgSAR accompany by the change of d, α, and β. However, the variation rate of the 48-h-average WB-avgSAR is only around 10%, which implies that the over-time average WB-avgSAR of two free rats can be roughly described by the SAR of one free rat unless the real-time precisely control of exposure dose is required.

DATA AVAILABILITY STATEMENT

The original contributions presented in the study are included in the article/**Supplementary Material**, further inquiries can be directed to the corresponding author/s.

ETHICS STATEMENT

The animal study was reviewed and approved by the Animal Experimental Ethics Committee of East China Normal University.

AUTHOR CONTRIBUTIONS

XW participated in the method establishing to characterize the relative gesture position of the two rats, and the analysis of calculation result and wrote the manuscript. CX designed the image processing algorithm to provide the statistics on rats' relative positions and orientations. LL performed the video recording, performed the calculation by using XFDTD. HQ participated in the program writing, the numerical simulation, and the calculation result reviewing. JZ participated in the study design and reviewed the results. He also participated in the adjustment of devices and methods establishing to characterize the relative gesture position of the two rats. All authors contributed to the article and approved the submitted version.

FUNDING

This study was funded by the National Natural Science Foundation of China (31600675).

SUPPLEMENTARY MATERIAL

The Supplementary Material for this article can be found online at: https://www.frontiersin.org/articles/10.3389/fpubh.2021.721166/full#supplementary-material

REFERENCES

1. Gokcek-Sarac C. Effects of 2.1 GHz electromagnetic radiation on locomotor activity, recognition memory, and anxiety-related behavior in rats. *Neurophysiology*. (2021) 52:261–6. doi: 10.1007/s11062-021-09881-w
2. Yang L, Zhang C, Chen Z, Li C, Wu T. Functional and network analyses of human exposure to long-term evolution signal. *Environ Sci Pollut Res*. (2021) 28:5755–73. doi: 10.1007/s11356-020-10728-w
3. Wei Y, Yang J, Chen Z, Wu T, Lv B. Modulation of resting-state brain functional connectivity by exposure to acute fourth-generation long-term evolution electromagnetic field: an fMRI study. *Bioelectromagnetics*. (2019) 40:42–51. doi: 10.1002/bem.22165
4. Cabre-Riera A, van Wel L, Liorni I, Thielens A, Birks LE, Pierotti L, et al. Association between estimated whole-brain radiofrequency electromagnetic fields dose and cognitive function in preadolescents and adolescents. *Int J Hyg Environ Health*. (2021) 231:113659. doi: 10.1016/j.ijheh.2020.113659
5. IEEE International Committee on Electromagnetic Safety. *IEEE Standard for Safety Levels With Respect to Human Exposure to Electric, Magnetic, and Electromagnetic Fields,0 Hz to 300 GHz*. New York, NY: IEEE Std C95.1TM-2019.
6. International Commission on Non-Ionizing Radiation Protection. ICNIRP guidelines for limiting exposure to electromagnetic fields (100 kHz to 300 GHz). *Health Phys*. (2020) 118:483–524. doi: 10.1097/HP.0000000000001210
7. Mason PA, Hurt WD, Walters TJ, D'Andrea JA, Gajsek P, Ryan KL, et al. Effects of frequency, permittivity, and voxel size on predicted specific absorption rate values in biological tissue during electromagnetic-field exposure. *IEEE Transact Microwave Theory Techn*. (2000) 48:2050–8. doi: 10.1109/22.884194
8. Chen BX, Wang JM, Qi HX, Zhang J, Chen SD, Wang XH. The specific absorption rate of tissues in rats exposed to electromagnetic plane waves in the frequency range of 0.05–5 GHz and SARwb in free-moving rats. *Australas Phys Eng Sci Med*. (2017) 40:21–8. doi: 10.1007/s13246-017-0522-x
9. Gabriel C. Dielectric properties of biological tissue: variation with age. *Bioelectromagnetics*. (2005), 26:S12–8. doi: 10.1002/bem.20147
10. Gabriel C, Gabriel S, Corthout E. The dielectric properties of biological tissues: I. Literature survey. *Phys Med Biol*. (1996) 41:2231–49. doi: 10.1088/0031-9155/41/11/001
11. Gabriel S, Lau R W, Gabriel C. The dielectric properties of biological tissues: II. Measurements in the frequency range 10 Hz to 20 GHz. *Phys Med Biol*. (1996) 41:2251–69. doi: 10.1088/0031-9155/41/11/002
12. Gabriel S, Lau RW, Gabriel C. The dielectric properties of biological tissues: III. Parametric models for the dielectric spectrum of tissues. *Phys Med Biol*. (1996) 41:2271–93. doi: 10.1088/0031-9155/41/11/003
13. Xie T, Zaidi H. Age-dependent small-animal internal radiation dosimetry. *Mol Imaging*. (2013) 12:7290.2013.00053. doi: 10.2310/7290.2013.00053
14. Kuster N, Torres VB, Nikoloski N, Frauscher M, Kainz W. Methodology of detailed dosimetry and treatment of uncertainty and variations for *in vivo* studies. *Bioelectromagnetics*. (2006) 27:378–91. doi: 10.1002/bem.20219
15. Shi JJ, Chakarothai J, Wang JQ, Wake K, Watanabe S, Fujiwara O. Dosimetry and verification for 6-ghz whole-body non-constraint exposure of rats using reverberation chamber. *IEICE Transact Communi*. (2015) E98B:1164–72. doi: 10.1587/transcom.E98.B.1164
16. Wu T, Hadjem A, Wong MF, Gati A, Picon O, Wiart J. Whole-body new-born and young rats' exposure assessment in a reverberating chamber operating at 2.4 GHz. *Phys Med Biol*. (2010) 55:1619–30. doi: 10.1088/0031-9155/55/6/006

17. Meyer F. Topographic distance and watershed lines. *Signal Process.* (1994) 38:113–25. doi: 10.1016/0165-1684(94)90060-4
18. Meyer F, Beucher S. Morphological segmentation. *J Visual Commun Image Represent*. (1990) 1:21–46. doi: 10.1016/1047-3203(90)90014-M
19. Manda MP, Park CS, Oh BC, Kim HS. Marker-based watershed algorithm for segmentation of the infrared images. In: *2019 International SoC Design Conference (ISOCC)*. Jeju: IEEE (2019). p. 227–8. doi: 10.1109/ISOCC47750.2019.9027721
20. Li C, Yang L, Li CH, Xie Y, Wu T. Dosimetric variability of the rats' exposure to electromagnetic pulses. *Electromag Biol Med*. (2015) 34:334–43. doi: 10.3109/15368378.2014.925472
21. Gong YJ, Capstick MH, Kuehn S, Wilson PF, Ladbury JM, Koepke G, et al. Life-time dosimetric assessment for mice and rats exposed in reverberation chambers for the two-year ntp cancer bioassay study on cell phone radiation. *IEEE Transact Electromagn Compatibil*. (2017) 59:1798–808. doi: 10.1109/TEMC.2017.2665039

Conflict of Interest: The authors declare that the research was conducted in the absence of any commercial or financial relationships that could be construed as a potential conflict of interest.

Publisher's Note: All claims expressed in this article are solely those of the authors and do not necessarily represent those of their affiliated organizations, or those of the publisher, the editors and the reviewers. Any product that may be evaluated in this article, or claim that may be made by its manufacturer, is not guaranteed or endorsed by the publisher.

frontiers in Public Health

ORIGINAL RESEARCH
published: 11 November 2021
doi: 10.3389/fpubh.2021.761069

Exposure to 10 Hz Pulsed Magnetic Fields Do Not Induce Cellular Senescence in Human Fetal Lung Fibroblasts

Chuan Sun[1†], Zheng Huang[2†], Houbing Qin[3†], Jing Zhang[1], Sanying Wang[1], Xiaogang Xu[1], Shibo Ying[4] and Genxiang Mao[1*]*

[1] Zhejiang Provincial Key Lab of Geriatrics and Geriatrics Institute of Zhejiang Province, Department of Geriatrics, Zhejiang Hospital, Hangzhou, China, [2] School of Stomatology, Hangzhou Normal University, Hangzhou, China, [3] Department of Respiratory Medicine, Children's Hospital of Nanjing Medical University, Nanjing, China, [4] Hangzhou Medical College, Hangzhou, China

OPEN ACCESS

Edited by:
Lei Zhang,
Third Military Medical University, China

Reviewed by:
Tao Song,
Chinese Academy of Sciences (CAS), China
Frank Barnes,
University of Colorado Boulder, United States

***Correspondence:**
Chuan Sun
sunchuan@sina.cn
Genxiang Mao
maogenxiang@163.com

[†]These authors have contributed equally to this work and share first authorship

Specialty section:
This article was submitted to Radiation and Health, a section of the journal Frontiers in Public Health

Received: *19 August 2021*
Accepted: *07 October 2021*
Published: *11 November 2021*

Citation:
Sun C, Huang Z, Qin H, Zhang J, Wang S, Xu X, Ying S and Mao G (2021) Exposure to 10 Hz Pulsed Magnetic Fields Do Not Induce Cellular Senescence in Human Fetal Lung Fibroblasts. Front. Public Health 9:761069. doi: 10.3389/fpubh.2021.761069

Rapid population aging has led to a global burden of late-life diseases. As the largest risk factor for a multitude of age-related diseases, aging is not only the result of genotype but also closely related to external factors. With the rapid expansion in the usage of electromagnetic fields (EMFs), the effect of EMFs on aging has also attracted attention. Cells are the basic unit of organs and body tissues, and cellular senescence plays an important role in the aging process. The effect of EMFs on cellular senescence has been investigated in a few studies, but the information is limited, and the results are inconsistent; thus, further investigation is required. In this study, we investigated the effect of 10 Hz pulsed magnetic fields (MFs) on cellular senescence in a 2BS cell line, isolated from human fetal lung fibroblasts, and found that intermittent (1 d on/1 d off) exposure to 10 Hz pulsed MFs at 1.0 mT for 2 weeks induced DNA damage, but no other significant phenotype of cellular senescence in 2BS cells.

Keywords: electromagnetic fields (EMFs), aging, DNA damage, pulsed electromagnetic field, cellular senescence, human fetal lung fibroblasts

INTRODUCTION

Nowadays, modern electromagnetic technology is developing rapidly, and humans are constantly exposed to various types of electromagnetic fields (EMFs) or magnetic fields (MFs) originating from different man-made sources. The possible adverse effects of EMFs on human health have attracted significant public attention (1, 2). Although non-ionizing EMFs do not have enough energy to directly ionize bio-macromolecules, many institutions, such as, the WHO, have issued warnings regarding their potential biological effects (3, 4). The International Agency for Research on Cancer (IARC) has categorized both radiofrequency and extremely low-frequency EMFs as possible carcinogens to humans and has warned the public about the potential risks (5, 6).

As the largest risk factor for a multitude of age-related diseases, aging is becoming one of the most serious public health problems in the case of the rapid aging of the population (7). The aging process can be affected by many external factors, such as exercise and nutrition (8). The effect of EMF exposure on the aging process is also a concern. In 2013, Makarov and Khmelinskii (9) reported that three-dimensional oscillating low-frequency electric EMFs have an effect on the control of the *Drosophila melanogaster* life span, indicating that EMFs might affect the aging process; however, the mechanism is unknown.

Cellular senescence is the origin of aging, which promotes organismal aging and dysfunction (10, 11), and senescence-associated secretory phenotype (SASP) secreted by senescent cells can cause inflammation and change the microenvironment to promote senescence (10). Cellular senescence can be triggered by various stresses, such as activated oncogenes, oxidative stress, shortening of telomeres, DNA damage, and insufficient supplementation (12–14). EMFs have also been reported to induce oxidative stress, DNA damage, and other biological effects, although the results are not definitive (15, 16). Thus, it is necessary to consider the effects of EMFs on cellular senescence.

The effect of EMFs on cellular senescence has been investigated in several studies, but the results have been inconsistent. First, several studies have reported that EMFs can induce cellular senescence. Kim et al. reported that 1.76 GHz radiofrequency EMFs induced cellular senescence in HaCaT human keratinocytes (17). Choi et al. (18) reported that 1.7 GHz radiofrequency EMFs induced senescence in human adipose tissue-derived stem cells (ASCs) and Huh7 liver cancer stem cells. Fathi et al. (19) reported that exposure to 50 Hz MFs induces senescence in rat adipose-derived mesenchymal stem cells. Second, several other studies did not find a significant effect of EMFs on cellular senescence. Alessio et al. (20) reported that 169 MHz radiofrequency EMF exposure had no effect on cellular senescence in human adipose-derived mesenchymal stem cells. Hong et al. (21) reported that exposure to 60 Hz MFs had no effect on cellular senescence in human breast epithelial cells (MCF10A). Finally, some studies have reported that EMFs might be effective in delaying cellular senescence. Perez et al. (22) reported that engineered repeated EMFs therapy upregulates the HSR/HSF1 pathway and delays cellular senescence in young cells. Xu et al. (23) reported that 4 Hz rotating MFs delayed human umbilical vein endothelial cell (HUVEC) senescence. Maredziak et al. (24) reported that static MFs delayed human adipose-derived mesenchymal stem cell senescence. The types of EMFs, cellular models, and endpoints were different in these studies, which might have contributed to the inconsistent results. Although the results were inconsistent, and it was difficult to draw a clear conclusion about the impact of EMFs on cellular senescence, the current available studies provide information that EMFs might have an effect on cellular senescence under specific conditions. However, the specific conditions are unknown, and more information about the effect of EMFs on cell senescence is needed.

In recent years, low-frequency-pulsed (<100 Hz) MF exposure is increasing, that has been frequently applied as a non-invasive, easy, cheap, and reliable alternative method for clinical treatment, such as pain management (25, 26), brain stimulation (27), and bone fracture repair (28). In this study, we investigated the effect of 10 Hz pulsed MF exposure on cellular senescence in 2BS cell line isolated from human fetal lung fibroblasts, a cellular senescence model, and detected cellular senescence-related phenotypes, that is, DNA damage, senescence-associated β-galactosidase (SA-β-gal) activity, SASP, and mitochondrial function. The results showed that intermittent (1 d on/1 d off) exposure to 1.0 mT 10 Hz pulsed MFs for 2 weeks induced DNA damage, but no other significant cellular senescence phenotype in 2BS cells.

MATERIALS AND METHODS

Cell Culture

Human fetal lung fibroblasts (2BS cell line) were obtained from the National Institute of Biological Products (Beijing, China) and have been well-characterized as a cellular senescence model (29–31). Cells were cultured in high-glucose Dulbecco's modified Eagle's medium (DMEM) (Gibco, Grand Island, NY, USA) with 10% fetal bovine serum (FBS, Gibco), 100 U/ml penicillin, and 100 mg/ml streptomycin at 37°C with 5% CO_2 in an incubator (Thermo Scientific, Shanghai, China). The cells were sub-cultured in a 1:2 or 1:4 ratio when the culture confluence was almost 85%. The formula $\log_2$(D/D0) was used for the calculation of cell cumulative population doubling (CPD), where D and D0 are the densities of cells at the time of harvesting and seeding, respectively. Cells were considered young at <30 population doubling (PD) and replicative senescent around 55 PD or later.

The EMF Exposure System

The system was designed and manufactured by CH_HAIL Electronic Devices Inc. (Beijing, China). A pair of Helmholtz coils (CHY15-20J, CH_HAIL), 30 cm in diameter and 9 cm apart, combined with a signal generator (DG1022U, RIGOL, Beijing, China), a power amplifier (CH-EA-500G, CH_HAIL), and a gauss meter (CH-1600, CH_HAIL; **Supplementary Figure 1**). The system could generate 0–1 kHz, 0–2.0 mT MFs. Helmholtz coils were placed in an incubator (Thermo Scientific) in a humidified atmosphere of 5% CO_2 at 37°C. Culture flasks and plates were placed between the coils on a transparent polymethylmethacrylate holder, 1 cm below the center of the coils. The coils were oriented on the left and right sides of the flasks and plates. In this configuration, the MFs were parallel to the bottom of the flasks and plates. The temperature of the medium was determined using a medical thermometer, and no significant increase was found compared to the control group during exposure. Total 1.0 mT 10 Hz pulsed MFs (duty ratio = 0.50) were used in the present study. The strengths of the MFs were monitored using a gauss meter at the center of the two coils, and the MF was homogeneous from the coil center to the origin, in the 10 cm of the spherical region, the uniform index < 4% (**Supplementary Figure 3**).

The background static MFs density was 4.32 ± 1.75 μT (**Supplementary Figure 2A** and **Supplementary Data**). The root mean square (RMS) value of 10 Hz pulsed MFs density was 1.0 mT (**Supplementary Figures 2B,C** and **Supplementary Data**). The pulse period was 100 ms, the pulse width was 50 ms, the rise and fall time was about 20 ns, respectively (**Supplementary Figure 2D**).

Exposure Protocol

Cells in the exposure group were exposed to 1.0 mT 10 Hz pulsed MFs (1 d on/1 d off) for 2 weeks. At the same time, cells in the control group were cultured in another incubator (Thermo Scientific) under the same conditions without MF exposure.

Cell subcultures progressed during the exposure interval. After exposure, the cells were harvested for further analyses.

Alkaline Comet Assay

After exposure, the cells were digested, resuspended in a culture medium, and then placed on ice. The sandwich agarose gels were made up of 0.65% normal-melting agarose that had been pre-coated on a slice and 0.65% low-melting agarose mixed with cells on normal-melting agarose. The cells were lysed in lysis buffer containing 1% Triton X-100 at 4°C for 1 h and then enzymatically hydrolyzed in lysis buffer containing 0.5 mg/ml DNase-free proteinase K (Beyotime, Shanghai, China) at 37°C for 2 h. Before electrophoresis, DNA in cells was unwind in ice-cold alkaline electrophoresis solution for 20 min and then electrophoresis at 20 V for 20 min. After electrophoresis, cells were neutralized in Tris buffer (0.4 M, pH 7.5) for 2 × 5 min. DNA "comets" were stained by Gel-red (Beyotime) and photographed by a fluorescence microscope (Zeiss, Oberkochen, German). Approximately 30 comets for each sample were calculated using the CASP 1.2.2 software (Krzysztof Konca, Wroclaw, Poland). Additional details can be found in a previously described protocol (32).

Western Blotting

After exposure, cells were washed with ice-cold PBS and then lysed with radioimmunoprecipitation assay (RIPA) lysis buffer (P0013B, Beyotime) with 1 × protease inhibitor cocktail (Roche Diagnostics, Indianapolis, IN, USA) on ice. Cell lysates were separated by electrophoresis on 10% sodium dodecyl sulfate (SDS)-polyacrylamide gels, transferred to polyvinylidene fluoride (PVDF) membranes (Bio-Rad Laboratories, Hercules, CA, USA), blocked with 5% skimmed milk PBS with 0.05% Tween 20, and blotted with the primary antibody for 2 h at room temperature. This was followed by incubation with horseradish peroxidase (HPR)-conjugated goat anti-mouse or goat anti-rabbit IgG at room temperature for 1 h. Immunoreactive bands were detected using the enhanced chemiluminescence (ECL) method. The primary rabbit anti-γH2AX antibody was purchased from Beyotime Technology and anti-$p21^{Waf1}$, $p16^{INK4a}$, and GAPDH antibodies were from Cell Signaling Technology (Danvers, MA, USA), and the anti-p53 antibody was from Santa Cruz Biotechnology (Santa Cruz, CA, USA).

SA-β-Gal Staining

Senescence-associated β-galactosidase staining was performed using a commercial kit (C0602, Beyotime). In brief, after exposure, the cells were fixed for 15 min and then incubated with staining solution at 37°C without a CO_2 supply overnight. The cells were visualized using a microscope (Zeiss), and the percentage of positively stained cells was calculated. A total of 200 cells per sample were analyzed.

Quantitative Real-Time PCR

Total RNA was extracted from the cells using a total RNA extraction reagent (TRIzol, Thermo Scientific) and transcribed to cDNA using a reverse transcription kit (BL699A, Biosharp, Hefei, China) with a PCR system (Bio-Rad). RNA expression was quantified using an SYBR Green qPCR Mix kit (BL698A, Biosharp) using a qPCR system (Roche, Basel, Switzerland). The expression of miRNA was defined from the threshold cycle, and relative expression levels were calculated using the $2^{-\Delta\Delta Ct}$ method after normalization with reference to the expression of 18S mRNA. Primer sequences were obtained from a published article (33) and were synthesized by Tsingke Biotechnology Co., Ltd. (Hangzhou, China).

Cell Cycle Analysis

The cells were harvested, resuspended in pre-cooled PBS with 70% ethanol, and stored at −20°C overnight. Cells were then stained with 50 μg/ml propidium iodide (Beyotime) diluted in PBS containing 50 mg/ml RNase A (Thermo Scientific) at room temperature (25°C) for 30 min. The cell cycle distribution was analyzed by flow cytometry (Cytoflex, Beckman Coulter, CA, USA), in which 1×10^4 events per sample were acquired, and the proportions of cells in the G0/G1, S, and G2/M phases were determined.

Cell Viability Analysis

After exposure, the cells were detached using 200 μl of 0.25% trypsin-EDTA (Gibco) and resuspended in 500 μL of culture medium. Then, 3,000 cells per well were seeded into a 96-well-plate (Corning, NY, USA). Cell viability was determined using Cell Counting Kit-8 (CCK-8, Dojindo Molecular Technologies, Kumamoto, Japan) at 24 and 48 h after seeding. The values were detected using a microplate reader (Tecan, Hombrechtikon, Switzerland).

Cell Proliferation Assay

Cell proliferation was determined using a 5-ethyny-2′-deoxyuridine (EdU) cell proliferation kit (C0071S, Beyotime). In brief, cells were incubated with EdU for 1 h and then harvested. Cells were fixed in 70% ethanol at −20°C overnight. EdU signal per cell was detected by flow cytometry (Cytoflex, Beckman Coulter). More details can be found in the instructions of manufacturer.

Intracellular Reactive Oxygen Species Measurement

Intracellular ROS were detected using 2,7-dichlorodihydrofluorescein diacetate (H_2DCFDA) (Beyotime). After exposure, cells were washed twice with an FBS-free culture medium and then incubated with 10 μM H_2DCFDA diluted in an FBS-free culture medium at 37°C for 20 min. The cells were then harvested and washed with PBS. H_2DCFDA signaling was determined using flow cytometry (Cytoflex, Beckman Coulter).

Mitochondrial Membrane Potential Determination

Mitochondrial membrane potential in cells was determined using an MMP assay kit with JC-1 (Beyotime). Briefly, cells were detached and resuspended in a 0.5 ml culture medium. The cells were then incubated with JC-1 at 37°C for 20 min, and then the intensities of JC-1 (red and green fluorescence) were determined by flow cytometry (Cytoflex, Beckman Coulter).

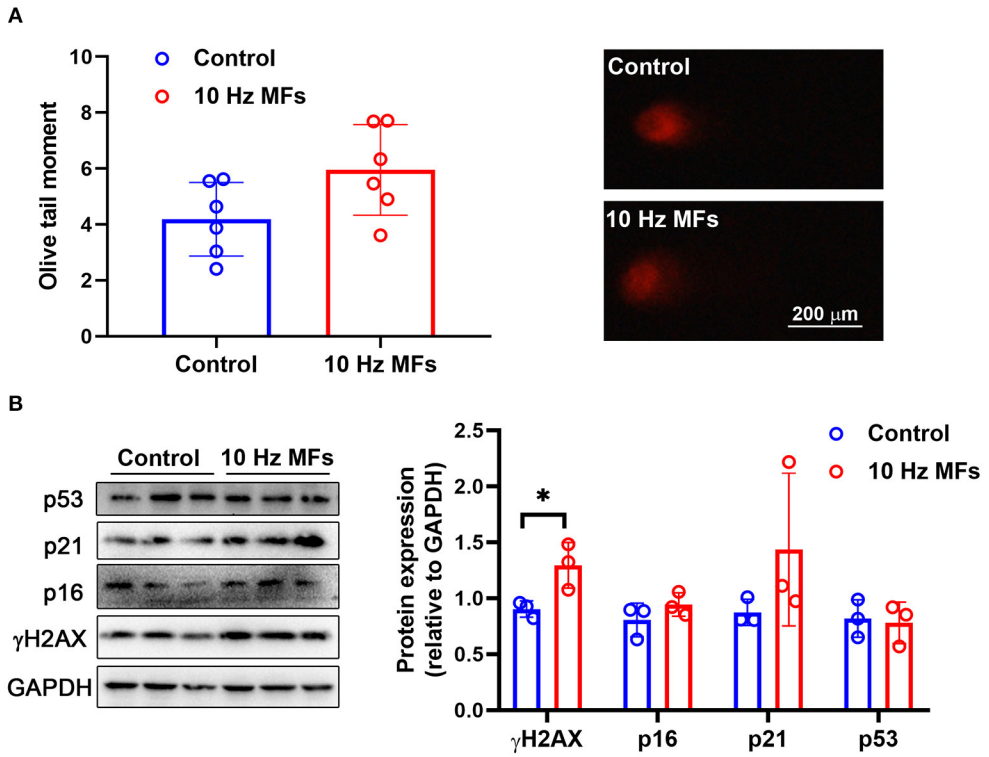

FIGURE 1 | The effect of 10 Hz pulsed MFs exposure on DNA damage and p16, p21, and p53 expressions in 2BS cells. **(A)** The statistical values of DNA fragmentation (Olive tail moment) in 2BS cells of control and 10 Hz pulsed MFs exposure group and representative images of alkaline comet assay; **(B)** the statistical graphic of protein expression (relative to GAPDH) and blot images of γH2AX, p16, p21, and p53 in 2BS cells. All data were presented as mean ± SD. *$P < 0.05$.

Adenosine 5′-Triphosphate (ATP) Detection

Adenosine 5′-triphosphate levels were determined using an ATP Assay Kit (Beyotime). Briefly, after exposure, the cells were lysed at 4°C. After centrifugation, ATP and protein concentrations in the supernatant were determined. The concentration of ATP per unit protein in each sample was then calculated. A microplate reader (Tecan) was used to read the data.

Enzyme-Linked Immunosorbent Assay

The levels of interleukin (IL)-6, CXC chemokine ligand 8 (IL-8), and growth-regulated oncogene alfa (GRO-α) in the culture medium were determined using commercial ELISA kits (SolelyBio, Shanghai, China). Briefly, after exposure, the cell culture medium was collected and added to the test plate. After reaction at 37°C for 30 min, the culture medium was removed, and an enzyme labeling reagent was added to the plate. After reaction at 37°C for 30 min, the enzyme labeling reagent was removed, and a chromogenic solution was added to the plate. After reaction at 37°C for 10 min, the reaction stop solution was added to stop the reaction, and the values were immediately detected using a microplate reader (Tecan). More details can be found in the manufacturer's instructions.

Statistical Analysis

All experiments were performed in triplicate at least. Student's *t*-test was applied for comparisons between two groups in which the data followed a normal distribution, and Wilcoxon rank-sum test was applied when the data were not a normal distribution, all the data were analyzed in R software (Version 3.6.1), and the differences were considered statistically significant at $P < 0.05$.

RESULTS

Effect of 10 Hz Pulsed MFs on DNA Damage in 2BS Cells

DNA damage accumulation is not only a phenotype but also a cause of cellular senescence (11, 34). In our results, the alkaline comet assay showed that exposure to 1.0 mT 10 Hz pulsed MFs for 2 weeks increased DNA fragmentation, but the difference was not statistically significant (**Figure 1A**). To further confirm this, we detected γH2AX, a sensitive marker of DNA damage (35), and found that 10 Hz pulsed MFs exposure significantly increased γH2AX in 2BS cells compared to the control group (**Figure 1B**), indicating that 10 Hz pulsed MFs exposure has an effect on DNA damage in 2BS cells.

Effect of 10 Hz Pulsed MFs on p16, p21, and p53 Expression in 2BS Cells

Cellular senescence is characterized as a stable and terminal state of growth arrest in which cells are unable to proliferate (36). Accumulated DNA damage activated DNA damage response

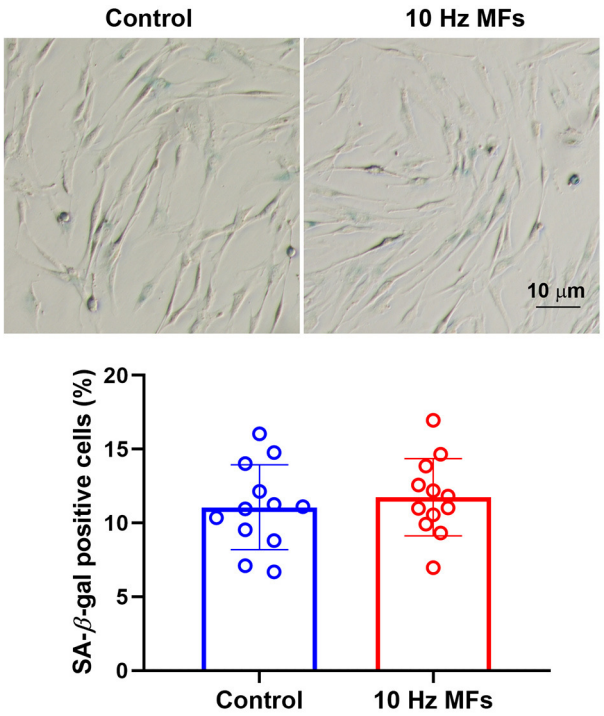

FIGURE 2 | The effect of 10 Hz pulsed MFs exposure on SA-β-gal staining in 2BS cells. Representative images show the SA-β-gal staining in 2BS cells of control and 10 Hz pulsed MFs exposure group, bar = 10 μm, and the graphic shows the statistical values of SA-β-gal staining (Percentage of positive staining cells), data were presented as mean ± SD. SA-β-gal, senescence-associated β-galactosidase.

(DDR), a factor that activates cell cycle arrest. At the bottom of the DDR cascade, the tumor suppressor p53, the cyclin-dependent kinase inhibitor p21, and CDK4 and CDK6 inhibitor p16 all play critical roles in senescence entry and the maintenance of the senescence phenotype (36). We determined the expressions of p16, p21, and p53 *via* western blot assay, and the results showed that 10 Hz pulsed MF exposure did not significantly increase p16, p21, or p53 expression levels in 2BS cells compared to the control group (**Figure 1B**).

Effect of 10 Hz Pulsed MFs on SA-β-gal Staining in 2BS Cells

Senescence-associated β-galactosidase is a lysosomal enzyme whose accumulation is the most widely used biomarker for detecting cellular senescence (37). The results of the SA-β-gal staining assay showed that 10 Hz pulsed MF exposure did not significantly increase the percentage of positively stained cells in 2BS cells compared to the control group (**Figure 2**).

Effect of 10 Hz Pulsed MFs on SASP in 2BS Cell

Senescence-associated secretory phenotype is a typical phenotype of senescent cells, such as pro-inflammatory cytokines, chemokines, growth factors, and proteases (37). SASP is also a potential mechanism through which senescent cells exert their pleiotropic biological functions (37). The levels of proinflammatory IL-6, CXC chemokine ligand 8 (IL-8), and growth-regulated oncogene (GRO-α) in the culture medium of 2BS cells were determined by ELISA. The results showed that 10 Hz pulsed MF exposure did not increase IL-6 secretion compared to the control group, and IL-8 and GRO-α levels were below the detection limit (**Figure 3A**). The mRNA expression of several SASP factors was determined by qPCR. The results showed that ANKRD1, CDKN1A, CDKN2A, CSF2, CXCL1, CXCL2, EDN1, IL-6, IL-7, and IL-8 were not significantly affected by 10 Hz pulsed MF exposure compared to that in the control group (**Figure 3B**).

Effect of 10 Hz Pulsed MFs on Cell Proliferation and Cell Cycle Progression in 2BS Cells

Cellular senescence is defined as the irreversible arrest of cell proliferation in response to exogenous or endogenous stimuli (38). Thus, we determined cell proliferation and cell cycle progression. The results showed that neither cell proliferation nor cell cycle progression was significantly affected in 10 Hz pulsed MFs exposed 2BS cells compared to that in the control group (**Figure 4**).

Effect of 10 Hz Pulsed MFs on ROS Generation, MMP, and ATP Levels in 2BS Cells

Mitochondria are important organelles that provide energy for cell metabolism. Mitochondrial dysfunction is a hallmark of cellular senescence (11), which leads to insufficient energy supply and excessive ROS generation, such as cell damage and aging (38, 39). Thus, we determined the cellular ROS, MMP, and ATP levels. The results showed that neither ROS levels, MMP, nor ATPs were significantly changed in 2BS cells that were exposed to 10 Hz pulsed MFs compared to that in the control group (**Figure 5**).

DISCUSSION

As the largest risk factor for a multitude of age-related diseases, rapid population aging has led to a global burden of late-life disease (7, 40). Aging-related senescence leads to progressive deterioration of bodily functions, which is associated with a loss of complexity in a wide range of physiological processes and anatomic structures (40). The aging process is not only the result of genotype but also closely related to external factors. For decades, the rapid increase in the use of EMFs has raised public concerns about the potential biological effects of EMFs, and the effect of EMFs on aging has also attracted attention. Cellular senescence is the basis of aging, which results in tissue and organ senescence and leads to body dysfunction (10, 11). Thus, it is important to understand the effects of EMF exposure on cellular senescence. Although there have been several investigations, the results were inconsistent and the effects of EMFs on cellular senescence are not completely understood, therefore, more

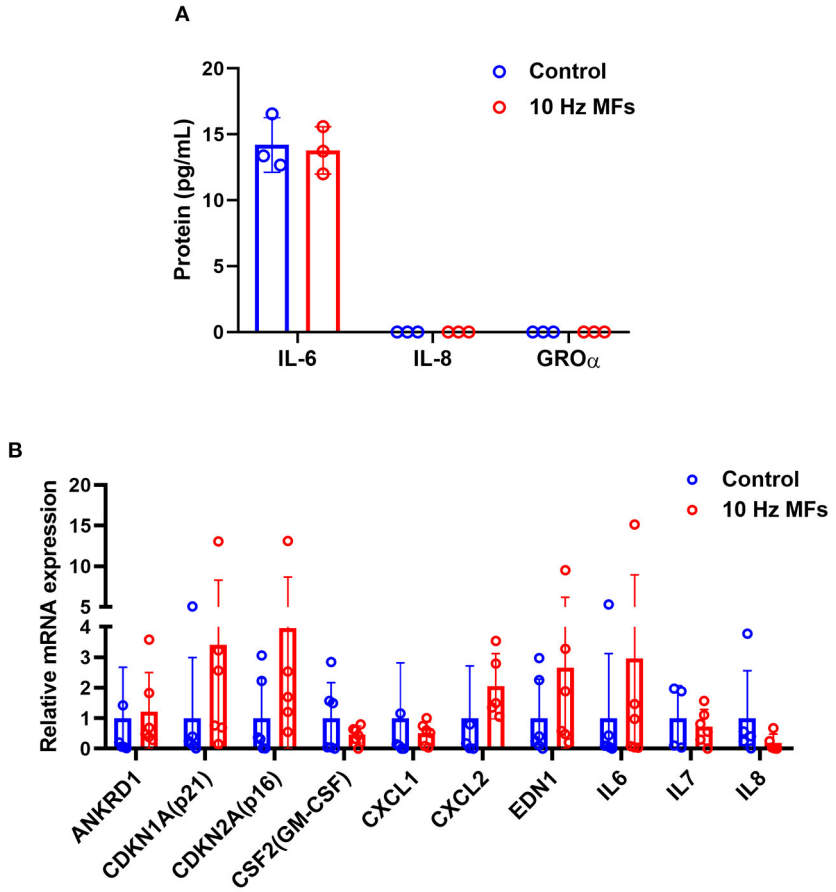

FIGURE 3 | The effect of 10 Hz pulsed MFs exposure on SASP in 2BS cells. **(A)** The levels of IL-6, IL-8, and GROα in the culture medium and **(B)** mRNA expression of ANKRD1, CDKN1A, CDKN2A, CSF2, CXCL1, CXCL2, EDN1, IL-6, IL-7, and IL-8 in 2BS cells of control and 10 Hz pulsed MFs exposure group. Data were presented as mean ± SD. SASP, senescence-associated secretory phenotype. IL-8, CXC chemokine ligand 8; IL-6, interleukin 6; GRO-α, growth-regulated oncogene alfa.

studies are required. In this study, we investigated the effect of 10 Hz pulsed MFs on cellular senescence in human fetal lung fibroblasts (2BS) by detecting several hallmarks of senescent cells, such as DNA damage, p53, p21, and p16 expression levels, SA-β-gal activity, SASP, and mitochondria function (33) and found that 10 Hz pulsed MFs only increased DNA damage but no other senescent phenotypes in 2BS cells.

Impaired DNA damage is not only a hallmark of aging but also a causal factor of the aging process, which will constantly activate DDR to arrest the cell cycle and growth (11, 34). In this study, the results of the alkaline comet assay and γH2AX expression levels showed that 10 Hz pulsed MF exposure induced DNA damage in 2BS cells (**Figure 1**), but no other significant senescence phenotypes were observed compared to the control, such as p53, p21, and p16 (**Figure 1**), which are important factors in DNA damage-induced cellular senescence (34, 36), and cell cycle progression and proliferation (**Figure 4**) were also not significantly changed. These results suggest that the DNA damage induced by 10 Hz pulsed MFs is repairable or too small to induce significant senescence in 2BS cells after 2 weeks of exposure.

To further investigate the effect of 10 Hz pulsed MFs on cellular senescence, SA-β-gal activation, and SASP factors, two typical characteristics of senescent cells were determined in this study. SA-β-gal staining is a common and widely used marker for detecting cell senescence (41). SASP is comprised of a packet of pro-inflammatory cytokines, chemokines, growth factors, and proteases that are important for senescent cells to exert their pleiotropic biological functions, such as self-reinforcing senescence or affecting the microenvironment (36). In this study, no significant changes in SA-β-gal activation (**Figure 2**) and several SASP levels (**Figure 3**) were detected in the 10 Hz pulsed MF exposure group compared to that in the control group. These results suggested that 10 Hz pulsed MFs do not induce significant cell senescence in 2BS cells.

Senescent cells are also characterized by mitochondrial dysfunction, which plays an important role in the establishment of senescence, such as increased oxidative stress (36). In this study, to determine the function of mitochondria, we detected MMP, ROS, and ATP generation, and no significant effect was observed (**Figure 5**), indicating that mitochondrial function was not affected by 10 Hz pulsed MF exposure in 2BS cells.

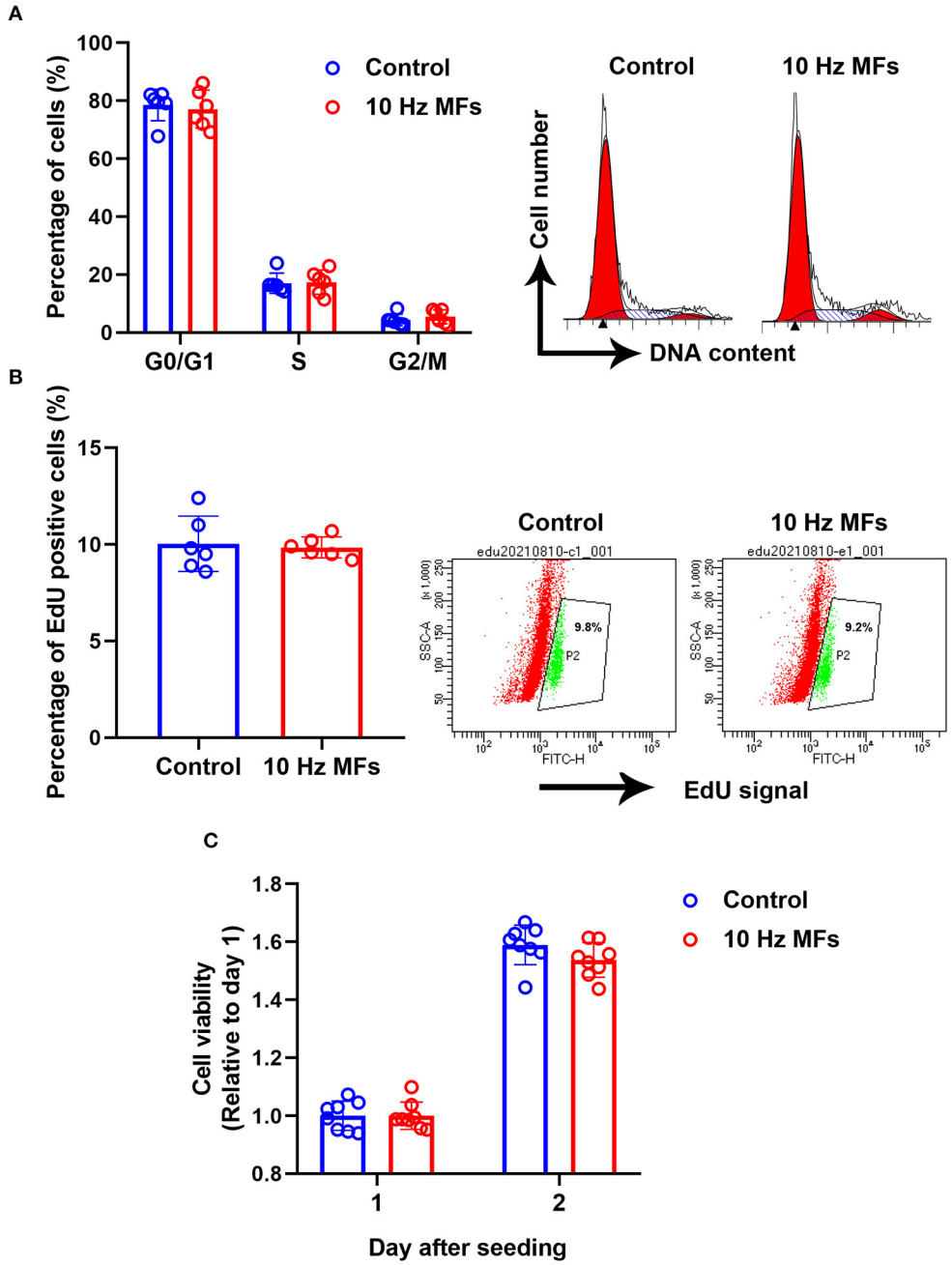

FIGURE 4 | The effect of 10 Hz pulsed MFs exposure on cell cycle progression and proliferation. **(A)** Cell cycle distributions were determined by PI staining, **(B)** cell proliferation was determined by EdU assay, and **(C)** cell viability was determined by CCK8 assay of 2BS cells in control and 10 Hz pulsed MFs exposure group. Data were presented as mean ± SD. MFs, magnetic fields.

The 2BS cells used in this study were isolated from human fetal lung fibroblasts by the National Institute of Biological Products (Beijing, China) and have been well-characterized and widely used as a cellular senescence model (29–31). Cells are defined as young at a number lower than 30 PD and replicative senescent around 55 PD or later (39). In this study, exposure to MFs was started at 30 PD and ended at 40–42 PD of the 2BS cells that the cells were in the process of aging but not completely senescent. Thus, this study only investigated the effect of 10 Hz pulsed MFs on the aging process of 2BS cells, whether 10 Hz pulsed MF exposure has an effect on young or senescent 2BS cells requires further study.

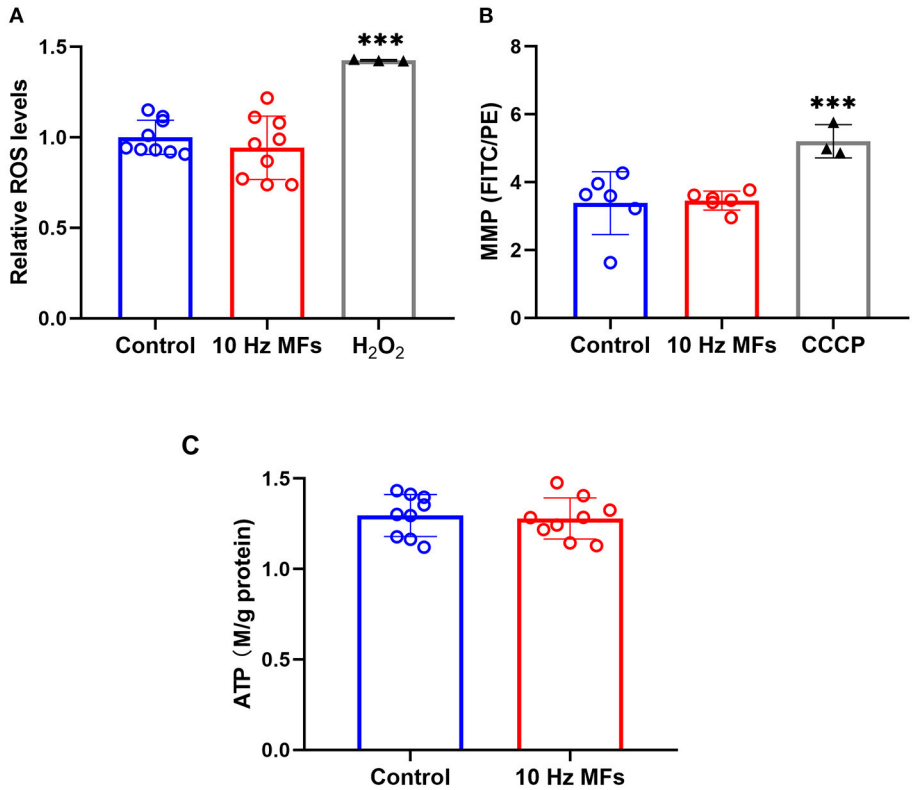

FIGURE 5 | The effect of 10 Hz pulsed MFs exposure on ROS, MMP, and ATP levels in 2BS cells. **(A)** Relative intracellular ROS levels were determined by H_2DCFDA, **(B)** MMP determined by JC-1, and **(C)** ATP concentration in 2BS cells of control and 10 Hz pulsed MFs exposure group. Hydrogen peroxide (H_2O_2) and CCCP were applied as the positive control, respectively. Data were presented as mean ± SD. ***$P < 0.001$. MFs, magnetic fields; ROS, reactive oxygen species; H_2DCFDA, 2,7-dichlorodihydrofluorescein diacetate; MMP, Mitochondrial membrane potential; ATP, adenosine 5′-triphosphate.

In conclusion, under current conditions, intermittent (1 d on/1 d off) exposure to 10 Hz pulsed MFs at 1.0 mT for 2 weeks did not induce significant cellular senescence in 2BS cells.

DATA AVAILABILITY STATEMENT

The raw data supporting the conclusions of this article will be made available by the authors, without undue reservation.

AUTHOR CONTRIBUTIONS

CS contributed to the idea, design, experiments, data analysis, and manuscript writing. ZH did the comet assay, ELISA, qPCR, and western blot. HQ did the flow cytometry and data analysis. JZ, SW, XX, and SY contributed to the data analysis and manuscript writing. GM contributed to the idea, design, and manuscript writing. All authors agree to be accountable for the content of the work.

FUNDING

This work was supported by grants from the Medical Science and Technology Project of Zhejiang Province (2021KY005, 2020KY387, and 2019KY257), National Science Foundation of China (31700734, 81973011, and 81701393), Zhejiang Provincial Natural Science Foundation (LGF21H250002), and Chinese Traditional Medicine Science and Technology Projects of Zhejiang Province (2021ZB002).

SUPPLEMENTARY MATERIAL

The Supplementary Material for this article can be found online at: https://www.frontiersin.org/articles/10.3389/fpubh.2021.761069/full#supplementary-material

REFERENCES

1. Magiera A, Solecka J. Radiofrequency electromagnetic radiation from Wi-fi and its effects on human health, in particular children and adolescents. Review. *Rocz Panstw Zakl Hig.* (2020) 71:251–9. doi: 10.32394/rpzh.2020.0125
2. Karimi A, Ghadiri Moghaddam F, Valipour M. Insights in the biology of extremely low-frequency magnetic fields exposure on human

health. *Mol Biol Rep.* (2020) 47:5621–33. doi: 10.1007/s11033-020-05563-8
3. World Health Organizations. *Radiation: Electromagnetic Fields.* Available online at: https://www.who.int/news-room/q-a-detail/radiation-electromagnetic-fields (accessed August 18, 2021).
4. Garcia-Minguillan O, Maestu C. 30 Hz, could it be part of a window frequency for cellular response? *Int J Mol Sci.* (2021) 22:3642. doi: 10.3390/ijms22073642
5. Non-ionizing radiation, Part 1: static and extremely low-frequency (ELF) electric and magnetic fields. *IARC Monogr Eval Carcinog Risks Hum.* (2002) 80:1–395.
6. Non-ionizing radiation, Part 2: Radiofrequency electromagnetic fields. *IARC Monogr Eval Carcinog Risks Hum.* (2013) 102(Pt 2):1–460.
7. Niccoli T, Partridge L. Ageing as a risk factor for disease. *Curr Biol.* (2012) 22:R741–R52. doi: 10.1016/j.cub.2012.07.024
8. Campisi J, Kapahi P, Lithgow GJ, Melov S, Newman JC, Verdin E. From discoveries in ageing research to therapeutics for healthy ageing. *Nature.* (2019) 571:183–92. doi: 10.1038/s41586-019-1365-2
9. Makarov VI, Khmelinskii I. External control of the Drosophila melanogaster lifespan by combination of 3D oscillating low-frequency electric and magnetic fields. *Electromagn Biol Med.* (2014) 33:276–81. doi: 10.3109/15368378.2013.817335
10. Guo G, Watterson S, Zhang SD, Bjourson A, McGilligan V, Peace A, et al. The role of senescence in the pathogenesis of atrial fibrillation: a target process for health improvement and drug development. *Ageing Res Rev.* (2021) 69:101363. doi: 10.1016/j.arr.2021.101363
11. Lopez-Otin C, Blasco MA, Partridge L, Serrano M, Kroemer G. The hallmarks of aging. *Cell.* (2013) 153:1194–217. doi: 10.1016/j.cell.2013.05.039
12. Campisi J. Senescent cells, tumor suppression, and organismal aging: good citizens, bad neighbors. *Cell.* (2005) 120:513–22. doi: 10.1016/j.cell.2005.02.003
13. Herbig U, Sedivy JM. Regulation of growth arrest in senescence: telomere damage is not the end of the story. *Mech Ageing Dev.* (2006) 127:16–24. doi: 10.1016/j.mad.2005.09.002
14. Ramirez RD, Morales CP, Herbert BS, Rohde JM, Passons C, Shay JW, et al. Putative telomere-independent mechanisms of replicative aging reflect inadequate growth conditions. *Genes Dev.* (2001) 15:398–403. doi: 10.1101/gad.859201
15. Schuermann D, Mevissen M. Manmade electromagnetic fields and oxidative stress-biological effects and consequences for health. *Int J Mol Sci.* (2021) 22:3772. doi: 10.3390/ijms22073772
16. Panagopoulos DJ. Comparing DNA damage induced by mobile telephony and other types of man-made electromagnetic fields. *Mutat Res Rev Mutat Res.* (2019) 781:53–62. doi: 10.1016/j.mrrev.2019.03.003
17. Kim JH, Kang DJ, Bae JS, Lee JH, Jeon S, Choi HD, et al. Activation of matrix metalloproteinases and FoxO3a in HaCaT keratinocytes by radiofrequency electromagnetic field exposure. *Sci Rep.* (2021) 11:7680. doi: 10.1038/s41598-021-87263-2
18. Choi J, Min K, Jeon S, Kim N, Pack JK, Song K. Continuous exposure to 1.7 GHz LTE electromagnetic fields increases intracellular reactive oxygen species to decrease human cell proliferation and induce senescence. *Sci Rep.* (2020) 10:9238. doi: 10.1038/s41598-020-65732-4
19. Fathi E, Farahzadi R, Rahbarghazi R, Samadi Kafil H, Yolmeh R. Rat adipose-derived mesenchymal stem cells aging reduction by zinc sulfate under extremely low frequency electromagnetic field exposure is associated with increased telomerase reverse transcriptase gene expression. *Vet Res Forum.* (2017) 8:89–96.
20. Alessio N, Santoro E, Squillaro T, Aprile D, Briccola M, Giubbini P, et al. Low-level radiofrequency exposure does not induce changes in msc biology: an *in vitro* study for the prevention of NIR-related damage. *Stem Cells Cloning.* (2019) 12:49–59. doi: 10.2147/SCCAA.S204166
21. Hong MN, Han NK, Lee HC, Ko YK, Chi SG, Lee YS, et al. Extremely low frequency magnetic fields do not elicit oxidative stress in MCF10A cells. *J Radiat Res.* (2012) 53:79–86. doi: 10.1269/jrr.11049
22. Perez FP, Zhou X, Morisaki J, Ilie J, James T, Jurivich DA. Engineered repeated electromagnetic field shock therapy for cellular senescence and age-related diseases. *Rejuvenation Res.* (2008) 11:1049–57. doi: 10.1089/rej.2008.0793
23. Xu J, Liu K, Chen T, Zhan T, Ouyang Z, Wang Y, et al. Rotating magnetic field delays human umbilical vein endothelial cell aging and prolongs the lifespan of *Caenorhabditis elegans*. *Aging (Albany NY).* (2019) 11:10385–408. doi: 10.18632/aging.102466
24. Maredziak M, Tomaszewski K, Polinceusz P, Lewandowski D, Marycz K. Static magnetic field enhances the viability and proliferation rate of adipose tissue-derived mesenchymal stem cells potentially through activation of the phosphoinositide 3-kinase/Akt (PI3K/Akt) pathway. *Electromagn Biol Med.* (2017) 36:45–54. doi: 10.3109/15368378.2016.1149860
25. Coskun C, Ocal I, Gunay I. A low-frequency pulsed magnetic field reduces neuropathic pain by regulating NaV1.8 and NaV1.9 sodium channels at the transcriptional level in diabetic rats. *Bioelectromagnetics.* (2021) 42:357–70. doi: 10.1002/bem.22343
26. Attia M, McCarthy D, Abdelghani M. Repetitive transcranial magnetic stimulation for treating chronic neuropathic pain: a systematic review. *Curr Pain Headache Rep.* (2021) 25:48. doi: 10.1007/s11916-021-00960-5
27. Xie YJ, Chen Y, Tan HX, Guo QF, Lau BW, Gao Q. Repetitive transcranial magnetic stimulation for lower extremity motor function in patients with stroke: a systematic review and network meta-analysis. *Neural Regen Res.* (2021) 16:1168–76. doi: 10.4103/1673-5374.300341
28. Daish C, Blanchard R, Fox K, Pivonka P, Pirogova E. The application of pulsed electromagnetic fields (PEMFs) for bone fracture repair: past and perspective findings. *Ann Biomed Eng.* (2018) 46:525–42. doi: 10.1007/s10439-018-1982-1
29. Zheng QH, Ma LW, Zhu WG, Zhang ZY, Tong TJ. p21Waf1/Cip1 plays a critical role in modulating senescence through changes of DNA methylation. *J Cell Biochem.* (2006) 98:1230–48. doi: 10.1002/jcb.20838
30. Mao GX, Zheng LD, Cao YB, Chen ZM, Lv YD, Wang YZ, et al. Antiaging effect of pine pollen in human diploid fibroblasts and in a mouse model induced by D-galactose. *Oxid Med Cell Longev.* (2012) 2012:750963. doi: 10.1155/2012/750963
31. Li J, Zhang Z, Tong T. The proliferative response and anti-oncogene expression in old 2BS cells after growth factor stimulation. *Mech Ageing Dev.* (1995) 80:25–34. doi: 10.1016/0047-6374(94)01557-3
32. Xu S, Chen G, Chen C, Sun C, Zhang D, Murbach M, et al. Cell type-dependent induction of DNA damage by 1800 MHz radiofrequency electromagnetic fields does not result in significant cellular dysfunctions. *PLoS One.* (2013) 8:e54906. doi: 10.1371/journal.pone.0054906
33. Noren Hooten N, Evans MK. Techniques to induce and quantify cellular senescence. *J Vis Exp.* (2017) 123:55533. doi: 10.3791/55533
34. Ou HL, Schumacher B. DNA damage responses and p53 in the aging process. *Blood.* (2018) 131:488–95. doi: 10.1182/blood-2017-07-746396
35. Kopp B, Khoury L, Audebert M. Validation of the γH2AX biomarker for genotoxicity assessment: a review. *Arch Toxicol.* (2019) 93:2103–14. doi: 10.1007/s00204-019-02511-9
36. Di Micco R, Krizhanovsky V, Baker D, d'Adda di Fagagna F. Cellular senescence in ageing: from mechanisms to therapeutic opportunities. *Nat Rev Mol Cell Biol.* (2021) 22:75–95. doi: 10.1038/s41580-020-00314-w
37. Zhou D, Borsa M, Simon AK. Hallmarks and detection techniques of cellular senescence and cellular ageing in immune cells. *Aging Cell.* (2021) 20:e13316. doi: 10.1111/acel.13316
38. Pyo IS, Yun S, Yoon YE, Choi JW, Lee SJ. Mechanisms of aging and the preventive effects of resveratrol on age-related diseases. *Molecules.* (2020) 25:4649. doi: 10.3390/molecules25204649
39. Mao GX, Xu XG, Wang SY, Li HF, Zhang J, Zhang ZS, et al. Salidroside delays cellular senescence by stimulating mitochondrial biogenesis partly through a miR-22/SIRT-1 pathway. *Oxid Med Cell Longev.* (2019) 2019:5276096. doi: 10.1155/2019/5276096
40. Partridge L, Deelen J, Slagboom PE. Facing up to the global challenges of ageing. *Nature.* (2018) 561:45–56. doi: 10.1038/s41586-018-0457-8

41. Dimri GP, Lee X, Basile G, Acosta M, Scott G, Roskelley C, et al. A biomarker that identifies senescent human cells in culture and in aging skin *in vivo*. *Proc Natl Acad Sci U S A.* (1995) 92:9363–7. doi: 10.1073/pnas.92.20.9363

Conflict of Interest: The authors declare that the research was conducted in the absence of any commercial or financial relationships that could be construed as a potential conflict of interest.

Publisher's Note: All claims expressed in this article are solely those of the authors and do not necessarily represent those of their affiliated organizations, or those of the publisher, the editors and the reviewers. Any product that may be evaluated in this article, or claim that may be made by its manufacturer, is not guaranteed or endorsed by the publisher.

frontiers in Public Health

ORIGINAL RESEARCH
published: 22 November 2021
doi: 10.3389/fpubh.2021.771508

1,800 MHz Radiofrequency Electromagnetic Irradiation Impairs Neurite Outgrowth With a Decrease in Rap1-GTP in Primary Mouse Hippocampal Neurons and Neuro2a Cells

*Yanqi Li, Ping Deng, Chunhai Chen, Qinlong Ma, Huifeng Pi, Mindi He, Yonghui Lu, Peng Gao, Chao Zhou, Zhixin He, Yanwen Zhang, Zhengping Yu and Lei Zhang**

Key Laboratory of Medical Protection for Electromagnetic Radiation, Department of Occupational Health, Ministry of Education, Third Military Medical University, Chongqing, China

OPEN ACCESS

Edited by:
Mats-Olof Mattsson, SciProof International, Sweden

Reviewed by:
Stefania Romeo, National Research Council (CNR), Italy
Florence Poulletier De Gannes, UMR5218 Laboratoire d'Integration du Materiau au Systeme (IMS), France

***Correspondence:**
Lei Zhang
zlepo1980@163.com

Specialty section:
This article was submitted to Radiation and Health, a section of the journal Frontiers in Public Health

Received: *06 September 2021*
Accepted: *29 October 2021*
Published: *22 November 2021*

Citation:
Li Y, Deng P, Chen C, Ma Q, Pi H, He M, Lu Y, Gao P, Zhou C, He Z, Zhang Y, Yu Z and Zhang L (2021) 1,800 MHz Radiofrequency Electromagnetic Irradiation Impairs Neurite Outgrowth With a Decrease in Rap1-GTP in Primary Mouse Hippocampal Neurons and Neuro2a Cells. Front. Public Health 9:771508. doi: 10.3389/fpubh.2021.771508

Background: With the global popularity of communication devices such as mobile phones, there are increasing concerns regarding the effect of radiofrequency electromagnetic radiation (RF-EMR) on the brain, one of the most important organs sensitive to RF-EMR exposure at 1,800 MHz. However, the effects of RF-EMR exposure on neuronal cells are unclear. Neurite outgrowth plays a critical role in brain development, therefore, determining the effects of 1,800 MHz RF-EMR exposure on neurite outgrowth is important for exploring its effects on brain development.

Objectives: We aimed to investigate the effects of 1,800 MHz RF-EMR exposure for 48 h on neurite outgrowth in neuronal cells and to explore the associated role of the Rap1 signaling pathway.

Material and Methods: Primary hippocampal neurons from C57BL/6 mice and Neuro2a cells were exposed to 1,800 MHz RF-EMR at a specific absorption rate (SAR) value of 4 W/kg for 48 h. CCK-8 assays were used to determine the cell viability after 24, 48, and 72 h of irradiation. Neurite outgrowth of primary hippocampal neurons (DIV 2) and Neuro2a cells was observed with a 20× optical microscope and recognized by ImageJ software. Rap1a and Rap1b gene expressions were detected by real-time quantitative PCR. Rap1, Rap1a, Rap1b, Rap1GAP, and p-MEK1/2 protein expressions were detected by western blot. Rap1-GTP expression was detected by immunoprecipitation. The role of Rap1-GTP was assessed by transfecting a constitutively active mutant plasmid (Rap1-Gly_Val-GFP) into Neuro2a cells.

Results: Exposure to 1,800 MHz RF-EMR for 24, 48, and 72 h at 4 W/kg did not influence cell viability. The neurite length, primary and secondary neurite numbers, and branch points of primary mouse hippocampal neurons were significantly impaired by 48-h RF-EMR exposure. The neurite-bearing cell percentage and neurite length of Neuro2a cells were also inhibited by 48-h

RF-EMR exposure. Rap1 activity was inhibited by 48-h RF-EMR with no detectable alteration in either gene or protein expression of Rap1. The protein expression of Rap1GAP increased after 48-h RF-EMR exposure, while the expression of p-MEK1/2 protein decreased. Overexpression of constitutively active Rap1 reversed the decrease in Rap1-GTP and the neurite outgrowth impairment in Neuro2a cells induced by 1,800 MHz RF-EMR exposure for 48 h.

Conclusion: Rap1 activity and related signaling pathways are involved in the disturbance of neurite outgrowth induced by 48-h 1,800 MHz RF-EMR exposure. The effects of RF-EMR exposure on neuronal development in infants and children deserve greater focus.

Keywords: radiofrequency electromagnetic radiation, neurite outgrowth, Rap1, Rap1-GTP, Neuro2a cell, primary mouse hippocampal neurons

INTRODUCTION

The increasing demand for communication technology in modern society has led to an increased use of radiofrequency electromagnetic radiation (RF-EMR) (1). The popularity of mobile phone communication is expanding rapidly. The proportion of 13-year-old teenagers using mobile phones has reached 90% in Korea (2–4). With the use of radio equipment for monitoring and receiving information in neonatal intensive care units, infants are also becoming increasingly exposed to RF-EMR. Thus, the impact of radio frequency devices on infants, children, and adolescents has attracted global attention.

The brain is known to be one of the most sensitive organs to RF-EMR exposure. Neuronal and cognitive functions are found to be influenced by RF-EMR exposure. Studies have indicated that teenagers using mobile phones and thus receiving RF-EMR exposure may experience memory and attention loss, learning and cognitive impairment, increased irritability, sleep problems, increased sensitivity to stress, and increased risk of seizures (5). The use of mobile phones by teenagers has been shown to be related to emotional and behavioral disorders, while reducing mobile phone use can improve children's cognitive ability (6). Our previous epidemiological studies also showed that inattention and fatigue were associated with mobile phone use in children and adolescents (7, 8), Hippocampal tissues relates to learning and memory, is one of the sensitive targets of RF-EMR. Primary hippocampal neurons are classical model cells to evaluate neurite outgrowth. The assessments of average neurite length, number of primary and secondary branches of primary hippocampal neurons were applied in many other studies (9, 10).

As an important functional executor in brain, neuronal cells have attracted the greatest attention in the study of the effects and mechanism of RF-EMR exposure. Delivery of RF-EMR exposure for 24 h can cause marked cell death in rat cortical neurons (11). There is also evidence that the electrical activity of cultured cortical neurons decreases during RF-EMR exposure (12). Furthermore, RF-EMR exposure inhibits the length and number of axon branches of cortical neurons (13). The activity and density of mature spines in primary hippocampal neurons decrease significantly when exposed to 2.4 W/kg RF-EMR, and the average length of dendrites per neuron is also reduced (14). We also showed that RF-EMR exposure impairs neurite outgrowth in neural stem cell-derived neurons (15, 16). However, a study using a pulsed radiofrequency electromagnetic field reported that it can potentiate neurite outgrowth in the dopaminergic MN9D cell line (17). The influence of RF-EMR exposure on neuronal cells remains controversial, but it is generally agreed that neuronal cells, specifically neurite outgrowth, are sensitive to RF-EMR exposure (18, 19). Therefore, it is important to elucidate the effect of RF-EMR exposure on neurite outgrowth.

Rap1 protein, a member of the RAS family, interacts with cAMP, calcium and other second messengers, turning extracellular stimulation into intracellular signals (20). The Rap1 protein acts as a molecular switch by cycling between two states (an inactive GDP-binding form and active GTP-binding form). These modifications are strictly controlled by guanine nucleotide exchange factors (GEFs) and GTPase activating proteins (GAPs) (21). Recent research further confirmed that Rap1 can affect the rearrangement of the cytoskeleton and promote neurite outgrowth and dendritic spine formation in the brain (22). Genetic interaction analysis showed that the repulsive guidance function mediated by the Sema-1a/PlexA signaling pathway, which contributes to axon growth and guidance, was regulated by Rap1 (23). In newborn neurons, Rap1 is a critical regulator in the formation of axons, leading and maintaining the radial migration of neuronal processes (24). Rap1-GTP, the active form of Rap1, is considered to affect the growth and differentiation of neuronal cells (25, 26). Rap1GAP, hydrolyzing the active form of Rap1, is degraded by the ubiquitin proteasome system (27). In the process of angiotensin II-stimulated neurite outgrowth in NG108-15 cells, the Rap1/B-Raf signal cascade activates Mitogen-Activated Protein Kinase Kinase (MEK) and induces sustained activation of p42/p44 Mitogen-Activated Protein Kinase (MAPK) and finally neurite outgrowth (28, 29). Although the role of Rap1 in neurite outgrowth has been widely studied, whether Rap1 is involved in neurite outgrowth regulation when neuronal cells are exposed to RF-EMR remains unclear.

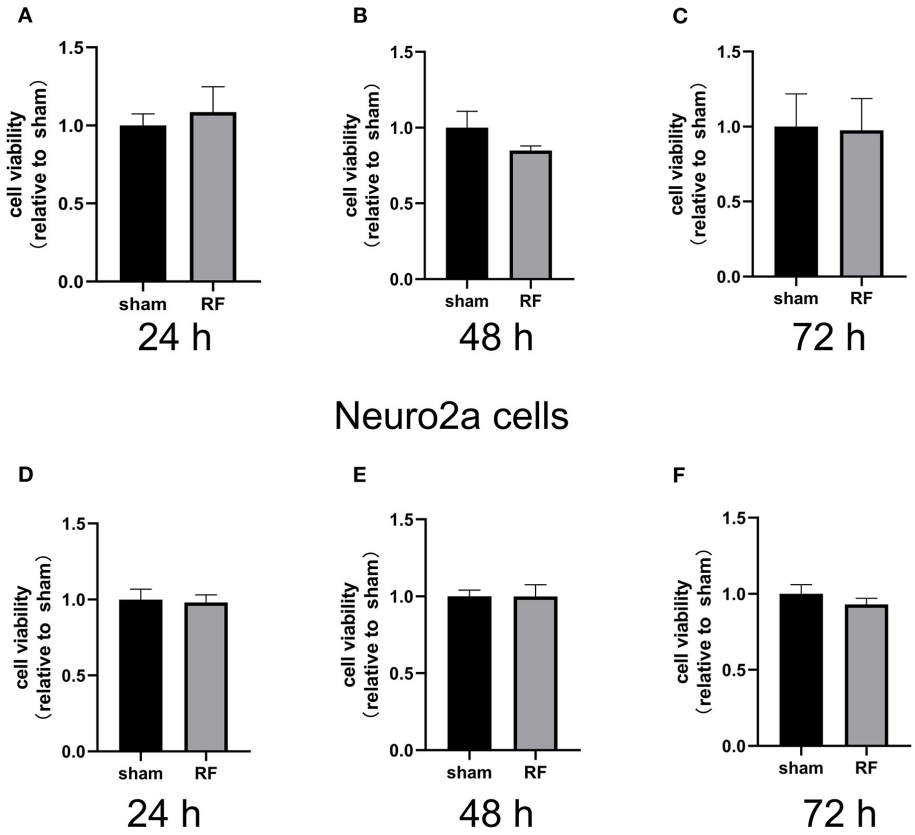

FIGURE 1 | Effects of RF-EMR exposure on neuronal cell viability. Cell viability was determined using a CCK-8 assay in primary mouse hippocampal neurons from C57BL/6 mice **(A–C)** and Neuro2a cells **(D–F)** irradiated by 24-, 48-, and 72-h 1,800 MHz RF-EMR at 4 W/kg. Data are represented as fold changes relative to sham from three independent experiments. The values are presented as the means ± SEM. Student's *t*-test was performed to compare groups.

The purpose of this study was to investigate the effect of 1,800 MHz RF-EMR exposure on neurite outgrowth in primary mouse hippocampal neurons and Neuro2a cells and to further explore the role of Rap1 in this process.

RESULTS

48-H 1,800 MHz RF-EMR Exposure Impairs Neurite Outgrowth in Neuronal Cells

Cell viability was unaffected by 24- to 72-h exposure to 1,800 MHz RF-EMR at 4 W/kg in either primary cultured hippocampal neurons or Neuro2a cells (**Figure 1**). In primary hippocampal neurons, the total neurite length per cell and the number of primary and secondary branches decreased after 48 h of 1,800 MHz RF-EMR exposure. The average number of branch points of each primary hippocampal neuron decreased after irradiation. The number of neurons with an average total neurite length between 0 and 100 μm increased, while the number of neurons with an average total neurite length between 100 and 200 μm and >200 μm decreased (**Figures 2A–F**). Similarly, the average total neurite length and neurite-bearing cell percentage of Neuro2a cells stimulated by retinoic acid (RA) decreased after 48 h of 1,800 MHz RF-EMR exposure at 4 W/kg. However, there was no significant difference in the average number of neurites among neurite-bearing Neuro2a cells between the sham and RF-EMR exposure groups (**Figures 2G–J**). In primary hippocampal neurons, BDNF treatment (positive control) can increase the average neurites length of each neuron by 50% compared with the sham group, and can increase the primary neurites number per neurons. However, PD98059 treatment (negative control) can inhibit the total neurites length of each cell by about 60%, and can decrease the number of primary, secondary neurites and branch points per neuron (**Supplementary Figures 1B–F**).

Rap1 Activity Is Decreased After 48-H 1,800 MHz RF-EMR Exposure Without Expression Alteration

The gene expression of Rap1a and Rap1b and the protein expression of Rap1, Rap1a, and Rap1b were not significantly

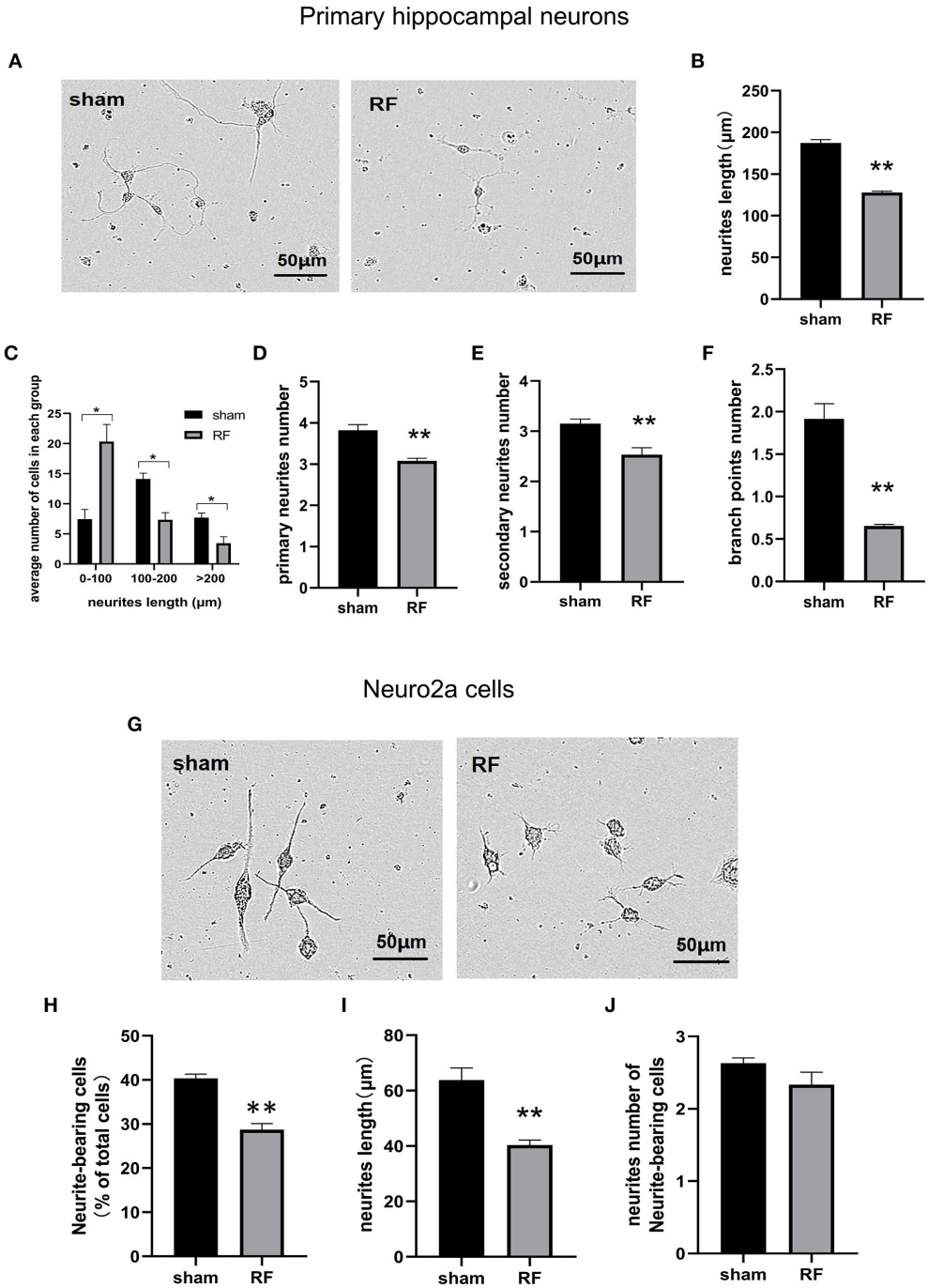

FIGURE 2 | Effects of RF-EMR exposure on neurite outgrowth in neuronal cells. Primary hippocampal neurons **(A–F)** and Neuro2a cells **(G–J)** were exposed to 1,800 MHz RF-EMR at 4 W/kg for 48 h. Morphological parameters were identified according to the description in the methods. Representative images of primary hippocampal neurons **(A)** and Neuro2a cells **(G)** were taken under a (20×) Leica microscope, and pictures were analyzed with ImageJ software. **(B)** shows the total neurite length per primary hippocampal neuron, **(C)** shows the number of cells in the groups with a total neurite length per primary hippocampal neuron larger than 100 μm, **(D,E)** shows the primary and secondary neurite numbers per primary hippocampal neuron, **(F)** shows the branch point number per primary hippocampal neuron, **(H)** shows the neurite-bearing cell percentage in Neuro2a cells, **(I)** shows the total neurite length per Neuro2a cell, and **(J)** shows neurite number of neurite-bearing Neuro2a cells after RF-EMR exposure. $^{*}P < 0.05$, $^{**}P < 0.01$, Student's *t*-test. Scale bar: 50 μm.

altered after 48 h of 1,800 MHz RF-EMR exposure at 4 W/kg in neuronal cells (**Figures 3**, **4**). Immunoprecipitation was used to detect the expression of the active Rap1 form, Rap1-GTP. Rap1-GTP decreased after RF-EMR exposure in both primary cultured hippocampal neurons and Neuro2a cells (**Figure 5**).

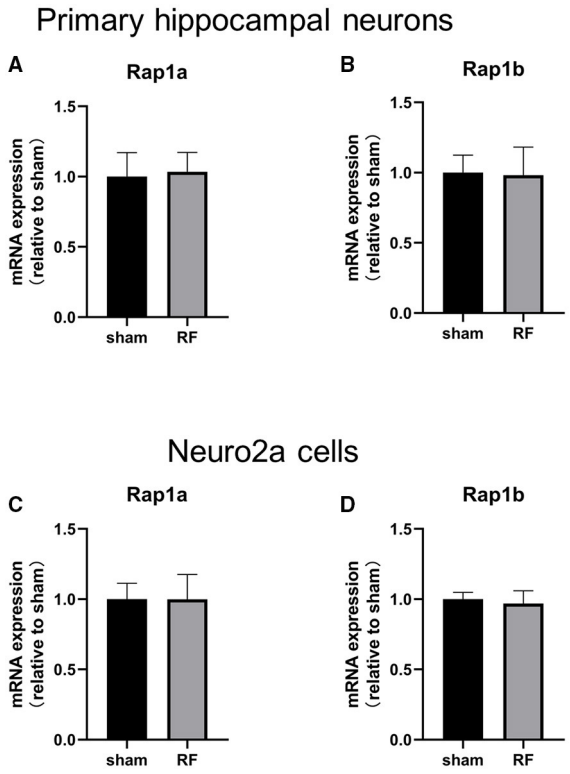

FIGURE 3 | Effects of RF-EMR exposure on the gene expression of Rap1a and Rap1b in neuronal cells. Neuronal cells were exposed to 1,800 MHz RF-EMR for 48 h at 4 W/kg. Gene expression was analyzed using real-time quantitative PCR. The Rap1 gene expression in primary hippocampal neurons **(A,B)** and Neuro2a cells **(C,D)** after RF-EMR exposure.

48-H 1,800 MHz RF-EMR Exposure Enhances the Protein Expression of Rap1GAP and Decreases the Protein Expression of p-MEK1/2 in Neuronal Cells

Rap1-GTP is a molecular switch that can be activated by GEFs and inactivated by GTPase activating proteins (Rap1GAPs). Rap1GAPs are representative molecules inactivating Rap1-GTPase (30). MEK1/2, a downstream molecule of Rap1, is a key molecule in the cascade reaction of the MAPK signaling pathway. When phosphorylated, MEK1/2 can activate downstream MAPK. Rap1-MEK-MAPK signaling can impact neuronal development, plasticity, and survival, especially by regulating neurite outgrowth (31). We found that the protein expression of Rap1GAP was enhanced while that of p-MEK1/2 decreased after 48 h of RF-EMR exposure in neuronal cells (**Figure 6**).

Overexpression of Constitutively Active Rap1 Reverses the Neurite Outgrowth Impairment Induced by 48-H RF-EMR Exposure in Neuro2a Cells

To further verify the role of Rap1-GTP in the impairment of neurite outgrowth induced by RF-EMR exposure, we

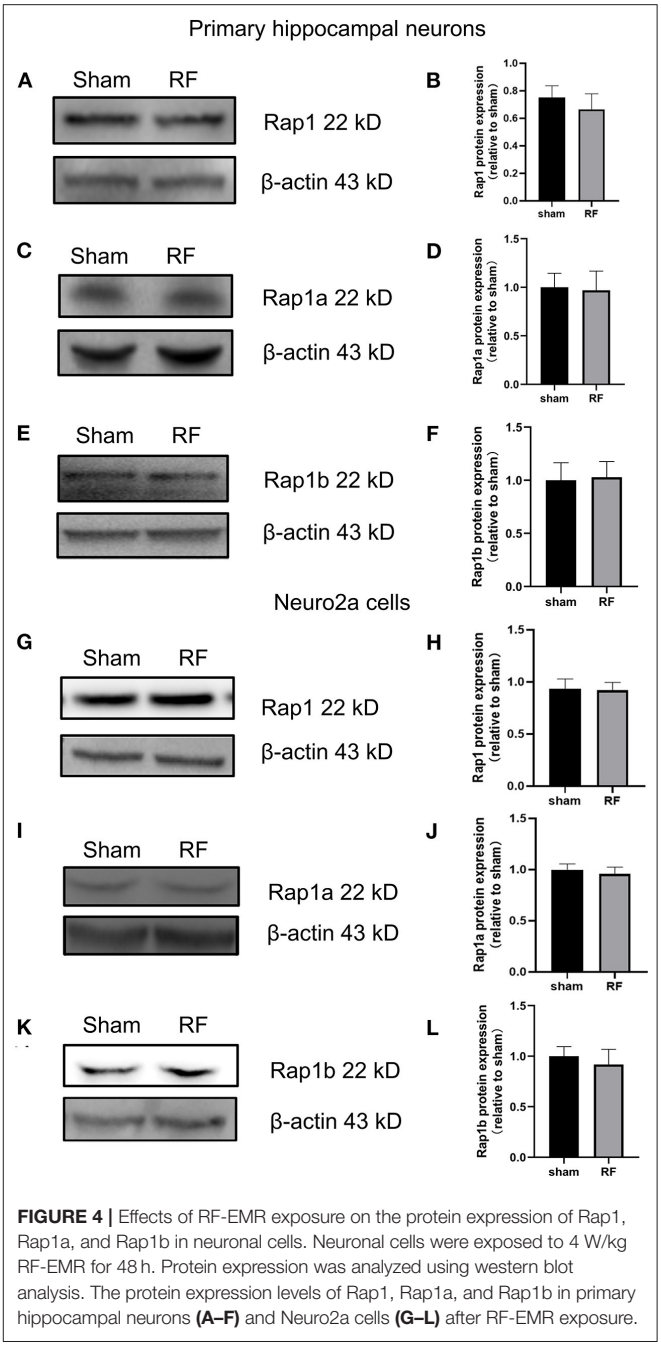

FIGURE 4 | Effects of RF-EMR exposure on the protein expression of Rap1, Rap1a, and Rap1b in neuronal cells. Neuronal cells were exposed to 4 W/kg RF-EMR for 48 h. Protein expression was analyzed using western blot analysis. The protein expression levels of Rap1, Rap1a, and Rap1b in primary hippocampal neurons **(A–F)** and Neuro2a cells **(G–L)** after RF-EMR exposure.

overexpressed Rap1-GTP by transfecting a constitutively active mutant Rap1 plasmid (Rap1-Gly_Val-GFP) into Neuro2a cells. Changing the 12th amino acid of the mutant plasmid from glycine to valine constitutively activates Rap1 (32, 33). After transfection of the constitutively active Rap1, its gene and protein expression levels increased in Neuro2a cells (**Supplementary Figure 2**). After transfection of the mutant plasmid, the expression of Rap1-GTP increased after 48 h of irradiation (**Figure 7**). Overexpression of Rap1-GTP reversed the disturbance of neurite outgrowth induced by 48 h of RF-EMR exposure (**Figure 8**).

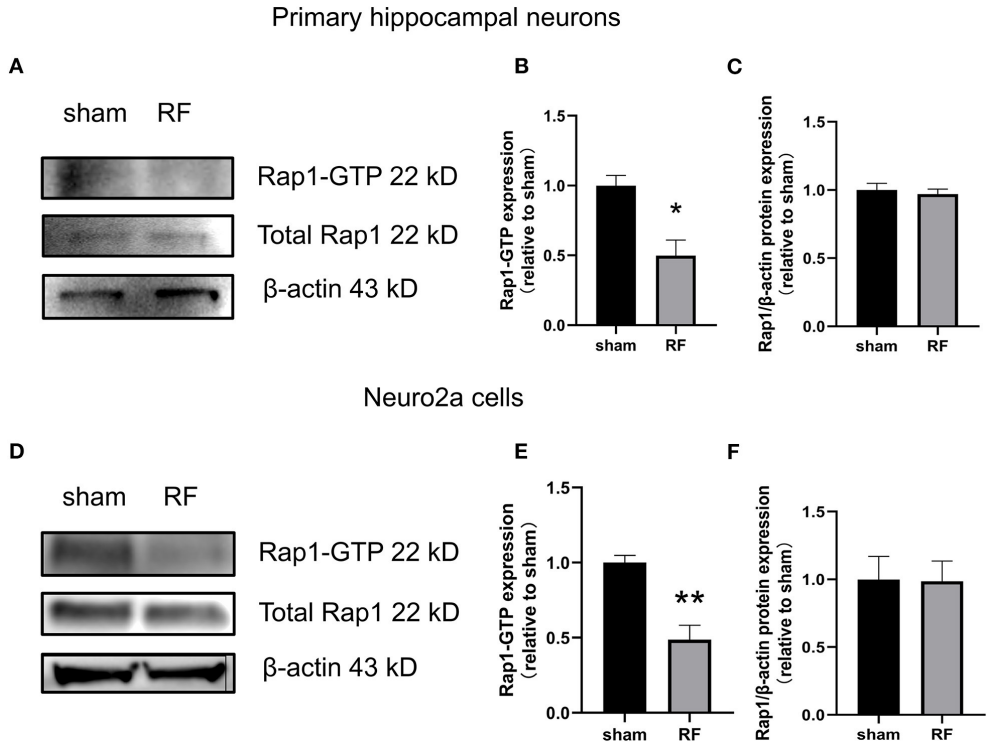

FIGURE 5 | Effects of RF-EMR exposure on Rap1-GTP protein expression in neuronal cells. Neuronal cells were exposed to 4 W/kg RF-EMR for 48 h. The protein expression of Rap1-GTP protein in primary hippocampal neurons **(A–C)** and Neuro2a cells **(D–F)** is shown. Protein expression was analyzed by immunoprecipitation and western blot analysis. *$P < 0.05$, **$P < 0.01$, Student's *t*-test.

DISCUSSION

Neurite outgrowth is an important process of morphological change in neuronal differentiation and development, which is tightly controlled and regulated by several interior and exterior signals. Disturbance of neurite outgrowth will cause defective neural development and neuronal diseases. In our study, we found that 48-h 1,800 MHz RF-EMR exposure interrupted neurite outgrowth in primary cultured hippocampal neurons and Neuro2a cells. Rap1, which plays a critical role in controlling neurite outgrowth and dendrite spine morphology, was inactivated by RF-EMR exposure, while overexpression of constitutively active Rap1-GTP reversed the impairment of neurite outgrowth induced by RF-EMR exposure.

The brain is one of the most sensitive organs to the biological effects of RF-EMR. The results from epidemiological investigations showed that the use of mobile phones can lead to the perceived health impairment in adolescents (34). Another study indicated that mobile phone usage induces anxiety, depression, and stress (35). Animal experiments also showed that RF-EMR exposure causes abnormal neural behavior and impacts dendritic arborization patterns (36). As the brains and skulls of infants and young children are still in developing state, the same electromagnetic background may cause their brains to absorb more electromagnetic energy than adult individuals. The specific absorption by brain tissue in children is 60–125% higher than that in adults (37).

Neurite outgrowth plays a key role in the formation of neural networks during neural development and nerve regeneration after trauma or disease. Neurite outgrowth is regulated by precise signal networks that control processes from sprouting and extending to the formation of axons and dendrites (38, 39). Abnormal neurite outgrowth may cause aberrant polarity, abnormal synaptic plasticity of neuronal cells, and damage to axons and dendrites. Unusual neurodevelopment can induce autism, hyperactivity disorder, dyslexia and so on (40). Deformed neuronal cell morphology may also cause neurodegenerative diseases such as Alzheimer's disease and Parkinson's disease.

In this study, we found that 48-h 1,800 MHz RF-EMR exposure could interfere with neurite outgrowth in hippocampal neurons, including decreasing neurite length and the number of neurite branches. Additionally, neuronal differentiation induced by RA was inhibited by RF-EMR exposure in Neuro2a cells. Kim et al. reported that the total number of dendritic spines was significantly decreased in hippocampal neurons after RF-EMR exposure at 4 W/kg for 4 weeks (9). Our previous studies also showed that 72 h of 1,800 MHz RF-EMR exposure significantly inhibited neurite outgrowth in embryonic neural stem cells (eNSCs) at 4 W/kg, in which the BHLH gene and

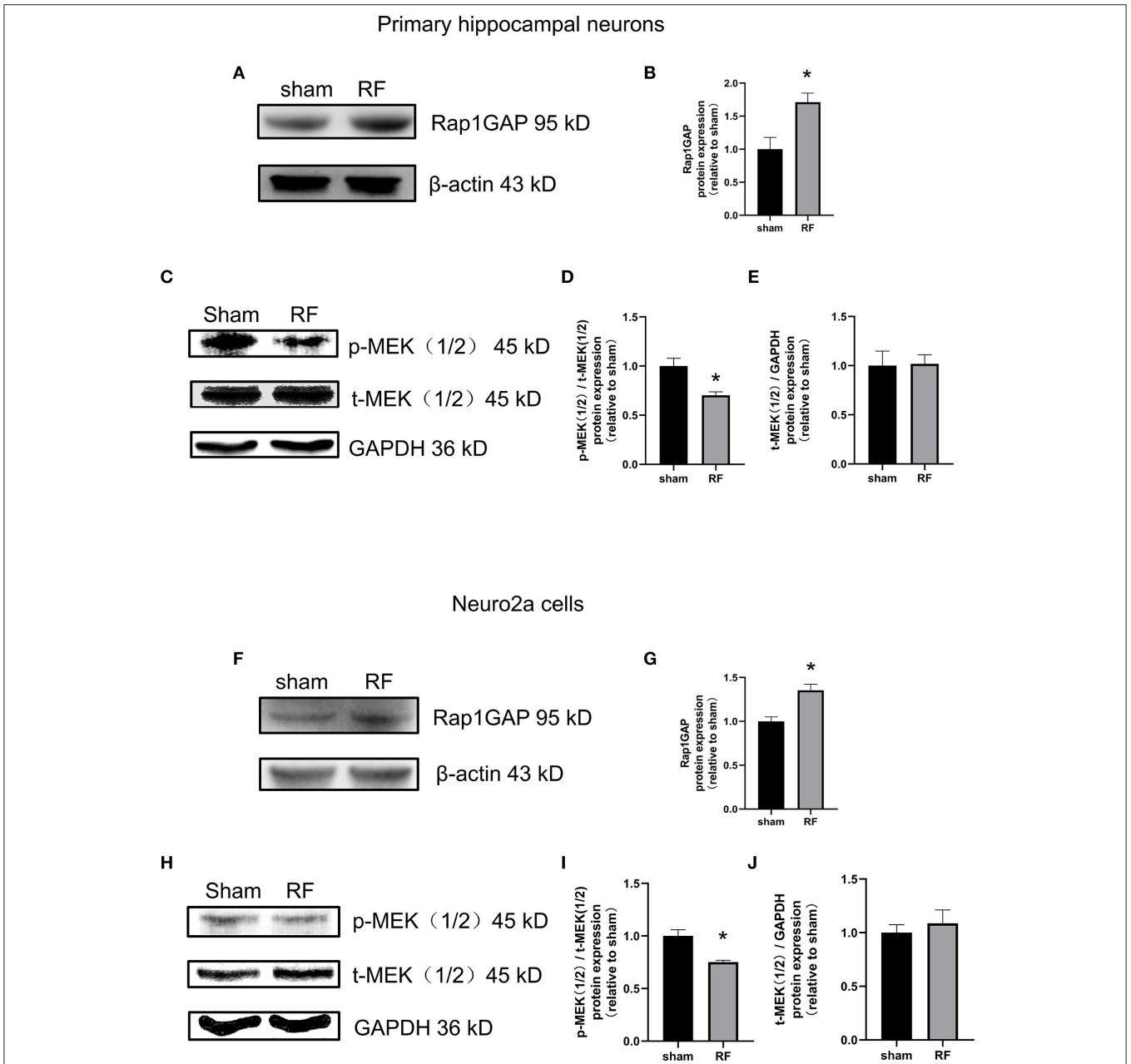

FIGURE 6 | Effects of RF-EMR exposure on the protein expression of Rap1GAP and p-MEK1/2 in neuronal cells. Neuronal cells were exposed to 4 W/kg RF-EMR for 48 h. The protein expression of Rap1GAP in primary hippocampal neurons **(A–E)** and Neuro2a cells **(F–J)** were detected by western blot. **(A,B)** shows protein expression of Rap1GAP in primary hippocampal neurons, and **(F,G)** in Neuro2a cells. The expression levels of MEK1/2 and p-MEK1/2 after RF-EMR exposure for 48 h were detected by western blot analysis in primary hippocampal neurons **(C–E)** and Neuro2a cells **(H–J)**. *$P < 0.05$, Student's *t*-test.

the EPHA5 signaling pathway were involved (15, 16). The mechanisms underlying the effects of RF-EMR exposure on neurite outgrowth or synaptic plasticity are thought to include changes in calcium ion channels, the myelin sheath, oxidative stress and the glutamate receptor signaling pathway (36, 41, 42). However, additional evidence and further study are required to confirm these hypotheses. This study confirmed that 1,800 MHz RF-EMR exposure affects neurite outgrowth, neurite length, and the number of branch points in each cell, which is consistent with previous studies.

The International Commission on Non-Ionizing Radiation Protection (ICNIRP) sets the limit of local head exposure in the general population at 2 and 10 W/kg for the occupational population (43). The SAR

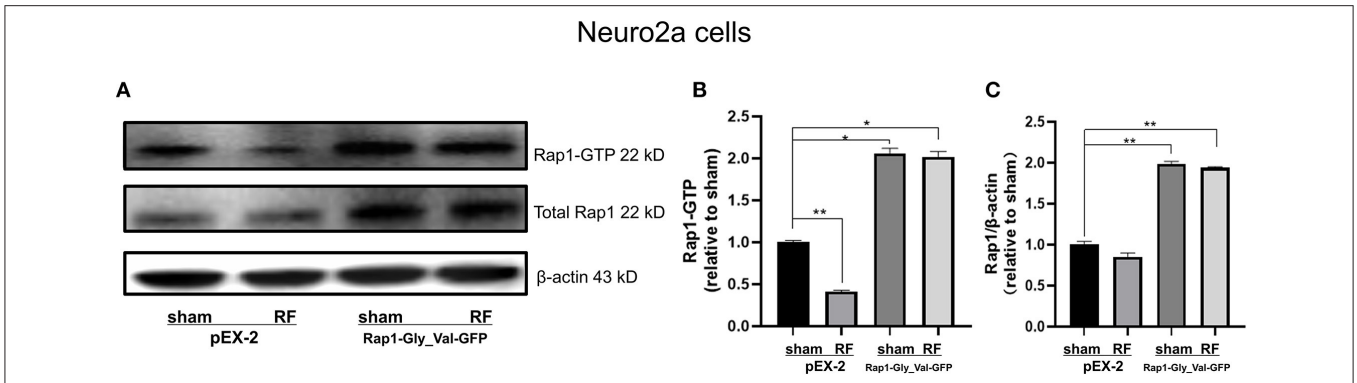

FIGURE 7 | The transfection of constitutively active Rap1 can reverse the decrease in Rap1-GTP induced by 1,800 MHz RF-EMR exposure in Neuro2a cells. Neuro2a cells were transfected by Rap1 constitutively active mutant plasmid (Rap1-Gly_Val-GFP) for 24 h. Transfected Neuro2a cells were exposed to RF-EMR for 48 h at 4 W/kg. The expression of Rap1-GTP was detected by immunoprecipitation. **(A)** is the representative bands of Rap1-GTP, Rap1, and β-actin in each group in Neuro2a cells, **(B)** is the statistical graph made from the data identified according to the gray value and area from the bands. **(C)** is the ratio of protein expression of Rap1 to β-actin in Neuro2a cells. $^{*}P < 0.05$, $^{**}P < 0.01$, one-way ANOVA followed by Bonferroni *post hoc* test.

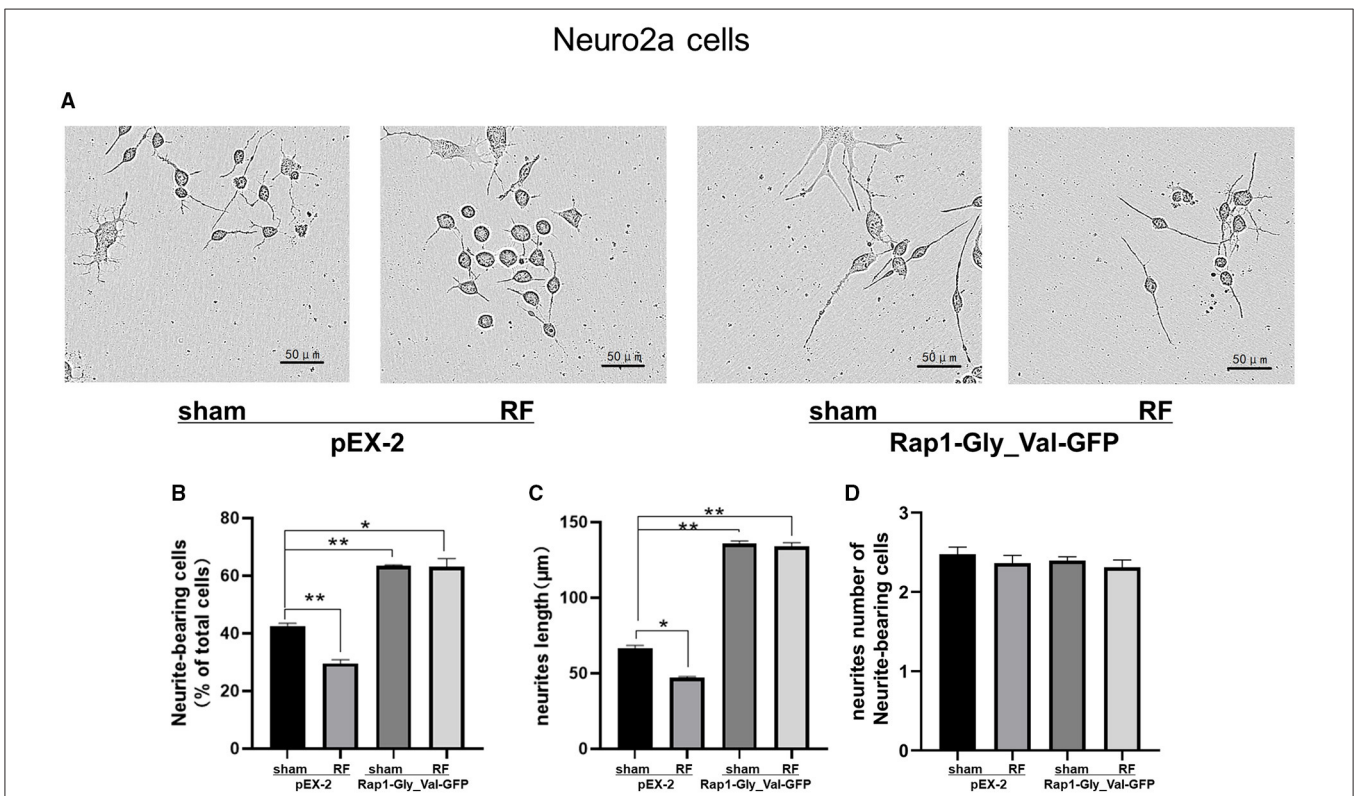

FIGURE 8 | Effects of 1,800 MHz RF-EMR exposure on neurite outgrowth after constitutively active Rap1 transfection in Neuro2a cells. Neuro2a cells were transfected by Rap1 constitutively active mutant plasmid (Rap1-Gly_Val-GFP) for 24 h. The neurite outgrowth of transfected Neuro2a cells induced by RF-EMR exposure for 48 h was assessed by ImageJ software as mentioned before. **(A)** shows representative pictures of transfected Neuro2a cells with or without irradiation. **(B)** shows Neurite-bearing cell ratio, **(C)** shows neurite length per cell, and **(D)** shows neurite number of neurite-bearing cells. $^{*}P < 0.05$, $^{**}P < 0.01$, one-way ANOVA followed by Bonferroni *post hoc* test.

dose of 4 W/kg was usually used to explore the possible biological effects of RF-EMR. Several previous studies have observed the effects of RF-EMR on neuronal cells at SAR value of 4 W/kg, showing the confirmed effect of RF-EMR exposure on dendritic development, cell cycle, etc. (9, 44–46).

Rap1, a member in a small family of monomer GTP-binding proteins, plays a key role in cell proliferation, differentiation, survival, adhesion, and migration (28). Rap1 signaling mediates the role of Semas-Plexins in neuropolarity generation, neurogenesis, axonal growth cone formation, and guidance (47). Rap1-GTP can affect morphological changes in neuronal cells without changing the gene and protein expression of Rap1 (26). In this study, the active form of Rap1, but not its gene and protein expression levels, was decreased after RF-EMR exposure. Altered Rap1-GTP levels were found in the prefrontal cortex of depressed individuals who had committed suicide and in the frontal cortex of patients with schizophrenia and severe depressive disorders (48). Transfection of a constitutively active Rap1 (F64A) plasmid reversed the inhibitory effect of Myelin-associated glycoprotein (MAG) on the neurite growth of dorsal root ganglion (DRG) neurons, possibly by decreasing the expression of Rap1-GTP, limiting neurite outgrowth (25). Rap1 activity is impaired by SynGAP-β, which leads to affected synaptic plasticity and dendrite development in the hippocampus (49). To further verify the role of Rap1-GTP in RF-EMR exposure, we transfected Rap1 mutant plasmid (Rap1-Gly_Val-GFP) to reverse the damage to neurite growth. Compared with indirect Rap1 agonist or inhibitor Rap1, the mutant active Rap1 plasmid can better verify the effect of Rap1 activity. By comparing neurite outgrowth after transfection of the negative control plasmid and constitutively active Rap1 plasmids, we showed that transfection of the constitutively active Rap1 plasmid effectively promoted neurite outgrowth without considering RF-EMR exposure, and transfection of the mutant plasmid also reversed the neurite outgrowth restriction caused by irradiation. Although the neuronal cells transfected with mutant plasmid were irradiated, the neurites still grew well and grew better than the negative control plasmid group without irradiation. The increase in Rap1-GTP could promote neurite outgrowth. This is consistent with the result that transfection of a constitutively active Rap1 plasmid can contribute to neurite complexity (50).

Rap1 links extracellular signals to intracellular signals through second messengers. Rap1 may affect the growth of neurites through a variety of mechanisms. When Rap1 is activated by Ca^{2+} and diacylglycerol-activated guanine nucleotide exchange factors (CalDAG-GEFs), it becomes a downstream molecule of Ca^{2+} signaling pathway. When activated by cAMP-dependent GEF, Rap1 can regulate the concentration of cytoplasmic Ca^{2+} and become its upstream molecule (51). The calcium signaling pathway promotes the growth of neurites, possibly by increasing the activity of calcium binding protein, which reduces the concentration of calcium (52). The interaction between Rap1 and Ca^{2+} also provides a theoretical basis for the regulation of neurite outgrowth of neuronal cells by Rap1. RA-RhoGAP is a direct downstream target of Rap1 in the neurite growth process that possesses a lipid-bound (PH) domain. Inactivity of Rap1 can weaken the GAP activity of Rho, and finally affect nerve axon extension (53). RF-EMR exposure may also reduce the binding of phosphatidylic acid to this PH domain by reducing the activity of Rap1. Rap1-GTP activates PSD-95/discs large/ZO-1 (PDZ)-GEF1 through a positive feedback mechanism (54). So the effect of irradiation on the interaction between Rap1 and PDZ-GEF1 may exist.

Although the above mechanisms regulating Rap1 cannot be ruled out, in this experiment, the expression of Rap1GAP increased after irradiation. Therefore, we consider that the active form of Rap1 may be weakened by Rap1GAP. The active form of Rap1 hydrolyzed by Rap1GAP in non-electromagnetic environment has been reported. Higher level of active Rap1-GTP was found in the brain of Go2 α defective mutant mice, indicating that Go2 α may increase Rap1GAP activity and affect Rap1 activation/inactivation cycle. Go2 α deficient mutant mice developed more branches than those of wild-type mice (27). In striatum medium polyspinous neurons, following activation of the D1 dopamine receptor, Ser441 and Ser499 of Rap1GAP can be phosphorylated by PKA. This inhibits GAP activity and increases Rap1 activity, resulting in better dendritic spine growth (55).

In this study, the expression of phosphorylated form of MEK1/2 decreased after irradiation. We consider that RF-EMR exposure may damage the neurite outgrowth through MEK, the downstream of Rap1 active form. It has been reported that the Rap1-MEK-MAPK signaling pathway promotes the growth of neurites in NG108-15 cells (56). Previous studies have shown that an increase in endogenous β-amyloid peptide leads to an increase in the expression of cAMP response element-related genes and finally promotes synaptic plasticity through the Rap1-MEK signaling pathway in PC12 cells (57). Nerve growth factor also continuously activates ERK through the Rap1-MEK pathway (58). Therefore, RF-EMR exposure may reduce the activity of Rap1 through Rap1GAP and then cause a decrease in p-MEK1/2, resulting in impaired neurite outgrowth.

Despite our findings from this study, more researches need to be done regarding the irradiation-induced decrease in Rap1 activity and how this leads to impaired neurite outgrowth. According to the previous reports, the effect of the transfection of wild-type Rap1 on neurite outgrowth is very limited, so in this study we applied a constitutively active Rap1 plasmid to verify the role of Rap1-GTP in neurite outgrowth impairment induced by RF-EMR exposure (59).

Rap1 is activated by a specific GEF, the role of which in RF-EMR exposure-impaired neurite outgrowth needs to be investigated by further researches, as does the specific regulation of Rap1GAP after irradiation. As Rap1 activity is influenced by RF-EMR exposure and the constitutively active Rap1 can rescue neurite outgrowth impairment induced by RF-EMR, Rap1 may be a potential new candidate for interfering the disruption of developing brain by RF-EMR exposure.

CONCLUSION

We found that Rap1 is involved in the disturbance of neurite outgrowth induced by 1,800 MHz RF-EMR exposure in neuronal cells. Due to the developmental sensitivity of infants and

adolescents, the neuronal impairment induced by 1,800 MHz RF-EMR exposure can interrupt programmatic neural development and cause abnormal neuronal behavior and diseases. Rap1 activity and related signaling pathways may be critical targets in the neuronal effects induced by RF-EMR exposure. The influence of RF-EMR exposure on the developing brain requires greater attention.

MATERIALS AND METHODS

Cell Culture

A mouse neuroblastoma cell line (Neuro2a) (Chunmai, China) was maintained at 37.0 ± 0.2°C and 5% CO_2. Neuro2a cells were cultured in high-glucose Dulbecco's modified Eagle's medium (DMEM; Sigma, USA) with 10% fetal bovine serum (FBS; Biological Industries, ISR) and 50 mg/ml penicillin-streptomycin (Sigma, USA). Cells were subcultured every 2 days. Neuro2a cells were seeded in 35 mm plastic dishes (Thermo Scientific, USA) for 12 h before exposure to RF-EMR exposure. Neuro2a cells induced by retinoic acid were used. This model has been proved to be efficient in several studies (22, 60). The culture medium was changed to differentiation medium immediately before irradiation. The differentiation medium was composed of 99% DMEM, 1% FBS, and 10 μM retinoic acid (Sigma, USA). FBS and retinoic acid concentration were slightly regulated to obtain optimized differentiation effects according to different cell density. The seeding densities of Neuro2a cells were 3×10^4 cells/35 mm dish for cell viability assay, 2×10^5 cells/35 mm dish for neurite outgrowth analysis, 5×10^5 cells/35 mm dish for RNA, protein extraction and transfection.

Primary hippocampal neurons were prepared from newborn C57/BL mice within 1–3 days of birth. Dissociated neurons were plated in 35-mm dishes with the seeding medium containing 79% DMEM/F12 (Sigma, USA), 20% fetal bovine serum (FBS; Biological Industries, ISR), and 1% penicillin-streptomycin (50 mg/ml) (Sigma, USA). After 12 h of seeding, the culture medium was changed to the maintenance medium consisted of 95% Neurobasal-A Medium (Gibco, USA), 2% B-27 plus supplement (Gibco, USA), 1% culture one supplement (Gibco, USA), 1% Glutamax (Gibco, USA), and 1% penicillin-streptomycin (Gibco, USA). The seeding densities of primary hippocampal neurons were 2×10^5 cells/35 mm dish for neurite outgrowth analysis, 10^6 cells/35 mm dish for cell viability, RNA and protein extraction.

The animal study was reviewed and approved by Laboratory Animal Welfare and Ethics Committee of Third Military Medical University (AMUWEC20210443).

Radiofrequency Electromagnetic Irradiation (RF-EMR) at 1,800 MHz

Primary mouse hippocampal neurons and Neuro2a cells were irradiated in an sXc-1800 exposure system (IT'IS Foundation, Zurich, Switzerland) using the irradiation method introduced in previous studies (15, 16). RF-EMR exposure system is mainly composed of the following four parts: narrowband amplifier, arbitrary function generator, RF generator, and two waveguide. Each chamber is equipped with a plastic holder hosting 6 dishes arranged in two stacks. A total of 6 dishes were exposed, 6 dishes in the other chamber served as the sham group. The metal housing of the two chambers ensures that radiation exists only indoors and does not interfere with the outdoors. The operation of fans in chambers can avoid the thermal effect caused by irradiation (61). The sensors and fans in the exposure system were connected to a computer that monitored the SAR value during exposure and maintained a constant temperature and environment for the waveguides (37°C, 5% CO_2, 95% atmospheric air). 35mm dishes were placed in the H-field maxima and exposed to a polarized E-field (an electric field perpendicular to the H-field). To perform double-blind experiments, the computer randomly determines which of the two waveguides was exposed in each trial. Experiments were also conducted in blind modality where the researchers who performed biological assays did not know which of the two chambers was active, and which acted as sham. RF-EMR exposure was delivered using the GSM talk signal mode at an exposure interval of 5 min irradiation field on and 10 min irradiation field off and an SAR value of 4 W/kg.

Cell Viability Assay

Cell viability was evaluated by a CCK-8 (Dojindo, Japan) assay following the manufacturer's instructions. Briefly, after 24-, 48-, and 72- h irradiation, 10% CCK-8 solution was added to the medium and incubated at 37°C for 3 h. The absorbance at 450 nm was read by a microplate reader (Tecan, Austria).

Neurite Outgrowth Analysis

Neurite outgrowth analysis was performed as previously described (15). Briefly, primary hippocampal neurons and Neuro2a cells were cultured in 35-mm dishes, exposed to RF-EMR for 48 h. Neurite outgrowth of primary hippocampal neurons (DIV 2) and Neuro2a cells was observed with a Leica microscope (20×). Forty nanogram per milliliter BDNF (MCE, USA) was used as positive control and 50 μM MEK1/2 inhibitor PD98059 (SIGMA, USA) was used as negative control (62, 63). BDNF and PD98059 were added into the maintenance medium and incubated with the neurons for 48 h, respectively. ImageJ software was used to evaluate neurite outgrowth. Thirty cells per group were identified among the primary hippocampal neurons, and 100 cells per group were counted among the Neuro2a cells. The total length of the neurites in each neuronal cell was measured from the cell center to the end of the neurite. The primary neurite was identified as the directly separated process from the cell body, the secondary neurite was the process separated from the primary neurite, and the remaining branches were the branch points. Neuro2a cells with arbitrary neurite lengths greater than the cell body diameter were recognized as neurite-bearing cells. Neurites whose length was greater than the cell body diameter were counted as neurites of neurite-bearing cells.

Real-Time Quantitative PCR

TRIzol reagent (Takara, JPN) was used to extract total RNA from neuronal cells after exposure to RF-EMR for 48 h. cDNA

was obtained by RT-qPCR performed on a CFX96TM real-time system (Bio-Rad, USA) using TB green (Takara, JPN). The Rap1a and Rap1b gene-specific primers used are shown in **Supplementary Table 1**. The gene expression fold change was calculated and normalized to the gene expression of endogenous β-actin. Then, the relative gene expression level was calculated with reference to the sham.

Western Blot Analysis

After RF-EMR exposure for 48 h, protein samples were obtained using RIPA buffer (Beyotime, China) containing protease and phosphatase inhibitors (Roche, USA). Twelve percent SDS-PAGE (Genscript, USA), PVDF membranes (Bio-Rad, USA), Quick Block Blocking Buffer (Beyotime, China), TBST solution (Thermo Fisher, USA), and primary and secondary antibodies (details in **Supplementary Table 2**) were used for western blot analysis. The PVDF membrane was scanned on a chemiDoc XRS+ machine (Bio-Rad, USA) by using ECL luminescent solution (Thermo Fisher, USA).

Rap1 Activity Assay

The activity of Rap1 was measured by immunoprecipitation after RF-EMR exposure for 48 h (64). The irradiated primary hippocampal neurons and Neuro2a cells were lysed with IP lysate (Beyotime, China) on ice for 15 min, rotated and then centrifuged at 15,000 g for 30 min at 4°C to remove the precipitate. The protein concentration of the supernatant was measured by the BCA method (Beyotime, China). Three hundred micrograms of protein supernatant from each group was taken equally. IgG antibody (Beyotime, China) and 1 μg active Rap1 antibody was added to the sham group and irradiation group and rotated overnight. The next day, protein A/G agarose beads (Beyotime, China) were added to bind the FC segment of active Rap1 antibody to precipitate, and the non-specifically bound antigen was washed away with PBS (Beyotime, China). After adding loading buffer (Beyotime, China), IP samples were heated to denature and subjected to western blot analysis. In the above steps, the IgG group represents the background gray value, and the irradiated group and the control group represent the natural active form of Rap1.

Transfection of Constitutively Active Rap1 Mutant Plasmid

Glycine at the 12th position of the Rap1 gene was replaced with valine, and GFP fluorescence label was added. The steps for synthesizing the mutant plasmid were introduced in a previous article (31). The mutant plasmid (GenePharma, China) was transfected with the pEX-2 vector. Lipofectamine 3000 transfection reagent (Thermo Scientific, USA) and Opti-MEM medium (Invitrogen, USA) were used to help the mutant plasmids transfecting into cells and stabilize the expression in Neuro2a cells. In the sham group, negative control plasmid carrying the pEX-2 vector was transfected into the cells in the same way. After seeding for 24 h, the transfection reagent and mutant plasmid were added and incubated. After transfection for 24 h, retinoic acid was used for differentiation and irradiation for 48 h as depicted before.

Statistical Analysis

Statistical analysis was performed using GRAPH Prism 8.0 software. All data were collected from at least three independent duplicate experiments and are presented as the mean ± standard error of the mean (SEM). Student's *t*-tests, one-way ANOVA followed by the Brown–Forsythe test and Welch ANOVA were used to determine significance. $P < 0.05$ was considered statistically significant.

DATA AVAILABILITY STATEMENT

The original contributions presented in the study are included in the article/**Supplementary Material**, further inquiries can be directed to the corresponding author.

ETHICS STATEMENT

The animal study was reviewed and approved by Laboratory Animal Welfare and Ethics Committee of Third Military Medical University (AMUWEC20210443).

AUTHOR CONTRIBUTIONS

LZ and ZY designed the experiment and conceived the manuscript. YaL, PD, CZ, and ZH did the experiments. YaL, CC, and HP analyzed the data. YaL and LZ wrote the draft of the manuscript. MH, PG, YZ, and QM reviewed the manuscript. LZ and ZY critically revised the manuscript. All authors listed have made a substantial, direct and intellectual contribution to the work, and approved it for publication.

FUNDING

This research was supported by the National Natural Science Foundation of China (Grant Nos. 31670854 and 31770906).

ACKNOWLEDGMENTS

We thank Jia Xie, Li Tian, Mengyan Chen (Department of occupational health from Third Military Medical University, Chongqing, China) for helping immunoprecipitation and primer design. We thank Yidan Liang, Yajing Zhang (Guangxi University, Nanning, China) for data analysis. We thank Min Li (Department of occupational health from Third Military Medical University, Chongqing, China) for language polishing.

SUPPLEMENTARY MATERIAL

The Supplementary Material for this article can be found online at: https://www.frontiersin.org/articles/10.3389/fpubh.2021.771508/full#supplementary-material

REFERENCES

1. Pearce J. Limiting liability with positioning to minimize negative health effects of cellular phone towers. *Environ Res.* (2020) 181:108845. doi: 10.1016/j.envres.2019.108845
2. Szilágyi Z, Németh Z, Bakos J, Necz P, Sáfár A, Kubinyi G, et al. Evaluation of inflammation by cytokine production following combined exposure to ultraviolet and radiofrequency radiation of mobile phones on 3D reconstructed human skin *in vitro*. *Int J Environ Res Public Health*. (2020) 17:4401. doi: 10.3390/ijerph17124401
3. Lee J, Jang S, Ju Y, Kim W, Lee H, Park E. Relationship between mobile phone addiction and the incidence of poor and short sleep among korean adolescents: a longitudinal study of the Korean Children & Youth Panel Survey. *J Korean Med Sci.* (2017) 32:1166–72. doi: 10.3346/jkms.2017.32.7.1166
4. Ishihara T, Yamazaki K, Araki A, Teraoka Y, Tamura N, Hikage T, et al. Exposure to radiofrequency electromagnetic field in the high-frequency band and cognitive function in children and adolescents: a literature review. *Int J Environ Res Public Health.* (2020) 17:9179. doi: 10.3390/ijerph17249179
5. Hardell L. Effects of mobile phones on children's and adolescents' health: a commentary. *Child Dev.* (2018) 89:137–40. doi: 10.1111/cdev.12831
6. Miller A, Sears M, Morgan L, Davis D, Hardell L, Oremus M, et al. Risks to health and well-being from radio-frequency radiation emitted by cell phones and other wireless devices. *Front Public Health.* (2019) 7:223. doi: 10.3389/fpubh.2019.00223
7. Zheng F, Gao P, He M, Li M, Tan J, Chen D, et al. Association between mobile phone use and self-reported well-being in children: a questionnaire-based cross-sectional study in Chongqing, China. *BMJ Open.* (2015) 5:e007302. doi: 10.1136/bmjopen-2014-007302
8. Zheng F, Gao P, He M, Li M, Wang C, Zeng Q, et al. Association between mobile phone use and inattention in 7102 Chinese adolescents: a population-based cross-sectional study. *BMC Public Health.* (2014) 14:1022. doi: 10.1186/1471-2458-14-1022
9. Kim J, Chung K, Hwang Y, Park H, Kim H, Kim H, et al. Exposure to RF-EMF alters postsynaptic structure and hinders neurite outgrowth in developing hippocampal neurons of early postnatal mice. *Int J Molecular Sci.* (2021) 22:5340. doi: 10.3390/ijms22105340
10. O'Connor R, Madison S, Leveque P, Roderick H, Bootman M. Exposure to GSM RF fields does not affect calcium homeostasis in human endothelial cells, rat pheocromocytoma cells or rat hippocampal neurons. *PLoS ONE.* (2010) 5:e11828. doi: 10.1371/journal.pone.0011828
11. Liu M, Wen J, Fan Y. Potential protection of green tea polyphenols against 1800 MHz electromagnetic radiation-induced injury on rat cortical neurons. *Neurotox Res.* (2011) 20:270–6. doi: 10.1007/s12640-011-9240-4
12. El Khoueiry C, Moretti D, Renom R, Camera F, Orlacchio R, Garenne A, et al. Decreased spontaneous electrical activity in neuronal networks exposed to radiofrequency 1,800 MHz signals. *J Neurophysiol.* (2018) 120:2719–29. doi: 10.1152/jn.00589.2017
13. Su L, Yimaer A, Xu Z, Chen G. Effects of 1800 MHz RF-EMR exposure on DNA damage and cellular functions in primary cultured neurogenic cells. *Int J Radiat Biol.* (2018) 94:295–305. doi: 10.1080/09553002.2018.1432913
14. Ning W, Xu S, Chiang H, Xu Z, Zhou S, Yang W, et al. Effects of GSM 1800 MHz on dendritic development of cultured hippocampal neurons. *Acta Pharmacol Sin.* (2007) 28:1873–80. doi: 10.1111/j.1745-7254.2007.00668.x
15. Chen C, Ma Q, Liu C, Deng P, Zhu G, Zhang L, et al. Exposure to 1800 MHz radiofrequency radiation impairs neurite outgrowth of embryonic neural stem cells. *Sci Rep.* (2014) 4:5103. doi: 10.1038/srep05103
16. Chen C, Ma Q, Deng P, Lin M, Gao P, He M, et al. 1800 MHz radiofrequency electromagnetic field impairs neurite outgrowth through inhibiting EPHA5 signal. *Front Cell Dev Biol.* (2021) 9:657623. doi: 10.3389/fcell.2021.657623
17. Lekhraj R, Cynamon D, DeLuca S, Taub E, Pilla A, Casper D. Pulsed electromagnetic fields potentiate neurite outgrowth in the dopaminergic MN9D cell line. *J Neurosci Res.* (2014) 92:761–71. doi: 10.1002/jnr.23361
18. Inoue S, Motoda H, Koike Y, Kawamura K, Hiragami F, Kano Y. Microwave irradiation induces neurite outgrowth in PC12m3 cells via the p38 mitogen-activated protein kinase pathway. *Neurosci Lett.* (2008) 432:35–9. doi: 10.1016/j.neulet.2007.12.002
19. Wang K, Lu J, Xing Z, Zhao Q, Hu L, Xue L, et al. Effect of 18 GHz radiofrequency electromagnetic radiation on novel object associative recognition memory in mice. *Sci Rep*. (2017) 7:44521. doi: 10.1038/srep44521
20. Li W, Ma K, Jiang X, Yang R, Lu P, Nie B, et al. Molecular mechanism of panaxydol on promoting axonal growth in PC12 cells. *Neural Regen Res.* (2018) 13:1927–36. doi: 10.4103/1673-5374.239439
21. Jaśkiewicz A, Pajak B, Orzechowski A. The many faces of Rap1 GTPase. *Int J Mol Sci.* (2018) 19:2848. doi: 10.3390/ijms19102848
22. Huang M, Liang C, Li S, Zhang J, Guo D, Zhao B, et al. DOCK4 two autism/dyslexia linked variations of disrupt the gene function on Rac1/Rap1 activation, neurite outgrowth, and synapse development. *Front Cell Neurosci.* (2019) 13:577. doi: 10.3389/fncel.2019.00577
23. Yang D, Roh S, Jeong S. The axon guidance function of Rap1 small GTPase is independent of PlexA RasGAP activity in Drosophila. *Dev Biol.* (2016) 418:258–67. doi: 10.1016/j.ydbio.2016.08.026
24. Shah B, Lutter D, Tsytsyura Y, Glyvuk N, Sakakibara A, Klingauf J, et al. Rap1 GTPases are master regulators of neural cell polarity in the developing neocortex. *Cerebr Cortex.* (2017) 27:1253–69. doi: 10.1093/cercor/bhv341
25. Nikulina E, Gkioka V, Siddiq M, Mellado W, Hilaire M, Cain C, et al. Myelin-associated glycoprotein inhibits neurite outgrowth through inactivation of the small GTPase Rap1. *FEBS Lett.* (2020) 594:1389–402. doi: 10.1002/1873-3468.13740
26. Yin N, Hong X, Han Y, Duan Y, Zhang Y, Chen Z. Cortex Mori Radicis Extract induces neurite outgrowth in PC12 cells activating ERK signal pathway via inhibiting Ca(2+) influx. *Int J Clin Exp Med.* (2015) 8:5022–32. doi: 10.3892/mmr.2019.10839
27. Baron J, Blex C, Rohrbeck A, Rachakonda S, Birnbaumer L, Ahnert-Hilger G, et al. The α-subunit of the trimeric GTPase Go2 regulates axonal growth. *J Neurochem.* (2013) 124:782–94. doi: 10.1111/jnc.12123
28. Guimond M, Wallinder C, Alterman M, Hallberg A, Gallo-Payet N. Comparative functional properties of two structurally similar selective nonpeptide drug-like ligands for the angiotensin II type-2 (AT(2)) receptor. Effects on neurite outgrowth in NG108-15 cells. *Euro J Pharmacol.* (2013) 699:160–71. doi: 10.1016/j.ejphar.2012.11.032
29. Guimond M, Roberge C, Gallo-Payet N. Fyn is involved in angiotensin II type 2 receptor-induced neurite outgrowth, but not in p42/p44mapk in NG108-15 cells. *Mol Cell Neurosci.* (2010) 45:201–12. doi: 10.1016/j.mcn.2010.06.011
30. Spilker C, Kreutz M. RapGAPs in brain: multipurpose players in neuronal Rap signalling. *Eur J Neurosci.* (2010) 32:1–9. doi: 10.1111/j.1460-9568.2010.07273.x
31. Lin Y, Yamahashi Y, Kuroda K, Faruk M, Zhang X, Yamada K, et al. Accumbal D2R-medium spiny neurons regulate aversive behaviors through PKA-Rap1 pathway. *Neurochem Int.* (2021) 143:104935. doi: 10.1016/j.neuint.2020.104935
32. Fu Z, Lee S, Simonetta A, Hansen J, Sheng M, Pak D. Differential roles of Rap1 and Rap2 small GTPases in neurite retraction and synapse elimination in hippocampal spiny neurons. *J Neurochem.* (2007) 100:118–31. doi: 10.1111/j.1471-4159.2006.04195.x
33. Kitayama H, Matsuzaki T, Ikawa Y, Noda M. Genetic analysis of the Kirsten-ras-revertant 1 gene: potentiation of its tumor suppressor activity by specific point mutations. *Proc Natl Acad Sci USA*. (1990) 87:4284–8. doi: 10.1073/pnas.87.11.4284
34. Cho Y, Lim H, Jang H, Kim K, Choi J, Shin C, et al. A follow-up study of the association between mobile phone use and symptoms of ill health. *Environ Health Toxicol.* (2016) 32:e2017001. doi: 10.5620/eht.e2017001
35. Gao T, Li J, Zhang H, Gao J, Kong Y, Hu Y, et al. The influence of alexithymia on mobile phone addiction: the role of depression, anxiety and stress. *J Affect Disord.* (2018) 225:761–6. doi: 10.1016/j.jad.2017.08.020
36. Narayanan S, Mohapatra N, John PKN, Kumar R, Nayak S, et al. Radiofrequency electromagnetic radiation exposure effects on amygdala morphology, place preference behavior and brain caspase-3 activity in rats. *Environ Toxicol Pharmacol.* (2018) 58:220–9. doi: 10.1016/j.etap.2018.01.009
37. Lee A, Park J, Hong S, Taki M, Wake K, Wiart J, et al. Brain SAR of average male Korean child to adult models for mobile phone exposure assessment. *Phys Med Biol.* (2019) 64:045004. doi: 10.1088/1361-6560/aafcdc

38. Kim H, Triplet E, Radulovic M, Bouchal S, Kleppe L, Simon W, et al. The thrombin receptor modulates astroglia-neuron trophic coupling and neural repair after spinal cord injury. *Glia.* (2021). doi: 10.1002/glia.24012
39. Damenti M, Coceano G, Pennacchietti F, Bodén A, Testa I. STED and parallelized RESOLFT optical nanoscopy of the tubular endoplasmic reticulum and its mitochondrial contacts in neuronal cells. *Neurobiol Dis.* (2021) 155:105361. doi: 10.1016/j.nbd.2021.105361
40. Jeanne M, Demory H, Moutal A, Vuillaume M, Blesson S, Thépault R, et al. Missense variants in DPYSL5 cause a neurodevelopmental disorder with corpus callosum agenesis and cerebellar abnormalities. *Am J Hum Genet.* (2021) 108:951–61. doi: 10.1016/j.ajhg.2021.04.004
41. Kim J, Lee J, Kim H, Kim K, Kim H. Possible effects of radiofrequency electromagnetic field exposure on central nerve system. *Biomol Ther.* (2019) 27:265–75. doi: 10.4062/biomolther.2018.152
42. Gökçek-Saraç Ç, Er H, Kencebay Manas C, Kantar Gok D, Özen S, Derin N. Effects of acute and chronic exposure to both 900 MHz and 2100 MHz electromagnetic radiation on glutamate receptor signal pathway. *Int J Radiat Biol.* (2017) 93:980–9. doi: 10.1080/09553002.2017.1337279
43. Guidelines for Limiting Exposure to Electromagnetic Fields (100 kHz to 300 GHz). *Health phys.* (2020) 118:483–524. doi: 10.1097/HP.0000000000001210
44. Kim J, Jeon S, Choi H, Lee J, Bae J, Kim N, et al. Exposure to long-term evolution radiofrequency electromagnetic fields decreases neuroblastoma cell proliferation via Akt/mTOR-mediated cellular senescence. *J Toxicol Environ Health A.* (2021) 84:1–12. doi: 10.1080/15287394.2021.1944944
45. Zuo W, Hu Y, Yang Y, Zhao X, Zhang Y, Kong W, et al. Sensitivity of spiral ganglion neurons to damage caused by mobile phone electromagnetic radiation will increase in lipopolysaccharide-induced inflammation *in vitro* model. *J Neuroinflammation.* (2015) 12:105. doi: 10.1186/s12974-015-0300-1
46. Kim J, Huh Y, Kim H. Trafficking of synaptic vesicles is changed at the hypothalamus by exposure to an 835 MHz radiofrequency electromagnetic field. *Gen Physiol Biophys.* (2019) 38:379–88. doi: 10.4149/gpb_2019020
47. Wang N, Dhumale P, Chiang J, Püschel A. The Sema3A receptor Plexin-A1 suppresses supernumerary axons through Rap1 GTPases. *Sci Rep.* (2018) 8:15647. doi: 10.1038/s41598-018-34092-5
48. Kermath B, Vanderplow A, Bjornson K, Seablom E, Novak A, Bernhardt C, et al. The Rap1 small GTPase is a critical mediator of the effects of stress on prefrontal cortical dysfunction. *Mol Psychiatry.* (2020) 26:3223–39. doi: 10.1038/s41380-020-0835-0
49. Araki Y, Hong I, Gamache T, Ju S, Collado-Torres L, Shin J, et al. SynGAP isoforms differentially regulate synaptic plasticity and dendritic development. *ELife.* (2020) 9:E56273. doi: 10.7554/eLife.56273
50. Chen Y, Wang P, Ghosh A. Regulation of cortical dendrite development by Rap1 signaling. *Mol Cell Neurosci.* (2005) 28:215–28. doi: 10.1016/j.mcn.2004.08.012
51. Kosuru R, Chrzanowska M. Integration of Rap1 and calcium signal. *Int J Mol Sci.* (2020) 21:1616. doi: 10.3390/ijms21051616
52. Kusakabe M, Hasegawa Y. Nimodipine promotes neurite outgrowth and protects against neurotoxicity in PC12 cells. *Iran J Basic Med Sci.* (2021) 24:51–7. doi: 10.22038/ijbms.2020.48567.11152
53. Kurooka T, Yamamoto Y, Takai Y, Sakisaka T. Dual regulation of RA-RhoGAP activity by phosphatidic acid and Rap1 during neurite outgrowth. *J Biol Chem.* (2011) 286:6832–43. doi: 10.1074/jbc.M110.183772
54. Hisata S, Sakisaka T, Baba T, Yamada T, Aoki K, Matsuda M, et al. Rap1-PDZ-GEF1 interacts with a neurotrophin receptor at late endosomes, leading to sustained activation of Rap1 and ERK and neurite outgrowth. *J Cell Biol.* (2007) 178:843–60. doi: 10.1083/jcb.200610073
55. McAvoy T, Zhou M, Greengard P, Nairn A. Phosphorylation of Rap1GAP, a striatally enriched protein, by protein kinase A controls Rap1 activity and dendritic spine morphology. *Proc Natl Acad Sci USA.* (2009) 106:3531–6. doi: 10.1073/pnas.0813263106
56. Beaudry H, Gendron L, Guimond M, Payet M, Gallo-Payet N. Involvement of protein kinase C alpha (PKC alpha) in the early action of angiotensin II type 2 (AT2) effects on neurite outgrowth in NG108-15 cells: AT2-receptor inhibits PKC alpha and p21ras activity. *Endocrinology.* (2006) 147:4263–72. doi: 10.1210/en.2006-0411
57. Echeverria V, Ducatenzeiler A, Chen C, Cuello A. Endogenous beta-amyloid peptide synthesis modulates cAMP response element-regulated gene expression in PC12 cells. *Neuroscience.* (2005) 135:1193–202. doi: 10.1016/j.neuroscience.2005.06.057
58. York R, Yao H, Dillon T, Ellig C, Eckert S, McCleskey E, et al. Rap1 mediates sustained MAP kinase activation induced by nerve growth factor. *Nature.* (1998) 392:622–6. doi: 10.1038/33451
59. Jeon C, Moon M, Kim J, Kim H, Kim J, Li Y, et al. Control of neurite outgrowth by RhoA inactivation. *J Neurochem.* (2012) 120:684–98. doi: 10.1111/j.1471-4159.2011.07564.x
60. Tremblay R, Sikorska M, Sandhu J, Lanthier P, Ribecco-Lutkiewicz M, Bani-Yaghoub M. Differentiation of mouse Neuro 2A cells into dopamine neurons. *J Neurosci Methods.* (2010) 186:60–7. PubMed PMID: 1990349 doi: 10.1016/j.jneumeth.2009.11.004
61. Schuderer J, Samaras T, Oesch W, Spat D, Kuster N. High peak SAR exposure unit with tight exposure and environmental control for *in vitro* experiments at 1800 MHz. *IEEE Trans Microw Theory Tech.* (2004) 52:2057–66. doi: 10.1109/TMTT.2004.832009
62. Labelle C, Leclerc N. Exogenous BDNF, NT-3 and NT-4 differentially regulate neurite outgrowth in cultured hippocampal neurons. *Brain Res Dev Brain Res.* (2000) 123:1–11. doi: 10.1016/S0165-3806(00)00069-9
63. Veeranna, Amin N, Ahn N, Jaffe H, Winters C, Grant P, et al. Mitogen-activated protein kinases (Erk1,2) phosphorylate Lys-Ser-Pro (KSP) repeats in neurofilament proteins NF-H and NF-M. *J Neurosci.* (1998) 18:4008–21. doi: 10.1523/JNEUROSCI.18-11-04008.1998
64. Zhang G, Kimura S, Murao K, Yu X, Obata K, Matsuyoshi H, et al. Effects of angiotensin type I receptor blockade on the cardiac Raf/MEK/ERK cascade activated via adrenergic receptors. *J Pharmacol Sci.* (2010) 113:224–33. doi: 10.1254/jphs.09336fp

Conflict of Interest: The authors declare that the research was conducted in the absence of any commercial or financial relationships that could be construed as a potential conflict of interest.

Publisher's Note: All claims expressed in this article are solely those of the authors and do not necessarily represent those of their affiliated organizations, or those of the publisher, the editors and the reviewers. Any product that may be evaluated in this article, or claim that may be made by its manufacturer, is not guaranteed or endorsed by the publisher.

frontiers in Public Health

ORIGINAL RESEARCH
published: 30 November 2021
doi: 10.3389/fpubh.2021.777798

Artificial Neural Network-Based Uplink Power Prediction From Multi-Floor Indoor Measurement Campaigns in 4G Networks

Taghrid Mazloum, Shanshan Wang*, Maryem Hamdi, Biruk Ashenafi Mulugeta and Joe Wiart*

Chaire C2M, LTCI, Télécom Paris, Institut Polytechnique de Paris, Palaiseau, France

OPEN ACCESS

Edited by:
Tongning Wu,
China Academy of Information and Communications Technology, China

Reviewed by:
Congsheng Li,
China Academy of Information and Communications Technology, China
Fatemeh Ghasemifard,
Ericsson, Sweden

****Correspondence:***
Shanshan Wang
shanshan.wang@telecom-paris.fr
Taghrid Mazloum
taghrid.mazloum@telecom-paris.fr

Specialty section:
This article was submitted to Radiation and Health, a section of the journal Frontiers in Public Health

Received: *15 September 2021*
Accepted: *18 October 2021*
Published: *30 November 2021*

Citation:
Mazloum T, Wang S, Hamdi M, Ashenafi Mulugeta B and Wiart J (2021) Artificial Neural Network-Based Uplink Power Prediction From Multi-Floor Indoor Measurement Campaigns in 4G Networks. Front. Public Health 9:777798. doi: 10.3389/fpubh.2021.777798

Paving the path toward the fifth generation (5G) of wireless networks with a huge increase in the number of user equipment has strengthened public concerns on human exposure to radio-frequency electromagnetic fields (RF EMFs). This requires an assessment and monitoring of RF EMF exposure, in an almost continuous way. Particular interest goes to the uplink (UL) exposure, assessed through the transmission power of the mobile phone, due to its close proximity to the human body. However, the UL transmit (TX) power is not provided by the off-the-shelf modem and RF devices. In this context, we first conduct measurement campaigns in a multi-floor indoor environment using a drive test solution to record both downlink (DL) and UL connection parameters for Long Term Evolution (LTE) networks. Several usage services (including WhatsApp voice calls, WhatsApp video calls, and file uploading) are investigated in the measurement campaigns. Then, we propose an artificial neural network (ANN) model to estimate the UL TX power, by exploiting easily available parameters such as the DL connection indicators and the information related to an indoor environment. With those easy-accessed input features, the proposed ANN model is able to obtain an accurate estimation of UL TX power with a mean absolute error (MAE) of 1.487 dB.

Keywords: EMF exposure, indoor, uplink, LTE, transmit power, artificial neural networks

1. INTRODUCTION

Human exposure to radiofrequency electromagnetic field (RF-EMF) has been addressed and monitored over the years, especially with the succession of generations of cellular networks, the massive deployment of base stations, and the exponential increase in the number of RF devices (including connected objects of the Internet of Things IoT). Such monitoring aims to verify RF-EMF compliance with international guidelines such as the ones recommended by the International Commission on Non-Ionizing Radiation Protection (ICNIRP) (1) in order to reply to public concerns on the health impact of RF-EMF exposure. The characterization of human exposure to RF-EMF could be performed by carrying out measurement campaigns (2) and simulations (3). A survey on RF-EMF exposure in indoor environments is provided in (4).

There are several ways to measure RF-EMF exposure. Downlink (DL) exposure induced by outdoor base stations (5) or indoor access points/femtocells (6) could be assessed by measuring the electric field strength using a spectrum analyzer. Moreover, uplink (UL) exposure induced by a user equipment (UE), together with the DL exposure, could be evaluated by using network-based tools that allow recording a huge amount of data related to, e.g., number of connected UEs, UE transmit (TX) power, UE received power, and throughput (7–11). However, these data are just accessible to the network operator. Nevertheless, the UL exposure could also be assessed using mobile-phone based tools, such as a drive test solution (12, 13), and android-based applications, such as XMobiSense (14, 15). The former enables recording network information of air interface and mobile application quality-of-service and quality-of-experience, such as the Nemo Handy from KeySight Technologies (16). While drive test solutions are very expensive and not accessible for the public to perform daily personal measurements, android-based applications (e.g., XMobiSense) allow measuring several parameters but not the TX power nor throughput. Nonetheless, a specific equipment (i.e., OPTis-P8E, Innowireless Co., Ltd.) with a control software is also used for the recording of both DL and UL EMF exposure, even in fifth generation (5G) new radio environment (17, 18).

Recently, machine learning (ML) and artificial neural networks (ANNs) are intensively applied in the 5G cellular networks and beyond. The potential of ML and ANN are also being investigated in the field of RF propagation and human exposure to RF-EMF. From the DL point of view, the exposure map of the 14*th* district of Paris was built using a hybrid connected ANN, which is trained with both simulated drive test and sensor network measurements (19). In (20), a simple feed forward ANN was proposed for multi-source indoor WiFi scenarios, where three access points and several WiFi clients were distributed in the floor layout of the building. Both DL and UL exposure were evaluated by feeding the ANN model with position and type of WiFi sources, position and material characteristics of walls. The collection of data about the electric field strength (i.e., the ground truth) was performed through simulations according to a deterministic method. In (21), the UL exposure due to 4G connections is assessed by predicting the UE TX power using three different ML algorithms and by changing the set of input parameters. The ground truth was obtained through conducting measurement campaigns while driving a car in Germany. Different from an outdoor scenario, the indoor environment is much more complicated due to the existence of multi walls, multi floors, furniture and their different penetration losses. The challenges are how to incorporate the uncertainty caused by real-life indoor measurements and how to extract key features that affect UE TX power from measured network parameters as well as the indoor environments.

In this paper, we propose a feed-forward ANN model that allows predicting the UE TX power, while training the model with measurement data in an indoor environment. The Nemo Handy is used to collect data on each floor of a residential building, while it is connected to a 4G outdoor base station. Several usage services were scheduled on the Nemo Handy: WhatsApp voice calls, WhatsApp video calls, and file uploading to Dropbox. The possible parameters from the DL connection indicators and their correlation with TX power are analyzed. Then, the proposed prediction model is fed with the most influential and easily available input parameters that are recorded by the Nemo Handy, but also could be available from android-based mobile phone applications. Such input parameters reveal information about DL network connection, in addition to other parameters related to the environment. The difficulty remains in using measurement data instead of simulated data since we are not able to control the measurement results. Indeed, we do not control and manage the Nemo Handy since we do not know exactly how the recorded values are computed, as explained in section 2. Consequently, we tested different averaging duration of the measurement data to find a balance of removing noise of measurement and keep enough amount of measurement data. The performance of ANN models from the averaging duration of measurement data over 1, 3, and 5 s are compared. The results show averaging measurement data for 5 s can provide the best prediction accuracy with a mean absolute error (MAE) of 1.487 dB.

To the author's knowledge and according to the literature, very rare works investigate ML and ANN methods for the prediction of the LTE UE TX power from real empirical data. Accordingly, the main contributions of this work are the following:

1. The proposal of drive test measurement protocol considering various usage services over LTE connections, including WhatsApp voice calls, WhatsApp video calls, and file uploading.
2. The proposal and performing of multi-floor indoor measurement campaigns of both DL and UL LTE connections.
3. The proposal and validation of a simple feed-forward ANN model with easy-accessed input feature to predict LTE UE TX power from indoor empirical data.

The paper is organized as follows: section 2 presents the material used and describes the measurement and the data collection. Section 3 explains the proposed ANN model that is used to predict the UE TX power over 4G connections. Section 4 presents the results of the measurement analysis as well as the TX power estimation of the ANN model. Section 5 discusses and compares the results with related works. It also presents some future works. Section 6 gives the conclusion.

2. MATERIALS AND MEASUREMENT DESCRIPTION

2.1. UL Power Control Mechanism

The UE TX power P_{TX} (in dBm) is set through a power control algorithm according to the 3rd Generation Partnership Project (3GPP) LTE specification 36.213, as follows (22):

$$P_{TX} = min\{P_{max}, P_0 + 10Log_{10}(M) + \alpha PL + \Delta_{MCS} + \delta\}, \quad (1)$$

where

- P_{max} is the maximum allowed TX power, which is equal to 23 dBm for class 3 UE.

FIGURE 1 | Measurement environment. From **left** to **right**: Front look, Base station, Floor 5, Floor 6.

- P_0 is a cell specific parameter that represents the requested signal to interference and noise ratio per physical resource block for the reception at the base station side.
- M is the number of physical resource blocks allocated to the UE. It depends on the UE usage service and the cell traffic load.
- α is a cell specific parameter representing the path loss compensation factor.
- PL is the DL path loss estimated by the UE based on the reference signal received power (RSRP) or the received signal strength indicator (RSSI).
- Δ_{MCS} is a specific modulation and coding scheme factor.
- δ is a closed loop correction value that aims to compensate the fast fading variation.

2.2. Measurement Description and Protocol

We carried out measurement campaigns in a 6-floor residential building in May and August 2021. At each floor level (from ground floor to floor 6), one measurement location is considered, which corresponds to almost the same relative position in corridor of the stairs. The measurements were repeated 3 times over the journey: in the morning (10–11 a.m.), at noon (12–2 p.m.), and in the afternoon (4–5 p.m.), in order to take into consideration the time-varying traffic of the connected base station. We note that the measurements at night, which have the lowest traffic load (23), were not performed due to the requirement of human intervention. **Figure 1** shows the measurement environment. The residence from outside and the closest base station are, respectively, shown in the left two figures. The location of measurement inside the building on floors 5 and 6 are, respectively, shown in the right two figures. The floor plans from floor 1 to 5 are identical. It is noteworthy that the residence is very close to a base station. We aim to conduct the measurements at different floors to take into account the impact of the elevation plane and the elevation angle of the base station antenna. In other words, how does the UL exposure vary with respect to the floor level?

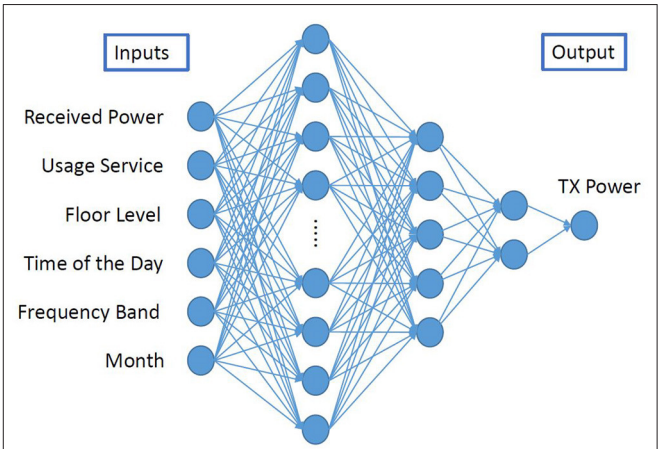

FIGURE 2 | Artificial neural network structure.

We focus in this work on predicting the UE UL TX power while connected to 4G networks. To this end, we need to gather data about the UE UL power as well as other parameters influencing it (as explained in section 3.1). The UE UL power is recorded using dedicated drive test mobile phone solutions. Accordingly, the Nemo Handy from KeySight Technologies (16) is used in our measurement campaigns in order to log data about the UE TX power and other network parameters. The Nemo Handy is equipped on a Samsung Galaxy S20+ 5G. It supports frequency bands from 2G to 5G NR networks (up to 40 GHz).

Moreover, Nemo Handy allows scheduling certain usage services by creating scripts. Indeed, it records network parameters and saves log files while running these scripts. This is crucial because the UE UL power depends on the usage service. In our measurement campaigns, we lock the Nemo Handy to 4G networks, without locking to a given frequency band. The Nemo Handy is scheduled to run automatically the following usage services:

1. WhatsApp voice call: It is a voice over IP (VoIP) service. It is performed by emitting a voice using a speaker. The voice is reading a well-formatted text with almost 50% silence. The duration of the voice call is 2 min.
2. WhatsApp video call: The same settings are considered for the WhatsApp voice call.
3. Data upload: A 200-MB file is uploaded to Dropbox. The duration of uploading such a file depends on the network quality. In our case, it varies between almost 3 and 12 min.

We note that we mimic a realistic usage scenario during the measurements. The mobile phone was held by the experimenter at a height of about 1 m.

After carrying out the measurements, we use the Nemo outdoor software (installed on a laptop) in order to extract from the log files several parameters, mainly the following data: the UE TX power, the RSRP, and RSSI. All these powers were recorded in dBm. Moreover, we extract the physical cell identity (PCI) of the connected base station in order to check if the active base station remains the same in all the measurements. We are not able to locate the connected base station since its PCI is not accessible to public. It is just known by the network operator. Furthermore, we note that Nemo sampling method of the recorded data is unknown. The number of samples per second is not constant, it changes between 0 and 5 samples per second. Indeed, it is not possible to know how the Nemo computes the recorded values: if they are instantaneous values, averaged values over how the long sample period, etc. Therefore, we decided to compute average values over different time periods (i.e., 1, 3, and 5 s) and compare the corresponding performance. The processing and analysis of extracted parameters, as well as building ANN using them, are provided in section 4.

TABLE 1 | Input parameters of ANN.

Input parameter	Value	Influence and significance
RSRP (dBm)	[−140,−44]	Signal quality, path loss distance to base station
RSSI (dBm)	[−113, −51]	Signal quality, path loss, interference distance to base station
Usage service	WhatsApp voice call WhatsApp Video call Data upload	Amount and rate of data
Floor level	0, 1, 2, 3, 4, 5, 6	Antenna elevation angle, environment
Time of the day	Morning, noon, and afternoon	Base station traffic load, environment
Frequency band (MHz)	1,800, 2,100, 2,600	Environment
Month	May, August	Base station traffic load, environment

3. ANN MODEL FOR TX POWER ESTIMATION

A classic feed-forward neural network is built to predict UL TX power in this work. The detailed network structure can be found in **Figure 2**. The input layer takes six features related to DL network connections and information from the measurement environment. Then three fully connected layers with decreasing number of neurons (10, 5, and 2) are followed after the input layer. The hyper-parameters of ANN used in the current paper, including the number of layers and neurons, are determined according to grid search methods. An exponential learning rate decay scheduler is adopted to help the optimization. A large initial learning rate can speed up the training and prevent the model from being trapped in local minima. However, it may cause high oscillation in minimizing the loss function. On the other hand, a small learning rate makes the ANN model converge slower and may end up with local minima. Therefore, a reducing

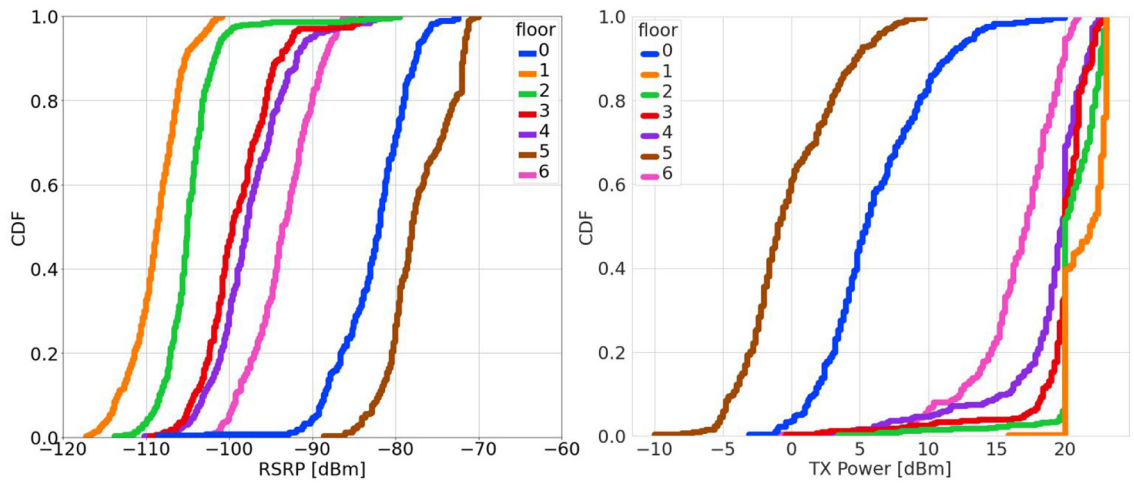

FIGURE 3 | Statistical distribution of reference signal received power (RSRP) and transmit (TX) power at different floors.

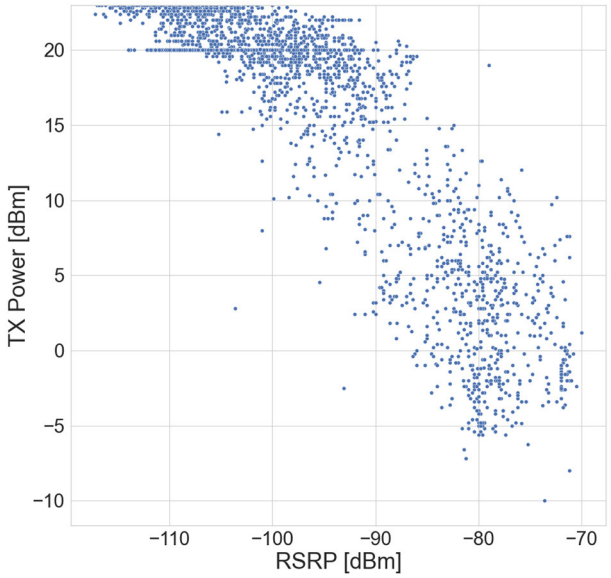

FIGURE 4 | Statistical correlation between Tx power and RSRP.

TABLE 2 | Pearson correlation coefficient between inputs and target TX power for different averaging durations.

	Average over 1 s	Average over 3 s	Average over 5 s
RSRP [dBm]	−0.811	−0.865	−0.876
RSSI [dBm]	−0.793	−0.854	−0.865
Usage service	0.138	0.209	0.224
Floor level	−0.149	−0.227	−0.241
Time of the day	0.015	0.012	0.009
Frequency band	−0.184	−0.192	−0.184
Month	0.145	0.202	0.224

learning rate scheduler is applied, in order to help the ANN model converge fast and smoothly.

3.1. Inputs of ANN

The inputs of the ANN with their typical values and significance are shown in **Table 1**. According to section 2.1, the UE TX power depends on the DL path loss, which is estimated by the UE based on RSRP and/or RSSI. Consequently, RSRP and RSSI are preferred to be used as input for the prediction of the TX power. While RSRP is a parameter that could be available from off-the-shelf commercial devices (e.g., android-based applications such as XMobiSense), RSSI is not always available and it depends on the version of the android operating system (24). Therefore, in order to address the impact of the RSSI on the UL TX power estimation, we decided to build two ANN models with different combinations of inputs, either RSRP or both RSRP and RSSI as inputs while keeping all the other parameters from **Table 1** unchanged.

According to Equation (1), the UE TX power also depends on the number of resource blocks M, which is not accessible via android-based applications. However, the dependence of M on the UE usage service implies the selection of the latter parameter as an alternative input to the ANN. The other parameters from **Table 1** are the features that can represent an unique property of measurement. The input "floor level" also reflects information about the path loss and the antenna elevation angle. The string values are transformed according to their type to numerical values that can be processed by the ANN. For example, the input parameter "time of the day" includes morning, noon, and afternoon that are transformed into 0, 1, and 2, respectively.

TABLE 3 | Hyper-parameters of ANN.

Hyper-parameters	Value
learning rate	$lr = lr_0 \exp(-kt), lr_0 = 0.03, k = 0.01$
Optimizer	Adam
Activation	"elu" (hidden layers), "linear" (output layer)
Weight initializer	he_uniform
epoch	150
Batch size	48
Loss function	MSE
Train : Validation : Test	0.8 : 0.2 : 0.2

TABLE 4 | Performance comparison with different inputs.

	RSSI	RSRP	RSSI+RSRP
MAE [dB]	1.663	1.487	1.558
RMSE [dB]	2.501	2.365	2.394
R^2	0.902	0.912	0.910

TABLE 5 | Performance comparison between different averaging duration.

	Average over 1 s (8,238)	Average over 3 s (4,044)	Average over 5 s (2,510)
MAE [dB]	2.334	1.791	1.487
RMSE [dB]	3.577	2.650	2.365
R^2	0.831	0.897	0.912

3.2. Assessment of Prediction Accuracy

The performance of ANN is evaluated by three metrics, MAE, root mean squared error (RMSE), and R-Squared (R^2). Both MAE and RMSE are computed in dB. Here, smaller values of MAE and RMSE indicate more accurate predictions. R^2 measures how close the ground truth and predictions are in terms of statistical distribution. While the perfect prediction would result in an R^2 value of 1, the most poor fitting results in an R^2 value approaching 0. R^2 is defined as follows:

$$R^2 = 1 - \frac{RSS}{TSS} \tag{2}$$

where RSS and TSS represent, respectively, the residual sum of squares and the total sum of squares.

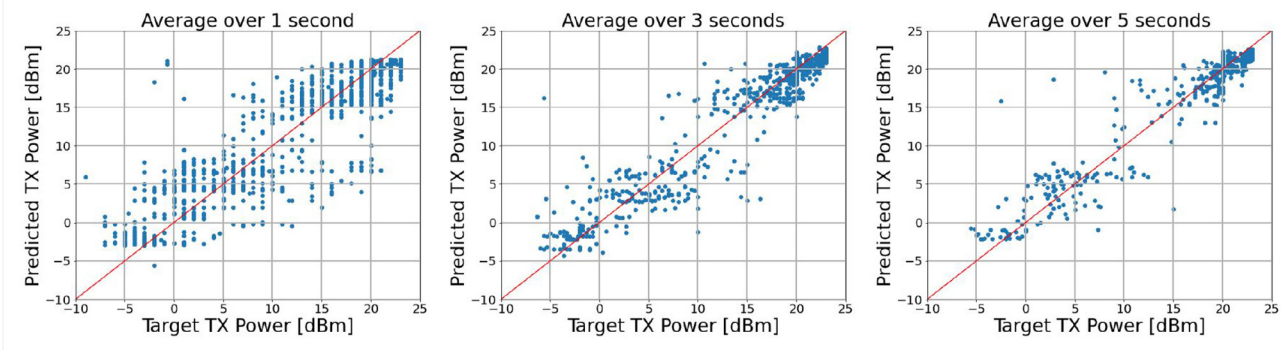

FIGURE 5 | Scattering plots between predictions and true values.

4. RESULTS

4.1. Measurement Analysis

Figure 3 shows the cumulative distribution function (CDF) of the RSRP and TX power variations at each floor, after aggregating all the usage services data at any time. The highest RSRP values are shown for floor 5, which means the lowest path loss and the best propagation condition. This may be due to the fact that the main gain of the active antenna base station is directed toward floor 5. The antenna gain will decrease with the antenna elevation angle and floors 1–5 have almost the same layout. This is supported by the observations in the **Figure 3** that start from floor 5, except the ground floor (i.e., floor 0), decreasing or increasing the floor level will obviously yield a decrease in the RSRP values. The RSRP values on floor 6 are higher than the others due to a glass window on the roof, which permits to pass more of electromagnetic waves. Furthermore, the ground floor provides very high RSRP values, which are very close to those of floor 5. The difference in the median is less than 4 dB. This is explained by the different layout of the ground floor, where we have the entrance of the building with two glass doors. Consistent results are shown with the statistical distribution of TX powers. We note, after checking with Nemo Handy, that all the measurements occur with the same connected base station.

The statistical correlation between the UE TX power and RSRP for all the measurement data is presented in **Figure 4**. Similar behavior is observed for the correlation between TX power and RSSI. Obviously, as RSRP/RSSI increases, the DL path loss decreases, and consequently TX power decreases. For each RSRP value, the variation in the TX power is due to other parameters involved in the UL power control algorithm (Equation 1), which are not accessible. However, those parameters are directly or indirectly influenced by the selected input parameters, whose correlations with TX power are shown in **Table 2**. We note that the Pearson correlation reflects the linear relationship between the parameters and does not reveal deeper correlations. All these reasons strengthen the requirement of the ANN model for the prediction of UE TX power, which is crucial for UL RF-EMF exposure assessment.

4.2. Implementation and Performance of ANN

As mentioned in section 3, the hyper-parameters of ANN are determined according to grid search methods. The neural network is trained with different potential combinations of hyper-parameters. Indeed, the optimal set of hyper-parameters with the best three-fold cross validation performance is selected. Accordingly, the hyper-parameters used in the current work are given in **Table 3**. In the pre-processing of measurement data, we remove the duplicates where we have the same inputs and outputs data set. Then, "RobustScaler" is used to scale the input features with outliers since it removes the median and scales the data according to the quantile range.

After implementing ANN, we first compare the performance from models trained with different combinations of RSSI and RSRP. Here, measurement data are averaged over 5 s and split into training and testing with the ratio of 80 and 20%. Results in **Table 4** show that all three models have almost the same prediction performance, which is consistent with the strong correlation between RSSI/RSRP and TX power as shown in **Table 2**. Moreover, RSSI and RSRP carry redundant information. Therefore, as explained in section 3.1, only RSRP is kept as an input feature in the following model due to its easy accessibility and strong correlation.

Since the measurement data exported from Nemo Handy gives approximately 0–5 samples per second, we pre-process the data by computing average values over 1, 3, and 5 s. From **Table 2**, the correlation between inputs and target TX power is stronger with the increase of averaging duration. This implies that the corresponding prediction results in terms of MAE, RMSE, and R^2 reveal the same improvement, as shown in **Table 5**. Consistently, the scattering plots in **Figure 5** show that a tighter prediction is obtained with the increase of averaging duration. More clearly, the problem of vertical lines with dots from the left figure, which is caused by noise in the input data, is solved. However, we

only did the averaging up to 5 s due to the limited number of measurement data (number of datasets after removal of duplicates are shown in **Table 5**).

5. DISCUSSION

To the authors' knowledge, very rare works investigate building ML or ANN models based on real measurement data for the estimation of the LTE UE TX power. Similar work is done in (21) but with drive testing measurement data in outdoor environments. For the estimation of the UL TX power, they use and compare three ML methods and test different input sets. They consider uploading a file of three different sizes (i.e., 1, 3, and 5 MB) to a web server via Hypertext Transfer Protocol (HTTP), while we consider in our work more different usage services. We note that the lowest MAE in (21) is 3.166 dB with a full featured model. It raises to 4.33 dB when limiting the input features to RSRP, upload size, and velocity.

The main novelty of the current work is the exploitation of the ANN model for the LTE TX power prediction from measurement data in multi-floor indoor environments. Measurement campaigns have been carried out on a single location at each floor of a 6-floor residential building. While using several usage services (i.e., WhatsApp voice and video calls, file uploading via DropBox), data on UE TX power and input features, such as RSRP, are collected. The results are very promising with a MAE of 2.334 dB. Indeed, we believe that the proposed model has high potential in applying to more general scenarios. As shown in **Table 2**, UE TX power is closely dependent on the DL received power, which is RSSI or RSRP in our study. This strong correlation guarantees an acceptable prediction. So, the difficulty is to further improve the prediction performance by taking into account the varying environments. Even though measurement campaigns are very time-consuming and complicated to perform in indoor environments, more measurements are required to cover several location points on the same floor. More input features related to the floor layout, such as the number of walls, the number of windows and their penetration losses, should be considered in future work. Moreover, data should be collected over several months in order to account for the seasonality of the traffic. Last and not least, the model can include more usage services, such as voice over LTE (VoLTE).

6. CONCLUSION

The evaluation of UE TX power is very crucial for the assessment of the UL RF-EMF exposure. However, recording UE TX power requires specific equipment and carrying out measurement campaigns is complicated and time-consuming. Therefore, we aim in the present work to predict the LTE UE TX power by investigating the ANN model with easily available input features, for multi-floor indoor measurement data. First, the LTE network parameters in the indoor environment with an outdoor connected base station are collected using a specific handheld measurement device, i.e., Nemo Handy. The correlation between the DL network parameters and the target TX power are analyzed. Both DL received power indicators, RSSI and RSRP, have a strong correlation with TX power. Accordingly and since RSRP is easily available, we build a feed-forward ANN model with RSRP as input together with other parameters influencing the TX power and related to the measurement environment. Afterward, the influence of averaging duration in the data pre-processing, e.g., 1, 3, and 5 s, on the prediction accuracy is compared. The results show that averaging over 5 s for measurement data keeps a good trade-off between noise removal and a sufficient number of training data, which also has best prediction accuracy in terms of MAE, RMSE, and R^2.

DATA AVAILABILITY STATEMENT

The raw data supporting the conclusions of this article will be made available by the authors, without undue reservation.

AUTHOR CONTRIBUTIONS

TM and SW conceived and wrote the manuscript. TM and MH designed and conducted the measurement campaigns. MH, SW, TM, and BA analyzed measurement and built ANN model. TM, SW, and JW reviewed the paper. All authors listed have made a substantial, direct, and intellectual contribution to the work and approved it for publication.

FUNDING

The current work was partly supported by the following ANSES projects: EXPO-ENFANT (ref: 2018/RF/031) and SPUTNIC (ref: 2017/RF/017).

REFERENCES

1. ICNIRP. Guidelines for limiting exposure to electromagnetic fields (100 kHz to 300 GHz). *Health Phys*. (2020). 118:483–524. doi: 10.1097/HP.0000000000001210
2. Yang L, Zhang C, Chen Z, Li C, Wu T. Functional and network analyses of human exposure to long-term evolution signal. *Environ Sci Pollut Res*. (2021) 28:5755–73. doi: 10.1007/s11356-020-10728-w
3. Li C, Xu C, Wang R, Yang L, Wu T. Numerical evaluation of human exposure to 3.5-GHz electromagnetic field by considering the 3GPP-like channel features. *Ann Telecommun*. (2019) 74:25–33. doi: 10.1007/s12243-018-0682-z
4. Chiaramello E, Bonato M, Fiocchi S, Tognola G, Parazzini M, Ravazzani P, et al. Radio frequency electromagnetic fields exposure assessment in indoor environments: a review. *Int J Environ Res Public Health*. (2019) 16:955. doi: 10.3390/ijerph16060955
5. Onishi T, Ikuyo M, Tobita K, Liu S, Taki M, Watanabe S. Radiofrequency exposure levels from mobile phone base stations in outdoor environments and an underground shopping mall in Japan. *Int J Environ Res Public Health*. (2021) 18:8068. doi: 10.3390/ijerph18158068
6. Moraitis N, Popescu I, Nikita KS. Frequency selective EMF measurements and exposure assessment in indoor office environments. In: *14th European Conference on Antennas and Propagation (EuCAP)*. Copenhagen: IEEE (2020). p. 1–5. doi: 10.23919/EuCAP48036.2020.9135502

7. Lonn S, Forssen U, Vecchia P, Ahlbom A, Feychting M. Output power levels from mobile phones in different geographical areas; implications for exposure assessment. *Occup Environ Med*. (2004) 61:769–72. doi: 10.1136/oem.2003.012567
8. Persson T, Tornevik C, Larsson LE, Loven J. Output power distributions of terminals in a 3G mobile communication network. *Bioelectromagnetics*. (2012) 33:320–5. doi: 10.1002/bem.20710
9. Joshi P, Colombi D, Thors B, Larsson LE, Tornevik C. Output power levels of 4G user equipment and implications on realistic RF EMF exposure assessments. *IEEE Access*. (2017) 5:4545–50. doi: 10.1109/ACCESS.2017.2682422
10. Joshi P, Ghasemifard F, Colombi D, Tornevik C. Actual output power levels of user equipment in 5G commercial networks and implications on realistic RF EMF exposure assessment. *IEEE Access*. (2020) 8:204068–75. doi: 10.1109/ACCESS.2020.3036977
11. Colombi D, Joshi P, Xu B, Ghasemifard F, Narasaraju V, Tornevik C. Analysis of the actual power and EMF exposure from base stations in a commercial 5G network. *Appl Sci*. (2020) 10:5280. doi: 10.3390/app10155280
12. Mazloum T, Fetouri B, Elia N, Conil E, Grangeat C, Wiart J. Assessment of RF human exposure to LTE small-and macro-cells: UL case. In: *11th European Conference on Antennas and Propagation (EUCAP)*. Paris (2017). p. 1592–3. doi: 10.23919/EuCAP.2017.7928743
13. Mazloum T, Aerts S, Joseph W, Wiart J. RF-EMF exposure induced by mobile phones operating in LTE small cells in two different urban cities. *Ann Telecommun*. (2019) 74:35–42. doi: 10.1007/s12243-018-0680-1
14. Langer CE, de Llobet P, Dalmau A, Wiart J, Goedhart G, Hours M, et al. Patterns of cellular phone use among young people in 12 countries: implications for RF exposure. *Environ Int*. (2017) 107:65–74. doi: 10.1016/j.envint.2017.06.002
15. Mazloum T, Danjou A, Schaz J, Bories S, Huss A, Conil E, et al. XMobiSensePlus: an updated application for the assessment of human exposure to RF-EMFs. In: *23rd General Assembly and Scientific Symposium of the International Union of Radio Science*. Rome (2020). p. 1–2. doi: 10.23919/URSIGASS49373.2020.9232310
16. Nemo. *Nemo Handy Handheld Measurement Solution* (2021). Available online at: https://www.keysight.com/fr/en/product/NTH00000B/nemo-handy-handheld-measurement-solution.html (accessed September 14, 2021).
17. Lee AK, Choi HD. Brain EM Exposure for voice calls of mobile phones in wireless communication environment of Seoul, Korea. *IEEE Access*. (2020) 8:163176–85. doi: 10.1109/ACCESS.2020.3020831
18. Lee AK, Jeon SB, Choi HD. EMF levels in 5G new radio environment in Seoul, Korea. *IEEE Access*. (2021) 9:19716–22. doi: 10.1109/ACCESS.2021.3054363
19. Wang S, Wiart J. Sensor-Aided EMF Exposure assessments in an urban environment using artificial neural networks. *Int J Environ Res Public Health*. (2020) 17:3052. doi: 10.3390/ijerph17093052
20. Tognola G, Plets D, Chiaramello E, Gallucci S, Bonato M, Fiocchi S, et al. Use of machine learning for the estimation of down-and up-link field exposure in multi-source indoor WiFi scenarios. *Bioelectromagnetics*. (2021) 40:550–61. doi: 10.23919/URSIGASS51995.2021.9560437
21. Falkenberg R, Sliwa B, Piatkowski N, Wietfeld C. Machine learning based uplink transmission power prediction for LTE and upcoming 5G networks using passive downlink indicators. In: *2018 IEEE 88th Vehicular Technology Conference (VTC-Fall)*. Chicago, IL (2018). p. 1–7. doi: 10.1109/VTCFall.2018.8690629
22. ETSI, TS. *LTE: Evolved Universal Terrestrial Radio Access (E-UTRA), Physical Layer Procedures-corresponding to 3GPP TS36 213*. 3GPP TS 36.211 V13.2.0.
23. De Lellis P, Iudice FL, Pasquino N. Time-series-based model and validation for prediction of exposure to wideband radio frequency electromagnetic radiation. *IEEE Trans Instrument Meas*. (2019) 69:3198–205. doi: 10.1109/TIM.2019.2927649
24. AndroidDeveloper. *Android Developer* (2021). Available online at: https://developer.android.com/reference/android/telephony/CellSignalStrengthLte (accessed September 14, 2021).

Conflict of Interest: The authors declare that the research was conducted in the absence of any commercial or financial relationships that could be construed as a potential conflict of interest.

Publisher's Note: All claims expressed in this article are solely those of the authors and do not necessarily represent those of their affiliated organizations, or those of the publisher, the editors and the reviewers. Any product that may be evaluated in this article, or claim that may be made by its manufacturer, is not guaranteed or endorsed by the publisher.

frontiers in Public Health

ORIGINAL RESEARCH
published: 06 December 2021
doi: 10.3389/fpubh.2021.777712

Novel 60 GHz Band Spatial Synthetic Exposure Setup to Investigate Biological Effects of 5G and Beyond Wireless Systems on Human Body

Takashi Hikage[1]*, *Ryunosuke Ozaki*[1], *Tatsuya Ishitake*[2] and *Hiroshi Masuda*[2]

[1] Faculty of Information Science and Technology, Hokkaido University, Hokkaido, Japan, [2] Department of Environmental Medicine, Kurume University School of Medicine, Fukuoka, Japan

The global spread of 5th generation (5G) wireless systems causes some concern about health effects of millimeter waves (MMW). To investigate biological effects of local exposure to 5G-MMW on human body, a novel 60 GHz band exposure setup was developed, and its performance was validated. A spatial synthetic beam-type exposure setup using two dielectric lens antennas was proposed to achieve high intensity 60 GHz irradiation to the target area of human skin. Variety distributions and intensities of electromagnetic fields at the exposed area, which is modified by incident angles of the combined beams, were simulated using finite-difference time-domain methods. The exposure performance we estimated was verified by temperature elevations of surface in a physical arm-shaped silicone phantom during the MMW exposure. The interference fringes generated in the exposed area due to the combined two-directional beam radiations were observed both in the simulation and in the phantom experiment but eliminated by applying an orthogonalizing polarized feeding structure. Under these exposure conditions, the local temperature changes, which could evoke warmth sensations, were obtained at the target area of the human forearm skin, which means the achievement of exposure performance we intended.

Keywords: human exposure, millimeter-waves, biological effects, thermal perception, safety guideline

OPEN ACCESS

Edited by:
Tongning Wu,
China Academy of Information and Communications Technology, China

Reviewed by:
Yinliang Diao,
Nagoya Institute of Technology, Japan
Shanshan Wang,
Télécom ParisTech, France

***Correspondence:**
Takashi Hikage
hikage@wtemc.ist.hokudai.ac.jp

Specialty section:
This article was submitted to Radiation and Health, a section of the journal Frontiers in Public Health

Received: *15 September 2021*
Accepted: *03 November 2021*
Published: *06 December 2021*

Citation:
Hikage T, Ozaki R, Ishitake T and Masuda H (2021) Novel 60 GHz Band Spatial Synthetic Exposure Setup to Investigate Biological Effects of 5G and Beyond Wireless Systems on Human Body. Front. Public Health 9:777712. doi: 10.3389/fpubh.2021.777712

INTRODUCTION

The use of millimeter waves (MMW) such as 5th generation (5G) wireless systems and WiGig (IEEE 802.11ad) is now widely expanding. But this causes some new concerns about possible adverse health effects on the human body. To provide protection against known adverse health effects, the International Commission on Non-Ionizing Radiation Protection (ICNIRP) established guidelines (1), which specify the basic restriction values in terms of specific absorption rates (SAR, W/kg) or absorbed power density (W/m^2) for occupational or general public. For example, the restriction values in occupational and general public exposures for the local exposure (6–300 GHz) including the MMW band are 100–20 W/m^2, respectively. These restriction values are based on evidence of microwave-induced thermal effects and dosimetric findings of thermal changes (2–5) and also include the safety factor considered with the individual differences and age.

However, novel biological evidence is now required for the validation or revision of the guidelines. In particular, it is imperative to accumulate the evidence for 5G-MMW exposure because of its rapid expansion. In addition, 5G-MMW is known to be absorbed mainly into the body surface, but not penetrate into deep tissues (6). Thus, direct effects of the exposure on skin tissue or indirect effects on other physiological functions *via* the skin should be focused on. Several research groups have been exploring the biological effects of exposure to 5G-MMW so far. But these are mainly examined for eyes (7, 8) and cultured cells (9, 10). In contrast, there is little information about the effects on human body surface (6) that include the regulations of skin blood flow or sweating. Moreover, the physiological responses to the differences in intensity or signal modulation of the exposure are neither clear. Therefore, these physiological data under the 5G-MMW exposure could be helpful for the reevaluation of the safety guidelines.

There have been several technical difficulties to advance the studies on human exposure to 5G-MMW. For example, one is about the size of amplifier. A wide range of exposure intensity including high level is needed to obtain a dose-dependent response of physiological parameters. But the high-power amplifier that can generate the modulated MMW is not so very small that its installation with other experimental equipment will be trouble for a limited place of general laboratories. Another difficulty is to provide a sufficient space between the wave source and the exposure target. Some physiological parameters such as skin temperature and blood flow are observed as two-dimensional images using infrared cameras (11). In this case, a sufficient distance from the exposure systems to the target is required not to interrupt a field of vision for the camera. However, this brings a contradictory problem because the longer distance to the target attenuates of the exposure intensity.

The aim of this study was to develop exposure systems to investigate the biological effects of local 5G-MMW exposure on human skin and to validate its performance. To overcome the difficulties mentioned above, we devised a novel spatial synthetic exposure setup for 60 GHz band, which is a candidate frequency band in the 5G and beyond wireless systems. The main components of the setup were two dielectric lenses of antennas, which can irradiate focused beam on required exposure area, and parallel amplifier circuits. Using a physical phantom and human volunteers, we experimentally confirmed whether the setup provided the localized exposure without interference fringes and sufficient intensity for applying to the human study.

DEVELOPMENT OF 60 GHz BAND SPATIAL SYNTHETIC EXPOSURE SETUP

Performance Requirement for the Exposure Setup

To investigate biological effects of the local MMW exposure on human body, we have a plan to measure several physiological parameters simultaneously during the exposure. For example, skin temperature and warmth sensation are must for the evaluation to be compared with the previous study (6). Heat pain, skin blood flow, sweating, and heart rate are also the possible candidates to find the effects. In particular, the latter parameters may need higher temperature elevation than the thermal threshold in human skin (12). Moreover, changes in skin temperature and skin blood flow are most likely to be informative if they are observed as two-dimensional images by cameras.

Then, real-time measurement systems based on our previous studies (13–15) were designed for human studies under the exposure to 60 GHz MMW (**Figure 1**). However, we found that a sufficient space between the wave source and the exposure target was needed to take the two-dimensional images. Therefore, main requirements to develop our MMW exposure setup were as follows:

1) To realize highly localized MMW exposure spot on the human skin in a predetermined area with desired power densities and frequencies
2) To keep enough space between the human body and the exposure antenna for measuring temperature rise and biological reactions simultaneously in real time during the MMW exposure.

Based upon these requirements and our technical experiences, we redesigned specifications for the exposure setup construction as summarized in **Table 1**.

Evaluation of the Exposure Setup Using FDTD Method

A focused beam exposure system using a dielectric lens has been investigated (14–18) as MMW exposure equipment. In this study, a lens antenna with a focal length of 300 mm and a 3 dB beamwidth of 20 mm at 60 GHz were developed. We firstly estimated the maximum output power of MMW amplifier that was required to detect some biological effects of the exposure. Although it was observed in the exposure experiment with 28 GHz MMW, the local MMW exposure at 1,800 W/m^2 of IPD elevated about 7°C of skin temperature in the human forearm (14). Therefore, at least this IPD value was likely to be necessary to evoke changes in several physiological parameters, because the warm detection temperature was reported to be 32.2–40.7°C in the human skins of several body regions, which means the temperature rise was 0.2–8.7°C from the starting temperature of 32°C (12). Based on these findings, the maximum output power of MMW amplifier was estimated as 4 W or more in the case of using the single lens antenna of 60 GHz.

However, it was difficult to obtain a current commercially available stand-alone amplifier with such a high output power in the 60 GHz band. Even if a traveling wave tube amplifier or impact ionization avalanche transit-time diode is used, the dimensions of the exposure device will be huge. In addition, these devices are incapable of exposure using 5G/beyond 5G modulated signal and cause loud noise and

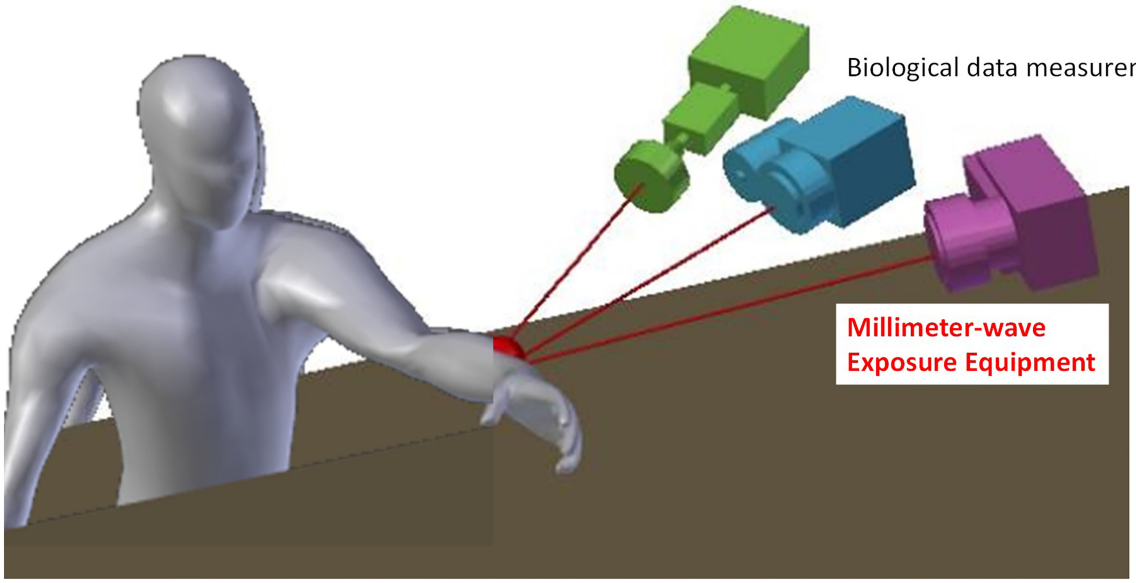

FIGURE 1 | Overview of experimental design to investigate biological effects of 60 GHz MMW exposure on human body.

TABLE 1 | Specifications for developed exposure setup.

Exposure frequency [GHz]	60 +/– 0.5
Focal length [mm]	300
Diameter of focused exposure area (@-3 dB) [mm]	20
Handling averaged power density on the exposure area [W/m^2]	0–1940

low power-handling problems. Consequently, these devices seemed to be unsuitable for experimental studies in human volunteers. Therefore, we proposed the application of a spatial synthesis beam technique that could achieve a total averaged output power of 5 W or more. **Figure 2** shows the designed block diagram of the exposure setup. The 60 GHz MMW signal from the signal generator was divided into two waveguides. Each signal was amplified, and the focused beams were radiated from the antennas with the same amplitude and phase.

However, interference fringes were generated in the exposure area when the beam radiations from two directions were combined on the spot, even if their amplitude and phase of the antenna input signal are perfectly coincident. To eliminate the interference fringes, we also proposed to apply to orthogonalize the polarization of the two antennas, as shown in **Figure 3**. We estimated electromagnetic fields on the exposure area irradiated by focused beams, using commercial finite-difference time-domain (FDTD) software (Sim4Life V 5.2.2.1924, Schmid & Partners Engineering AG, Zürich, Switzerland). Based upon the simulation results, we designed that the angle between the two lens antennas for spatial synthesis was set at 36° in considering the size of the lens antenna element and the focal length of 300 mm. Resultantly, the incident angle of each beam radiated from the antenna became not perpendicular (±18°) to the surface of exposure plane. As well known, transmission and reflection coefficients are varied depending upon the incident angle and polarization characteristics (19). We also estimated the exposure characteristics due to the polarization angle of diagonal incidence irradiation using the FDTD simulation. It was confirmed that the effect due to the different incident angles of ±18° relative to normal was approximately <0.1 dB in absorbed power density (20, 21), and it was negligible. Estimated electric field distributions on a numerical flat plate that dielectric parameter was the same as dry skin exposed to spatial synthetic beams at 60 GHz. **Figures 4A,B** show the results for applying the copolarized feed and the orthogonally polarized feed, respectively. From the figures, interference fringes in the exposure area were highly suppressed by applying orthogonalizing polarized feed. The size of the focused circle on the exposure plane was 20 mm in diameter in half-power width. We confirmed that the reason why the interference fringes were not completely suppressed was due to the crosspolarization property of the lens antenna and the reflection on the phantom surface.

ARM-SHAPED SILICONE PHANTOM FOR BASIC PERFORMANCE MEASUREMENT

A solid phantom material composed of carbon nanotubes, silicone rubber, and carbon black (CB) was developed to evaluate the basic performance of the developed 60 GHz band exposure setup. By using the novel phantom, it can be safely confirmed

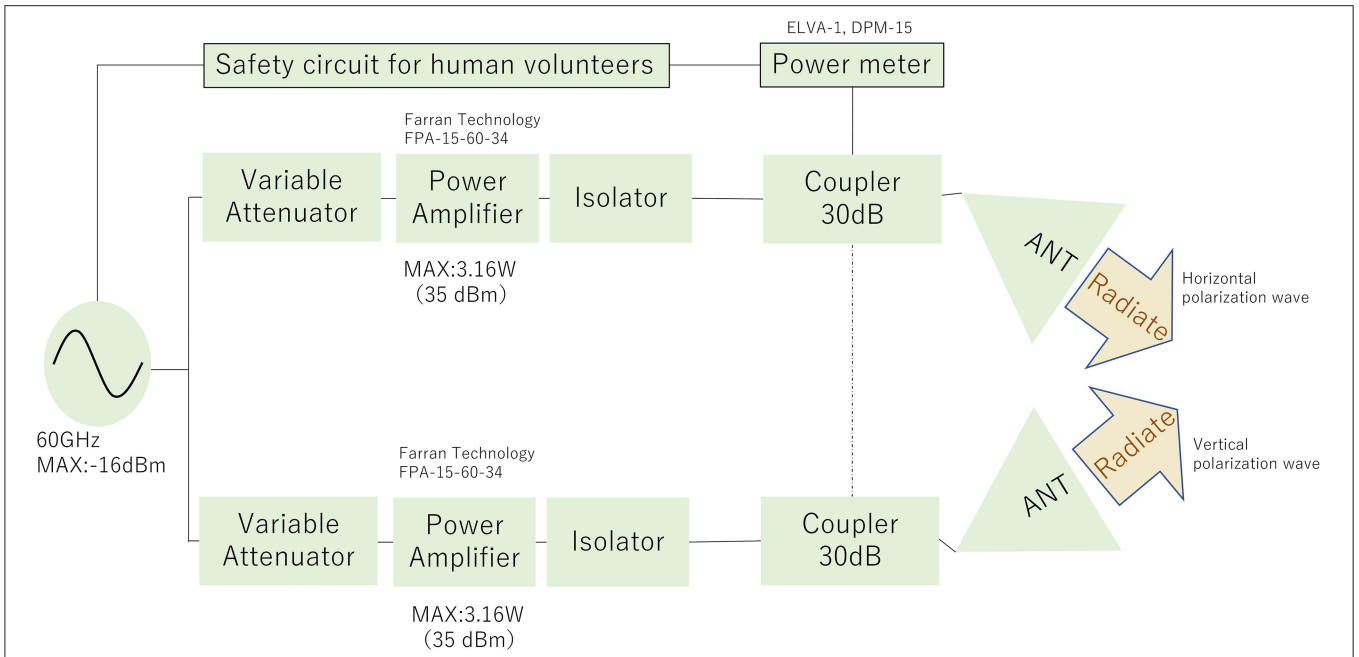

FIGURE 2 | Designed block diagram of the proposed exposure setup using spatial synthetic technique.

that the exposure setup meets the required specifications before human studies. The carbon nanotubes took the form of cylindrical carbon molecules, with at least one end-capped with a hemisphere of the structure. The diameter of a carbon nanotube was the order of a few nanometers, and it was up to several micrometers in length. Carbon black was a form of amorphous carbon that had an extremely high surface area to volume ratio. By using these carbon materials mixed within silicone rubber, an arm-shaped human skin phantom was suitable for 60 GHz band. This phantom material's complex permittivity was controlled by changing the composition ratio of carbon nanotubes and carbon black within the silicone base. The penetration depth of the MMW in biological tissue was minimal, and it became approximately 0.4 mm at 60 GHz band. Therefore, the target value of dielectric properties of the phantom was decided as the averaged value of skin tissues, and those are summarized in **Table 2**.

EXPERIMENTAL MEASUREMENTS AND DISCUSSIONS

Incident Power Density Measured at the Target Area

To estimate the exposure characteristics when the orthogonal antennas were used, we measured electric field distribution on the exposed area using a V-band open-ended waveguide probe antenna (SAGE Millimeter, Inc SAP-15-R2). Based upon the conversion formula between the probe antenna receiving power and electric field intensity, we evaluated the electric field distribution of each orthogonal polarization component from each antenna with total input power of 1 W, and the composite distribution was obtained. When the interference fringes are generated in the exposure area, the fluctuation of receiving power along with the measured line should be clearly observed. As shown in **Figure 5**, it was found that the exposure intensity distribution of the spatial synthetic beam was almost identical to that of single-focused beam irradiation. Thus, the suppression of the interference fringes by applying orthogonalizing polarized feed was confirmed. In addition, we found that the developed exposure systems could achieve the free-space power density of 970 W/m^2 when the total antenna input power was set to be 2 W.

Verification of the Simulated Results Using the Forearm Phantom

Based upon the designed block diagram and simulation results, we decided the set position and angle of the lens antennas and constructed the spatial synthetic exposure setup. **Figures 6A,B** show an overview of the developed setup in the anechoic chamber and an enlargement of the lens antennas and the arm-shaped phantom, respectively. Most of the MMW components were connected by rectangular waveguides of WR-15. The two lens antennas were connected to the lines with low-loss semirigid coaxial lines to control the feeding polarization and the angle between the two lens antennas.

Figure 7 shows surface temperature distributions of the arm-shaped phantom observed by thermal imaging camera (FLIR T530, FLIR Systems, Inc. USA) during exposure to 60 GHz-MMW at 2 W of total antenna input power. The characteristics of temperature distribution after the beginning of the exposure are shown every 10 s until 40 s. Interference fringes were clearly observed on the phantom surface when 60 GHz MMW radiation from copolarized feeding antennas was combined. In contrast,

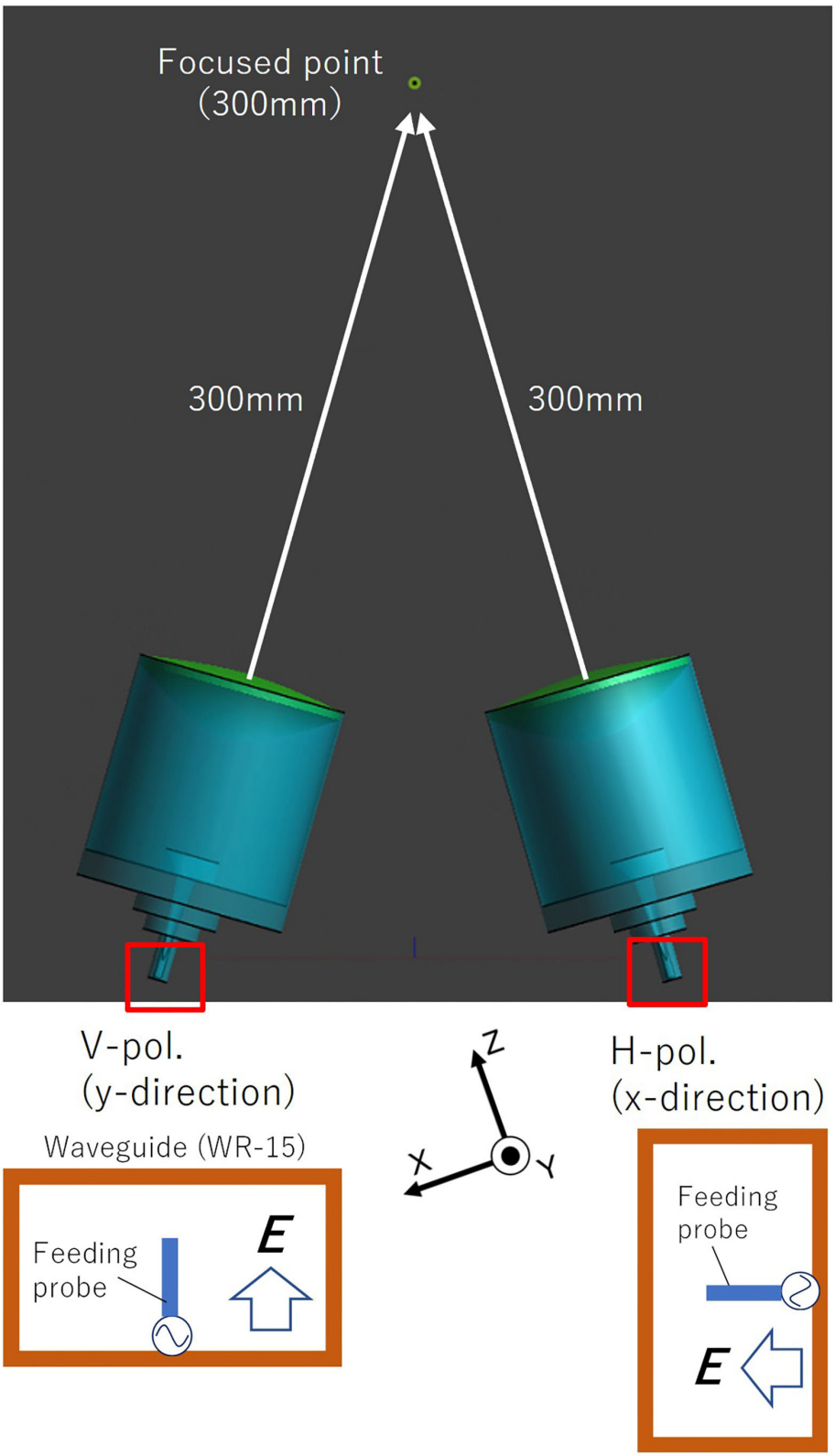

FIGURE 3 | Orthogonal polarized feeding for spatial synthetic beam.

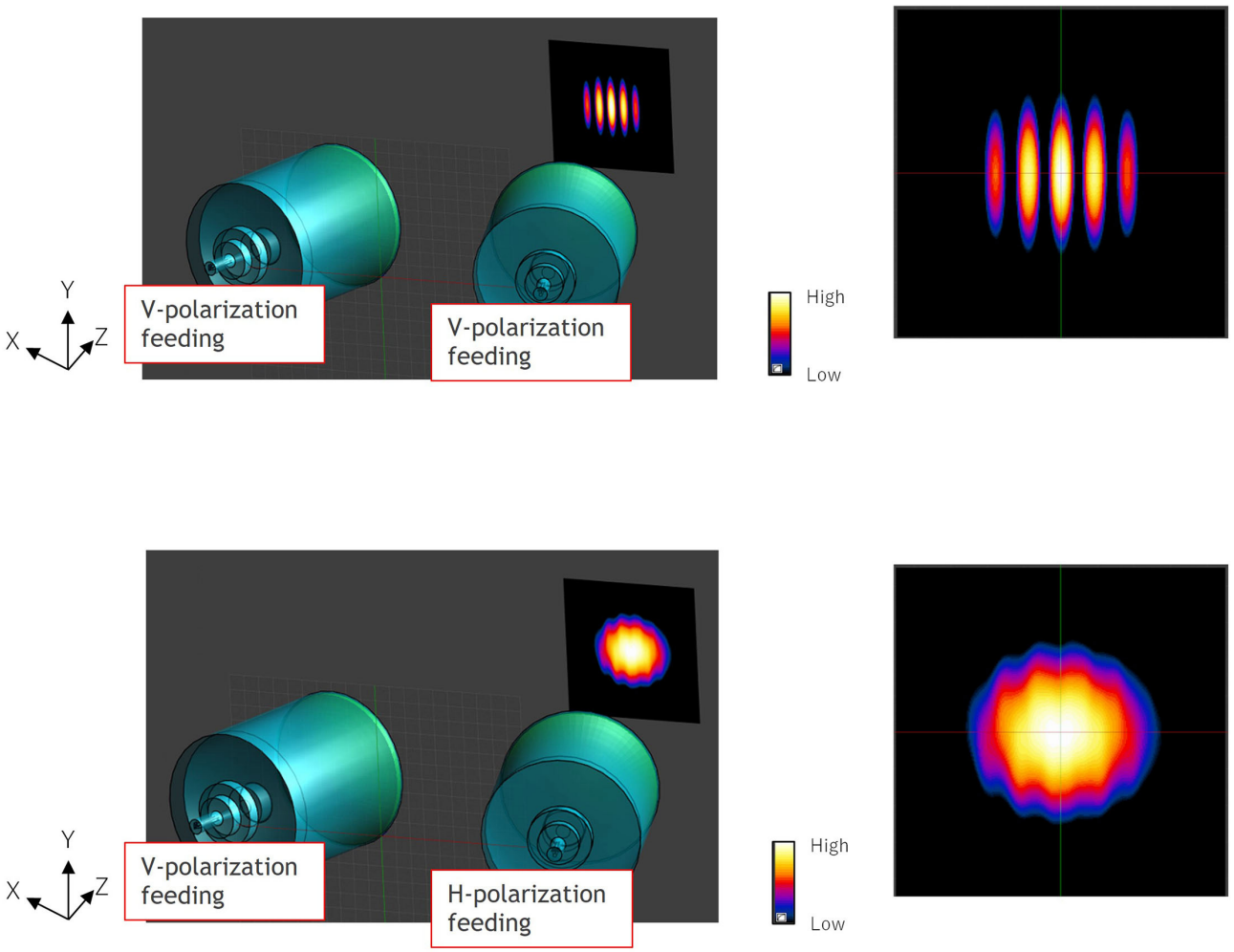

FIGURE 4 | Electric field distributions on a flat planer skin phantom exposed to spatial synthetic beams at 60 GHz. The values were normalized by the maximum value. **(A)** Copolarized feed. **(B)** Orthogonally polarized feed.

TABLE 2 | Dielectric properties of skin tissues (22).

	Relative permittivity	Loss tangent
Skin dry	7.9	1.4
Skin wet	10.2	1.2
Developed material	12	1.2

orthogonalizing the polarization of the two antennas eliminated these interference fringes. From the figure, it was confirmed that the exposure focused on a circular area of about 20 mm in diameter was realized.

The time- and dose-dependent characteristics of temperature rise were also evaluated using the phantom forearm under the measurement conditions shown in **Table 3**. These conditions except the room temperature were set to be similar to those in our future studies using human volunteers. Orthogonally polarized feed was adopted. The temperature of the phantom surface was measured when the antenna input power (total of two antennas) was at 1.0 W, 2.0 W, and 4.5 W. **Figure 8** shows a comparison of the characteristics of the temperature rise at target surface for each antenna input power. It is confirmed that the developed exposure setup provided the ideal local exposure on the target area. The surface temperatures elevated time-dependently similar to those we observed in the previous study using 28 GHz MMW. In addition, the maximum temperatures depended on the antenna input power, suggesting the differences in the IPD values, were reflected in the temperature elevation. However, the further experiments with several exposure intensities were needed to verify the linear relationship between the exposure intensity and temperature elevation.

Confirmation of the Local MMW Exposure in Human Forearm Skin

It was important to confirm whether the similar characteristics of local MMW exposure observed in the simulation and phantom

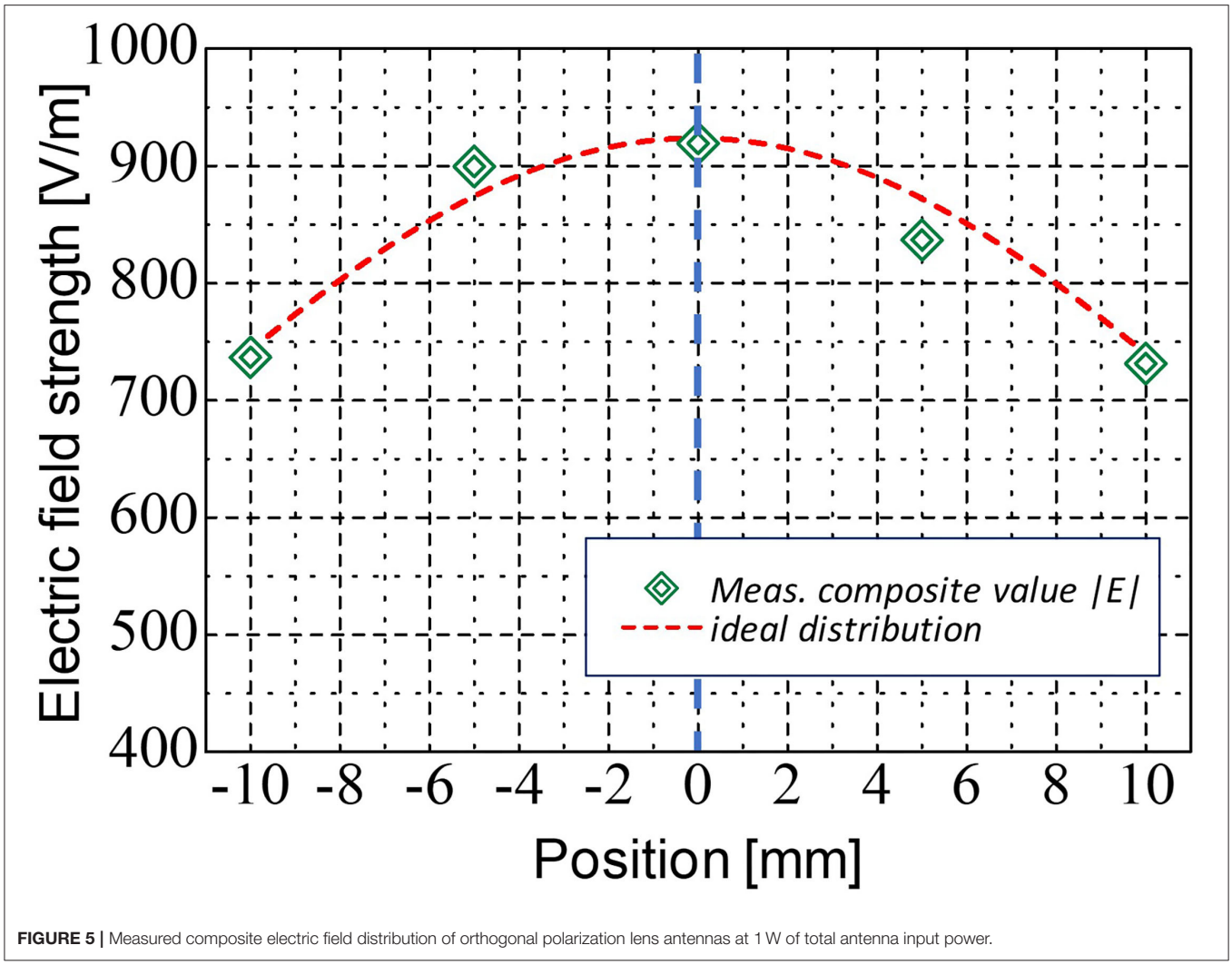

FIGURE 5 | Measured composite electric field distribution of orthogonal polarization lens antennas at 1 W of total antenna input power.

TABLE 3 | Experimental conditions for measuring temperature elevations in phantom.

Room temperature	20°C
Exposure frequency	60.0 GHz
Duration	0~900 sec.
Total input power for two antennas	1, 2, 4.5 W

experiment were actually obtained in human skin. Then, we conducted human volunteer experiments using the developed exposure setup. Six adult volunteers (five female volunteers and one male volunteer) were called and explained our studies in detail to obtain informed consent. The experiment was performed in a room kept at 26.5 ± 0.5°C of temperature and 45 ± 5% of relative humidity. Subjects sat in the chair and their right forearms were placed on the desk. The dorsal forearm skin positioned 300 mm in front of the lens antenna was exposed to 60 GHz MMW at 2 W of total antenna input power for 6 min. Changes in skin temperature were measured through the experiments using thermography. This study was approved by the Ethics Committee of Kurume University (approved number 17192).

Figure 9 shows representative images of thermography around the target area during the exposure. The temperature elevation was observed and found it localized at the target area. In addition, no striped distribution of temperature was confirmed. Although the thermoregulation or thermal diffusion in the skin should be taken into consideration for the temperature distribution, these findings were very similar to those of the phantom experiment. Furthermore, the average temperature of the target area exposed at 2 W of total antenna input power increased from 32.3 ± 0.9°C to 37.7 ± 1.0°C. This range of temperature change seemed to be enough for warm detection reported in the skins such as thenar and dorsal hand (32.3–35.3°C) (12). Therefore, it suggests that the local MMW

A

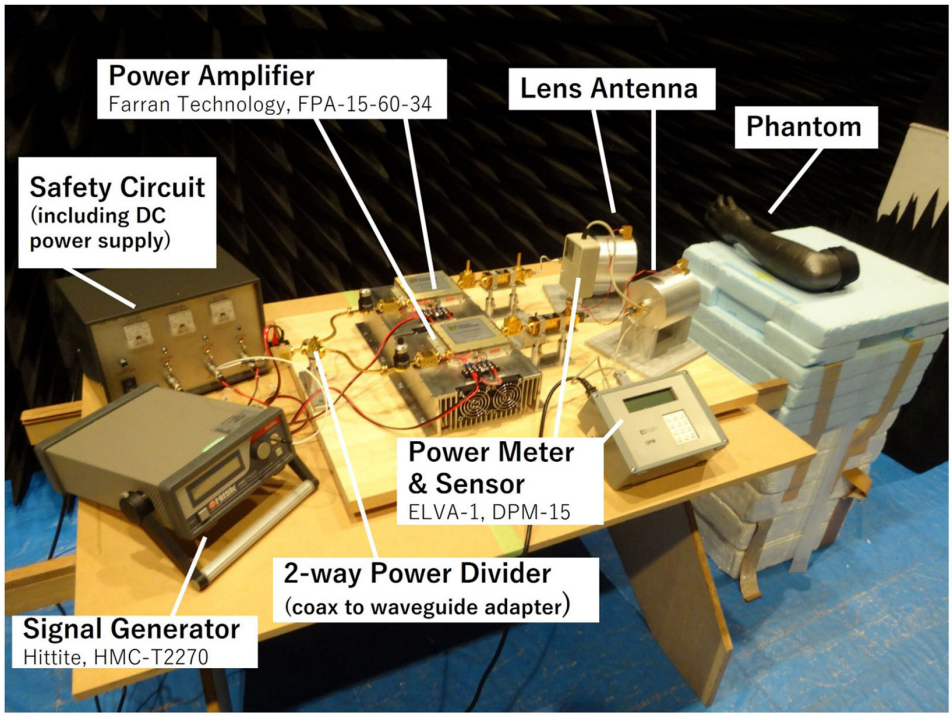

B

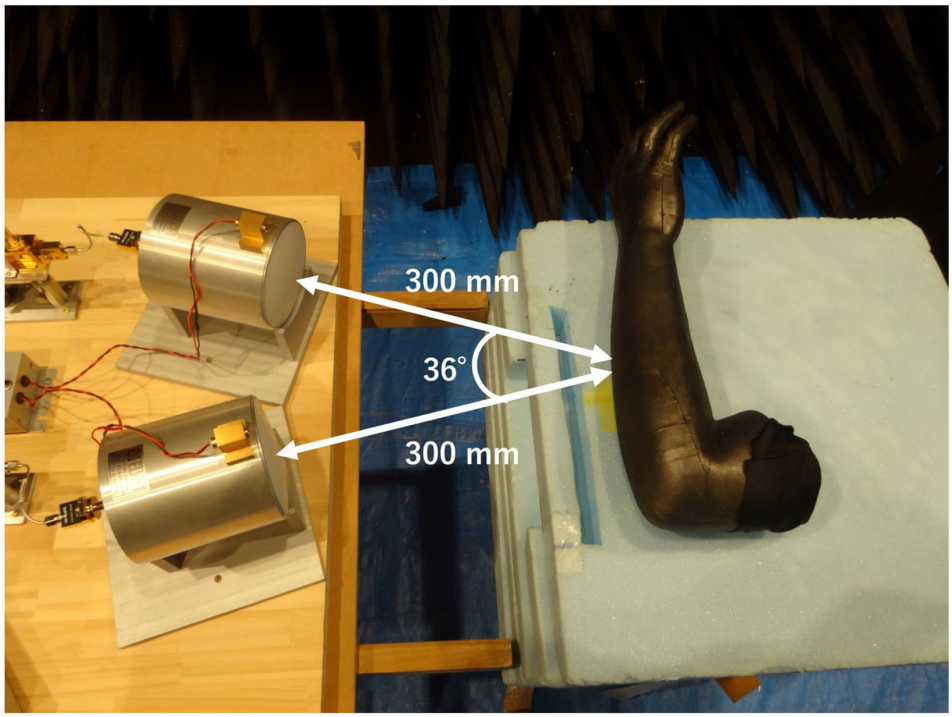

FIGURE 6 | 60 GHz spatial synthetic exposure setup. **(A)** Overview of the setup. **(B)** The lens antenna and arm-shaped phantom.

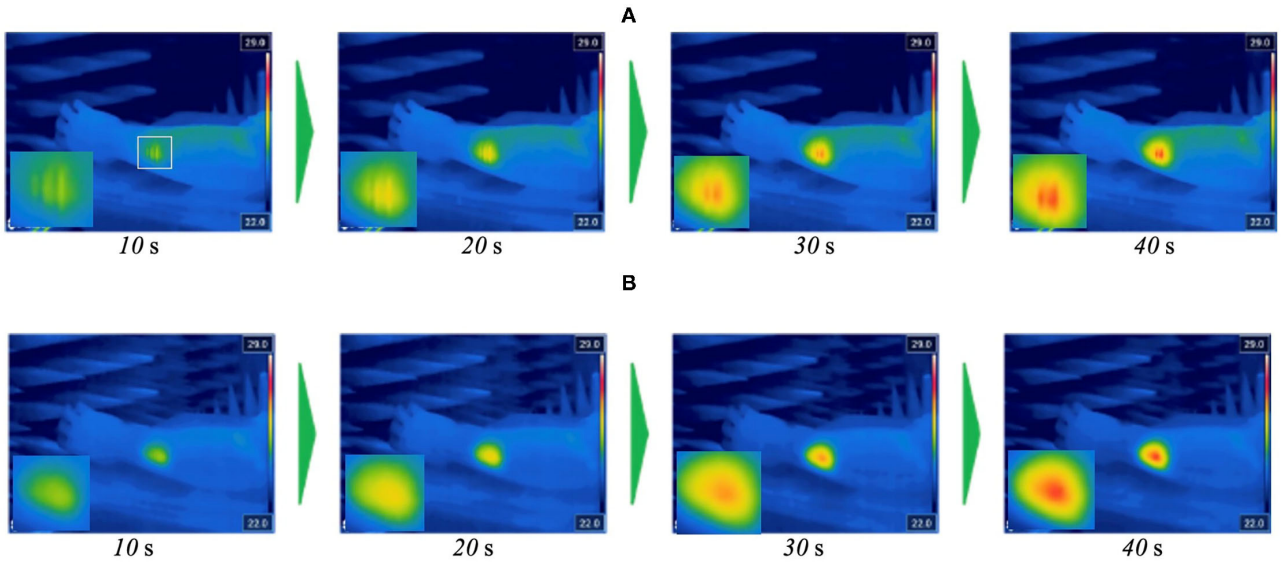

FIGURE 7 | Temperature distribution on arm-shaped phantom during the exposure to 60 GHz MMW at 2 W of total antenna input power. **(A)** Orthogonally polarized feed. **(B)** Copolarized feed.

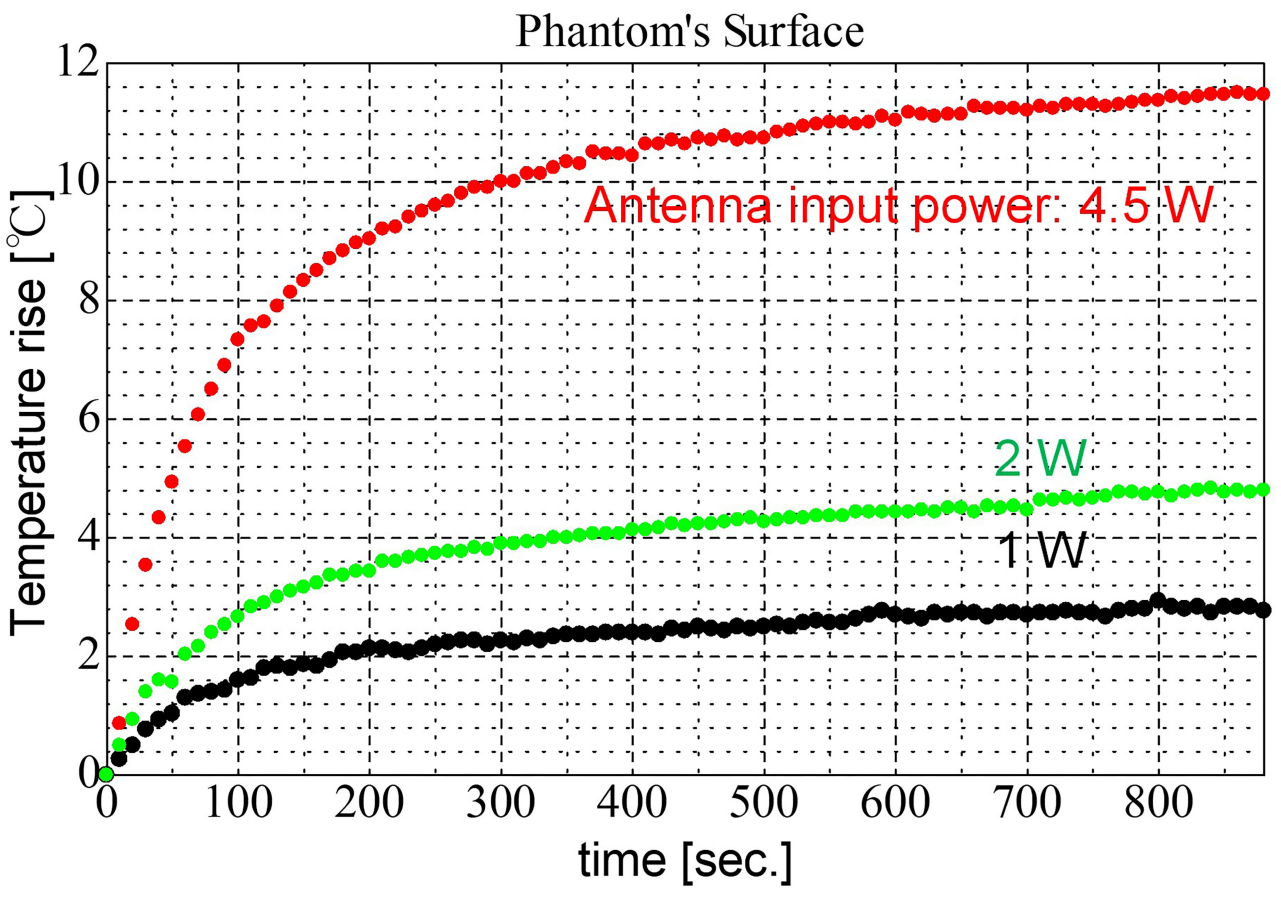

FIGURE 8 | Characteristics of temperature elevation during the exposure to 60 GHz MMW with orthogonal polarized feeding.

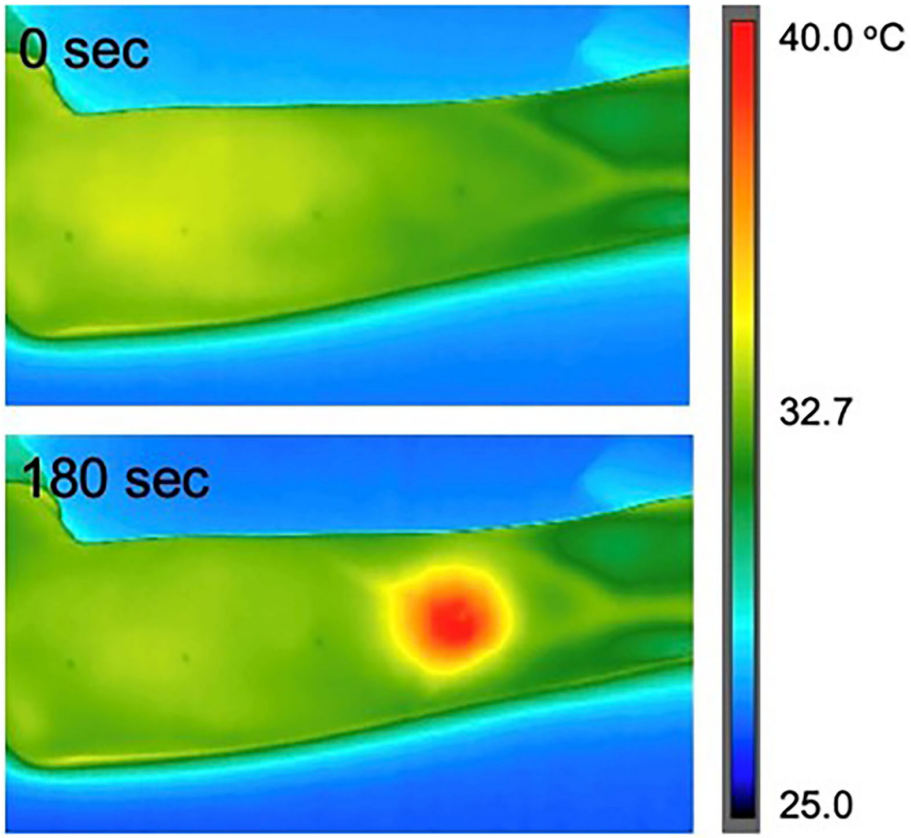

FIGURE 9 | Temperature elevation in the human forearm skin during the exposure to 60 GHz MMW at 2 W of total antenna input power.

exposure that we expected for human studies is realized in the human skin.

CONCLUSION

We developed a novel spatial synthetic exposure setup to explore the biological effects of local exposure to 60 GHz-MMW on human body. The setup using double lens antennas allowed to generate the highly localized exposure area on the human skin and provided enough space for measurements of the physiological parameters. In addition, even at 300 mm of the focal length between the target area and the antenna, the sufficient IPDs (0 to 1,940 W/m^2) to detect thermal threshold were obtained. This is the first report, to the best of the authors' knowledge, about the developments of the MMW spatial synthetic exposure setup using orthogonally polarized feeding structure to eliminate interference fringes in the exposure area. On the other hand, purposely using the interference fringes may also be capable of achieving more localized exposure with high intensity, namely multiple exposures using a synthetic electric field instead of composite power. The developed exposure setup will be useful for the future human studies. For example, the effects of 5G-MMW exposure on skin thermoregulation under various exposure conditions such as different IPDs or signal modulation will be considered.

DATA AVAILABILITY STATEMENT

The original contributions presented in the study are included in the article/supplementary material, further inquiries can be directed to the corresponding author.

ETHICS STATEMENT

The studies involving human participants were reviewed and approved by Ethics Committee of Kurume University. The patients/participants provided their written informed consent to participate in this study.

AUTHOR CONTRIBUTIONS

TH designed all the experiments and simulations and conceived the manuscript. RO performed the experiments and wrote the draft of the manuscript. HM and TI reviewed the manuscript. All authors have read and agreed to the published version of the manuscript.

FUNDING

This study was supported by Ministry of Internal Affairs and Communications in Japan. Grant number JPMI10001.

REFERENCES

1. Guidelines for Limiting Exposure to Electromagnetic Fields (100 kHz to 300 GHz). *Health Phys.* (2020) 118:483–524. doi: 10.1097/HP.0000000000001210
2. Stern S, Margolin L, Weiss B, Lu ST, Michaelson SM. Microwaves: effect on thermoregulatory behavior in rats. *Science.* (1979) 206:1198–201. doi: 10.1126/science.505008
3. Guy AW, Lin JC, Kramar PO, Emery AF. Effect of 2450-Mhz Radiation on the Rabbit Eye. *IEEE Trans Microw Theory Tech.* (1975) 23:492–8. doi: 10.1109/TMTT.1975.1128606
4. D'Andrea JA, DeWitt JR, Gandhi OP, Stensaas S, Lords JL. Nielson HC. Behavioral and physiological effects of chronic 2,450-MHz microwave irradiation of the rat at 05 mW/cm2. *Bioelectromagnetics.* (1986) 7:45–56. doi: 10.1002/bem.2250070106
5. Adair ER, Adams BW, Akel GM. Minimal changes in hypothalamic temperature accompany microwave-induced alteration of thermoregulatory behavior. *Bioelectromagnetics.* (1984) 5:13–30. doi: 10.1002/bem.2250050103
6. Blick DW, Adair ER, Hurt WD, Sherry CJ, Walters TJ, Merritt JH. Thresholds of microwave-evoked warmth sensations in human skin. *Bioelectromagnetics.* (1997) 18:403–9. doi: 10.1002/(SICI)1521-186X(1997)18:6<403::AID-BEM1>3.0.CO;2-6
7. Kojima M, Suzuki Y, Sasaki K, Taki M, Wake K, Watanabe S, et al. Ocular effects of exposure to 40, 75, and 95 GHz millimeter waves. *J Infrared Millim Terahertz Waves.* (2018) 39:912–25. doi: 10.1007/s10762-018-0497-z
8. Cross B. The human eye's response to millimeter-wave radiation. (2021). Available online at: https://www.ideals.illinois.edu/handle/2142/110323 (accessed September 12, 2021).
9. Haas AJ, Page YL, Zhadobov M, Sauleau R, Dréan YL. Effects of 60-GHz millimeter waves on neurite outgrowth in PC12 cells using high-content screening. *Neurosci Lett.* (2016) 618:58–65. doi: 10.1016/j.neulet.2016.02.038
10. Haas AJ, Le Page Y, Zhadobov M, Boriskin A, Sauleau R, Le Dréan Y. Impact of 60-GHz millimeter waves on stress and pain-related protein expression in differentiating neuron-like cells. *Bioelectromagnetics.* (2016) 37:444–54. doi: 10.1002/bem.21995
11. Wu Y, Nieuwenhoff MD, Huygen FJPM, van der Helm FCT, Niehof S, Schouten AC. Characterizing human skin blood flow regulation in response to different local skin temperature perturbations. *Microvasc Res.* (2017) 111:96–102. doi: 10.1016/j.mvr.2016.12.007
12. Hagander LG, Midani HA, Kuskowski MA, Parry GJ. Quantitative sensory testing: effect of site and skin temperature on thermal thresholds. *Clin Neurophysiol.* (2000) 111:17–22. doi: 10.1016/S1388-2457(99)00192-3
13. Sakakibara K, Sekiguchi T, Hikage. Development of 28 GHz band exposure equipment for studies on thermal perception thresholds of biological effects exposed to millimeter-wave at 5th generation wireless systems candidate frequency band. Slovenia: BioEM 2018. (2018) doi: 10.1109/CAMA47423.2019.8959816
14. Kageyama I, Hikage T, Sakakibara K, Hirata A, Kodera S, Taguchi K, et al. Characteristics of skin temperature elevation under the local exposure of 28GHz-millimeter-wave in phantom and real human body. Japan: BioEM 2019. (2019).
15. Kouzai M, Nishikata A, Sakai T, Watanabe S. Characterization of 60GHz Millimeter-Wave Focusing Beam for Living- Body Exposure Experiments. *EMC'09/Kyoto.* (2009) 22S1–1. doi: 10.34385/proc.14.22S1-1
16. Wake K, Soichi W, Nishikata A, Enomoto H, Ugawa Y. Dependence on spot size and Exposure duration to thermal sensation by millimeter-wave exposure at 60 GHz. In: *IEEE Conferences 2013 International Symposium on Electromagnetic Theory*. Hiroshima (2013). p. 540–1.
17. Sakiyama H, Nishikata A, Sasaki K, Ugawa Y. Analysis for skin surface temperature rise under convergence beam exposure of 40GHz and 95GHz millimeter wave. In: *IEICE Technical Report EMCJ2017-64*. (2017). p. 117:1–6
18. Sakakibara K HT. Development of 28 GHz band exposure equipment for studies on thermal perception thresholds of biological effects exposed to millimeter-wave at 5th generation wireless systems candidate frequency band. Slovenia: BioEM, 2018. (2018)
19. Collin RE. *Foundations for Microwave Engineering*. Hoboken, NJ: John Wiley & Sons. (2007).
20. Gandhi OP, Riazi A. Absorption of Millimeter Waves by Human Beings and its Biological Implications. *IEEE Trans Microw Theory Tech.* (1986) 34:228–35. doi: 10.1109/TMTT.1986.1133316
21. Wu T, Rappaport TS, Collins CM. The human body and millimeter-wave wireless communication systems: Interactions and implications. In: *2015 IEEE International Conference on Communications (ICC)*. (2015) p. 2423–9. doi: 10.1109/ICC.2015.7248688
22. Gabriel S. The dielectric properties of biological tissues. *Phys Med Biol.* (1996) 41:2271–93. doi: 10.1088/0031-9155/41/11/003

Conflict of Interest: The authors declare that the research was conducted in the absence of any commercial or financial relationships that could be construed as a potential conflict of interest.

frontiers in Public Health

ORIGINAL RESEARCH
published: 13 December 2021
doi: 10.3389/fpubh.2021.793418

Exposure Optimization Trial for Patients With Medical Implants During MRI Exposure: Balance Between the Completeness and Efficiency

Aiping Yao[1]*, *Pengfei Yang*[2], *Mingjuan Ma*[1] and *Yunfeng Pei*[1]

[1] Department of Information Science and Engineering, Lanzhou University, Lanzhou, China, [2] Centre for Medical Device Evaluation, National Medical Products Administration, Beijing, China

Elongated conductors, such as pacemaker leads, can couple to the MRI radio-frequency (RF) field during MRI scan and cause dangerous tissue heating. By selecting proper RF exposure conditions, the RF-induced power deposition can be suppressed. As the RF-induced power deposition is a complex function of multiple clinical factors, the problem remains how to perform the exposure selection in a comprehensive and efficient way. The purpose of this work is to demonstrate an exposure optimization trail that allows a comprehensive optimization in an efficient and traceable manner. The proposed workflow is demonstrated with a generic 40 cm long cardio pacemaker, major components of the clinical factors are decoupled from the redundant data set using principle component analysis, the optimized exposure condition can not only reduce the *in vivo* power deposition but also maintain good image quality.

Keywords: RF, medical implant, exposure optimization, MRI, *in silico*

OPEN ACCESS

Edited by:
Tongning Wu,
China Academy of Information and Communications Technology, China

Reviewed by:
Ji Chen,
University of Houston, United States
Xiaoxia Zhao,
MicroPort Medical Science Co., Ltd., China
Ye Li,
Shenzhen Institutes of Advanced Technology, Chinese Academy of Sciences (CAS), China

***Correspondence:**
Aiping Yao
yaoaiping@lzu.edu.cn

Specialty section:
This article was submitted to Radiation and Health, a section of the journal Frontiers in Public Health

Received: *12 October 2021*
Accepted: *10 November 2021*
Published: *13 December 2021*

Citation:
Yao A, Yang P, Ma M and Pei Y (2021) Exposure Optimization Trial for Patients With Medical Implants During MRI Exposure: Balance Between the Completeness and Efficiency. Front. Public Health 9:793418. doi: 10.3389/fpubh.2021.793418

INTRODUCTION

Patients with implantable medical devices are usually excluded from the MRI examinations due to the very complicated electromagnetic (EM) environment patients are exposed to during MRI, including static, gradient, and radiofrequency (RF) magnetic fields. The RF magnetic field with frequencies of 64 MHz (1.5 T MRI) and 128 MHz (3.0 T MRI) will induce a strong electric-field in patients based on Faraday law (1, 2). The conductive implants inside the patients will act like an antenna, couple with these induced fields, and deposit the power near the implant electrodes, leading to high local tissue temperature increase (3–5).

Many efforts are done to solve this RF safety problem by modifying the material composition and EM properties of the implanted devices to render them inherently safe for MRI (6, 7), but in most cases, this is not enough. Instead of modifying implanted devices for the MR environment, many explorations are focused on making the MR environment itself safer for existing devices by manipulating the MR exposure conditions (8, 9). On the other hand, the exposure condition selected to reduce the RF-induced heating may at the same time decrease the MRI imaging quality dramatically (10). Therefore, it is important that the exposure condition are optimized so that the RF-induced heating are reduced and at the same time certain MRI imaging quality is reserved.

The RF-induced heating is directly determined by the induced *in vivo* tangential electrical field along with the implant routing (E_{tan}), while the MRI

imaging quality can be indicated by the magnetic field strength and homogeneity. For patients with medical implants, the induced *in vivo* electrical field E_{tan} amounts to a multitude of variables specific to the MRI system (11, 12) (e.g., RF-coil design and manufacturing details), patient anatomy (13, 14), and imaging positions. Therefore, clinical trials performed with a limited number of scenarios are likely to be insufficient to ensure patient safety. It is essential that the exposure optimization be performed in as many relevant clinical scenarios as possible.

In this work, we established an *in silico* exposure optimization trial that comprises a data library with principle component analysis (PCA) to balance between the efficiency and completeness during the exposure optimization procedure. The proposed work-flow is applied to a generic 40-cm long cardio pacemaker under 1.5T MRI RF exposure. Big data containing more than 0.3 billion unique clinical scenarios are selected from the data library. The correlation coefficients between different clinical scenarios are analyzed based on PCA to decouple the major components of the clinical factors which produce significant and unique variation in the implant power deposition. The decoupled major clinical scenarios greatly reduce the data redundantly, therefore, enable a comprehensive and efficient exposure optimization resulting in both good imaging quality and patient safety.

MATERIALS AND METHODS

The proposed framework is illustrated in **Figure 1**, which is comprised of the following components:

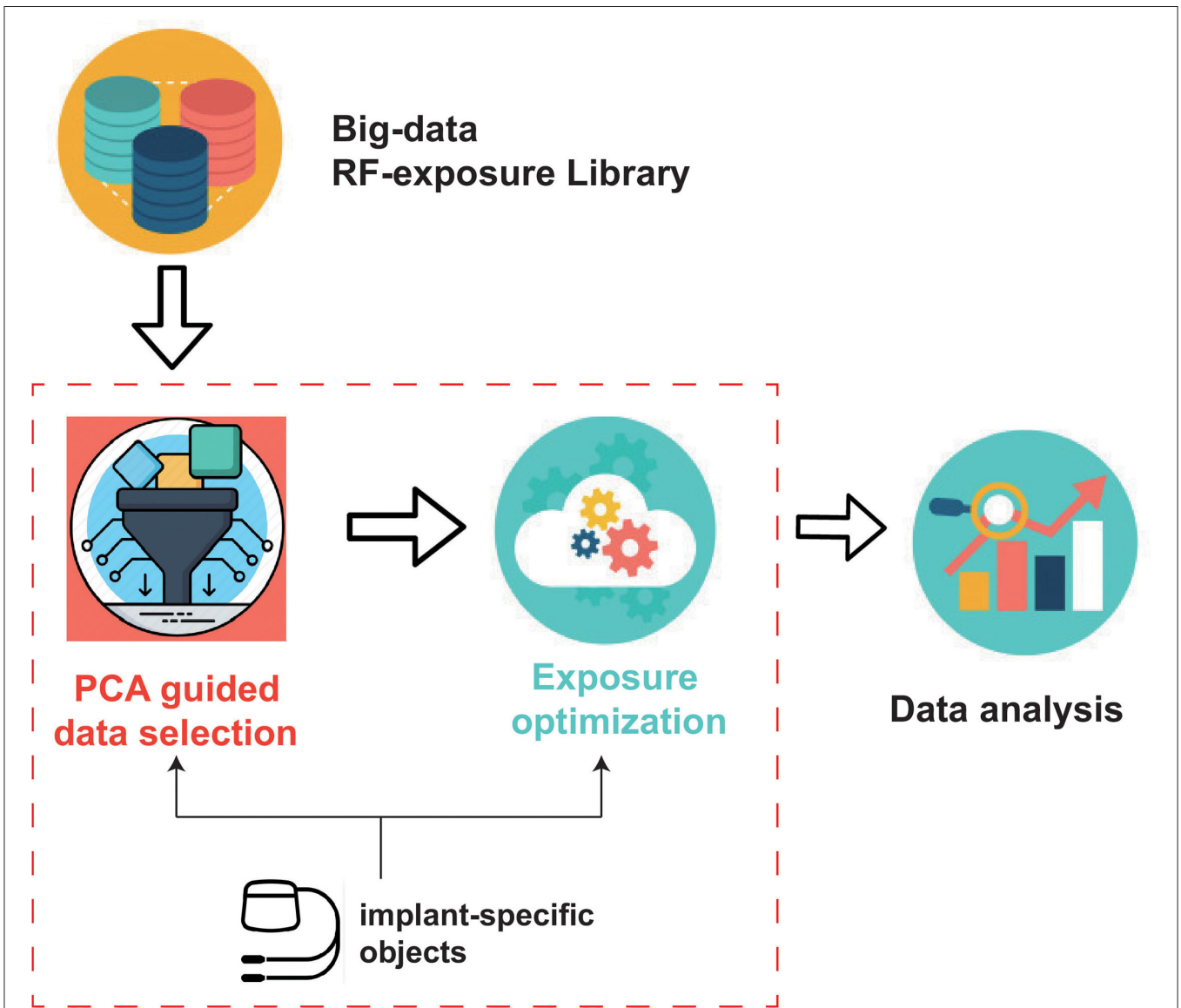

FIGURE 1 | Proposed exposure optimization work-flow.

TABLE 1 | Physiological parameters of the five selected anatomical models, obtained from discretized models with a uniform grid size of $0.5 \times 0.5 \times 0.5\,mm^3$.

Anatomical model	Gender	Age (Year)	Height (m)	Weight (kg)	BMI (Kg/m^2)
Fats	Male	37	1.82	119	36
Duke	Male	34	1.77	70.2	22.4
Ella	Female	26	1.63	57.3	21.6
Billie	Female	11	1.49	34	15.3
Thelonious	Male	6	1.16	18.6	13.8

TABLE 2 | Geometry of the radio frequency (RF) birdcage coil considered in the study.

Coil no.	Diameter (cm)	Length (cm)	Number of rungs	Shield diameter (cm)	Frequency (MHz)
1	65	50	16	70	64
2	65	60	16	70	64
3	65	70	16	70	64
4	75	40	16	70	64
5	75	50	16	70	64
6	75	60	16	70	64
7	75	70	16	70	64
8	80	50	16	70	64
9	80	60	16	70	64
10	80	70	16	70	64

- RF-exposure big-data library: This component provides pre-computed RF-induced field distributions inside a variety of patients during MRI exposure under different clinical scenarios.
- Implant-specific objects: This component includes the digital representations of clinical routings of the implant under test (IUT) and the RF model of the IUT.
- PCA guided data selection: This component uses PCA to get the decoupled clinical factors for an efficient data selection from the data library.
- Exposure Optimization: This component implements exposure optimization to achieve both good imaging quality and patient safety.

RF-Exposure Big-Data Library

Five high-resolution anatomical models from Virtual Population (ViP) (15) representing a large population range are selected and listed in **Table 1**. 10 RF coils with different coil diameter, and lengths covering the envelope of commercial MRI system are used as the incident RF field source. The geometry of the 10 selected RF coils is listed in **Table 2**. Each two-channel coil was tuned to resonate at 64 MHz, with selected polarization sweeps included:$\epsilon \in [-45^o, 45^o]$ with a step of 5^o; $\tau \in [0^o, 180^o]$ with a step of 10^o, covering a wide range of shimming used in MRI systems. τ and ϵ are two parameters defined to characterize the ellipticity and tilt angle of the field polarization (1). Each anatomical model was placed in the RF coils with imaging positions from head-to-foot with a step size of 10 cm along the longitudinal axis (as FATS is too big for coil No. 1–3, only coil from No. 4–10 are used for FATS). **Figure 2** summarized the anatomical marks corresponding to each imaging position (ZPOS) for the five anatomical models.

Computational EM (CEM) simulations were conducted by means of the finite different time domain (FDTD) simulation platform, Sim4Life V6.0 (ZMT Zurich MedTech, Zurich, Switzerland). It was ensured that a steady-state was attained before the simulations were determined. The anatomical models were discretized with a maximum grid size of 2.0 x 2.0 x 2.0 mm^3, and dielectric tissue properties at 64 MHz (16) were assigned to the tissues.

Implant-Specific Objects

Three clinical routing groups of the IUT were defined: (i) left and right deep brain stimulator (DBS) routing groups (DBS_L and DBS_R: the routings run underneath the skin from the proximal ends of the left and right pectoral muscles, along the side of the neck behind the left and right ears, up to the crown of the head, and through the skull, terminating in the distal end of the thalamus); (ii) left and right pacemaker (PM) routing groups (PM_L and PM_R): the routings run underneath the skin from the proximal end of the left and right pectoral and along the veins, terminating in the distal end of the right heart ventricle; and (iii) left and right spinal cord stimulator (SCS) routing groups (SCS_L and SCS_R: the routings run underneath the skin from left and right buttocks below the waistline, along with the epidural space from the T10 vertebra, and terminating at the C1 vertebra.

The RF-model of the IUT defined by the transfer function of the implant can be derived from the technique proposed (17) where the transfer function, henceforth referred to as $h(l)$, is defined as the locally induced electric field around an electrode with excitation along length l of the implant. **Figure 3** depicts a schematic of the method, where the generic 40 cm long implant is embedded in a homogeneous tissue simulating medium (TSM) with dielectric properties of $\sigma = 0.47$ S/m and $\epsilon = 78$. The

Algorithm 1 An algorithm with caption.

Require: M*M is the dimension of the pre-defined power deposition matrix **C**;
$i \leftarrow 1$
$j \leftarrow 1$
while $i \leq M$ **do**
  while $j \leq M$ **do**
    if $C_{ij} > 0.95$ **then**
      compress elements i and j in the same compressed group G
    else
      assign element j to a new compressed group G+1
    end if
    $j \leftarrow j + 1$
  end while
  $i \leftarrow i + 1$
end while

zpos	FATS	DUKE	ELLA	THELONIOUS	BILLIE
1	BRAIN	BRAIN	BRAIN	BRAIN	BRAIN
2	BRAIN	BRAIN	BRAIN	BRAIN	BRAIN
3	C2	C1	C3	C6	C5
4	C3	C2	C4	C7	C6
5	C7	C6	T3	T7	T4
6	T1	C7	T4	T8	T5
7	T5	T4	T8	L1	T9
8	T6	T5	T9	L2	T10
9	T9	T8	T11	S5	L1
10	T10	T9	T12	COCCYX	L2
11	T11	T10	L1	FEMORAL_HEAD	L4
12	L1	L1	L3	FEMORAL_HEAD	L5
13	L3	L2	S5	FEMUR_BODY_HI	FEMORAL_HEAD
14	L4	L3	COCCYX	FEMUR_BODY_MID	FEMORAL_HEAD
15	S5	S5		FEMUR_KNEE	FEMUR_BODY_HI
16	COCCYX	COCCYX	FEMORAL_HEAD	FEMUR_KNEE	FEMUR_BODY_HI
17	FEMORAL_HEAD	FEMORAL_HEAD	FEMUR_BODY_HI	TIBIA_BODY_HI	FEMUR_BODY_MID
18	FEMORAL_HEAD	FEMORAL_HEAD	FEMUR_BODY_HI	TIBIA_BODY_HI	FEMUR_BODY_MID
19	FEMUR_BODY_HI	FEMUR_BODY_HI	FEMUR_BODY_MID	TIBIA_BODY_MID	FEMUR_BODY_LO
20	FEMUR_BODY_HI	FEMUR_BODY_HI	FEMUR_BODY_MID	TIBIA_BODY_MID	FEMUR_BODY_LO
21	FEMUR_BODY_MID	FEMUR_BODY_MID	FEMUR_BODY_LO	CALCANEUS_HEEL	TIBIA_KNEE
22	FEMUR_BODY_MID	FEMUR_BODY_MID	FEMUR_BODY_LO	CALCANEUS_HEEL	TIBIA_KNEE
23	FEMUR_BODY_LO	FEMUR_BODY_LO	TIBIA_KNEE		TIBIA_BODY_HI
24	FEMUR_BODY_LO	FEMUR_BODY_LO	TIBIA_KNEE	-	TIBIA_BODY_HI
25	FEMUR_KNEE	FEMUR_KNEE	TIBIA_BODY_HI		TIBIA_BODY_LO
26	FEMUR_KNEE	FEMUR_KNEE	TIBIA_BODY_HI	-	TIBIA_BODY_LO
27	TIBIA_KNEE	TIBIA_KNEE	TIBIA_BODY_MID		TALUS_ANKLE
28	TIBIA_KNEE	TIBIA_KNEE	TIBIA_BODY_MID	-	TALUS_ANKLE
29	TIBIA_BODY_MID	TIBIA_BODY_MID	TIBIA_LO		
30	TIBIA_BODY_MID	TIBIA_BODY_MID	TIBIA_LO	-	-
31	TIBIA_BODY_LO	TIBIA_BODY_LO	FOOT		
32	TIBIA_BODY_LO	TIBIA_BODY_LO	FOOT	-	-
33	TIBIA_LO	TALUS_ANKLE			

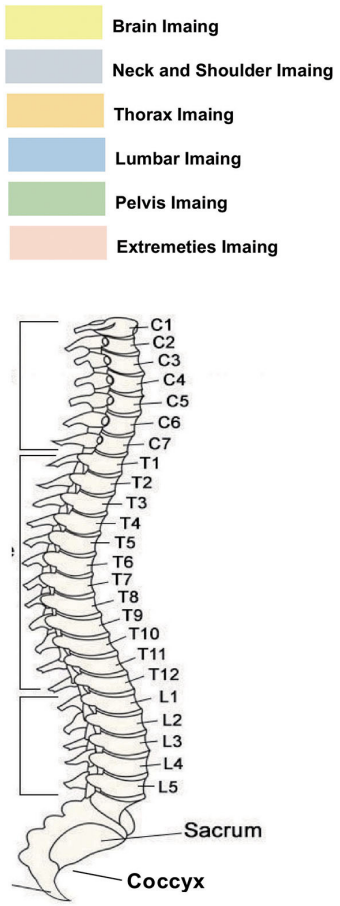

FIGURE 2 | Illustration of the corresponding anatomical marks in each anatomical model for each imaging position (ZPOS), different color represents different imaging range.

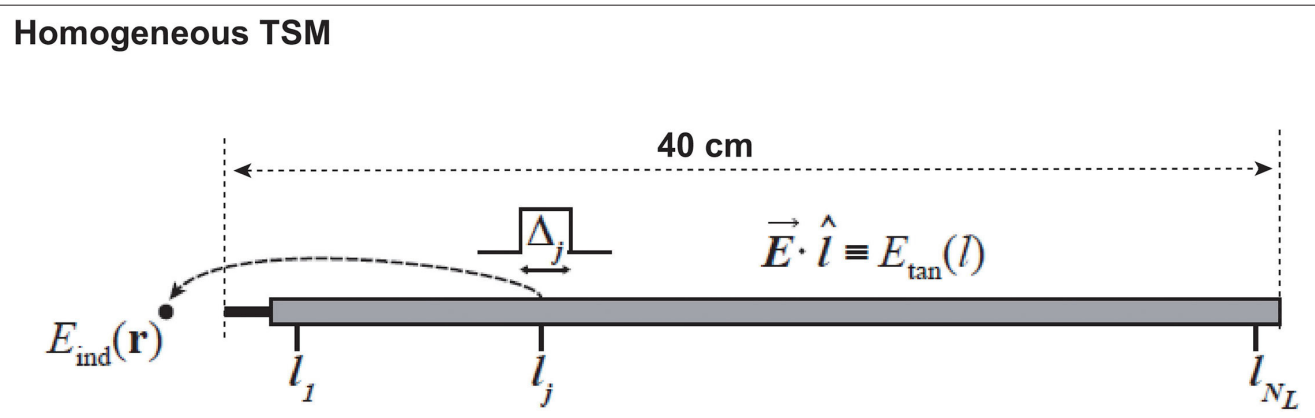

FIGURE 3 | Schematic of the transfer function derived method. *l* is the unit tangential vector along the implant at length *l*.

tangential component of the local incident electric field, E_{tan}, is coupled with the implant at length l and the induced electric field around the implanted electrode at $\mathbf{r}$, $E_{ind}(\boldsymbol{r})$, is evaluated as the transfer function $h(l)$.

PCA Guided Data Selection

To provide guidance for an efficient RF field data selection, PCA (18) is applied to an implant routing groups, RF coils, and image positions, respectively, to decouple the critical clinical factors

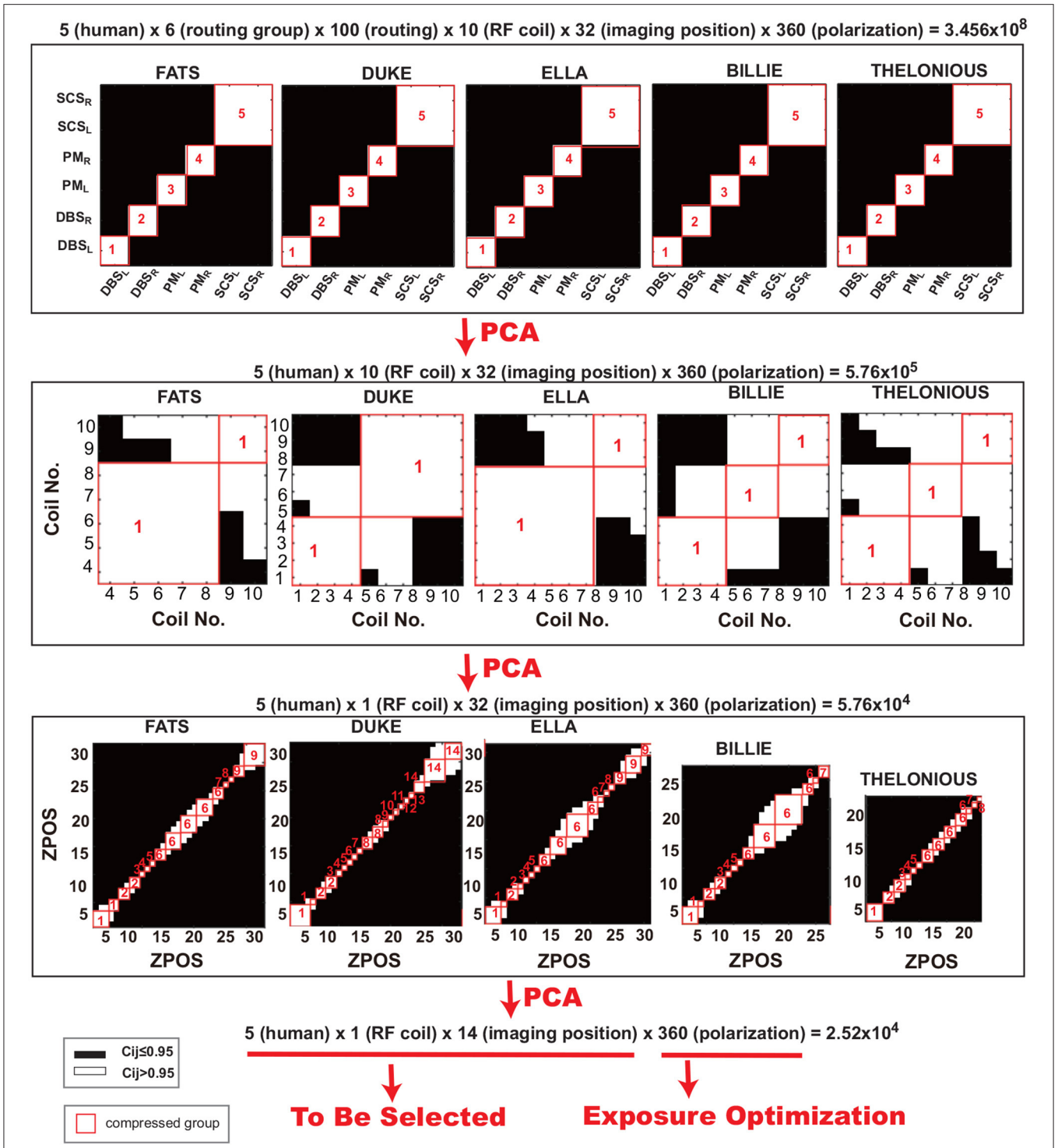

FIGURE 4 | Illustration of the principle component analysis (PCA) guided data compression procedure: covariance matrix $\boldsymbol{C}$ of implant routing **(Top Row)**, RF coil **(Middle Row)**, and imaging position **(Botoom Row)** are shown following the data compression order.

from the redundant data. The PCA algorithm performed in this work is defined as follows:

For clinical factors that has M variables (e.g., there are 6 implant routing groups, M = 6), let $A_i \in R^{1\times N}$ and $A_j \in R^{1\times N}$ be the observed power deposition (P_{dep}) data set for variable i and j, respectively, the covariance matrix $\mathbf{C} \in R^{M\times M}$ can be obtained through Equation 1:

$$C_{i,j} = \frac{1}{N-1}\left(\frac{A_i - hu_i^T}{\sigma_i}\right)\left(\frac{A_j - hu_j^T}{\sigma_j}\right)^H (i,j \in [1,M]) \quad (1)$$

where u_i^T and σ_i are the mean and SD of data set $A_i \in R^{1\times N}$, u_j^T and σ_j are the mean and SD of data set $A_j \in R^{1\times N}$. h is unity column vector. H donate the Hermitian transpose of matrix. Each element on the principal diagonal of the matrix is the correlation of a random variable with itself, which always equals 1.

The RF-induced power deposition P_{dep} of the implant under each clinical scenario can be estimated from:

$$P_{dep} = \left(\sum_{j=1}^{N_L} h(l_j)E_{tan}(l_j)\Delta_j\right)\left(\sum_{j=1}^{N_L} h(l_j)E_{tan}(l_j)\Delta_j\right)^* \quad (2)$$

where h_l is the transfer function of the implant, and $E_{tan}(l)$ is the *in vivo* tangential electrical field along the implant trajectory under the selected clinical scenario.

Exposure Optimization

The RF coil exposure condition can be characterized with poincare shpere parameters ϵ and τ (1). Therefore, different exposure conditions have different ϵ and τ values. When the RF coil is operating under N different exposure conditions, these exposure conditions can be represented by poincare sphere parameter vector $(\epsilon,\tau) = [(\epsilon^{(1)},\tau^1),(\epsilon^{(2)},\tau^2),\ldots,(\epsilon^{(N)},\tau^N)]$, where $(\epsilon^{(n)},\tau^{(n)})$ $(n \in [1,N]))$ is the poincare sphere parameter of the nth exposure condition.

For a RF birdcage coil or transmit coil with 2 channels, the total B_1^+ field at each region of interest (ROI) iso-plane can be expressed as the weighted superposition of the B_1^+ field generated by each channel in the RF coil. Let 2 x 1 vector, $\mathbf{b_1}=[b_1^{(1)}(\mathbf{r}), b_1^{(2)}(\mathbf{r})]^T$ be the complex B_1^+ field vector, where $b_1^{(1)}(\mathbf{r})$ and $b_1^{(2)}(\mathbf{r})$ are the complex B_1^+ field generated by the 1*st* and 2*nd* channel of the RF coil at location $\mathbf{r}$. Let 2 x 1 vector $\mathbf{v}_{(\epsilon^{(n)},\tau^{(n)})} = [v^{(1)}, v^{(2)}]^T$ be the complex excitation vector under exposure condition n, where $v^{(1)}$ and $v^{(2)}$ are the corresponding complex amplitude of the 1st and 2nd channels. The total B_1^+ field for each specific exposure condition n can then be expressed as follows:

$$\|B^+_{1,(\epsilon^{(n)},\tau^{(n)})}(r)\| = \|\boldsymbol{b_1}^T \boldsymbol{v}_{(\epsilon^{(n)},\tau^{(n)})}\| \quad (3)$$

The coefficient of variation of $\|B_1^+\|$, defined as the SD over the mean value, is a commonly accepted figure of merit as a measure of the homogeneity of $\|B_1^+\|$, can be obtained through Equation 4:

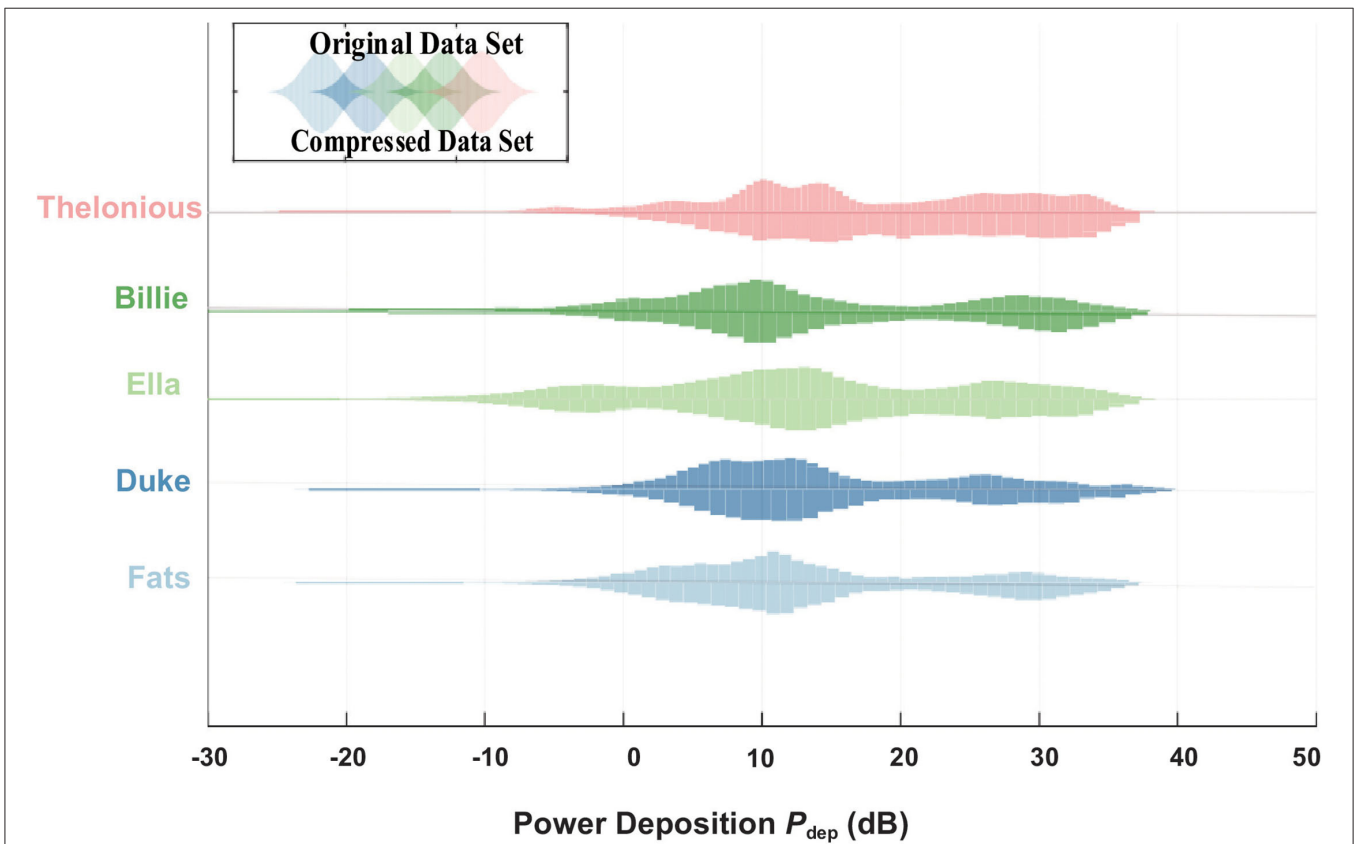

FIGURE 5 | Power deposition (P_{dep}) distribution of the original data set from the data library (up) and compressed data set by PCA (down).

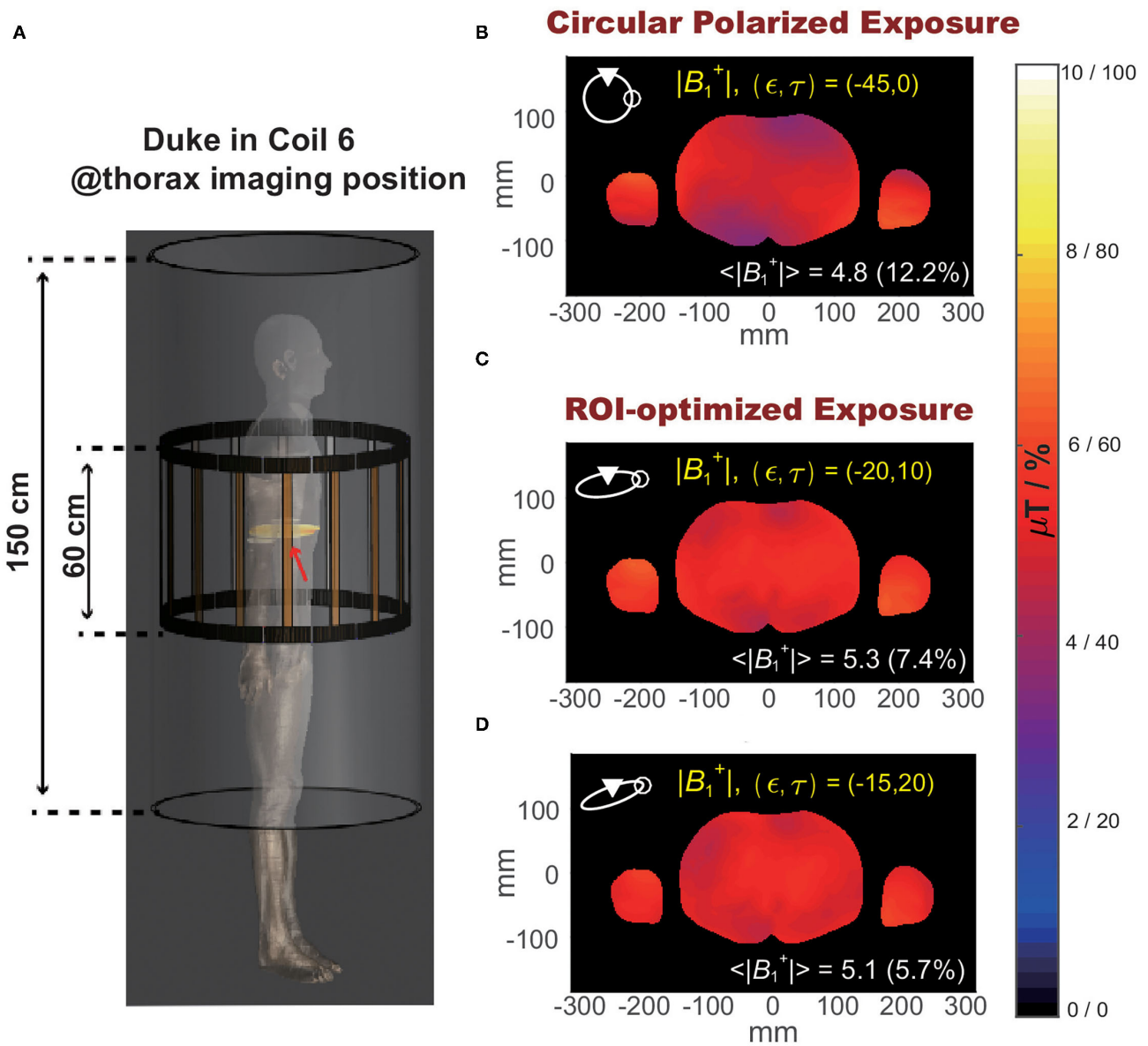

FIGURE 6 | (A) Illustration of the selected clinical scenario: Duke in RF coil 6 at thorax imaging position. **(B)** Spatial distribution of B_1^+ magnitude at an iso-center slice of Duke under circular polarized B_1 field. **(C)** Spatial distribution of B_1^+ magnitude at the iso-center slice of Duke under optimized exposure condition resulting in maximum B_1^+ magnitude. **(D)** Spatial distribution of B_1^+ magnitude over iso-center slice of Duke under optimized exposure condition resulting in minimum $B_{1,cov}^+$.

$$B^+_{1,cov,(\epsilon^{(n)},\tau^{(n)})} = \frac{\sigma}{\|\overline{B^+_{1,(\epsilon^{(n)},\tau^{(n)})}}\|} \tag{4}$$

where σ is the standard deviation of $\|B^+_{1,(\epsilon^{(n)},\tau^{(n)})}\|$ over the ROI iso-plane. Similar to the B_1 field, tangential electrical field under the n_{th} exposure condition $\mathbf{E}_{\mathbf{tan},(\epsilon^{(n)},\tau(n))}(\mathbf{l})$ can be expressed as the weighted superposition as follows:

$$\boldsymbol{E}_{\boldsymbol{tan},(\epsilon^{(n)},\tau^{(n)})}(\boldsymbol{l}) = \boldsymbol{e}_{\boldsymbol{tan}}\boldsymbol{v}^{\boldsymbol{T}}_{(\epsilon^{(n)},\tau^{(n)})} \tag{5}$$

where $\boldsymbol{e}_{\boldsymbol{tan}}=[e_{tan,1}, e_{tan,2}]^T$ is the tangential electric field generated by the two RF coil channels. Therefore, the local power deposition at the electrode-tissue interface under this exposure condition can be concisely expressed as follows:

$$P_{dep,(\epsilon^{(n)},\tau^{(n)})} = W_0\|\boldsymbol{h}^T\boldsymbol{E}_{\boldsymbol{tan},(\epsilon(n),\tau(n))}(\boldsymbol{l})\| \tag{6}$$

In this work, we selected one specific clinical scenario (anatomical model Duke inside RF coil 6 at the thorax imaging position) to perform the exposure optimization, the following Magnitude Least Squares (MLS) optimization strategy

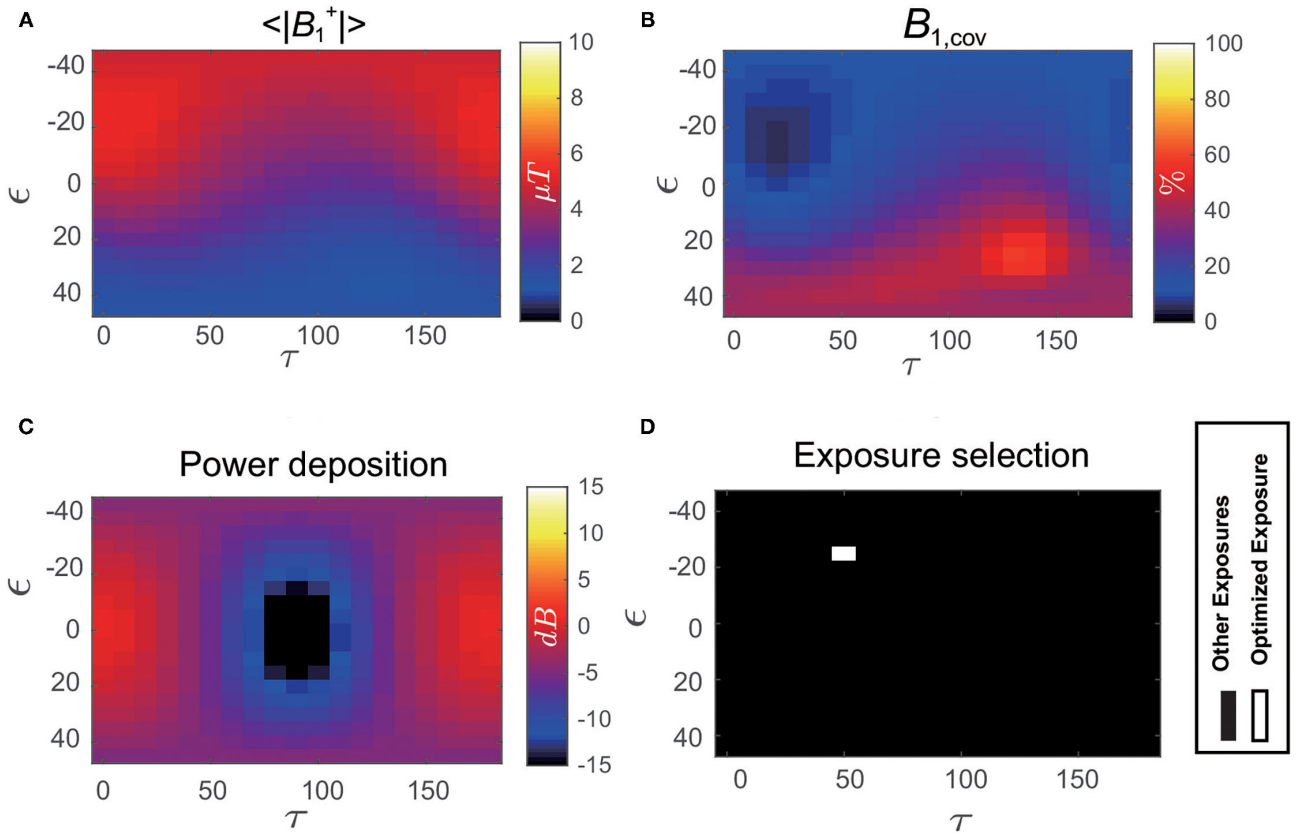

FIGURE 7 | (A) Distribution of B_1^+ magnitude averaged over the iso-center slice of Duke as a function of B_1 polarization (ϵ, τ). **(B)** Distribution of B_1^+ coefficient of variation $B_{1,cov}^+$ over the iso-center slice of Duke as a function of B_1 polarization (ϵ, τ). **(C)** Distribution of *in vivo* power deposition (P_{dep}) of the implant under test (IUT) implanted inside Duke as a function of B_1 polarization (ϵ, τ). **(D)** Optimized exposure condition using the exposure optimization procedure performed on Duke under selected clinical scenario is shown as white.

is performed to determine the optimized excitation parameter $(\epsilon^{(j)}, \tau^{(j)})$:

$$\min_{(\epsilon^{(j)},\tau^{(j)})} \|P_{dep,(\epsilon,\tau)} + B^+_{1,cov(\epsilon,\tau)} - \|B^+_{1,(\epsilon,\tau)}\|\|^2 \qquad (7)$$

RESULTS

Figure 4 demonstrates the PCA-guided clinical factor decoupling procedure. More than 0.3 billion clinical scenarios are contained in the data library, including 5 human models × 6 routing groups × 100 routings for each group × 10 RF coils × 32 imaging positions × 360 exposure polarization. First, to decouple the target implant routing (left-side cardio pacemaker, namely PM_L) from other routings, PCA procedure is performed on the six routing groups. The covariance matrix for the six routing groups (DBS_L, DBS_R, PM_L, PM_R, SCS_L, and SCS_R) are shown on the top row of **Figure 4**. We define two variables as correlated when $C_{i,j} \geq 0.95$ and shown as white, otherwise, it is considered to be uncorrelated and shown as black. The results show that, for the five anatomical models, all implant routings are independent to each other except for the SCS_L and SCS_R, this is due to the fact that the IUT is too short (40 cm) to see the separation between left side and right side. Same PCA procedure is performed on the 100 routings in each group. The resulting covariance matrix has all the elements $C_{i,j}$ bigger than 0.95, therefore, for each routing group, only 1 routing needs to be selected.

In the next setp, the covariance matrix of the RF coils are calculated as shown in the middle row of **Figure 4**, following the same PCA procedure, the RF coil is compressed to only one, here, we choose RF coil 6. After the selection of the RF coil, the imaging positions are decoupled using the same PCA procedure, as shown in the bottom row of **Figure 4**. From the covariance matirx we can see that the imaging positions can be compressed to at most 14 groups (e.g., for anatomical model ELLA, imaging positions 0–10 (head to thorax imaging positions) can be compressed as group 1, imaging position 15–20 (pelvis imaging position) may be compressed as group 6, and position 25–30 (extremeties imaging positions) can be compressed as group 9). After the PCA guided data compression procedure, only 0.25 million clinical scenarios are selected from the original more than 0.3 billion data set. Among these selected data sets, the exposure optimization only need to be done among the 70 specific clinical scenarios (5 human × 1 RF coil × 14 imaging positions), as the exposure dimension

(360 exposure polarizations) will be compressed by the exposure optimization procedure, where the optimized exposure condition will be selected to maintain patient safety and imaging quality.

The *in vivo* RF-induced heating of the generic 40 cm implant was estimated with both original clinical scenarios and the selected ones based on PCA guidance. As shown in **Figure 5**, the power deposition dynamic range of the selected clinical scenarios are the same as those with original clinical scenarios.

Figure 6 shows the slice view of the $\|B_1^+\|$ at an iso-center slice of an example clinical scenario: anatomical model Duke inside RF coil 6 at thorax imaging position (demonstrated in **Figure 6A**). Compared to the default circular polarized exposure (ϵ, τ)=$(45^o, 0)$ as shown in **Figure 6B**, the exposure allows maximum averaged B_1^+ field magnitude, shown in **Figure 6C**, improved averaged B_1^+ field magnitude $< \|B_{1,(\epsilon,\tau)}^+\| >$ from 4.8 to 5.3 μT, while the exposure allows minimum $B_{1,cov}^+(\epsilon, \tau)$, as shown in **Figure 6D**, decreased $B_{1,cov}^+(\epsilon, \tau)$ from 12.2 to 5.7%.

Figure 7 shows the distribution of power deposition of the IUT as a function of the B_1 polarization ($P_{dep}(\epsilon, \tau)$) evaluated at the normal operating mode. The optimized exposure conditions that satisfy not only the image quality requirement (high $< \|B_1^+\| >$ and small $B_{1,cov}^+$) but also RF-induced heating limitation (low P_{dep}) are shown as white in the bottom-right of **Figure 7**.

CONCLUSION

In this work, we established an *in silico* exposure optimization trial that comprises a data library with a large permutation of different clinical scenarios to increase the evaluation completeness. To balance between the efficiency and completeness during the exposure optimization procedure, critical clinical factors are recognized and decoupled from the data library using principle component analysis. The proposed work-flow is applied to a generic 40-cm long active medical implant devices implanted in a 34-year-old male adult anatomical model as a pacemaker and exposed under 1.5T MRI RF magnetic field. The results show that the established workflow facilitates exploratory data analysis during exposure optimization, exposure conditions maximizing both imaging quality and patient safety under critical clinical scenarios can be identified.

DATA AVAILABILITY STATEMENT

The datasets presented in this article are not readily available because the dataset is licensed. Requests to access the datasets should be directed to https://itis.swiss/virtual-population/explib/overview/.

AUTHOR CONTRIBUTIONS

All authors listed have made a substantial, direct, and intellectual contribution to the work and approved it for publication.

FUNDING

This work was supported by National Natural Science Foundation of China (Grant No. 6210010061).

ACKNOWLEDGMENTS

The authors would like to thank Zurich Medtech (ZMT, Zurich, Switzerland) for providing Sim4Life for scientific use.

REFERENCES

1. Kraus JD, Carver KR. *Electromagnetics*. New York, NY: McGraw-Hill (1973).
2. Balanis CA. *Advanced Engineering Electromagnetics*. Wiley (1989).
3. Nordbeck P, Ertl G, Ritter O. Magnetic resonance imaging safety in pacemaker and implantable cardioverter defibrillator patients: how far have we come? *Eur Heart J*. (2015) 36:1505–11. doi: 10.1093/eurheartj/ehv086
4. Davis L, Kaufman L, Margulis R. Potential Hazards in NMR Imaging: heating effects of changing magnetic fields and RF fields on small metallic implants. *Am J Roentgenol*. (1981) 137:857–60. doi: 10.2214/ajr.137.4.857
5. Brown T, Goldstein B, Little J. Severe burns resulting from magnetic resonance imaging with cardiopulmonary monitoring risks and relevant safety precautions. *Am J Phys Med Rehabil*. (1993) 77:166–7. doi: 10.1097/00002060-199306000-00012
6. Ladd ME, Quick HH. Reduction of resonant RF heating in intravascular catheters using coaxial chokes. *Magn Reson Med*. (2000) 43:615–9. doi: 10.1002/(SICI)1522-2594(200004)43:4<615::AID-MRM19>3.0.CO;2-B
7. Weiss S, Vernickel P, Schulz V, Gleich B. Transmission line for improved RF safety of interventional devices. *Magn Reson Med*. (2005) 54:182–9. doi: 10.1002/mrm.20543
8. Eryaman Y, Turk EA, Oto C, Algin O, Atalar E. Reduction of the radiofrequency heating of metallic devices using a dual-drive birdcage coil. *Magn Reson Med*. (2013) 69:845–52. doi: 10.1002/mrm.24316
9. Gudino N, Sonmez M, Yao Z. Parallel transmit excitation at 1.5T based on the minimization of a driving function for device heating. *Med Phys*. (2015) 42:359–71. doi: 10.1118/1.4903894
10. Etezadi-Amoli M, Stang P, Kerr A, Pauly J, Scott G. Controlling radiofrequency-induced currents in guidewires using parallel transmit. *Magn Reson Med*. (2015) 74:845–52. doi: 10.1002/mrm.25543
11. Yao A, Murbach M, Goren T, Kuster N. Radiofrequency-induced risks during magnetic resonance imaging: dependence upon birdcage design. In: *Proceedings of 28th International Society for Magnetic Resonance in Medicine (ISMRM) Annual Meeting*. (2020).
12. Lucano E, Liberti M, Mendoza GG, Lloyd T, Iacono MI, Apollonio F, et al. Assessing the electromagnetic fields generated by a radiofrequency MRI body coil at 64 MHz: defeaturing vesus accuracy. *IEEE Trans Biomed Eng*. (2016) 63:1591–601. doi: 10.1109/TBME.2015.2506680
13. Yao A, Zastrow E, Cabot E, Lloyd B, Schneider B, Kainz W, et al. Anatomical model uncertainty for RF evaluation of AIMD under MRI exposure. *Bioelectromagnetics*. (2019) 40:458–71. doi: 10.1002/bem.22206
14. Liu W, Wang H, Zhang P, Li C, Sun J, Chen Z, et al. Statistical evaluation of radiofrequency exposure during magnetic resonant imaging: Application of whole-body individual human model and body motion in the coil. *Int J Environ Res Public Health*. (2019) 16:1069. doi: 10.3390/ijerph1606106
15. Gosselin MC, Neufeld E, Moser H, Huber E, Farcito S, Gerber L, et al. Development of a new generation of high-resolution anatomical models for medical device evaluation: the virtual population 3.0. *Phys Med Biol*. (2013) 59:5287–303. doi: 10.1088/0031-9155/59/18/5287
16. Hasgall PA, Di Gennaro F, Baumgartner C, Neufeld E, Lloyd B, Gosselin MC, et al. *IT'IS Database for Thermal and Electromagnetic Parameters of Biological Tissues, Version 4.0*. (2018). doi: 10.13099/VIP21000-04-0.

17. Park SM, Kamondetdacha R, Nyenhuis JA. Anatomical model uncertainty for RF evaluation of AIMD under MRI exposure. *J Magn Reson Imaging*. (2007) 26:1278–85. doi: 10.1002/jmri.21159
18. Jolliffe IT. *Principle Component Analysis*. New York, NY: Springer-Verlag (2002).

Conflict of Interest: The authors declare that the research was conducted in the absence of any commercial or financial relationships that could be construed as a potential conflict of interest.

Publisher's Note: All claims expressed in this article are solely those of the authors and do not necessarily represent those of their affiliated organizations, or those of the publisher, the editors and the reviewers. Any product that may be evaluated in this article, or claim that may be made by its manufacturer, is not guaranteed or endorsed by the publisher.

frontiers in Public Health

ORIGINAL RESEARCH
published: 07 January 2022
doi: 10.3389/fpubh.2021.777759

A Monte Carlo Analysis of Actual Maximum Exposure From a 5G Millimeter-Wave Base Station Antenna for EMF Compliance Assessments

Bo Xu, David Anguiano Sanjurjo, Davide Colombi and Christer Törnevik*

Ericsson Research, Ericsson AB, Stockholm, Sweden

International radio frequency (RF) electromagnetic field (EMF) exposure assessment standards and regulatory bodies have developed methods and specified requirements to assess the actual maximum RF EMF exposure from radio base stations enabling massive multiple-input multiple-output (MIMO) and beamforming. Such techniques are based on the applications of power reduction factors (PRFs), which lead to more realistic, albeit conservative, exposure assessments. In this study, the actual maximum EMF exposure and the corresponding PRFs are computed for a millimeter-wave radio base station array antenna. The computed incident power densities based on near-field and far-field approaches are derived using a Monte Carlo analysis. The results show that the actual maximum exposure is well below the theoretical maximum, and the PRFs similar to those applicable for massive MIMO radio base stations operating below 6 GHz are also applicable for millimeter-wave frequencies. Despite the very low power levels that currently characterize millimeter-wave radio base stations, using the far-field approach can also guarantee the conservativeness of the PRFs used to assess the actual maximum exposure close to the antenna.

Keywords: 5G, base station antenna, beamforming, EMF exposure, incident power density, millimeter wave

OPEN ACCESS

Edited by:
Kun Li,
Kagawa University, Japan

Reviewed by:
Kensuke Sasaki,
National Institute of Information and Communications Technology, Japan
Tongning Wu,
China Academy of Information and Communications Technology, China

****Correspondence:***
Bo Xu
bo.xu@ericsson.com

Specialty section:
This article was submitted to Radiation and Health, a section of the journal Frontiers in Public Health

Received: *15 September 2021*
Accepted: *17 November 2021*
Published: *07 January 2022*

Citation:
Xu B, Anguiano Sanjurjo D, Colombi D and Törnevik C (2022) A Monte Carlo Analysis of Actual Maximum Exposure From a 5G Millimeter-Wave Base Station Antenna for EMF Compliance Assessments. Front. Public Health 9:777759. doi: 10.3389/fpubh.2021.777759

INTRODUCTION

To meet the increasing demands on mobile traffic data, the fifth-generation cellular communication technology (5G) exploits the frequency spectrum above 24 GHz, which provides much wider and contiguous bands compared with the crowded and fragmented spectrum below 6 GHz. This frequency spectrum is also called millimeter-waves (mmW) or the frequency range 2 (FR2) in 5G (1). Before radio base stations (RBSs) are placed on the market, manufacturers normally need to conduct electromagnetic field (EMF) exposure assessments to determine the so-called compliance boundaries or exclusion zones. Outside the compliance boundary, the EMF exposure from an RBS is below the relevant EMF exposure limits, for example, those provided in the international EMF exposure guidelines. The most widely adopted EMF exposure guidelines are provided by the International Commission on Non-Ionizing Radiation Protection (ICNIRP) (2, 3). As the previous generations of mobile communication technologies, 5G equipment, including mmW RBSs, must comply with the same EMF exposure guidelines.

EMF exposure assessments for RBSs are normally carried out using the far-field antenna radiation patterns (4). This approach, referred to as the far-field approach in the rest of the article, is accurate when the resulting compliance boundary is located sufficiently far from the RBS antenna. When the transmitted power of an RBS is very low, the EMF exposure levels might be greatly overestimated by the far-field approach (5). In such scenarios, estimation formulas based on cylindrical models (6), full-wave simulation methods, and field strength measurements (7) are usually used (4) to get more accurate compliance boundaries.

For RBSs enabling multi-input multi-output (MIMO), massive MIMO, and beamforming, the antenna radiation pattern changes dynamically according to the real-time channel conditions. When determining the compliance boundary using maximum configured power and the envelope of all possible radiation patterns, the results are very conservative. This is because such an approach assumes that all the power is constantly transmitted in all directions without considering the effects of time-averaging. The EMF exposure determined based on these unrealistic assumptions is referred to as the theoretical maximum exposure. Therefore, the International Electrotechnical Commission (IEC) (4) has developed methodologies that allow for more accurate exposure assessments based on the actual maximum exposure. This approach is described in an IEC technical report (8), and it will be part of the new edition of the international standard IEC 62232 (9), which is currently under revision. The actual maximum exposure considers the effects of dynamical radiation pattern changes on the time-averaged EMF levels and can be determined by applying a power reduction factor (PRF) to the theoretical maximum transmitted power. In literature, the PRF is normally determined by statistically conservative models, for instance, based on the 95th percentile time-averaged exposure derived from the cumulative distribution function (CDF) (10–14). Results from recent measurement campaigns (15–17) also show that the EMF exposure from real massive MIMO RBS sites is well below the actual maximum exposure derived from the statistical models.

Unlike massive MIMO RBSs operating below 6 GHz, which are characterized by high-peak equivalent isotropically radiated power (EIRP) and support wide coverage in ranges of a few kilometers, mmW RBSs usually aim at providing smaller cell coverage in a radius of a few hundred meters but with higher capacity. Therefore, the peak EIRP levels of mmW RBSs are usually lower, resulting in a smaller compliance boundary with a typical front compliance distance of a few meters or less. When applied very close to the antenna, the estimation of exposure levels using the far-field approach may be very conservative. In addition, it is not clear whether the PRFs derived from the far-field radiation patterns obtained in some other studies (10–14) are still applicable when compliance boundaries are in the radiating near-field region. Several works, for example, Refs (18–31), addressing the EMF compliance and assessments for lower-power mmW devices can be found in literature, but only a few (32) address the actual maximum exposure from mmW RBSs.

This article presents a case study of the actual maximum exposure for a typical mmW RBS antenna configuration. The Monte Carlo method is applied to the time-averaged exposure using a predefined user equipment (UE) distribution and a beamforming codebook. The actual maximum exposure and the PRF in the radiating near-field region are derived through full-wave simulations. The results are also compared with the actual maximum exposure computed using the far-field approach.

METHODS

Array Antenna Model and Beam Patterns

In this study, an 8 × 24 patch array is considered as the mmW RBS antenna using the model built in Ref (33), as shown in **Figure 1**. The array antenna operates at 28 GHz. A predefined codebook based on progressive phase shift is created to enable the spatial coverage of 30 degrees in elevation and 120 degrees in azimuth. As the UE distribution considered below is set at $\theta = 93^\circ$ and spread over the azimuthal plane [see Equation (5)], only the beams pointing at the plane of $\theta = 93^\circ$ contribute to the Monte Carlo analysis. The used beam patterns, in EIRP, are shown in **Figure 2**. As an example, the azimuthal cut of the far-field pattern for the beam closest to the broadside direction is shown in **Figure 2A**, and the far-field patterns for the beams pointing at the cut of $\theta = 93^\circ$ are shown in **Figure 2B**. For simplicity, only one polarization is used, and the fields generated by the orthogonal polarization is conservatively summed up by adding 3 dB to the peak EIRP. The combined peak EIRP level is 58.4 dBm. A time division duplex (TDD) downlink duty cycle of 75% is used. The peak total EIRP is thus $(58.4 + 10\log_{10}0.75)$ dBm. The field strength distributions on different planes and the radiation pattern for each beam are computed using the full-wave simulation software Altair Feko with the multilevel fast multipole method (MLFMM) solver. The electric field and magnetic field

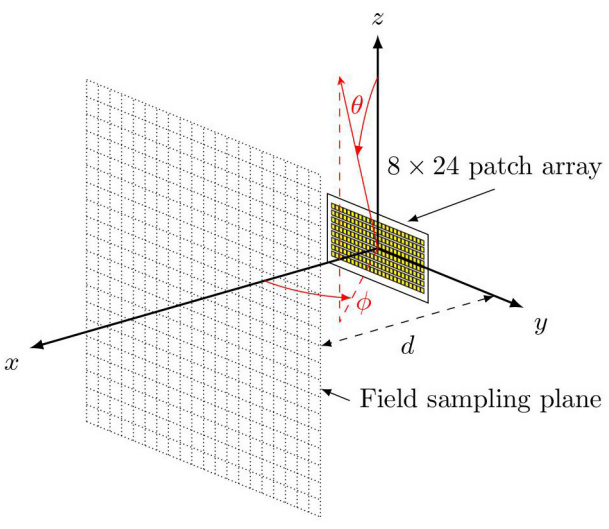

FIGURE 1 | Feko model of the 8 × 24 patch antenna array. The red markers indicate the convention of the used spherical coordinate system.

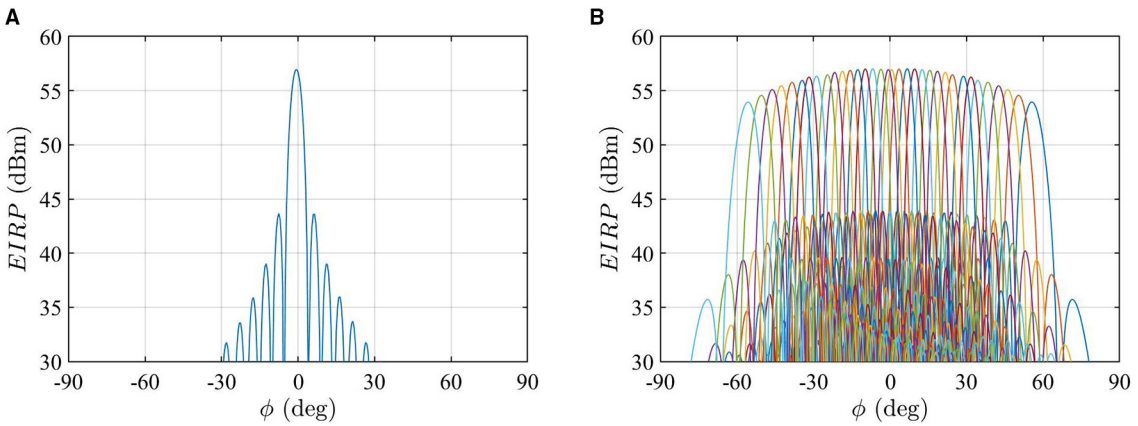

FIGURE 2 | (A) The azimuthal cut of the radiation pattern for the beam pointing at $\theta_0 = 93°$ and $\phi = -1°$, which is the closest beam to the broadside direction in the used codebook. **(B)** The azimuthal cut of simulated beam patterns at $\theta_0 = 93°$, which are those used in the Monte Carlo analysis. The beam patterns with different colors from the left to the right correspond to beam indices *I* denoted from 1 to 34.

are sampled with a 5 mm interval on a 2 m × 2 m area in the *yz*-planes at different distances. The far-field radiation pattern for each beam is sampled with 0.5 degrees over the sphere.

EMF Exposure Metrics

The EMF exposure metric used in this study is incident power density. For short, it is referred to as power density in the following. The power density limits are intended as spatial average and time average values according to the ICNIRP 1998 guidelines (2) and the ICNIRP 2020 guidelines (3). The implications on EMF assessments of RBSs between the ICNIRP 1998 and ICNIRP 2020 guidelines are addressed in a separate article (34). Hereafter, only the differences relevant to the investigated mmW RBS are presented.

For the ICNIRP 1998 guidelines, the power density is averaged over any 20 cm^2 of exposed area and over $68f^{-1.05}$ min where f is the frequency in GHz (about 2 min and 3 s at 28 GHz.), while for the ICNIRP 2020 guidelines, the power density at 28 GHz is averaged over a 4 cm^2 square and over 6 min. For the ICNIRP 1998 limits, the power density is averaged over square-shaped areas in this article. The applicable general public limit values are 10 W/m^2 and $55f^{-0.177}$ W/m^2 (about 30.5 W/m^2 at 28 GHz) for the ICNIRP 1998 and ICNIRP 2020 guidelines, respectively.

When assessing compliance with the ICNIRP 2020 guidelines and for the power levels used in this article (lower than 1 W), the local exposure is the limiting factor determining the compliance boundary. Compliance with the whole-body exposure limits is implicitly met using the whole-body exclusion criteria[1]. The mentioned power density limits and requirements on spatial averaging and time averaging are summarized in **Table 1**.

The spatially averaged power density is expressed as

$$S = \frac{1}{A}\int_A \mathrm{Re}\left[\boldsymbol{E} \times \boldsymbol{H}^*\right] \cdot \hat{\boldsymbol{n}}\, \mathrm{d}A, \tag{1}$$

where A is the averaging area in m^2; $\boldsymbol{E}$ and $\boldsymbol{H}$ are the root-mean-square (rms) electric and magnetic fields in V/m and A/m, respectively; * denotes the conjugate; and $\hat{\boldsymbol{n}}$ is the unit vector normal to A. This expression is in line with the definition in Refs (35, 36). In this article, the spatially averaged power density is computed in planes parallel to the antenna surface and for different distance d (see **Figure 1**). This is referred to as the near-field approach in the following.

When applying this expression on devices operating close to the human body, such as 5G mobile phones using mmW bands, the assessment plane and the average areas parallel to the outer surface of the device are mostly relevant. For distances up to a few meters of interest in this study, the orientation of the averaging area may be arbitrary considering the real usage scenarios. Thus, for mmW RBSs, the magnitude of the Poynting vector may also be a reasonable quantity for EMF assessments

$$S = \frac{1}{A}\int_A \left|\mathrm{Re}\left[\boldsymbol{E} \times \boldsymbol{H}^*\right]\right| \mathrm{d}A. \tag{2}$$

The results using Equation (1) are presented in the main body of the article, whereas the comparison between Equations (1) and (2) for actual maximum power density is given in the **Supplementary Material**. The differences in actual maximum power density are found to be small (<5%, see **Supplementary Figure 1**).

In the far-field region, the power density is well characterized by the spherical model (also called the far-field formula) (4). In a spherical coordinate system, the power density can be

[1]For RBSs with transmitted power less than 1 W, the whole-body–specific absorption rate (SAR) is below the whole-body SAR limit for general public (0.08 W/kg) by conservatively assuming that all power is absorbed by the body with a mass of 12.5 kg for a 4-year-old child, as described in Ref (4).

TABLE 1 | Incident power density limits for the general public at 28 GHz and assumed number of active UEs during the averaging time.

	Incident power density limits for local exposure	Averaging area	Averaging time	Assumed number of active UEs during EMF averaging time for Monte Carlo analysis
ICNIRP 1998	10 W/m^2	20 cm^2	2 min and 3 s	$N = 33,\ 66,\ 100$
ICNIRP 2020	30.5 W/m^2	4 cm^2	6 min	$N = 100,\ 200,\ 300$

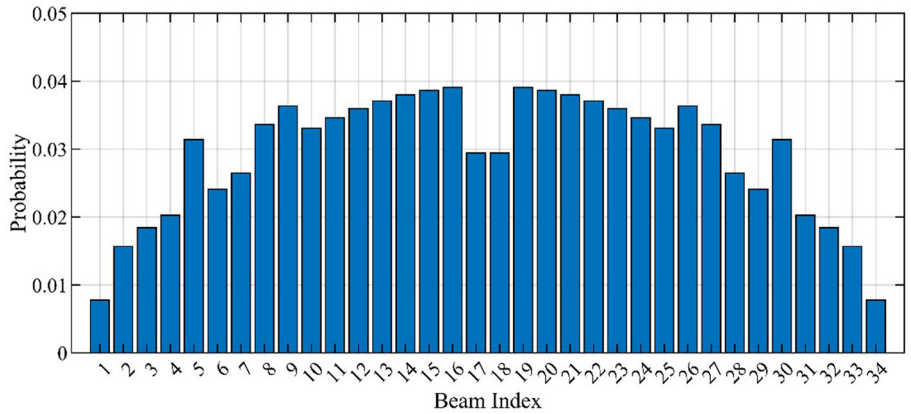

FIGURE 3 | Service probabilities of the selected beams.

expressed as

$$S(r,\theta,\phi) = \frac{PG(\theta,\phi)}{4\pi r^2} = \frac{EIRP(\theta,\phi)}{4\pi r^2}, \tag{3}$$

where P is the transmitted power in watts, G is the radiation gain in linear scale, r is the radius in meters, θ is the polar angle in degrees, and ϕ is the azimuthal angle in degrees. In the far-field region, the fields are uniform over the averaging area, and Equation (3) can also be considered to provide the spatially averaged results.

In the ICNIRP 2020 guidelines, in addition to the time-averaged power density, the so-called brief exposure limits are defined for local exposure and apply to any pulse, group of pulses, or subgroup of pulses in a train, as well as from the summation of exposures (including non-pulsed EMFs), occur within 6 min. The brief exposure limits corresponding to incident power density limits are given in terms of incident energy density. Between >6 and 300 GHz, the incident energy density limits in kJ/m^2 for the general public are expressed as

$$U(t) = 55f^{-0.177} \times 0.36\left[0.05 + 0.95\,(t/360)^{0.5}\right] \tag{4}$$

where f is the frequency in GHz and t is time in seconds. U is to be averaged over 4 cm^2 square at 28 GHz as for power density. When $t = 360\ s$, Equation (4) gives the same value as if integrating the power density limits (see **Table 1** for the ICNIRP 2020 guidelines) over 6 min.

In this study, the actual maximum exposure levels and PRFs are derived using Equations (1) and (3) with the following conditions.

Service Probability

For a statistical approach, the service probability of each beam depends on the distribution of active UE in space. In this study, the spatial UE distribution defined in Refs (10) and (14) is reused, which is a cosine-shaped function:

$$w(\theta,\phi) = \begin{cases} \frac{3}{4}\delta(\theta-\theta_0)\cos\frac{3\phi}{2}, & -60^\circ \le \phi \le 60^\circ \\ 0, & \text{otherwise} \end{cases} \tag{5}$$

where $\theta_0 = 93^\circ$ for the used beams. Such a distribution can be found in Figure 3 of (10) and Figure 4 of (14). It implies that more UEs are located close to the boresight direction ($\int_\theta w(\theta, 0^\circ)\mathrm{d}\theta = \frac{3}{4}$) and fewer UEs are located close to the angular edge of the cell ($\int_\theta w(\theta, \pm 60^\circ)\mathrm{d}\theta = 0$). This distribution conservatively assumes that the UEs are only distributed in the azimuthal direction, and no beam scanning in elevation is therefore applied during the Monte Carlo analysis. Consequently, the derived PRFs and actual maximum exposure are more conservative than those derived with beam-steering in elevation, as pointed in Ref (10).

Similar to those in Refs (10) and (14), the angular service establishment range for each beam is defined as

$$\left(\hat{\theta}_l, \hat{\phi}_l\right) = \left\{(\theta,\phi)\middle| EIRP\left(\theta,\phi,l\right) > EIRP\left(\theta,\phi,m\right), l \ne m\right\},$$
$$l, m = 1, 2, \cdots, c, \tag{6}$$

where l and m are the beam indices, and the total number of beams is denoted by c.

The service probability of the lth beam is thus defined as (10, 14).

$$p\left(l\right) = \int_{\hat{\theta}_l}\int_{\hat{\phi}_l} w(\theta,\phi)\sin\theta\ \mathrm{d}\theta\mathrm{d}\phi. \tag{7}$$

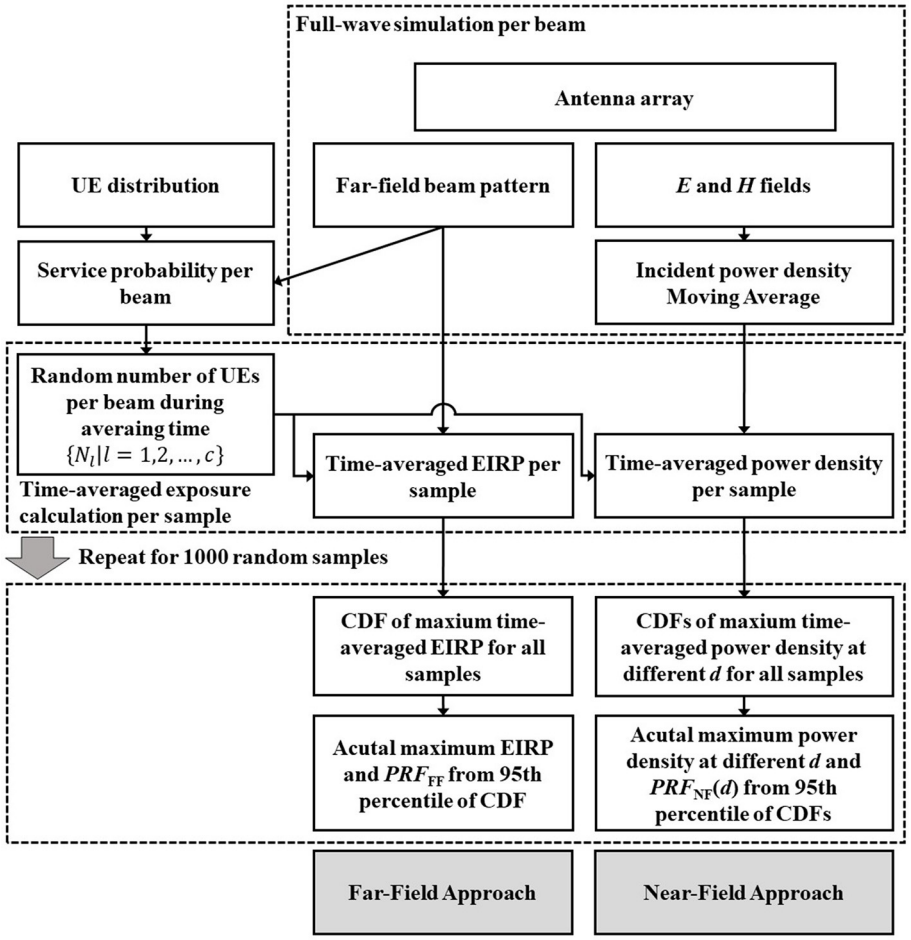

FIGURE 4 | Workflow of antenna simulation and Monte Carlo analysis.

Using the far-field beam patterns shown in **Figure 2B** and the UE distribution [Equation (5)], the service probabilities for the selected beams are shown in **Figure 3**. In **Figure 3**, the beam index from 1 to 34 corresponds to the beam pointing from −60 degrees to + 60 degrees. Note that the $p(l)$ values for the beam indices 17 and 18 closest to the broadside direction (see **Figure 3**) are slightly lower than the adjacent beams. This is because the beams are denser in the broadside direction for the used codebook (see **Figure 2**) and the beams closest to the broadside direction usually have narrower beamwidth.

Monte Carlo Analysis

The time-averaged EIRP and power density can be computed through the Monte Carlo method using Equation (7). Assuming that N active UEs are scheduled during the EMF averaging time, the number of UEs served by the lth beam, N_l, during the EMF averaging time is determined by the multinomial distribution,

$$\Pr\{N_l|N\} \sim \text{Multinom}\left(N, \{p(l)\}\right), \qquad l = 1, 2, \ldots, c \quad (8)$$

where $N = \sum_{l=1}^{c} N_l$. This is aligned with what is used in Ref (14). The energy transmitted to each UE is assumed equal, and the traffic load is assumed to be 100% (full buffer). It is well understood that a smaller N will result in larger PRF and actual maximum exposure. In this study, $N = 33$, 66, 100 and $N = 100$, 200, 300 are assumed for the ICNIRP 1998 (averaged over 2 min and 3 s) and ICNIRP 2020 (averaged over 6 min) limits, respectively. According to the network counter data from real operating networks (15–17), these chosen N values are very conservative. See **Table 1** for the summary of used limits and assumptions. The detailed description of Monte Carla analysis to address the implications of the incident energy density limits can be found in the **Supplementary Material**. For each sample used for the Monte Carlo analysis, the time-averaged EIRP can be written as

$$EIRP_{\text{av}}(\theta, \phi) = \sum_{l=1}^{c} \frac{N_l}{N} EIRP_l(\theta, \phi), \quad (9)$$

where $EIRP_l(\theta, \phi)$ is the EIRP of the lth beam in direction (θ, ϕ).

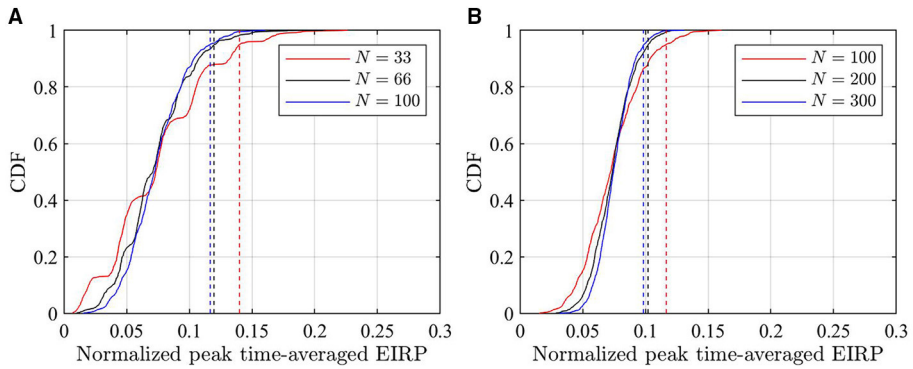

FIGURE 5 | CDFs of peak time-averaged EIRP normalized to the maximum EIRP using different *N* samples. **(A)** CDF considered for ICNIRP 1998 limits. **(B)** CDF considered for ICNIRP 2020 limits. The dashed lines indicate the corresponding 95th percentile.

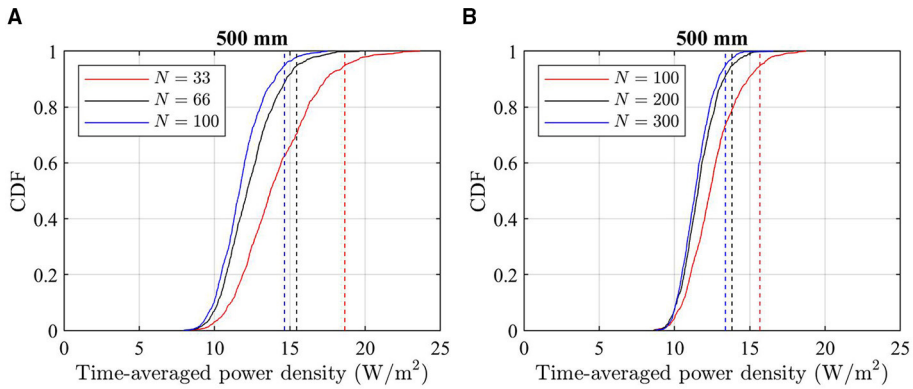

FIGURE 6 | Examples of CDFs of peak time-averaged, spatially averaged power density for different *N* at $d = 500$ mm. **(A)** Peak 20 cm^2 averaged power density considered for ICNIRP 1998 guidelines. **(B)** Peak 4 cm^2 averaged power density considered for ICNIRP 2020 guidelines. The dashed lines indicate the corresponding 95th percentile.

For each sample, the peak time-averaged, spatially averaged power density in different planes $x = d$ can be written as

$$S_{\mathrm{av}}\left(d\right) = \max_{y,z} \sum_{l=1}^{c} \frac{N_l}{N} S_l\left(d, y, z\right), \tag{10}$$

where $S_l\left(d, y, z\right)$ is the spatially averaged power density on the plane of $x = d$ for the lth beam.

For a given N, the Monte Carlo analysis is carried out using $EIRP_{\mathrm{av}}\left(\theta, \phi\right)$ and $S_{\mathrm{av}}\left(d\right)$ from 1000 samples. Different samples are generated with different combinations of $\left\{N_l | l = 1, 2, \ldots, c\right\}$. For a given N, The CDF of $EIRP_{\mathrm{av}}$ is calculated using the results of Equation (9) for all samples. The CDFs for the near-field approach are computed for different d and N with Equation (10). The workflow of the Monte Carlo analysis can be found in **Figure 4**. The PRF for the far-field approach is calculated using the 95th percentile of the CDF of $EIRP_{\mathrm{av}}$

$$PRF_{\mathrm{FF}}\left(\theta, \phi\right) = \frac{EIRP_{\mathrm{av},0.95}\left(\theta, \phi\right)}{EIRP_{\mathrm{evlp}}\left(\theta, \phi\right)} \tag{11}$$

where $EIRP_{\mathrm{av},0.95}\left(\theta, \phi\right)$ is the 95th percentile in the CDF of $EIRP_{\mathrm{av}}\left(\theta, \phi\right)$ in each direction and $EIRP_{\mathrm{evlp}}\left(\theta, \phi\right) = \max_{l=1,2,\ldots,c} EIRP_l\left(\theta, \phi\right)$ is the envelope of traffic beam patterns in terms of EIRP. In the following, the PRF for the far-field approach is referred to as the maximum $PRF_{\mathrm{FF}}\left(\theta, \phi\right)$ value over the scan range, $PRF_{\mathrm{FF,m}}$, which is chosen to determine the compliance distance in the following.

In the near-field approach, the PRF at each distance d is calculated using the 95th percentile of the CDF of $S_{\mathrm{av}}\left(d\right)$.

$$PRF_{\mathrm{NF}}(d) = \frac{S_{\mathrm{av},0.95}\left(d\right)}{\max\limits_{l,y,z} S_l\left(d, y, z\right)} \tag{12}$$

where $S_{\mathrm{av},0.95}\left(d\right)$ is the 95th percentile in the CDF of $S_{\mathrm{av}}\left(d\right)$.

Calculation of Compliance Distance in Front of RBS Antenna

For communication purposes, simplified compliance boundaries, for example, the box-shaped compliance boundary (4), are usually used instead of iso-surface compliance boundaries. In this

study, the compliance distance in front of the RBS is of interest. For the near-field approach, the compliance distance $CD_{\mathrm{NF},x}$ for the actual maximum exposure in front of RBS antenna can be calculated by

$$CD_{\mathrm{NF},x} = \min d, \ \text{ for } S_{\mathrm{av},0.95}\left(d\right) \leq S_{\mathrm{lim}} \tag{13}$$

where S_{lim} is the power density limit.

In general, the spherical model (or the far-field formula) determining the compliance boundary for actual maximum exposure can be written as

$$r\left(\theta,\phi\right) = \sqrt{\frac{EIRP_{\mathrm{evlp}}\left(\theta,\phi\right) \times PRF_{\mathrm{FF,m}}}{4\pi S_{\mathrm{lim}}}}. \tag{14}$$

The front distance of the box-shaped compliance boundary can be expressed as

$$CD_{\mathrm{FF},x} = \max_{\theta,\phi} r_x\left(\theta,\phi\right), \tag{15}$$

where $r_x\left(\theta,\phi\right)$ is $r\left(\theta,\phi\right)$ projected to the x-axis.

RESULTS

The CDFs of $EIRP_{\mathrm{av}}$ [Equation (9)] in the maximum EIRP direction and an example of CDFs for peak time-averaged incident power density [Equation (10)] with different N are shown in **Figures 5**, **6**, respectively. In **Figure 5**, the peak time-averaged EIRP is normalized to the maximum peak EIRP value of all used beams. It is clear that a smaller N results in larger 95th percentile of time-averaged EIRP and incident power density. This is well aligned with the findings of other works. As a conservative approach, $N = 33$ and $N = 100$ are selected in the following for ICNIRP 1998 and ICNIRP 2020 guidelines, respectively.

Figure 7 shows the PRFs for 4 cm^2 averaged and 20 cm^2 averaged power density obtained from the near-field approach. As can be seen from the figure, the PRF values decrease with d. Good converges to the PRF obtained from the far-field approach can be observed above 0.5 m, and above 1 m, the difference in PRFs obtained from the near-field and the far-field approaches is negligible.

In **Figure 8**, the power density levels in front of the array obtained using different approaches are compared at distances below 1.5 m. The power density levels computed using the far-field formula [Equation (3)] are determined for different PRF values, including PRF = 1, that is, the theoretical maximum exposure condition, PRF = 0.32, that is, the PRF value recommended in Ref (10) for sub-6 GHz massive MIMO RBSs, and PRF = 0.15 (for ICNIRP 1998 limits) or PRF = 0.12 (for ICNIRP 2020 limits), that is, the PRF values obtained from the far-field approach shown in **Figure 5**. The actual maximum power densities averaged over 4 and 20 cm^2, that is, $S_{\mathrm{av},0.95}\left(d\right)$, obtained from the near-field approach are also shown in **Figure 8**. The actual maximum power densities computed using the near-field approach are always smaller than or equal to those computed using the far-field approach.

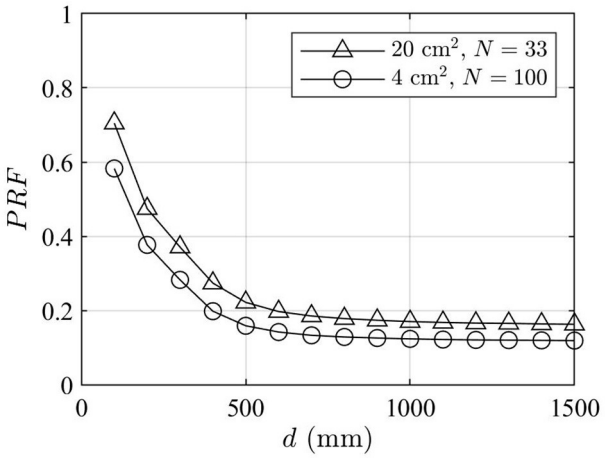

FIGURE 7 | PRFs vs. distance obtained from the near-field approach.

In the upper part of **Figure 9**, the ratios of theoretical maximum power density obtained using the far-field and the near-field approaches are shown. The lower part shows the ratios between PRFs obtained using the near-field and far-field approaches. On one hand, the PRFs at closer distances are higher than those derived from the far-field approach, in line with **Figure 7**. On the other hand, the power density levels computed using the far-field formula [Equation (3)] are significantly higher than the true power density levels computed using the near-field approach [Equation (1)]. Therefore, the far-field approach still provides a conservative estimate of the actual maximum exposure levels. **Table 2** compares the general public front compliance distance by using the results shown in **Figure 8**. The compliance distance results are rounded up to the nearest decimeter.

Figure 10 presents the Monte Carlo analysis results concerning the incident energy density limits. The blue curve is the incident energy density limits at 28 GHz. The position giving the actual maximum power density at $x = 0.4$ m is chosen to illustrate the incident energy density computed through the Monte Carlo analysis. The assumptions at the basis of such analysis are provided in the **Supplementary Material**. To illustrate the potential implications of the brief exposure limits on actual maximum exposure, the incident energy density results from the Monte Carlo analysis are also normalized in the figure, such that the 95th percentile of incident energy density at $t = 360$ s is equal to the limit value at $t = 360$ s (the red curve). The red curve is below the respective limit for intervals shorter than 360 s. This indicates that, according to the implemented model, the derived PRF based on the time-averaged power density ensures compliance also with the incident energy density limits on brief exposure. In addition, an example of Monte Carlo samples for normalized incident energy density is shown (the green curve). Similar figures can be drawn for other positions in space.

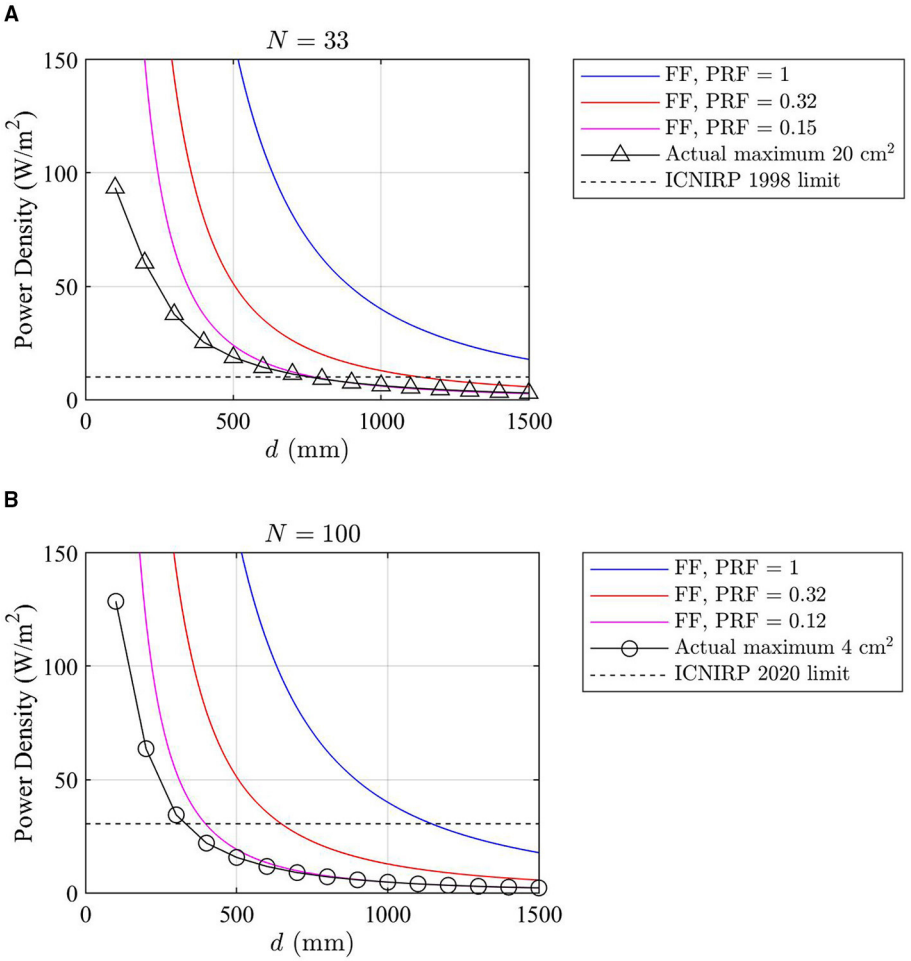

FIGURE 8 | The blue curves indicate the power density levels obtained for the theoretical maximum exposure, i.e., PRF = 1, using the far-field approach. The orange curves indicate the power density levels by applying PRF = 0.32 using the far-field approach. In **(A)**, the pink curve indicates the power density levels by applying PRF = 0.15 derived from the far-field approach considered for the ICNIRP 1998 limits; the black solid line with the triangular markers is the actual maximum exposure obtained from the near-field approach averaged over 20 cm^2; the black dashed line indicates the ICNIRP 1998 general public power density limit. PRF = 0.15 derived from the far-field approach and the actual maximum exposure derived from the near-field approach are based on $N = 33$ in the Monte Carlo analysis. In **(B)**, the pink curve indicates the power density levels by applying PRF = 0.12 derived from the far-field approach considered for the ICNIRP 2020 local exposure limits; the black solid line with the circular markers is the actual maximum exposure obtained from the near-field approach averaged over 4 cm^2; the black dashed line indicates the ICNIRP 2020 local power density limit for the general public. PRF = 0.12 derived from the far-field approach and the actual maximum exposure derived from the near-field approach are based on $N = 100$ in the Monte Carlo analysis.

DISCUSSION

The PRF values are derived for the specific array antenna configuration used in this study. Usually, the PRF is reversely proportional to the number of antenna elements because antenna arrays with more elements have narrower beamwidth and a greater number of available beams in a codebook. This implies that, if larger antenna arrays are used in a mmW RBS, the PRFs derived from the array antenna used in this study may be applied to larger arrays with extra margin in actual maximum exposure. For RBSs enabling massive MIMO with 64 elements and operating below 6 GHz, a PRF of 0.32 is commonly used to determine the actual maximum exposure (8, 10). As indicated by **Figure 8**, applying a PRF of 0.32 for mmW RBSs will still lead to conservative results for the compliance boundary calculated from far-field antenna patterns.

The results in **Figure 8** and **Table 2** are obtained assuming $N = 30$ and $N = 100$ under the full-buffer condition. It should be emphasized again that these are very conservative assumptions when compared to real operating network measurements (15–17).

The EMF exposure limits for occupational exposure are five times higher than those for general public, resulting in smaller compliance boundaries. As indicated in **Figure 8**, at closer distances, the actual maximum exposure computed using the far-field approach is still larger than that computed using the near-field approach, suggesting that the mentioned

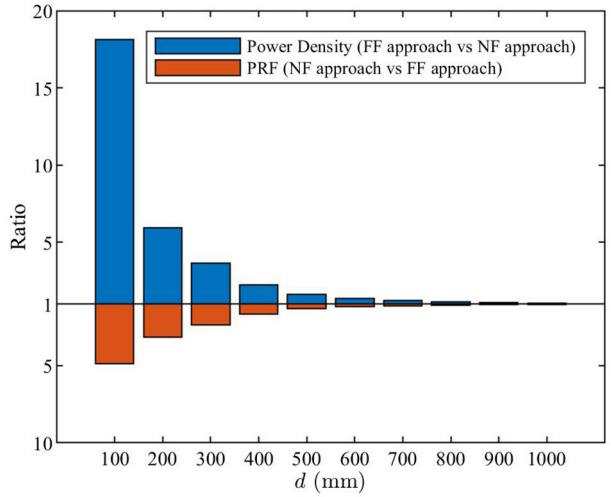

FIGURE 9 | The blue bars are the ratios of theoretical maximum power density obtained using the far-field approach [Equation (3)] to the near-field approach [Equation (1)]. The red bars are the ratios of PRF obtained using the near-field approach [$PRF_{NF}(d)$ in Equation (12)] to the far-field approach [$PRF_{FF,m}$ calculated from Equation (11)].

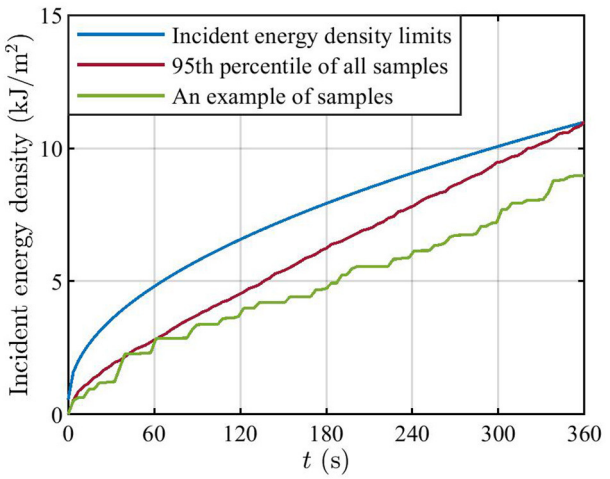

FIGURE 10 | The blue curve is the incident energy density limits at 28 GHz. The red curve is the 95th percentile of normalized incident energy density at the position where the peak time-averaged power density occurs at $x =$ 400 mm. The green curve is one example of samples at the same position. The curves for the 95th percentile and the sample are normalized such that the 95th percentile of incident energy density at 360 s is equal to the limit value at 360 s.

TABLE 2 | Front compliance distances obtained using different approaches and for general public exposure limits (results are rounded up to the nearest decimeter).

	ICNIRP 1998	ICNIRP 2020
Far-field approach (PRF = 1)	2.0 m	1.1 m
Far-field approach (PRF = 0.32)	1.1 m	0.6 m
Far-field approach (PRF = 0.15 or 0.12)	0.8 m	0.4 m
Near-field approach, actual maximum exposure	0.8 m	0.4 m

far-field approach can also be applied to occupational exposure assessments.

The PRF derived in this study based on the near-field approach are applicable to mmW RBS transmitting at power levels <1 W, for which the whole-body exclusion criteria apply. As **Figure 8** shows that the far-field approach is sufficiently accurate for distances larger than 0.5 m, for mmW RBSs operating above 1 W, the PRF that was derived based on the far-field approach may still be applicable.

Although the TDD downlink duty cycle was considered in the peak total EIRP calculation in this study, the derived PRF values do not include the effects of the TDD downlink duty cycle. If EIRP or power density values are provided for the maximum configured power level, the TDD downlink duty cycle should be considered in the calculation.

In this work, the actual maximum exposure is assessed using the ICNIRP incident power density limits. In the ICNIRP 2020 guidelines, a new exposure metric, absorbed power density, is introduced for local exposure above 6 GHz. The absorbed power density is directly related to the incident power density by the reflection coefficient of the exposed object. Therefore, the same PRFs as derived in this study are deemed to be applicable.

Below 6 GHz, measurement campaigns have confirmed that the actual maximum approach established using statistical models is conservative. Experimental studies conducted within 5G mmW live networks are also needed to validate the PRF levels derived in this study.

CONCLUSIONS

In this article, a case study has been presented assessing the actual maximum exposure and PRFs for a mmW RBS characterized by lower EIRP levels compared to massive MIMO RBSs operating below 6 GHz. The results suggest that applying the PRF derived from a far-field approach to the far-field formula provides conservative power density levels even when the evaluation distance is close to the RBS antenna. The used workflow can be applied to other mmW RBSs and for other antenna configurations.

DATA AVAILABILITY STATEMENT

The original contributions presented in the study are included in the article/**Supplementary Materials**, further inquiries can be directed to the corresponding author.

AUTHOR CONTRIBUTIONS

BX conceived the method, wrote the code script for the Monte Carlo analysis, analyzed the results, and wrote the manuscript. DA and BX created the simulation model and script. BX, DC, and CT conceived the project. All authors reviewed the work.

ACKNOWLEDGMENTS

The author thanks the colleagues at the Ericsson EMF Research Laboratory for useful discussion, suggestions, and comments.

SUPPLEMENTARY MATERIAL

The Supplementary Material for this article can be found online at: https://www.frontiersin.org/articles/10.3389/fpubh.2021.777759/full#supplementary-material

REFERENCES

1. Dahlman E, Parkvall S, Sköld J. 5G NR: The Next Generation Wireless Access Technology. *Elsevier Science.* (2020).
2. International Commission on Non-Ionizing Radiation Protection. Guidelines for Limiting Exposure to Time-Varying Electric, Magnetic, and electromagnetic fields (up to 300 GHz). *Health Physics.* (1998) 74:494–521.
3. International Commission on Non-Ionizing Radiation Protection. Guidelines for limiting exposure to electromagnetic fields (100 kHz to 300 GHz). *Health physics.* (2020) 118:483–524. doi: 10.1097/HP.0000000000001210
4. Int. Electrotechnical Commission. IEC 62232 Ed. 2.0 - Determination of RF field strength, power density and SAR in the vicinity of radiocommunication base stations for the purpose of evaluating human exposure (2017). Available online at: https://webstore.iec.ch/publication/28673
5. Xu B, Colombi D, Törnevik C. EMF Exposure Assessment of Massive MIMO Radio Base Stations Based on Traffic Beam Pattern Envelopes. *14th European Conference on Antennas and Propagation (EuCAP).* Copenhagen: IEEE (2020). p. 1–5. doi: 10.23919/EuCAP48036.2020.9135518
6. Cicchetti R, Faraone A. Estimation of the peak power density in the vicinity of cellular and radio base station antennas. *IEEE Trans Electromagn Compat.* (2004) 46:275–90. doi: 10.1109/TEMC.2004.826885
7. Thors B, Nord L, Colombi D, Törnevik C. Product Compliance Assessments of Low Power Radio Base Stations with Respect to Whole-Body Radiofrequency Exposure Limits. *7th European Conference on Antennas and Propagation (EuCAP).* (2013) 1762–1766. Available online at: https://ieeexplore.ieee.org/document/6546585
8. Int. Electrotechnical Commission. IEC TR 62669 - Case Studies Supporting IEC 62232 - Determination of RF Field Strength and SAR in the Vicinity of Radiocommunication Base Stations for the Purpose of Evaluation Human Exposure. Geneva: International Electrotechnical Commission (2019). Available online at: https://webstore.iec.ch/publication/62014
9. Int. Electrotechnical Commission. 106/550(F)/CDV Draft Standard IEC 62232 ED3 - Determination of RF field strength, power density and SAR in the vicinity of radiocommunication base stations for the purpose of evaluating human exposure (2021). Available online at: https://documents.iec.ch/ords/f?p=700:610:::::P610_DOCUMENT_FILE_ID:1110725
10. Thors B, Furuskar A, Colombi D, Törnevik C. Time-averaged realistic maximum power levels for the assessment of radio frequency exposure for 5G radio base stations using massive MIMO. *IEEE Access.* (2017) 5:19711–19. doi: 10.1109/ACCESS.2017.2753459
11. Baracca P, Weber A, Wild T, Grangeat C. A Statistical Approach for RF Exposure Compliance Boundary Assessment in Massive MIMO Systems. WSA 2018 - 22nd Int ITG Work Smart Antennas (2018) 1–6. Available online at: https://ieeexplore.ieee.org/abstract/document/8385449
12. Pinchera D, Migliore M, Schettino F. Compliance boundaries of 5G massive MIMO radio base stations: a statistical approach. *IEEE Access.* (2020) 8:182787–800. doi: 10.1109/ACCESS.2020.3028471
13. Shikhantsov S, Thielens A, Aerts S, Verloock L, Torfs G, Martens L, et al. Ray-tracing-based numerical assessment of the spatiotemporal duty cycle of 5g massive MIMO in an outdoor urban environment. *Appl Sci.* (2020) 10:1–15. doi: 10.3390/app10217631
14. Xu B, Colombi D, Törnevik C, Ghasemifard F, Chen J. On actual maximum exposure from 5G multicolumn radio base station antennas for electromagnetic field compliance assessment. *IEEE Trans Electromagn Compat.* (2021) 63:1680–89. doi: 10.1109/TEMC.2021.3090107
15. Colombi D, Joshi P, Pereira R, Thomas D, Shleifman D, Tootoonchi B, et al. Assessment of actual maximum RF EMF exposure from radio base stations with massive MIMO antennas. Progress in electromagnetics research symposium. Rome: IEEE (2019). p. 570–77. doi: 10.1109/PIERS-Spring46901.2019.9017343
16. Werner R, Knipe P, Iskra S. A comparison between measured and computed assessments of the RF exposure compliance boundary of an in-situ radio base station massive MIMO antenna. *IEEE Access.* (2019) 7:170682–89. doi: 10.1109/ACCESS.2019.2955715
17. Colombi D, Joshi P, Xu B, Ghasemifard F, Narasaraju V, Törnevik C. Analysis of the actual power and EMF exposure from base stations in a commercial 5G network. *Appl Sci.* (2020) 10:5280. doi: 10.3390/app10155280
18. Xu B, Zhao K, Thors B, Colombi D, Lundberg O, Ying Z, et al. Power density measurements at 15 GHz for RF EMF compliance assessments of 5G user equipment. *IEEE Trans Antennas Propag.* (2017) 65:6584–95. doi: 10.1109/TAP.2017.2712792
19. Pfeifer S, Carrasco E, Crespo-Valero P, Neufeld E, Kuhn S, Samaras T, et al. Total field reconstruction in the near field using pseudo-vector E-field measurements. *IEEE Trans Electromagn Compat.* (2019) 61:476–86. doi: 10.1109/TEMC.2018.2837897
20. Sasaki K, Li K, Chakarothai J, Iyama T, Onishi T, Watanabe S. Error analysis of a near-field reconstruction technique based on plane wave spectrum expansion for power density assessment above 6 GHz. *IEEE Access.* (2019) 7:11591–8. doi: 10.1109/ACCESS.2019.2891939
21. Pfeifer S, Fallahi A, Xi J, Neufeld E, Kuster N. Forward transformation from reactive near-field to near and far-field at millimeter-wave frequencies. *Appl Sci.* (2020) 10:1–16. doi: 10.3390/app10144780
22. Lundgren J, Helander J, Gustafsson M, Sjöberg D, Xu B, Colombi D, et al. Near-field measurement and calibration technique: radio-frequency electromagnetic field exposure assessment of millimeter-wave 5G devices. *IEEE Antennas Propag Mag.* (2021) 63:77–88. doi: 10.1109/MAP.2020.2988517
23. He W, Xu B, Scialacqua L, Ying Z, Scannavini A, Foged LJ, et al. Fast power density assessment of 5G mobile handset using equivalent currents method. *IEEE Trans Antennas Propag.* (2021) 69:6857–69. doi: 10.1109/TAP.2021.3070725
24. Omi S, Sasaki K, Wake K. Performance analysis of incident power density evaluation by inverse source method for compliance assessment at quasi-millimeter and millimeter wave bands. *IEEE Trans Electromagn Compat.* (2021) 63:1649–57. doi: 10.1109/TEMC.2021.3100575
25. Xu B, Gustafsson M, Shi S, Zhao K, Ying Z, He S. Radio frequency exposure compliance of multiple antennas for cellular equipment based on semidefinite relaxation. *IEEE Trans Electromagn Compat.* (2018) 61:327–36. doi: 10.1109/TEMC.2018.2832445
26. Xu B, Zhao K, Ying Z, Sjöberg D, He W, He S. Analysis of impacts of expected RF EMF exposure restrictions on peak EIRP of 5G user equipment at 28 GHz and 39 GHz bands. *IEEE Access.* (2019) 7:20996–1005. doi: 10.1109/ACCESS.2019.2897271
27. He W, Xu B, Yao Y, Colombi D, Ying Z, He S. Implications of incident power density limits on power and EIRP levels of 5G millimeter-wave user equipment. *IEEE Access.* (2020) 8:148214–25. doi: 10.1109/ACCESS.2020.3015231
28. Diao Y, Hirata A. Assessment of mmWave exposure from antenna based on transformation of spherical wave expansion to plane wave expansion. *IEEE Access.* (2021) 9:111608–15. doi: 10.1109/ACCESS.2021.3103813

29. Li K, Sasaki K, Wake K, Onishi T, Watanabe S. Quantitative comparison of power densities related to electromagnetic near-field exposures with safety guidelines from 6 to 100 GHz. *IEEE Access.* (2021) 9:115801–12. doi: 10.1109/ACCESS.2021.3105608
30. Zhekov SS, Zhao K, Franek O, Zhang S. Test reduction for power density emitted by handset mmwave antenna arrays. *IEEE Access.* (2021) 9:23127–38. doi: 10.1109/ACCESS.2021.3055420
31. Diao Y, Hirata A. Exposure assessment of array antennas at 28 GHz using hybrid spherical near-field transformation and FDTD method. *IEEE Trans Electromagn Compat.* (2021) 63:1690–8. doi: 10.1109/TEMC.2021.3074658
32. Dahlstedt M. Radio frequency exposure from 5G small cells utilizing massive MIMO [master's thesis]. Uppsala (Sweden): Uppsala University (2020).
33. Anguiano Sanjurjo D. Investigation of Hybrid Simulation Methods for Evaluation of EMF Exposure in Close Proximity of 5G Millimeter-Wave Base Stations [master's thesis]. Stockholm (Sweden): KTH Royal Institute of Technology (2020).
34. Colombi D, Xu B, Anguiano Sanjurjo D, Joshi P, Ghasemifard, Di Paola C, et al. Implications of ICNIRP 2020 exposure guidelines on the RF EMF compliance boundary of base stations. *Front Communicat Networks.* (in press).
35. Int. Electrotechnical Commission. IEC TR 63170 - Measurement procedure for the evaluation of power density related to human exposure to radio frequency fields from wireless communication devices operating between 6 GHz and 100 GHz (2018). Available online at: https://webstore.iec.ch/publication/62012
36. IEEE. C95.1-2019 - IEEE Standard for Safety Levels with Respect to Human Exposure to Electric, Magnetic, and Electromagnetic Fields, 0 Hz to 300 GHz. IEEE (2019).

Conflict of Interest: BX, DA, DC, and CT are employed by the company Ericsson AB.

Publisher's Note: All claims expressed in this article are solely those of the authors and do not necessarily represent those of their affiliated organizations, or those of the publisher, the editors and the reviewers. Any product that may be evaluated in this article, or claim that may be made by its manufacturer, is not guaranteed or endorsed by the publisher.

frontiers in Public Health

ORIGINAL RESEARCH
published: 13 January 2022
doi: 10.3389/fpubh.2021.734370

No Alteration Between Intrinsic Connectivity Networks by a Pilot Study on Localized Exposure to the Fourth-Generation Wireless Communication Signals

Lei Yang[1†], *Qingmeng Liu*[1†], *Yu Zhou*[1], *Xing Wang*[1], *Tongning Wu*[1*] *and Zhiye Chen*[2*]

[1] China Academy of Information and Communications Technology, Beijing, China, [2] Hainan Hospital of Chinese People's Liberation Army General Hospital, Hainan, China

OPEN ACCESS

Edited by:
Dariusz Leszczynski,
University of Helsinki, Finland

Reviewed by:
Peng Shang,
Northwestern Polytechnical University, China
Myles Capstick,
ETH Zurich, Switzerland

***Correspondence:**
Tongning Wu
wutongning@caict.ac.cn
Zhiye Chen
yyqf@hotmail.com

[†]These authors have contributed equally to this work

Specialty section:
This article was submitted to Radiation and Health, a section of the journal Frontiers in Public Health

Received: 01 July 2021
Accepted: 14 December 2021
Published: 13 January 2022

Citation:
Yang L, Liu Q, Zhou Y, Wang X, Wu T and Chen Z (2022) No Alteration Between Intrinsic Connectivity Networks by a Pilot Study on Localized Exposure to the Fourth-Generation Wireless Communication Signals. Front. Public Health 9:734370. doi: 10.3389/fpubh.2021.734370

Neurophysiological effect of human exposure to radiofrequency signals has attracted considerable attention, which was claimed to have an association with a series of clinical symptoms. A few investigations have been conducted on alteration of brain functions, yet no known research focused on intrinsic connectivity networks, an attribute that may relate to some behavioral functions. To investigate the exposure effect on functional connectivity between intrinsic connectivity networks, we conducted experiments with seventeen participants experiencing localized head exposure to real and sham time-division long-term evolution signal for 30 min. The resting-state functional magnetic resonance imaging data were collected before and after exposure, respectively. Group-level independent component analysis was used to decompose networks of interest. Three states were clustered, which can reflect different cognitive conditions. Dynamic connectivity as well as conventional connectivity between networks per state were computed and followed by paired sample *t*-tests. Results showed that there was no statistical difference in static or dynamic functional network connectivity in both real and sham exposure conditions, and pointed out that the impact of short-term electromagnetic exposure was undetected at the ICNs level. The specific brain parcellations and metrics used in the study may lead to different results on brain modulation.

Keywords: radiofrequency exposure, long-term evolution, resting-state fMRI, intrinsic connectivity network, dynamic connectivity

INTRODUCTION

Wireless communication technology has evolved drastically in the past 20 years. The emergence of the fourth generation (4G) wireless communication technology promoted the widespread applications of mobile network, and vice versa, and 4G rapidly became the popularly used wireless network. The unprecedentedly increasing exposure to radiofrequency (RF) field provoked public anxieties, especially over the effect on neurophysiological function (1). By the end of the third quarter of 2020, although 5G network had already been commercially deployed in many countries for 1 year, there were still 5.82 billion 4G subscriptions (accounting for 62.1% of global subscription) (2). Therefore, it is necessary to investigate the exposure effect of 4G wireless signal.

Subjects who attribute health complaints to everyday levels of electromagnetic fields are suspected of having electromagnetic hypersensitivity, and their symptoms include impaired sense of smell, feeling of pressure in ear, dizziness, and difficulties in concentration (3). However, many studies ascribed the symptoms to psychological suggestion due to the lack of proof of causality (4, 5). The analysis using neuroimaging techniques may help elucidate the concern whether RF radiation exposure would disturb behavioral cognitive function.

The human brain possesses intrinsic connectivity networks (ICNs) relating to underlying neural activity (6). They maintain structural stability at resting state and could be decomposed as spatial-distributed components (independent components, IC) with highly temporal-correlated fluctuations using independent component analysis (ICA) (7) or seed-based analysis (8). Functional network connectivity (FNC), defined by pairwise correlation between ICNs over a certain time course, can measure the averaged connectivity among these ICNs during the scan duration (9). It was conventionally assumed that correlation values stabilized within 4–5 min of data length (7). However, the average over the entire scanning time course may conceal the instantaneous change. Recent research demonstrated that the spontaneous blood oxygen level dependent (BOLD) signals measured during resting state exhibited intrinsic spatiotemporal dynamic organization (10). The dynamic FNC calculated by short time windows was able to track this oscillation over time. Furthermore, the results can be clustered into several connectivity patterns, which may associate with diverse perspectives from unconscious states relevant to anatomical structures to more complex information exchange states (11). By aids of the technique, new breakthroughs have been made in identifying brain dysfunction and cognitive behavior (12, 13). In contrast, relatively few non-ionizing exposure effects have been evaluated in terms of ICNs, and even less on dynamic FNC.

In this work, seventeen healthy participants were recruited and they experienced 30-min exposure. Group-level ICA was performed to decompose ICs across participants from their resting-state fMRI data. We identified 51 ICs in 14 ICNs of interest. Both static FNC over the entire scanning time course and the dynamic FNC using short-time windows were computed. Consequently, these dynamic FNCs were clustered in three states using k-means (14). Statistical analysis was preformed to assess the exposure effect. The study provided a novel approach of understanding the modulation of brain functional connectivity by RF radiation.

Abbreviations: RF, radiofrequency; ICA, independent component analysis; ICN, intrinsic connectivity network; FNC, functional network connectivity; ASN, Anterior salience network; AUN, Auditory network; BGN, Basal ganglia network; HVN, Higher visual network; VSN, Visuospatial network; LGN, Language network; LECN, Left executive control network; DDMN, Dorsal default mode network; PSN, Posterior salience network; PCN, Precuneus network; PVN, Primary visual network; VDMN, Ventral default mode network; RECN, Right executive control network; SMN, Sensorimotor network. AAL, anatomic automatic labeling; ALFF, Amplitude of Low Frequency Fluctuations.

METHODS AND MATERIALS

Participants and Experiment Settings

Seventeen healthy right-handed participants including 9 men and 8 women aged 26.1 ± 4.2 (mean ± standard deviation, from 18 to 38) were recruited for this study. They were asked to complete a Medical History Questionnaire before being admitted to the study and none of them had a history of mental illness or disorders related to cognitive dysfunction. They were asked to keep away from caffeine, alcohol, and electronic products the day before experiments. All of them were informed fully of the details and signed a written informed consent. This study conformed to the principles outlined in the Declaration of Helsinki and was approved by the local ethics committee.

As the paradigm in **Figure 1** shows, the experiment was divided into two sessions with an interval of 1 week. Each session consisted of three stages: fMRI, experiment conditions for 30-min real or sham exposure, and immediate fMRI again. Structural MRI was conducted for participants before the two sessions. The experiment was designed double blind. The real and sham exposure conditions were allocated randomly and counterbalanced across participants. Participants were asked to stay as still as possible. They started scanning immediately after the exposure so that the fMRI data collection could be initiated within 5 min. All participants reported that they kept conscious during the experiments.

The exposure was carried out in an anechoic chamber to avoid interference from the environment. A signal generator (CMW 500, Rohde and Schwarz, Munich, Germany) was used to generate QPSK modulated time-division LTE signals at 2.573 GHz. The radio frame (total length: 10 ms) consisted of 10 subframes, each 1 ms in length. In the exposure experiment, the maximal emission configuration was opted (simulating 6 uplink subframes in the radio frame). The radiation duration (including the uplink subframes and uplink pilot time slot subframes) accounted for 63.3% of the total frame length, which mimicked the maximum number of the uplink subframes, as prescribed by 3GPP (15). The time domain character is shown in **Figure 2**.

Signals were then amplified by an RF power amplifier (AR40S1G4, AR, WA, US). A standard dipole antenna (D2600V2, SPEAG, Zurich, Switzerland) exposed the subjects. Using dipole antenna could avoid the brain activation from temperature rise and sound due to the operation of the mobile phones. The distance between the antenna and the right ear of each participant was stuck to 1 cm. The reflected power due to the existence of the head was monitored and compensated so that the net power output to the dipole antenna was constant (23.0 ± 0.5 dBm). The power distribution in the head was calculated by finite-difference time-domain simulations. The results indicated that the peak SAR averaged over a 10-g mass (pSAR10g) was below 2.00 W/kg for all subjects during real exposure (**Figure 3**), with a mean ± standard deviation as 1.22 ± 0.24 W/kg. To note, individual head modeling was developed by a semiautomatic segmentation method (16), using in-house tool (17) and iSEG (ZMT, Zurich, Switzerland).

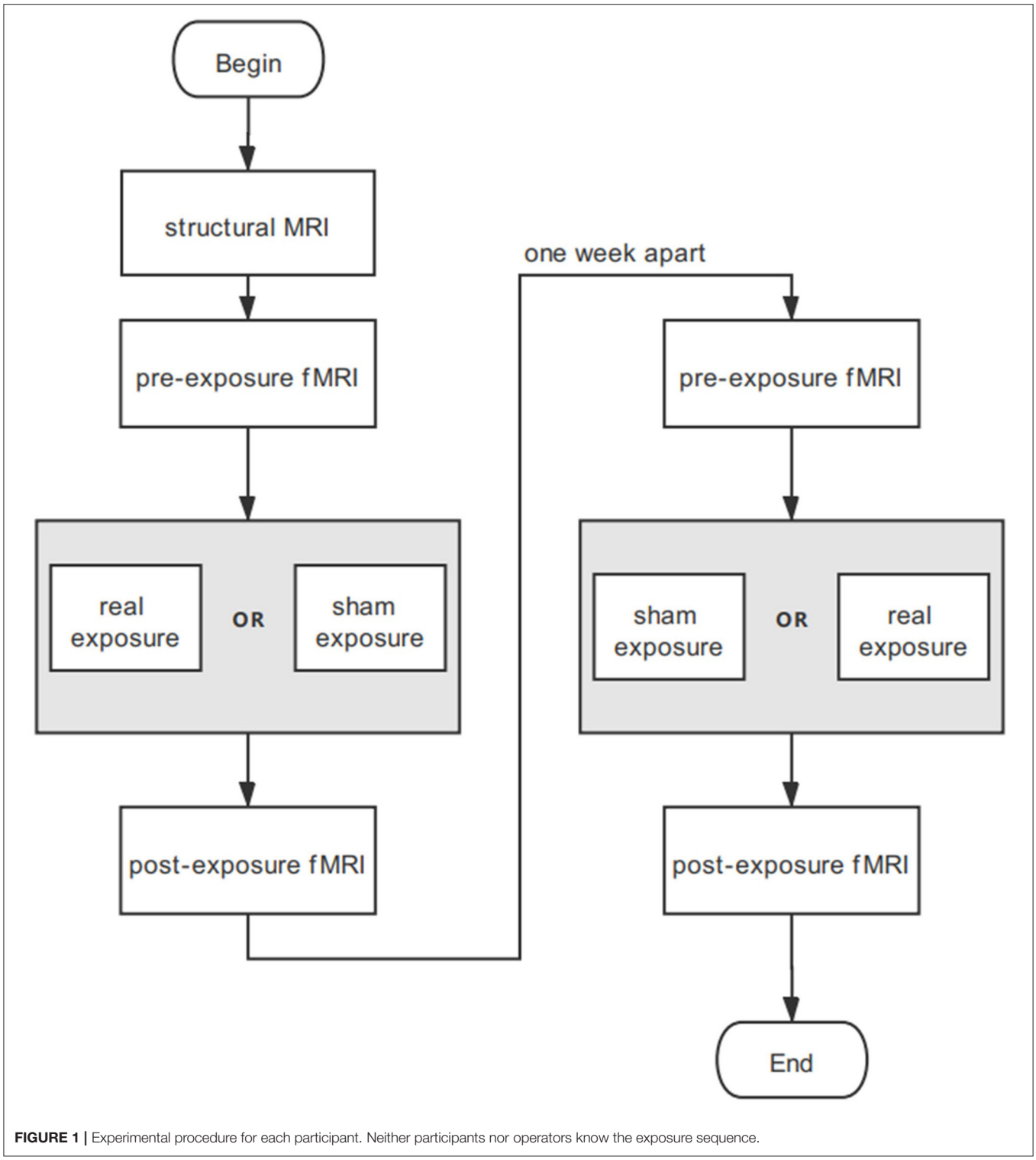

FIGURE 1 | Experimental procedure for each participant. Neither participants nor operators know the exposure sequence.

Data Acquisition and Preprocessing

All the MR data were generated from a 3.0 T system (SIGNA EXCITE, GE Healthcare) with a conventional eight-channel phased array surface coil. The T1-weighted images were acquired at the beginning with repetition time (TR) = 6.8 ms, echo time (TE) = 2.9 ms, field of view = 22 cm, matrix size = 256 × 256. T2-weighted functional images of the whole brain were collected using an echo-planar imaging sequence with TR = 2 s, TE = 30 ms, slice thickness = 3 mm, matrix size = 64 × 64, flip angle = 90°, gap = 0.8 mm. The pre- and post-exposure sessions shared

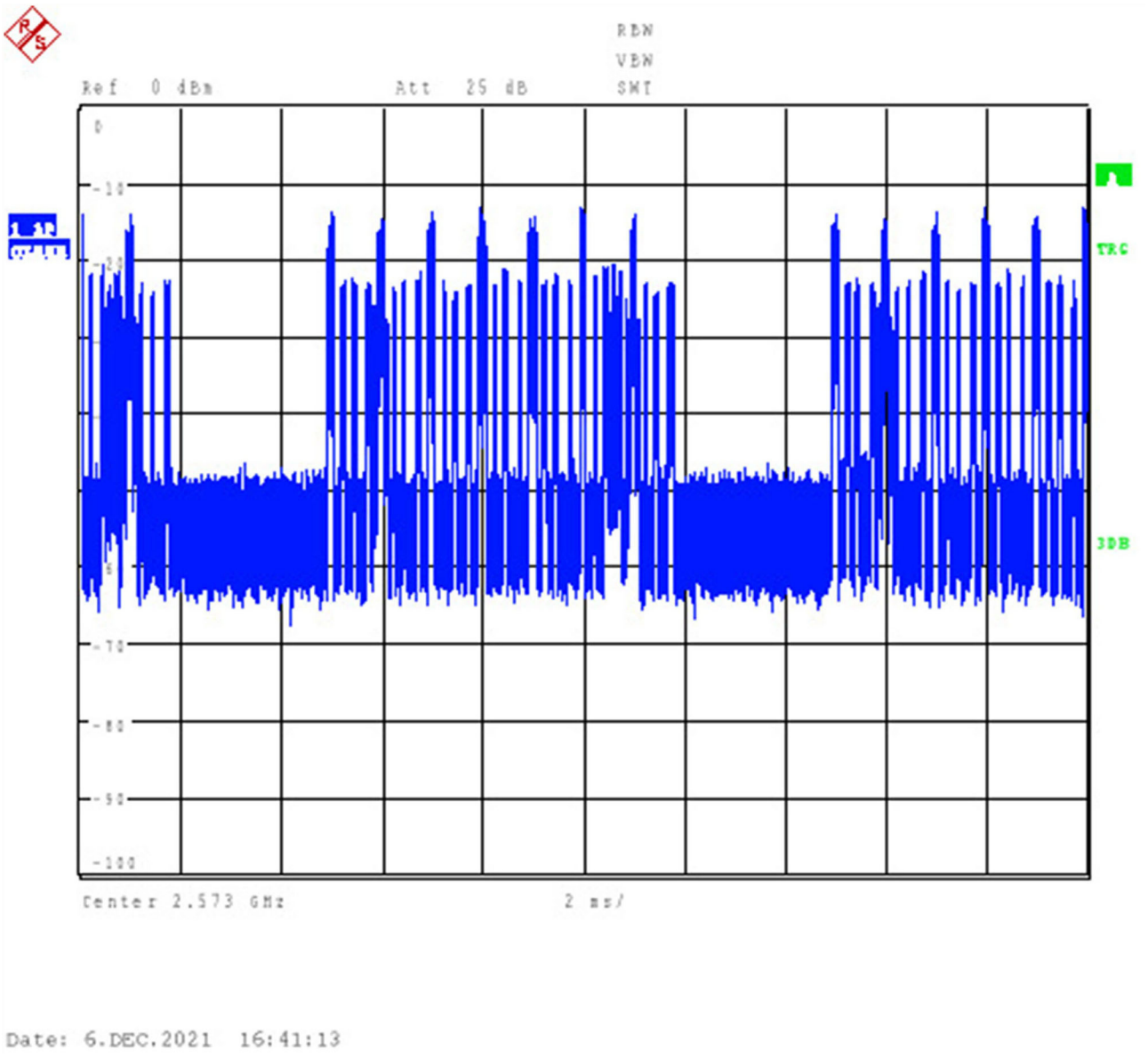

FIGURE 2 | Time-domain signal generated by CMW 500 and visualized by Rohde and Schwarz FSU26 Spectrum Analyzers.

the same parameters, and each lasted for 6 min to collect 180 image volumes. Thirty-two transversal slices were acquired in ascending order for each volume.

Preprocessing was conducted using an automatic pipeline based on SPM 12 (https://www.fil.ion.ucl.ac.uk/spm/software/spm12/). The first ten presteady-state volumes of the EPI time series were firstly removed. Realignment was implemented firstly considering the sequential acquisition. Images were registered to the first image in the series. Then slice timing was performed with the middle one as reference. A single T1-weighted image was co-registered with the corrected average functional image. Then all the functional images were spatially normalized using parameters estimated by nonlinearly registering gray matter and white matter images into MNI space. Their resampled voxel was 3 mm × 3 mm × 3 mm. Finally, the volumes were spatially smoothed with a Gaussian kernel of 6 mm full width at half maximum.

Group-level ICA to Derive ICNs

Independent component analysis (18), as a data-driven method, is a suitable tool to investigate ICNs at resting state. However, ICA is typically performed separately on each subject, leading to incompatible decompositions across subjects. Consequently, several group-level ICA methods for multisubject analysis have emerged (19).

By the method, the individual voxelwise time-course data were z-scored to reduce the variability, followed by a principal

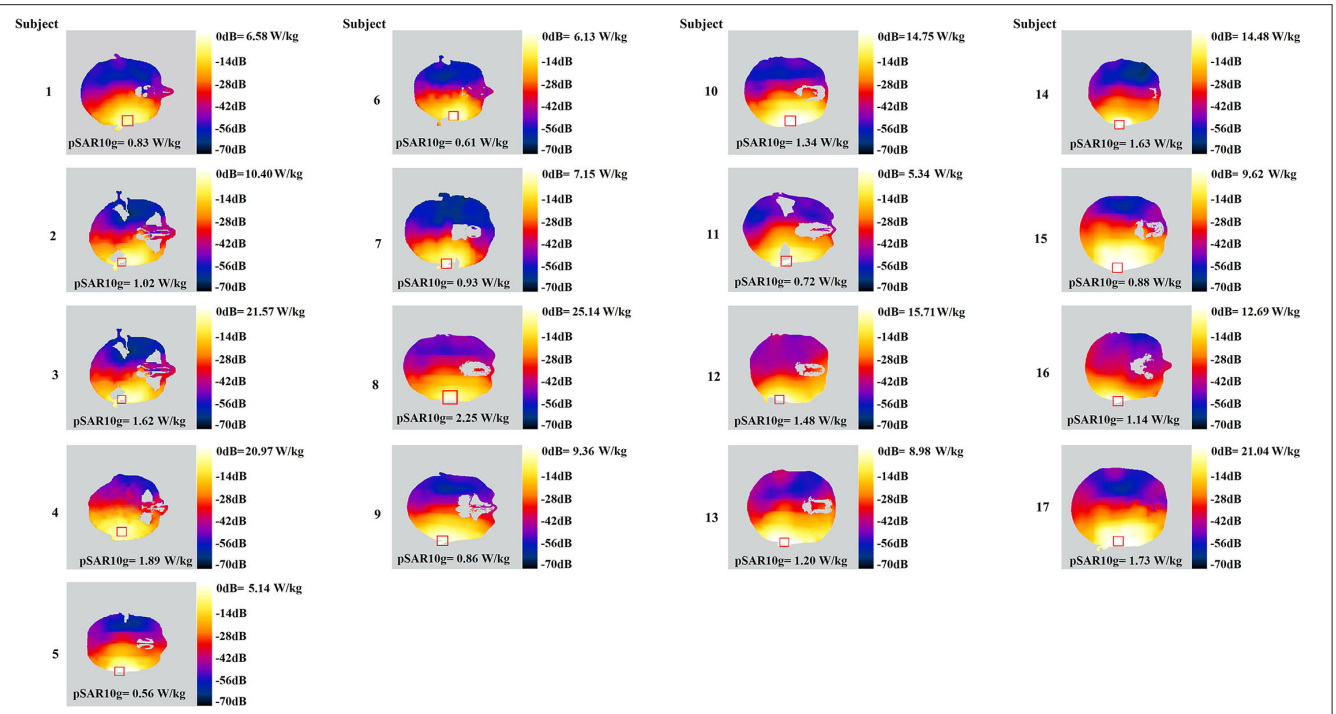

FIGURE 3 | SAR distribution on the transverse slice at the peak value level, for each of the 17 subjects. Square shape delineates the region of pSAR10g on the slice.

component analysis (PCA) to reduce the complexity of the individual data from 170 to 150 volumes using a standard economy-size decomposition. Next, individual data were temporally concatenated as (1):

$$Y \equiv [Y_1{}^{\mathrm{T}}, \ldots, Y_M{}^{\mathrm{T}}]^{\mathrm{T}} \tag{1}$$

where, Y_i is T_1-by-V matrix containing the data of subject i; $Y \in \mathbb{R}^{\mathrm{T_1M\times V}}$; T_1 is the PCA-reduced time course; V is the total number of the voxels for each image; M is the number of the dataset to be evaluated.

Consequently, PCA was conducted on the group level to reduce time-course dimension and yielded (2)

$$X = AS \tag{2}$$

where, X is T_2-by-V concatenated imaging dataset reduced by group-level PCA; A is T_2-by-T_2 mixing matrix; and S is T_2-by-V aggregated spatial map. T_2 was predefined as 100 to achieve a sufficient "functional parcellation" of refined cortical and subcortical components corresponding to the well-known anatomical and functional segmentations (20). The selected number corresponded to the previous studies (21).

The Infomax ICA algorithm (22) was repeated 10 times in ICASSO (23) to derive A and S.

Consequently, back reconstruction can be conducted to derive subject-specific spatial maps and time-course signals by (3) and (4) using least square:

$$S_i = A^T G_i Y_i \tag{3}$$

$$R_i = G_i A \tag{4}$$

where, G^T is the T_2-by-$T_1 \times M$ reducing matrix.

The abovementioned temporal concatenation (24) implemented in the GIFT toolbox (http://mialab.mrn.org/software/gift/) was used in this work for processing functional data from both real and sham exposure conditions. The procedures are described in **Figure 4**.

The aggregated images of all subject were rewritten in Nifti format so as to enable the labeling for ICs (obtained from spatial maps) according to the RSN templates from the GIFT toolbox (icatb/icatb_templates/RSN.zip).

The generated ICs may contain artifacts and should be removed from analysis according to two criteria. Firstly, the cross correlation between the generated ICs and the RSN templates was calculated, and the ICs with correlation value below 0.2 were considered as artifacts (25). Secondly, the spatial distribution of the IC and its temporal/spectral characteristics were assessed to further screen out the artifacts, and signal ICs should have a high spatial overlap with gray matter and a low overlap with other tissues (26).

Static and Dynamic FNC

We calculated static FNC over the entire time courses between ICNs. Preprocessing included detrending and low-pass filtering

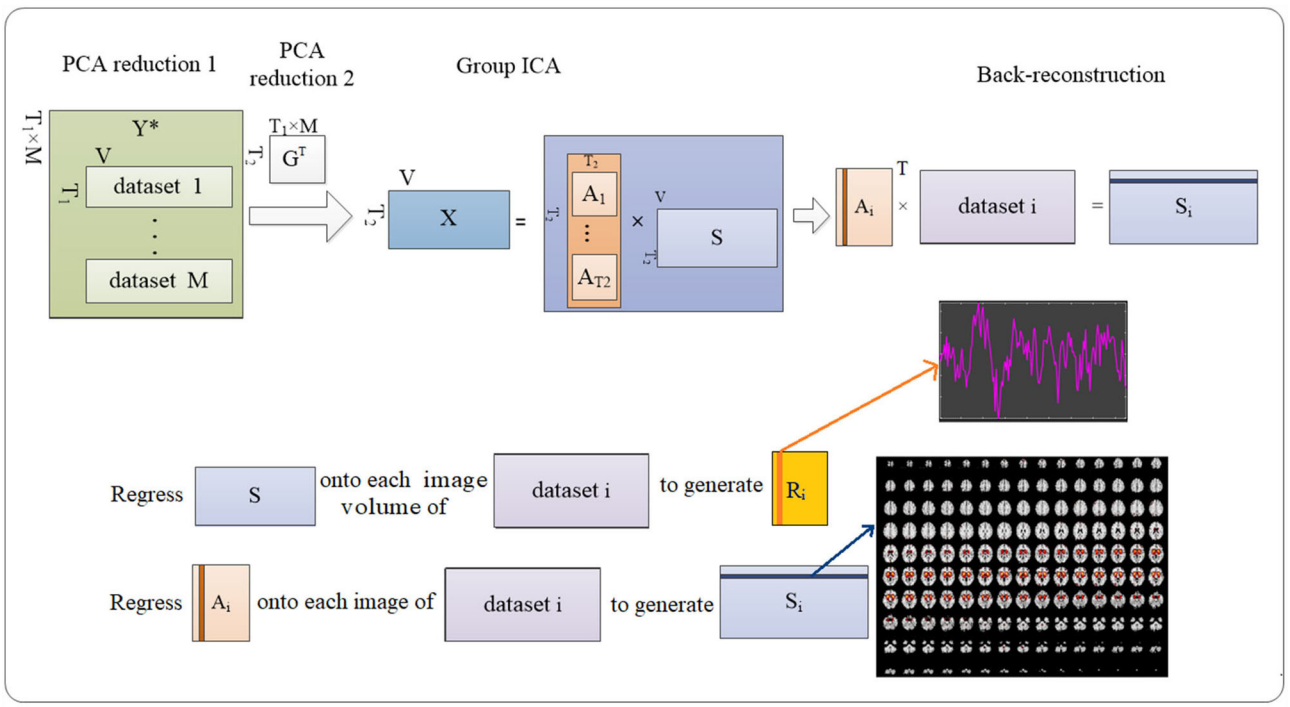

FIGURE 4 | Procedures to detecting the ICs. Group-level ICA decomposes resting-state data from the subjects into ICs (number = 100). Then back reconstruction estimates IC for each subject.

by a fifth-order Butterworth filter with a cut-off frequency of 0.1 Hz (27). Fisher's *z* transformation was then performed.

Consequently, dynamic FNC was computed with the relevant parameters as specified:

- TR = 2 s
- window size: 22 TRs
- step: 1 TR
- number of states: 3 (by *k* means).

To note, TR was set by the imaging protocol. Selection of the window size and step was in accordance to the recommendation by Damaraju et al. (12). Trials have been conducted from 2 to 9 to determine the appropriate number of states. The optimized number was 3 because it ensured that each state contained at least one dataset from qualified subject. The procedure is visualized in **Figure 5**.

Statistical Analysis

Paired sample *t*-test was conducted for static FNC within conditions, corrected using FDR with a p-value < 0.05. For dynamic analysis, subjects with no less than 10 windows for each state were qualified for statistical comparison.

To investigate if the effects of electromagnetic exposure were driven by certain dynamic FNC states, the median value of all windows for each subject in each state was used for paired sample *t*-test (12). The calculated p-value underwent FDR correction with $p < 0.05$.

RESULTS

Group-level ICA derived 100 spatial ICs was performed to define brain networks, and 100 spatial ICs were generated. By screening out the noise, they were classified into 51 signals whose correlation value was from 0.2058 to 0.5664. Detailed information for ICs are presented in **Figure 6**: ICs 26, 64, 66, and 91 are anterior salience network (ASN); 25, 44, and 86 are auditory network (AUN); 7, 23, and 29 are basal ganglia network (BGN); 40 and 60 are higher visual network (HVN); 5, 33, 49, and 70 are visuospatial network (VSN); 21, 34, 35, 46, and 57 are language network (LGN), 59, 79, and 87 are left executive control network (LECN); 20, 22, 31, 42, 72, 73, 80, and 100 are dorsal default mode network (DDMN); 68 is posterior salience network (PSN); 43 and 82 are precuneus network (PCN); 78 is primary visual network (PVN); 17, 53, 58, 65, 71, and 76 are ventral default mode network (VDMN); 30, 32, 37, 67, and 88 are right executive control network (RECN); 12, 14, 50, and 51 are sensorimotor network (SMN).

No statistically significant difference was found in static FNC in both real and sham exposure conditions.

The group-specific medians for each state are shown in **Figure 7**. State 1 accounted for 27% in terms of the occurrence of states across subjects, 66% for State 2, while 7% for State 3. State 1 was similar to State 2, which showed a weak connectivity within each ICN and demonstrated no strong connectivity between ICNs. On the contrary, State 3 showed strong connectivity of ICs within ICN (in particular, with in ASN, AUN, LGN, LECN,

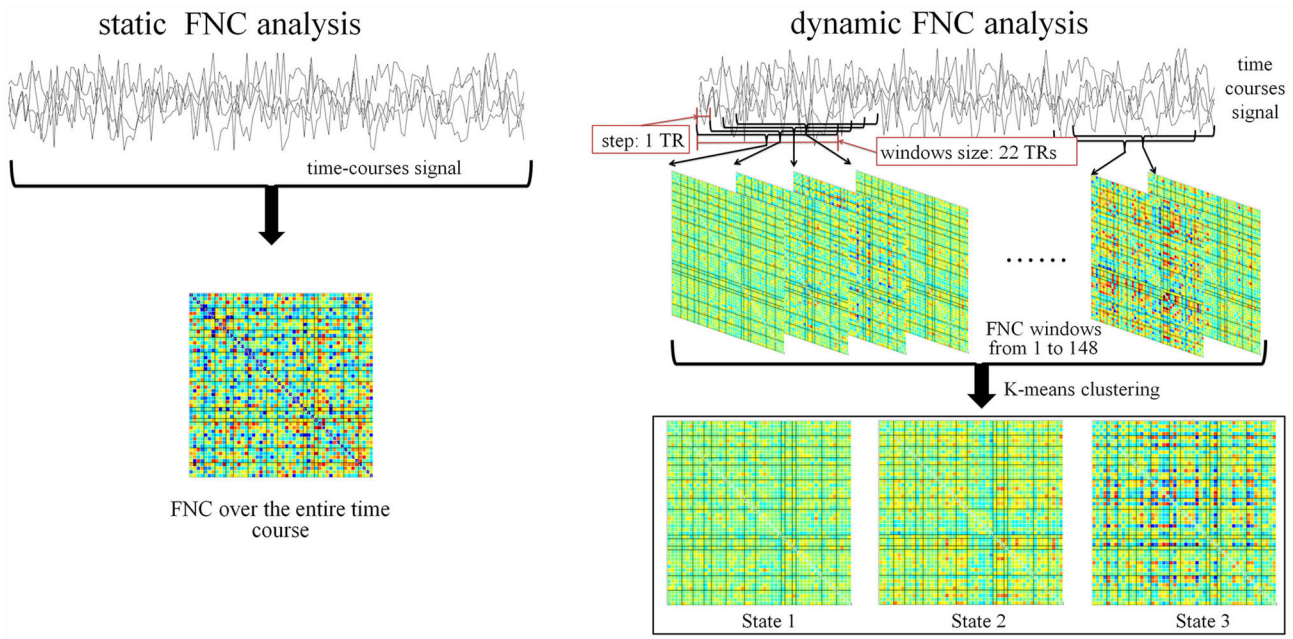

FIGURE 5 | Pipeline for static FNC and dynamic FNC analysis.

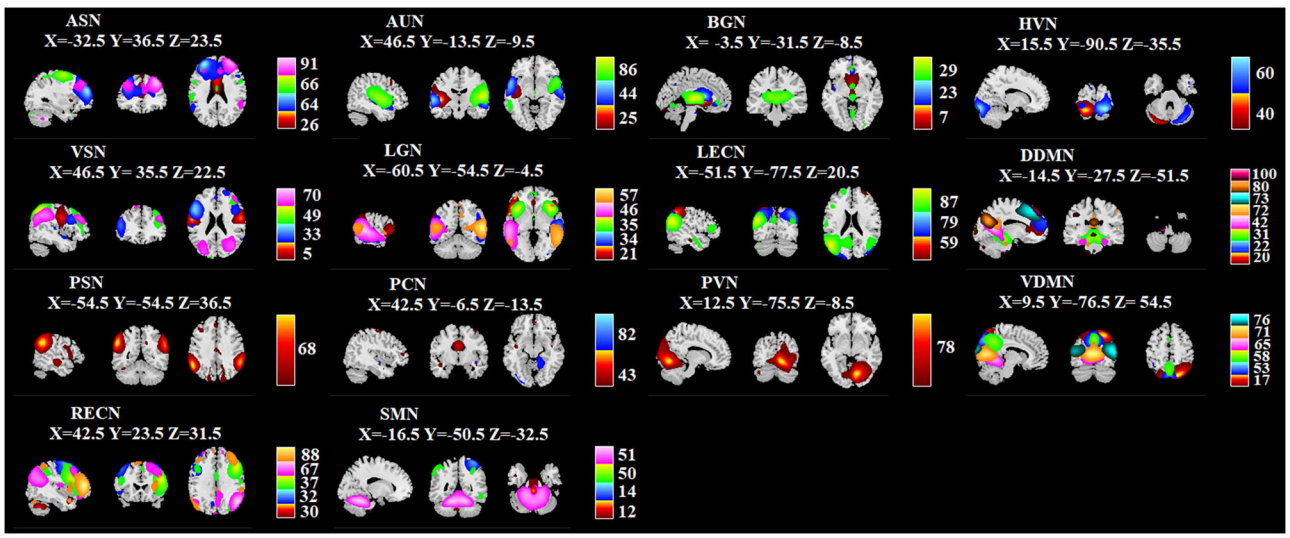

FIGURE 6 | Identified ICs. Within each ICN, the color of the component corresponds to No. of ICs. X, Y, Z corresponds to the MNI coordinates.

VDMN and RECN), enhanced connectivity between VDMN and LECN, PVN, SMN, PCN, PSN, also strong pairwise connectivity among ASN, BGN, AUN, and LGN.

For the dynamic analysis, paired sample *t*-test was performed on the subjects who got at least 10 windows for each state. In pre-exposure of real exposure condition, there were 8 subjects in State 1, 13 subjects in State 2, 3 subjects in State 3. In post-exposure of the same condition, there were 5 subjects in State 1, 12 subjects in State 2, 4 subjects in State 3. In contrast, in pre-exposure of sham exposure condition, there were 6 subjects in State 1, 13 subjects in State 2, and 3 subjects in State 3. The post-exposure in the sham exposure condition revealed 7 subjects in State 1, 12 subjects in State 2, and 4 subjects in State 3. No statistically within-condition significant difference has been detected in terms of real and sham exposure conditions. **Figure 8** shows the mean correlation (cross subjects) in all states within real and sham exposure conditions.

The raw data for **Figures 7**, **8** are provided in **Supplementary Tables 1, 2**.

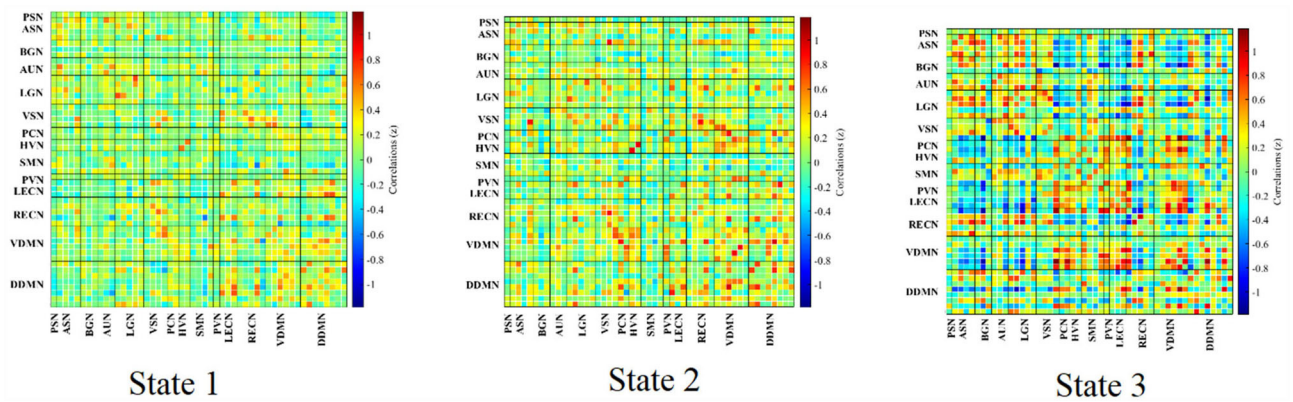

FIGURE 7 | Clustered states in dynamic FNC analysis averaged over the subjects.

DISCUSSION

In this study, we used a data-driven method (group-level ICA) to identify 51 ICs, which belonged to 14 ICNs, covering the functional areas of vision, hearing, and cognitive control etc. The identified components correlated well with the template and provided a reliable basis for subsequent analysis of static and dynamics FNC during resting state for exposure effects.

Accumulating evidence suggested that static FNC resembled the architecture of brain networks elicited by task-based paradigms (29) and reflected anatomical structure (7). However, the human brain activities were dynamic in nature, and thus, dynamic connectivity analysis was an insight tool to investigate the instantaneous change (30). The enriched information convoyed by the analysis might better reflect the temporally fluctuating brain states compared with static connectivity analysis, as shown in previous studies (31).

K-means clustering was used to identify these reoccurring short-term connectivity patterns, being described as FNC states. FNC state represented the large-scale models of neuronal connectivity that considered the repertoire of functional motifs generated by a given structural architecture (32). Three FC states were confirmed in this study. As shown in **Figure 7**, **8** and as described in Result, State 1 and State 2 generally showed a weak connectivity, and State 3 showed relatively stronger connectivity. The physiological meaning of the three states could be interpreted. During unconstrained resting-state MRI scan, it was possible for subjects to fall in deliberation or even mind wandering. Therefore, the FNC state representing specific cognitive states unlikely followed similar temporal characters across subjects, expect for the increased likelihood of drowsiness or sleep (32). In this study, State 1 was marked by the disconnection within BGN (thalamocortical neural loop) and the weakening connectivity within DDMN and VDMN. The characteristics were consistent with the features of falling to sleep, such as the reduced thalamocortical connectivity and a breakdown of default-mode connectivity (33, 34). State 3 had a stronger connectivity within DDMN, VDMN, and BGN, respectively. It indicated that this state was close to the awake state. State 2 had connectivity pattern in the BGN similar to State 1 but had a fairly strong connectivity in DDMN and VDMN, which could be regarded as a transitional state from drowsiness to waking state. Moreover, dwelling time in State 1 and 2 accounted for 93% of the total occurrence of all states across subjects. It was also consistent with our analysis on various conscious states during MRI. It revealed that the dynamic estimation/clustering approach had an advantage since it was sensitive to spontaneous state-transition during imaging and supported accessibility of the refined dynamic features of the dataset (12).

No statistically significant difference was found in static or dynamic functional connectivity of ICNs in both real and sham exposure conditions. The finding was seemingly inconsistent to the previous relevant literature on static state analysis. We attributed the difference to the distinctive brain parcellation or the metrics using in these studies. For example, Lv et al. (35) demonstrated that short-term LTE EMF exposure would modulate the interhemispheric homotopic functional connectivity, specifically decreasing amplitude of low frequency fluctuations (ALFF) in resting state around the medial frontal gyrus and the paracentral lobule during the real exposure (36). The study was based on brain anatomy of larger scale (hemisphere). Signals averaged over several ICs were computed for connectivity and may conceal the change in terms of individual IC. Wei et al. (37) detected that acute LTE-EMF exposures modulated both localized intraregional connectivity and interregional connectivity with the other voxels were computed. It evaluated the brain modulation on the level of voxels and without the conception of network structure. Yang et al. (38) indicated that acute LTE exposure modulated both the nodal functional connection and graph-based network properties. Those nodes were defined by AAL-90 template and the connectivity was evaluated for the rest of the nodes (39), which was a parcellation for the entire brain (some changes have been reported at the nodes close to Basal Ganglia). In contrast, our analysis was based on the functional parcellation, aiming to delineate more homogeneous and functionally coherent regions (40). The two parcellations were not completely overlapped. Moreover, the graph-based analysis considered the whole brain as a network to study the ensemble changes of its information transmission efficiency, function integration,

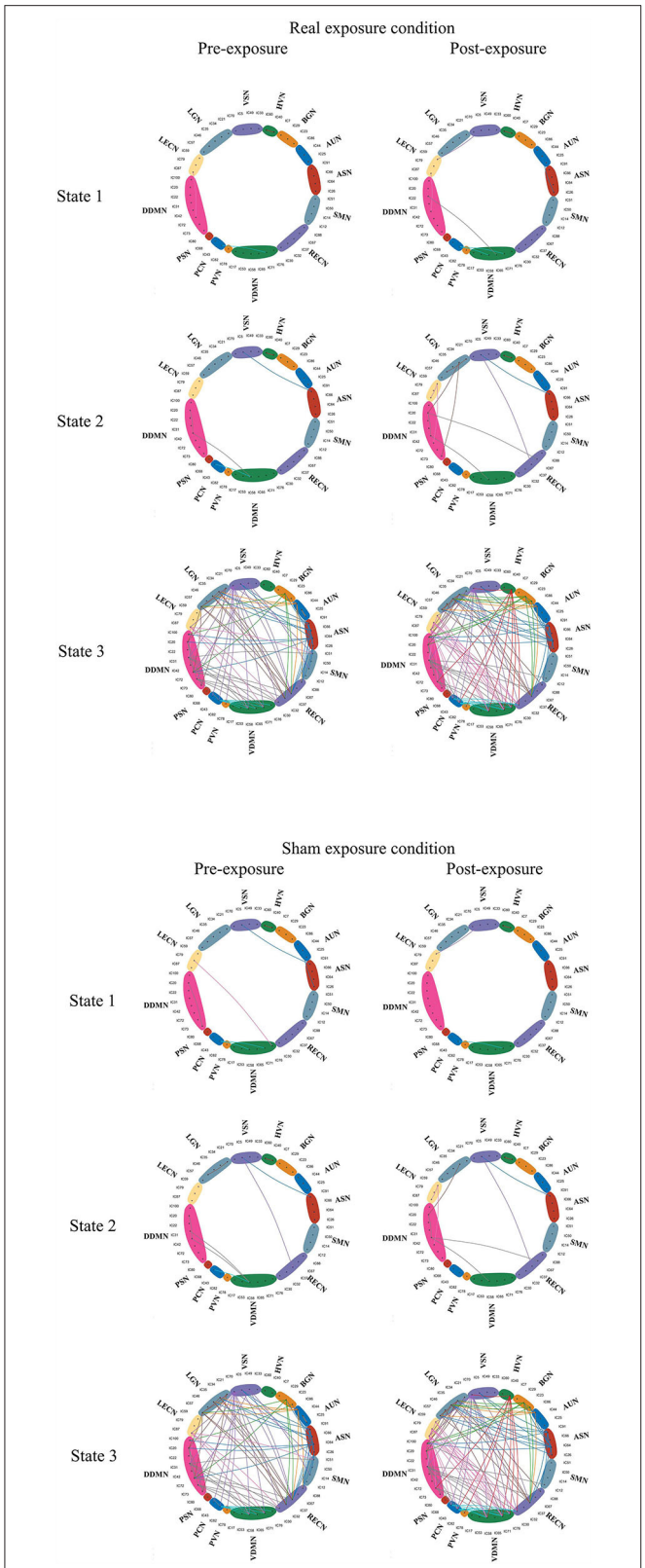

FIGURE 8 | The states derived from the experiments. Connections with correlation coefficients exceeding 0.6 are shown in the Figure (28).

network collectivization, and other attributes without paying attention to the special ICN architecture. In fact, ICNs, comprised of various physiological regions (ICs), was coordinated to provide integrative services on behalf of the central nervous system and have emerged as fundamental and organizational elements of human brain architecture. The finding may also indicate that the localized near-field exposure with the power emitted by a mobile phone may impact the regional or interregional BOLD dynamics, but would not affect the specific ICN relating to functional or behavior change. The study, as well as the abovementioned publications, provided useful information to comprehensively understand the change of brain function by EMF exposure.

There were several limitations. Firstly, only 17 subjects were exposed in the experiments. For example, in State 3, only 3–4 subjects were eligible for statistical comparison. In fact, many acute exposure studies on neurophysiological effects have the same problem. For example, Danker-Hopfe et al. (41) conducted a literature review and concluded that 14 out 22 papers on RF exposure and EEG included subjects $\leq$20. In such a case, the statistical power may only detect the large effects. However, the present study, although with limited number of subjects, has its merit as enriching the knowledge of EMF safety. Based on the work, researchers can continue to optimize the experimental design and to accumulate dataset. Secondly, there were no positive controls in the study. In such a case, it would be difficult to interpret the positive findings if any of them were found (although we did not detect them). Actually, we have considered to include positive control, but it was not allowed by the ethical committee since it may involve high risk, especially when the potential health implication of EMF exposure has not been elucidated. Thirdly, during 3 T MRI scan, the subjects were exposed to the static magnetic field, gradient magnetic field, and the RF fields (128 MHz). The effect may confound the results. Previous reports proposed activation of the sites at the anterior cingulate, the insula, hippocampus, and some parts of nasal gandlia (caudate) following exposure to MRI (42). It was consistent with our research on functional connectivity strength (38). In this work, no statistically significant difference has been reported in the real exposure group. This may be due to the clustering of the network which would smooth the particular activation at the locations. Low-frequency pulsed signals may influence sleep EEG (43, 44). Although the subjects were requested to stay awake during the experiments, completely ruling out the possibility that subjects fell asleep or experienced sleepiness during the MRI scan was difficult. In such a case, the impact should be taken into consideration. Moreover, each subject was only scanned for approximately 6 min (in order to minimize the effect of RF exposure during MRI). Longer scanning times (ideally tens of minutes) will improve the robustness for FC variability estimation.

CONCLUSION

We evaluated functional connectivity within and between ICNs identified by group-level ICA. Our results showed that there was no statistically significant different in terms of static and

dynamic FNC in both real and sham exposure conditions by exposure to LTE signals. Although previous results show that short-term electromagnetic exposure had an impact on the brain in terms of voxel-wise functional connectivity and graph-theory analysis of functional networks, the results of this work point out that the impact of short-term electromagnetic exposure was insufficient to be detected at the ICNs level. Appropriate metrics for evaluating the brain functional change should be discussed. Further work is needed in the perspective of behavioral change.

DATA AVAILABILITY STATEMENT

The datasets presented in this article are not readily available because the datasets generated and analyzed during the current study are not publicly available due [Data involves the subject's privacy]. Requests to access the datasets should be directed to Lei Yang, yanglei@caict.ac.cn.

ETHICS STATEMENT

The studies involving human participants were reviewed and approved by Chinese People's Liberation Army General Hospital. The patients/participants provided their written informed consent to participate in this study.

AUTHOR CONTRIBUTIONS

TW: conceptualization, supervision, and project administration. LY: methodology, formal analysis, and writing—review and editing. QL: methodology, investigation, and writing—original draft. YZ: validation. XW: data curation. ZC: funding acquisition. All authors have read and agreed to the published version of the manuscript.

FUNDING

This research was funded by National Natural Science Foundation of China (No. 61971445).

SUPPLEMENTARY MATERIAL

The Supplementary Material for this article can be found online at: https://www.frontiersin.org/articles/10.3389/fpubh.2021.734370/full#supplementary-material

REFERENCES

1. R. Westerman. Hocking B. Diseases of modern living: neurological changes associated with mobile phones and radiofrequency radiation in humans. *Neurosci Lett.* (2004) 361:13–6. doi: 10.1016/j.neulet.2003.12.028
2. LTE Ecosystem December 2020—Global update—GSA, (2020). Available from: https://gsacom.com/paper/lte-ecosystem-december-2020-global-update/ (accessed April 28, 2021).
3. Hillert L, Berglind N, Arnetz BB, Bellander T. Prevalence of self-reported hypersensitivity to electric or magnetic fields in a population-based questionnaire survey. *Scand J Work Environ Health.* (2002) 28:33–41. doi: 10.5271/sjweh.644
4. Rubin GJ, Nieto-Hernandez R. Wessely S. Idiopathic environmental intolerance attributed to electromagnetic fields (formerly 'electromagnetic hypersensitivity'): An updated systematic review of provocation studies. *Bioelectromagnetics.* (2010) 31:1–11. doi: 10.1002/bem.20536
5. Rubin GJ, Das Munshi J, Wessely *S.* Electromagnetic hypersensitivity: a systematic review of provocation studies. *Psychosom Med.* (2005) 67:224–32. doi: 10.1097/01.psy.0000155664.13300.64
6. Hutchison RM, Womelsdorf T, Allen EA, Bandettini PA, Calhoun VD, Corbetta M. et al. Dynamic functional connectivity: Promise, issues, and interpretations. *Neuroimage.* (2013) 80:360–78. doi: 10.1016/j.neuroimage.2013.05.079
7. Van Dijk KRA, Hedden T, Venkataraman A, Evans KC, Lazar SW, Buckner RL. Intrinsic functional connectivity as a tool for human connectomics: theory, properties, and optimization. *J Neurophysiol.* (2009) 103:297–321. doi: 10.1152/jn.00783.2009
8. Seewoo BJ, Joos AC, Feindel KW. An analytical workflow for seed-based correlation and independent component analysis in interventional resting-state fMRI studies. *Neurosci Res.* (2020) 165:26–37. doi: 10.1016/j.neures.2020.05.006
9. Park HJ, Friston K. Structural and functional brain networks: from connections to cognition. *Science.* (2013) 342:1238411. doi: 10.1126/science.1238411
10. Makeig S, Debener S, Onton J, Delorme A. Mining event-related brain dynamics. *Trends Cogn Sci.* (2004) 8:204–10. doi: 10.1016/j.tics.2004.03.008
11. Ma Y, Hamilton C, Zhang N. Dynamic connectivity patterns in conscious and unconscious brain. *Brain Connect.* (2017) 7:1–12. doi: 10.1089/brain.2016.0464
12. Damaraju E, Allen EA, Belger A, Ford JM, McEwen S, Mathalon DH. et al. Dynamic functional connectivity analysis reveals transient states of dysconnectivity in schizophrenia. *NeuroImage: Clin.* (2014) 5:298–308. doi: 10.1016/j.nicl.2014.07.003
13. Wang Y, Berglund IS, Uppman M, Li TQ. Juvenile myoclonic epilepsy has hyper dynamic functional connectivity in the dorsolateral frontal cortex. *Neuroimage Clin.* (2019) 21:101604. doi: 10.1016/j.nicl.2018.11.014
14. Wu T, Lv B, Chen Z. Dosimetric studies involving in the experiments for the evaluation of the brain activation by LTE exposure. In: *International Symposium on Electromagnetic Compatibility—EMC EUROPE.* (2012). p. 1–4.
15. *SPEC-3GPP TS 36.521-1—Evolved Universal Terrestrial Radio Access (E-UTRA); User Equipment (UE) conformance specification; Radio transmission and reception; Part 1: Conformance testing.* Available from: https://itectec.com/archive/3gpp-specification-ts-36-521-1/
16. Li C, Chen Z, Yang L, Lv B, Liu J, Varsier N, et al. Generation of infant anatomical models for evaluating electromagnetic field exposures. *Bioelectromagnetics.* (2015) 36:10–26. doi: 10.1002/bem.21868
17. Wu T, Shao Q, Yang L. Simplified segmented human models for whole body and localised SAR evaluation of 20 MHz to 6 GHz electromagnetic field exposures. *Radiat Prot Dosimetry.* (2013) 153:266–72. doi: 10.1093/rpd/ncs105
18. McKeown MJ, Sejnowski TJ. Independent component analysis of fMRI data: examining the assumptions. *Hum Brain Mapp.* (1998) 6:368–72. doi: 10.1002/(SICI)1097-0193(1998)6:5/6<368::AID-HBM7>3.0.CO;2-E
19. Schmithorst VJ, Holland SK. Comparison of three methods for generating group statistical inferences from independent component analysis of functional magnetic resonance imaging data. *J Magn Reson Imaging.* (2004) 19:365–8. doi: 10.1002/jmri.20009
20. Kiviniemi V, Starck T, Remes J, Long X, Nikkinen J, Haapea M. et al. Functional segmentation of the brain cortex using high model order group PICA. *Hum Brain Mapp.* (2009) 30:3865–86. doi: 10.1002/hbm.20813

21. Abou-Elseoud, Starck T, Remes J, Nikkinen J, Tervonen O, Kiviniemi V. The effect of model order selection in group PICA. *Hum Brain Mapp*. (2010) 31:1207–16. doi: 10.1002/hbm.20929
22. Bell AJ, Sejnowski TJ. An information-maximization approach to blind separation and blind deconvolution. *Neural Comput*. (1995) 7:1129–59. doi: 10.1162/neco.1995.7.6.1129
23. Himberg J, Hyvarinen A. ICASSO: Software for investigating the reliability of ICA estimates by clustering and visualization. In: *Proceedings of the NNSP, Toulouse, France*. (2003). p. 259–68.
24. Calhoun VD, Adali T, Pearlson GD, Pekar JJ. A method for making group inferences from functional MRI data using independent component analysis. *Hum Brain Mapp*. (2001) 14:140–51. doi: 10.1002/hbm.1048
25. Lee MJ, Park BY, Cho S, Park H, Kim ST, Chung CS. Dynamic functional connectivity of the migraine brain. *PAIN*. (2019) 160:2776–86. doi: 10.1097/j.pain.0000000000001676
26. Griffanti L, Douaud G, Bijsterbosch J, Evangelisti S, Alfaro-Almagro F, Glasser MF, et al. Hand classification of fMRI ICA noise components, *Neuroimage*. (2017) 154:188–205. doi: 10.1016/j.neuroimage.2016.12.036
27. Cordes D, Haughton VM, Arfanakis K, Carew JD, Turski PA, Moritz CH, Quigley MA, Meyerand ME. Frequencies contributing to functional connectivity in the cerebral cortex in "resting-state" data. *AJNR Am J Neuroradiol*. (2001) 22:1326–33
28. Armitage P, Berry G. In: *Statistical Methods in Medical Research*, 3rd edn. Oxford: Blackwell Scientific Publications (1994) p. 312–41.
29. Fox MD, Raichle ME. Spontaneous fluctuations in brain activity observed with functional magnetic resonance imaging. *Nat Rev Neurosci*. (2007) 8:700–11. doi: 10.1038/nrn2201
30. Chang C, Glover GH. Time-frequency dynamics of resting-state brain connectivity measured with fMRI. *Neuroimage*. (2010) 50:81–98. doi: 10.1016/j.neuroimage.2009.12.011
31. Park BY, Moon T, Park H. Dynamic functional connectivity analysis reveals improved association between brain networks and eatingbehaviors compared to static analysis. *Behav Brain Res*. (2018) 337:114–21. doi: 10.1016/j.bbr.2017.10.001
32. Allen EA, Damaraju E, Plis SM, Erhardt EB, Eichele T, Calhoun VD. *Tracking whole-brain connectivity dynamics in the resting state. Cereb Cortex*. (2014) 24:663–76. doi: 10.1093/cercor/bhs352
33. Spoormaker VI, Schröter MS, Gleiser PM, Andrade KC, Dresler M, Wehrle R, et al. Development of a large-scale functional brain network during human non-rapid eye movement sleep. *J Neurosci*. (2010) 30:11379–87. doi: 10.1523/JNEUROSCI.2015-10.2010
34. Larson-Prior LJ, Power JD, Vincent JL, Nolan TS, Coalson RS, Zempel J, et al. Modulation of the brain's functional network architecture in the transition from wake to sleep. In: van Someren EJW, editor. *Slow Brain Oscillations of Sleep, Resting State and Vigilance*. Amsterdam, Netherlands: Elsevier (2011). p. 277–94. doi: 10.1016/B978-0-444-53839-0.00018-1
35. Zou QH, Zhu CZ, Yang Y, Zuo XN, Long XY, Cao QJ. et al. An improved approach to detection of amplitude of low-frequency fluctuation (ALFF) for resting-state fMRI: Fractional ALFF. *J Neurosci Meth*. (2008) 172:137–41. doi: 10.1016/j.jneumeth.2008.04.012
36. Lv B, Chen Z, Wu T, Shao Q, Yan D, Ma L, et al. The alteration of spontaneous low frequency oscillations caused by acute electromagnetic fields exposure. *Clin Neurophysiol*. (2014) 125:277–86. doi: 10.1016/j.clinph.2013.07.018
37. Wei Y, Yang J, Chen Z, Wu T. B. Lv. Modulation of resting-state brain functional connectivity by exposure to acute fourth-generation long-term evolution electromagnetic field: An fMRI study. *Bioelectromagnetics*. (2019) 40:42–51. doi: 10.1002/bem.22165
38. Yang L, Zhang C, Chen Z, Li C, Wu T. Functional and network analyses of human exposure to long-term evolution signal. *Environ Sci Pollut Res*. (2021) 28:5755–73. doi: 10.1007/s11356-020-10728-w
39. Tzourio-Mazoyer N, Landeau B, Papathanassiou D, Crivello F, Etard O, Delcroix N, et al. Automated anatomical labeling of activations in SPM using a macroscopic anatomical parcellation of the MNI MRI single-subject brain. *NeuroImage*. (2002) 15:273–89. doi: 10.1006/nimg.2001.0978
40. Arslan S, Ktena SI, Makropoulos A, Robinson EC, Rueckert D, Parisot S. Human brain mapping: A systematic comparison of parcellation methods for the human cerebral cortex. *NeuroImage*. (2018) 170:5–30. doi: 10.1016/j.neuroimage.2017.04.014
41. Danker-Hopfe H, Eggert T, Dorn H, Sauter C. Effects of RF-EMF on the human resting-state EEG-the inconsistencies in the consistency. Part 1: non-exposure-related limitations of comparability between studies. *Bioelectromagnetics*. (2019) 40:291–318. doi: 10.1002/bem.22194
42. Robertson AJ, Theberge J, Weller J, Drost JD, Prato SF, Thomas WA. Low-frequency pulsed electromagnetic field exposure can alter neuroprocessing in humans. *J R Soc Interface*. (2010) 7:467–73. doi: 10.1098/rsif.2009.0205
43. Schmid MR, Loughran SP, Regel SJ, Murbach M, Bratic Grunauer A, Rusterholz T, et al. Sleep EEG alterations: effects of different pulse-modulated radio frequency electromagnetic fields. *J Sleep Res*. (2011) 21:50–8. doi: 10.1111/j.1365-2869.2011.00918.x
44. Hinrikus H, Bachmann M, Lass J, Tomson R, Tuulik V. Effect of 7, 14 and 21 Hz modulated 450 MHz microwave radiation on human electroencephalographic rhythms. *Int J Radiat Biol*. (2008) 84:69–79. doi: 10.1080/09553000701691679

Conflict of Interest: The authors declare that the research was conducted in the absence of any commercial or financial relationships that could be construed as a potential conflict of interest.

Publisher's Note: All claims expressed in this article are solely those of the authors and do not necessarily represent those of their affiliated organizations, or those of the publisher, the editors and the reviewers. Any product that may be evaluated in this article, or claim that may be made by its manufacturer, is not guaranteed or endorsed by the publisher.

frontiers in Public Health

ORIGINAL RESEARCH
published: 03 February 2022
doi: 10.3389/fpubh.2021.794564

Numerical Evaluation of Human Body Near Field Exposure to a Vehicular Antenna for Military Applications

*Micol Colella[1], Marianna Biscarini[1], Marco de Meis[2], Roberto Patrizi[2], Tino Ciallella[2], Daniele Ferrante[3], Alessandro De Gaetano[3], Marco Capuano[3], Giovanni Pellegrino[3], Emanuele Martini[3], Marta Cavagnaro[1], Francesca Apollonio[1] and Micaela Liberti[1]**

[1] Department of Information Engineering, Electronics and Telecommunications, Sapienza University of Rome, Rome, Italy, [2] Larimart S.p.A., Rome, Italy, [3] Centro Polifunzionale di Sperimentazione (CEPOLISPE), Rome, Italy

OPEN ACCESS

Edited by:
Ruiyun Peng,
Academy of Military Medical Sciences (AMMS), China

Reviewed by:
Tongning Wu,
China Academy of Information and Communications Technology, China
Aiping Yao,
Lanzhou University, China

***Correspondence:**
Micaela Liberti
micaela.liberti@uniroma1.it

Specialty section:
This article was submitted to Radiation and Health, a section of the journal Frontiers in Public Health

Received: 13 October 2021
Accepted: 31 December 2021
Published: 03 February 2022

Citation:
Colella M, Biscarini M, de Meis M, Patrizi R, Ciallella T, Ferrante D, De Gaetano A, Capuano M, Pellegrino G, Martini E, Cavagnaro M, Apollonio F and Liberti M (2022) Numerical Evaluation of Human Body Near Field Exposure to a Vehicular Antenna for Military Applications. Front. Public Health 9:794564. doi: 10.3389/fpubh.2021.794564

Background: The use of electromagnetic (EM) technologies for military applications is gaining increasing interest to satisfy different operational needs, such as improving battlefield communications or jamming counterpart's signals. This is achieved by the use of high-power EM waves in several frequency bands (e.g., HF, VHF, and UHF). When considering military vehicles, several antennas are present in close proximity to the crew personnel, which are thus potentially exposed to high EM fields.

Methods: A typical exposure scenario was reproduced numerically to evaluate the EM exposure of the human body in the presence of an HF vehicular antenna (2–30 MHz). The antenna was modeled as a monopole connected to a 3D polygonal structure representing the vehicle. Both the EM field levels in the absence and in the presence of the human body and also the specific absorption rate (SAR) values were calculated. The presence of the operator, partially standing outside the vehicle, was simulated with the virtual human body model Duke (Virtual Population, V.3). Several exposure scenarios were considered. The presence of a protective helmet was modeled as well.

Results: In the area usually occupied by the personnel, E-field intensity radiated by the antenna can reach values above the limits settled by international safety guidelines. Nevertheless, local SAR values induced inside the human body reached a maximum value of 14 mW/kg, leading to whole-body averaged and 10-g averaged SAR values well below the corresponding limits.

Conclusion: A complex and realistic near-field exposure scenario of the crew of a military vehicle was simulated. The obtained E-field values radiated in the free space by a HF vehicular antenna may reach values above the safety guidelines reference levels. Such values are not necessarily meaningful for the exposed subject. Indeed, SAR and E-field values induced inside the body remain well below safety limits.

Keywords: computational dosimetry, vehicular antenna, human body model, RF exposure, safety

INTRODUCTION

Electromagnetic (EM) technologies for military applications are extensively used to satisfy a variety of operational requirements. Particularly, military vehicles are equipped with several antennas that work in a wide frequency range (e.g., high frequency–HF−3 to 30 MHz, very high frequency–VHF−30 to 300 MHz, and ultra-high frequency–UHF−300 to 3,000 MHz) and transmit high-power values for communications and jamming (1, 2). Due to their position in proximity to the manholes, vehicular antennas potentially expose the crew personnel to high-intensity EM fields (EMF) (3–5). International regulatory bodies, such as the International Commission on Nonionizing Radiation Protection (ICNIRP, mainly considered in Europe) or the IEEE Technical Committee 95 (IEEE-TC95, mainly considered in North America), aim to prevent health risks caused by EMF on both the general population and the workers, by setting limits in the exposure levels. For the workers, the limits are less conservative, since this category is considered to be exposed under controlled conditions (6). In this context, only IEEE-TC95 proposes a standard to specifically protect the personnel in a military workplace (7), whereas the ICNIRP does not distinguish for this category among the occupationally exposed individuals. Both IEEE and ICNIRP guidelines recommend two kinds of exposure limits. The first ones are based on dosimetric thresholds for established adverse health effects and are defined as *dosimetric reference limits* (DRLs) by the IEEE-TC95 (7) or *basic restrictions* (BRs) by the ICNIRP (6). Both limits can be expressed in terms of internal electric (E-)field strength and/or specific absorption rate, SAR (i.e., the power absorbed per unit mass), depending on the operating frequency (6, 7). In the frequency range between 1 and 30 MHz, IEEE DRLs are expressed in terms of SAR and impose a threshold value equal to 0.4 W/kg as averaged over the whole body (SAR_{wb}), and 10 W/kg peak averaged over any 10 g of tissue (SAR_{10Avg}), with the exception of extremities and pinnae where the limit is set at 20 W/kg (7). In the same frequency range, ICNIRP BRs are very close to those settled by IEEE, for exposure durations greater than 6 min. The second settled limits are the IEEE *exposure reference levels* (ERLs) and the ICNIRP *reference levels* (RLs), which represent a more practical method to determine compliance with the guidelines (6, 7). The IEEE ERLs are derived from the DRLs and are given as RMS quantities spatially averaged over an area equivalent to the vertical cross-section of the human body (projected area). In the frequency range between 1 MHz and 30 MHz, the limit is calculated as $1842/f_M$ (V/m), where f_M is the frequency in MHz (7). Such ERL level is valid in the so-called Zone 1, where only informed and instructed personnel is allowed (7). The ICNIRP guidelines do not include such differentiation in the exposure location (6), but they introduce differences in the settled limits related to the duration of the exposure. ICNIRP RLs represent the unperturbed electric field or power density values, calculated in the area in which the human body can be located but in its absence. They are derived from the BRs (6). In the 2020 ICNIRP guidelines, RLs for exposures longer than 30 min are given as equal to $660/f_M^{0.7}$ (RMS, whole-body averaged unperturbed values), whereas shorter exposures allow more relaxed values. In the frame of the European legislation, the Directive 2013/35/UE referred to the previous ICNIRP 2010 guidelines (8), to derive the so-called *exposure level values* and the *action levels*, that establish the minimum health and safety requirements regarding the exposure of workers to the risks arising from EMF exposure (9, 10). In particular, the exposure level values are derived from ICNIRP 2010 BRs, whereas action values are derived from the RLs, with the important modification that action levels are considered as the maximum field value in the area occupied by the human body, rather than whole-body volume averaged values. Finally, in the context of personnel protection from EMF, each European Member State can adopt the EU directive or implement equivalent or more specific protection systems, such as the North Atlantic Treaty Organization (NATO) international standard agreement (STANAG 2345 (11)) that specifically protects armed forces. The rationale proposed by both IEEE and ICNIRP and adopted by the European directive, of providing two exposure limits, allows for a first and rapid verification of compliance with the guidelines by a direct measure of external quantities, such as power density or field strength. In the case of exceeding the RLs, further investigation must be carried out to verify that the BRs are respected (12). Within this framework, computational dosimetry becomes a fundamental tool as it gives the possibility to realistically reproduce an exposure scenario and study the EM quantities induced inside the human body. Different numerical studies have been conducted to evaluate exposure levels around and inside standard (3, 13, 14), or military (1, 2, 15) vehicles equipped with radiofrequency (RF) antennas. Nevertheless, they either account for the presence of the human body with homogeneous virtual phantoms (13, 14) or do not account for it at all (1, 2, 15). More recently, a study took into account heterogeneous body models (3). Particularly, the aim of the study conducted by Guellab and Wu (3) was to develop a four-pole Debye model of the dielectric properties of each tissue, to take into account the frequency dependence. To validate such model, they simulated the exposure of the crew placed inside a military vehicle equipped with a UHF (100 MHz−1 GHz) high-power antenna. Nevertheless, as pointed out by Sobiech and colleagues (4), inside the vehicle, the EM hazard is reduced because of the extended distance between the antennas and personnel, and thanks to the shielding effect of the vehicle metallic structure. Conversely, in the area outside the vehicle and near the EMF source, the maximum intensity can exceed the guideline limits. To this regard, current literature does not provide a deep analysis of the personnel exposure in the proximity of a high-power radiating antenna, as would happen in correspondence of the turret manhole. Furthermore, there is a lack of information about the effect of wearing personal protective equipment (i.e., a helmet) or cabled instrumentation for communication. Thus, the aim of this study was to investigate realistic scenarios of an operator standing partially outside the vehicle, close to a vehicular antenna working in the HF frequency range (2–30 MHz), to deepen knowledge in terms of both induced electric field and SAR inside the body. Furthermore, conditions such as the use of a helmet equipped with a headset were investigated to verify whether it exposes the head of the operator to potentially high intensities. To the best of the authors' knowledge, this is the first time that a dosimetric analysis is performed in such a realistic scenario with safety purposes.

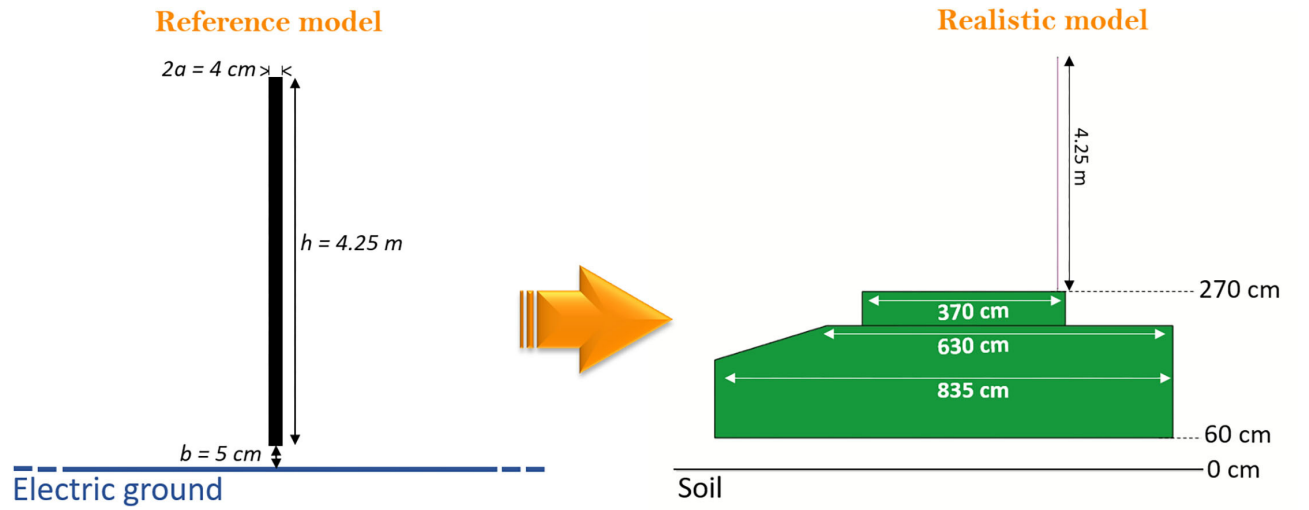

FIGURE 1 | Numerical model of the antenna. In the reference model, the monopole (4.25 m high, diameter, *2a,* of 4 cm and feeding gap, *b,* of 5 cm) is placed over an ideal infinite electric ground. In the realistic model, the monopole is mounted over a simplified 3D model of the vehicle, reproducing typical dimensions. A 60cm gap is considered between the bottom of the vehicle and the soil to simulate the presence of the tires.

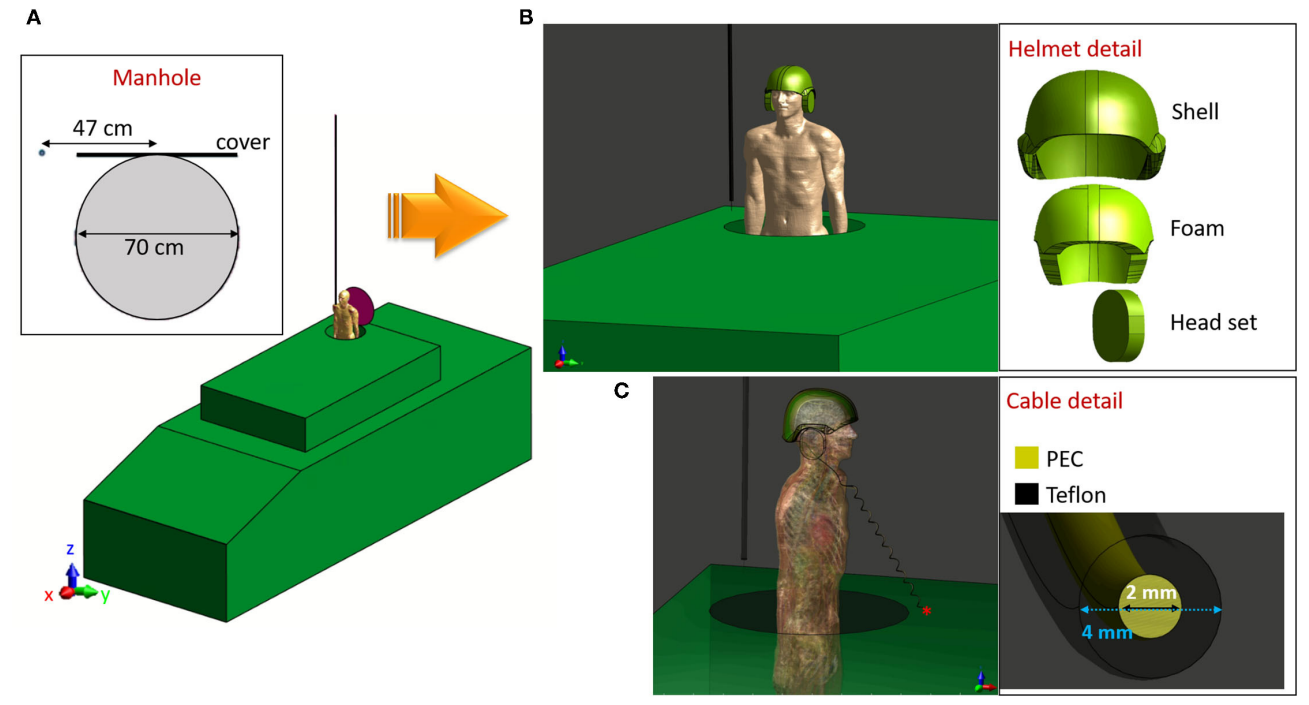

FIGURE 2 | Military personnel exposure scenario: **(A)** Unequipped operator standing partially outside the manhole, inset: detail of manhole position and dimensions. **(B)** Equipped operator wearing the protective helmet, inset: detail of the helmet composition. **(C)** Equipped operator wearing the protective helmet and the cabled headset, connected to the vehicle through a 10μF capacitor, inset: detail of the connecting cable.

MATERIALS AND METHODS

Modeling the Vehicular Antenna

HF vehicular antennas operate in the frequency range between 2 and 30 MHz. Usually, they are monopoles with the vehicle metal sheet that makes the monopole ground. In this study, the antenna was made by a conductor 4.25 m long. The radius *a* and the feeding gap *b* (**Figure 1**) were dimensioned based on antenna theory (16), resulting in 2 and 5 cm, respectively. Further details on the model can be found in the **Supplementary Material**. The study was performed at the HF central frequency of 16 MHz with 25 W of input power. Ideally, a monopole should be

TABLE 1 | Dielectric properties of the materials considered to model the helmet and the cable.

Material	Conductivity	Relative permittivity
Polyamide	6.6 *times* 10^{-6} S/m	3.5
Nylon	0.0057 S/m	2.84
Teflon	4.62 *times* 10^{-4} S/m	1

connected to an infinite (>> λ) ground plane, as shown in **Figure 1**. Nevertheless, in such applications, the antenna is placed on the roof of the vehicle, which is characterized by finite dimensions. Therefore, to respect a typical military exposure scenario, the infinite electric ground was replaced with a 3D simplified reproduction of a military vehicle, respecting the dimensions of all the critical sections, as shown in **Figure 1**. In the vehicle model, the base has a size of 835 x 300 cm, and the middle part (630 x 280 cm) is tapered and connects the base to the turret (370 x 220 cm). The manhole on the turret and its door were considered as well. The manhole has a diameter of 70 cm and is placed at about 50 cm from the antenna (**Figure 2**, manhole inset). The vehicle, the monopole, and the manhole door were assigned to a perfectly conductive (PEC) material. To investigate a possible coupling between the monopole and the metallic door, the latter was simulated open. The soil was simulated as a plane of PEC, and a 60 cm gap was considered to mimic the tires, as shown in **Figure 1**.

Modeling the Exposure Scenario

To take into account the presence of the operator, the whole-body model Duke (standard adult men, aged 34 years, 1.77 cm tall and 70 kg) weight of the Virtual Population (ViP v.3) was used (17). The Duke model was located in correspondence of the manhole, with 70 cm of the body (i.e., the trunk) standing outside the vehicle, as shown in **Figure 2A**. The level of detail used in modeling the exposure scenario was progressively increased by adding a protective helmet and a cabled headset. The helmet is made of a ballistic shell, a liner containing a foam padding, and the headset case (**Figure 2B**, helmet inset). The model of the intercom cable passes through the headset case and around the nape to fall along the operator's body in a helix of a length of 120 cm (**Figure 2C**). The cable is made of a Teflon jacket of 4 mm diameter and a copper wire of 2 mm diameter (**Figure 2C**, cable inset), and it is connected to the external surface of the vehicle (functioning as the ground), by a 10 μF capacitor. As a whole, four exposure scenarios were simulated:

- *Exposure scenario a*: vehicle with open manhole,
- *Exposure scenario b*: vehicle with the operator partially outside the manhole,
- *Exposure scenario c*: vehicle with the operator partially outside the manhole, wearing the protective helmet,
- *Exposure scenario d*: vehicle with the operator partially outside the manhole, wearing the protective helmet, and the cabled headset.

Additionally, exposure scenario d was further investigated in the absence of the human body, to understand the effect of the cabled headset on the E-field intensity radiated in air. In Scenarios c and d, polyamide was assigned to the shell and the foam padding of the helmet, nylon to the headset case. The copper wire of the cable was modeled as PEC, and the cable's insulating jacket was modeled as Teflon. The dielectric properties assigned to each material at 16 MHz can be found in **Table 1**. The physical properties (i.e., electrical conductivity, electrical permittivity, and mass density) of each of the 305 anatomical elements of the Duke model were assigned from the IT'IS data base (18) at the working frequency. In all the scenarios, the reference system was chosen as oriented with the Z-axis along the length of the antenna, and the XY plane parallel to the surface of the vehicle, with the length of the vehicle along the X-axis and the width along the Y-axis, as shown in **Figure 2**.

Electromagnetic Simulations

The exposure scenarios were modeled and simulated within the simulation software Sim4Life (v.5, Zurich MedTech, Zurich). The EM problem was solved using the finite difference time domain (FDTD) method (19), considering a 16 MHz sinusoidal source feeding the monopole. To ensure free propagation of the E-field outside the simulation domain, absorbing boundary conditions with perfectly matched layer (PML) were assigned to the lateral and superior walls, whereas a PEC condition was assigned to the inferior wall to simulate the presence of the reflecting soil. A non-uniform grid was applied to each scenario. The vehicle was discretized with a 5-cm isotropic grid, whereas an anisotropic grid (2 mm x 2 mm x 3 cm) was considered for the monopole antenna. Additionally, Duke's head, the helmet, and the cable were discretized with an isotropic 2-mm resolution, whereas 2.5 mm was used on Duke's trunk. The overall number of cells in the simulation space was 13 MCells for *scenario a*, 66 MCells for *scenario b*, 68 MCells for *scenario c*, and 98 MCells for *scenario d*. The results of the simulations were analyzed focusing on the induced E-field, and also on the whole-body averaged SAR (SAR_{wb}), for global exposure, and on the peak of the SAR averaged over 10 g of tissue in the head (SAR_{10Avg}), for local exposure. Following the safety guidelines rationale, that is, to always look for the worst-case exposure, the calculated field values are analyzed with respect to the lowest limit among those settled in the different guidelines. Accordingly, 86.3 V/m is taken in the following as the threshold for RLs, derived from the 61 V/m (RMS), considered as the E-field maximum value in the area where the body can be located (8, 9). As described in the Introduction section, in the cases in which the unperturbed field values are above the thresholds, SAR values should be considered. In this latter case, all reported guidelines set the same limits, that is, 0.4 W/kg averaged over the whole body, or 10 W/kg peak SAR averaged over 10 g of tissue (6, 7, 9).

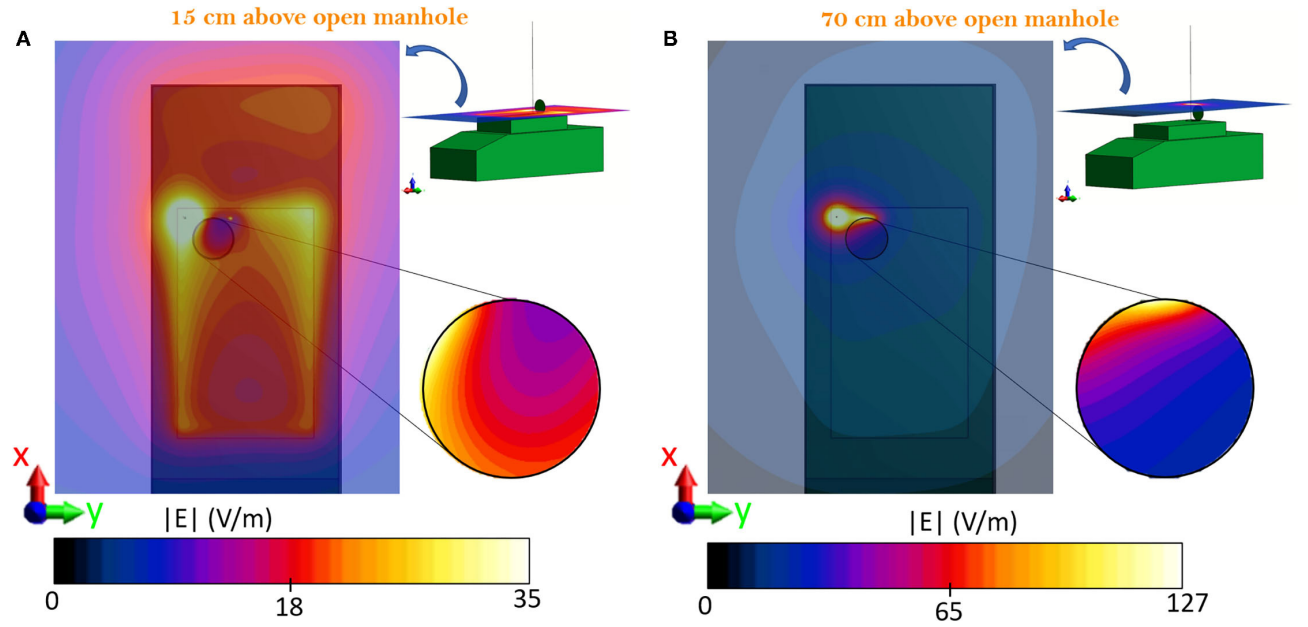

FIGURE 3 | Top view of the vehicle and distribution map of the E-field radiated by the antenna model fed with 25 W at 16 MHz. **(A)** Distribution at 15 cm above the manhole, circular inset: detail of the manhole area. **(B)** Distribution at 70 cm above the manhole, circular inset: detail of the manhole area. The vehicle and manhole boundaries are shown by the light black lines.

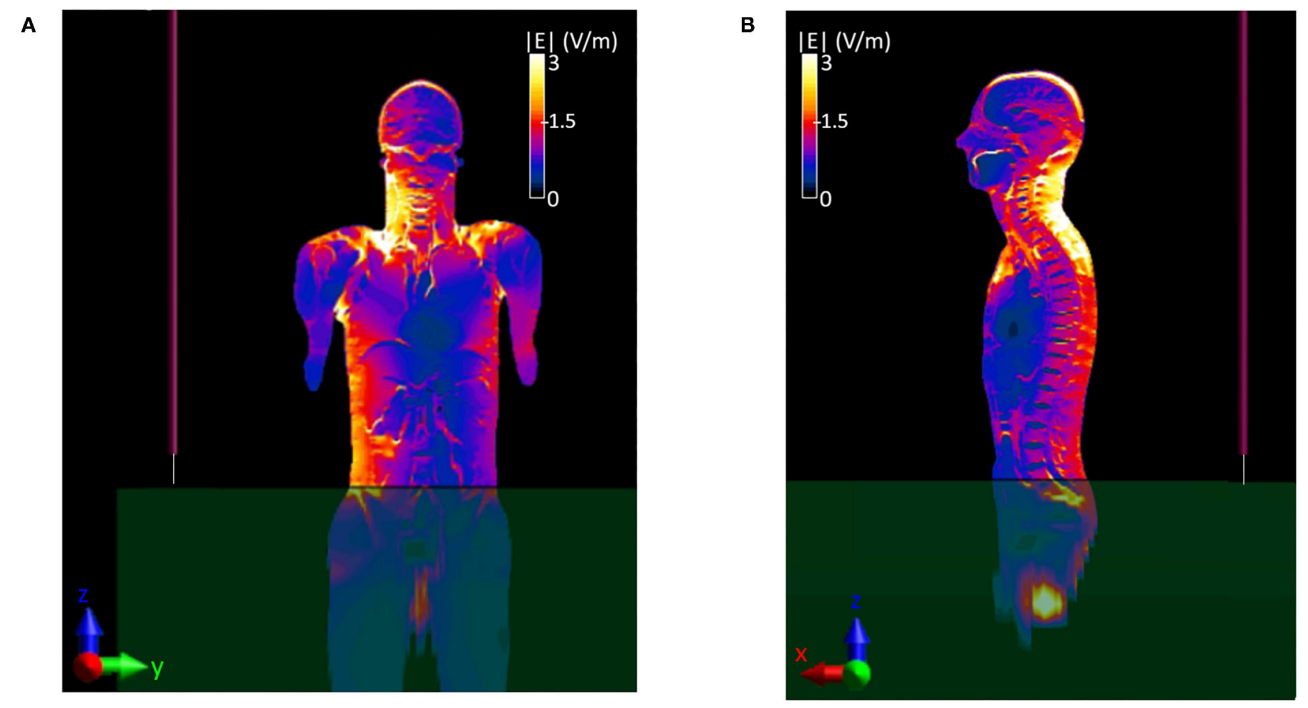

FIGURE 4 | Distribution of the E-field induced inside the virtual body model Duke. **(A)** Coronal or frontal plane-YZ, **(B)** sagittal or lateral plane-XZ.

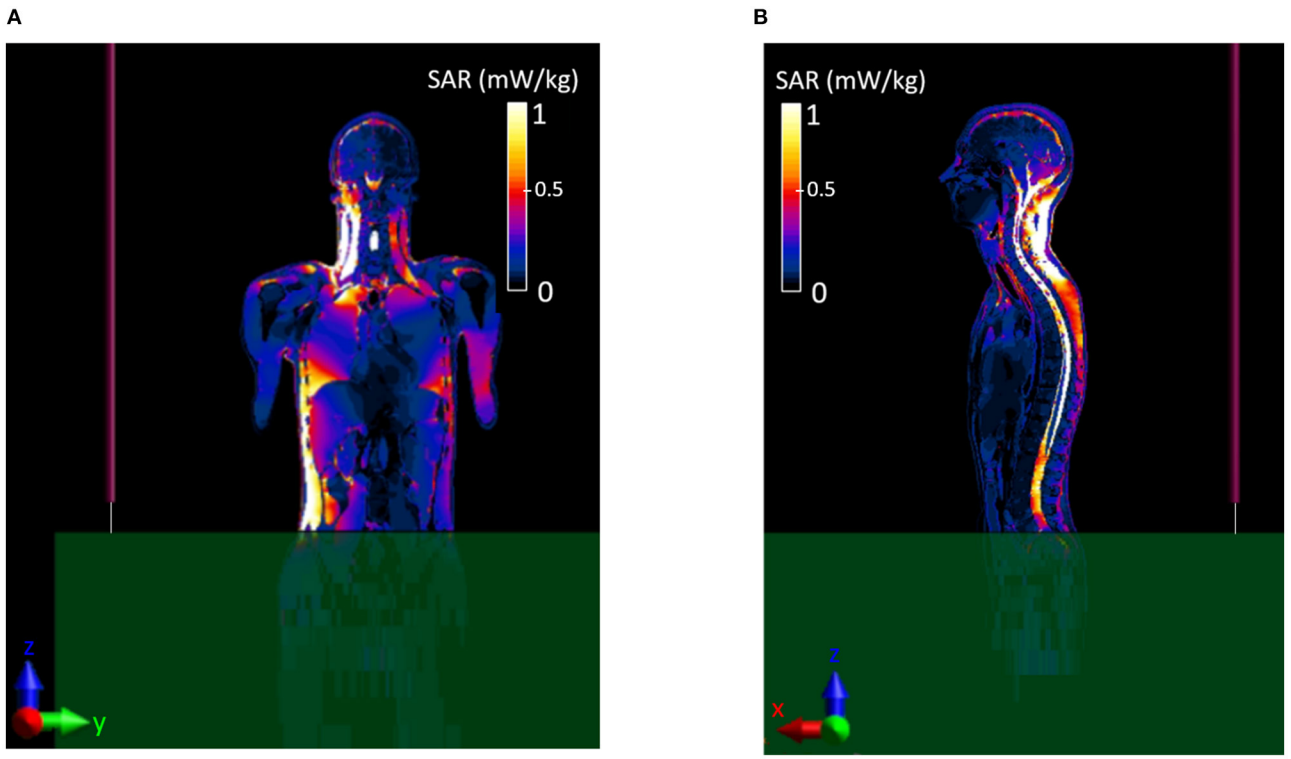

FIGURE 5 | Local distribution of the induced SAR inside the virtual body model Duke. **(A)** Coronal or frontal plane-YZ, **(B)** sagittal or lateral plane-XZ.

RESULTS

Exposure Scenario *a*: Vehicle With Open Manhole

The E-field generated by the monopole placed over the simplified model of the vehicle was analyzed in the absence of the human body, with particular attention to the values estimated in the proximity of the manhole. Assuming that the space above the manhole would be usually occupied by the trunk of an average size man, it was of interest to evaluate the E-field distribution in areas located at different heights from the surface of the manhole, that is, $h_1 = 15$ cm and $h_2 = 70$ cm, which approximately correspond to the location of the waist and of the head, respectively. The E-field distributions at the two heights h_1 and h_2 are reported in **Figure 3**. In both planes, a coupling between the monopole and the metallic manhole door and the influence of the open manhole are visible. At $h_1 = 15$ cm, a decrease in the E-field intensity is caused by the presence of the open manhole. In particular, within a 10 cm radius around the antenna, levels above 100 V/m were estimated, that decrease to values between 35 and 11 V/m over the manhole (**Figure 3A**). A hotspot of 40 V/m was found at the farther extremity of the manhole door, and, as expected, an increase in the field intensity occurred in correspondence of the sharp corner of the turret of the vehicle, as well. Higher intensity values were found at 70 cm (**Figure 3B**), where the presence of the metallic door deforms the E-field distribution causing peaks above 100 V/m close to the door area. Inside the area directly above the manhole, the non-uniform distribution of the E-field was characterized by an intensity that ranged from 127 to 20 V/m, with an average value of 37.45 V/m. To conclude, in the exposure scenario herein depicted, local E-field intensity values may be above the considered RL (9), particularly at 70 cm. Therefore, further dosimetric analysis is required to ensure compliance with the SAR BRs.

Exposure Scenario *b*: Vehicle With Open Manhole in the Presence of the Operator

Figure 4 shows the E-field distribution that was induced inside the Duke model over two planes, YZ (**Figure 4A**) e XZ (**Figure 4B**), at the center of the body. The right side of the body is majorly interested by the exposure, as it is located in the proximity of the monopole. A hotspot of 12.3 V/m is induced in the valley between neck and shoulders (**Figure 4A**) and in the cervical area (**Figure 4B**), whereas values below 3 V/m are induced in the rest of the body. To evaluate the impact of such values, the corresponding induced SAR values were evaluated as well. The local SAR distributions over the same two planes are reported in **Figure 5**. Location of the hotspot is maintained with a peak SAR value of 14.7 mW/kg. Given the previously shown high E-field intensity values radiated in free space at 70 cm from the manhole, the values that were induced inside the Duke model at the same location, which corresponded to the center of the head, were evaluated (**Figure 6A**). Results showed that values below 2.8

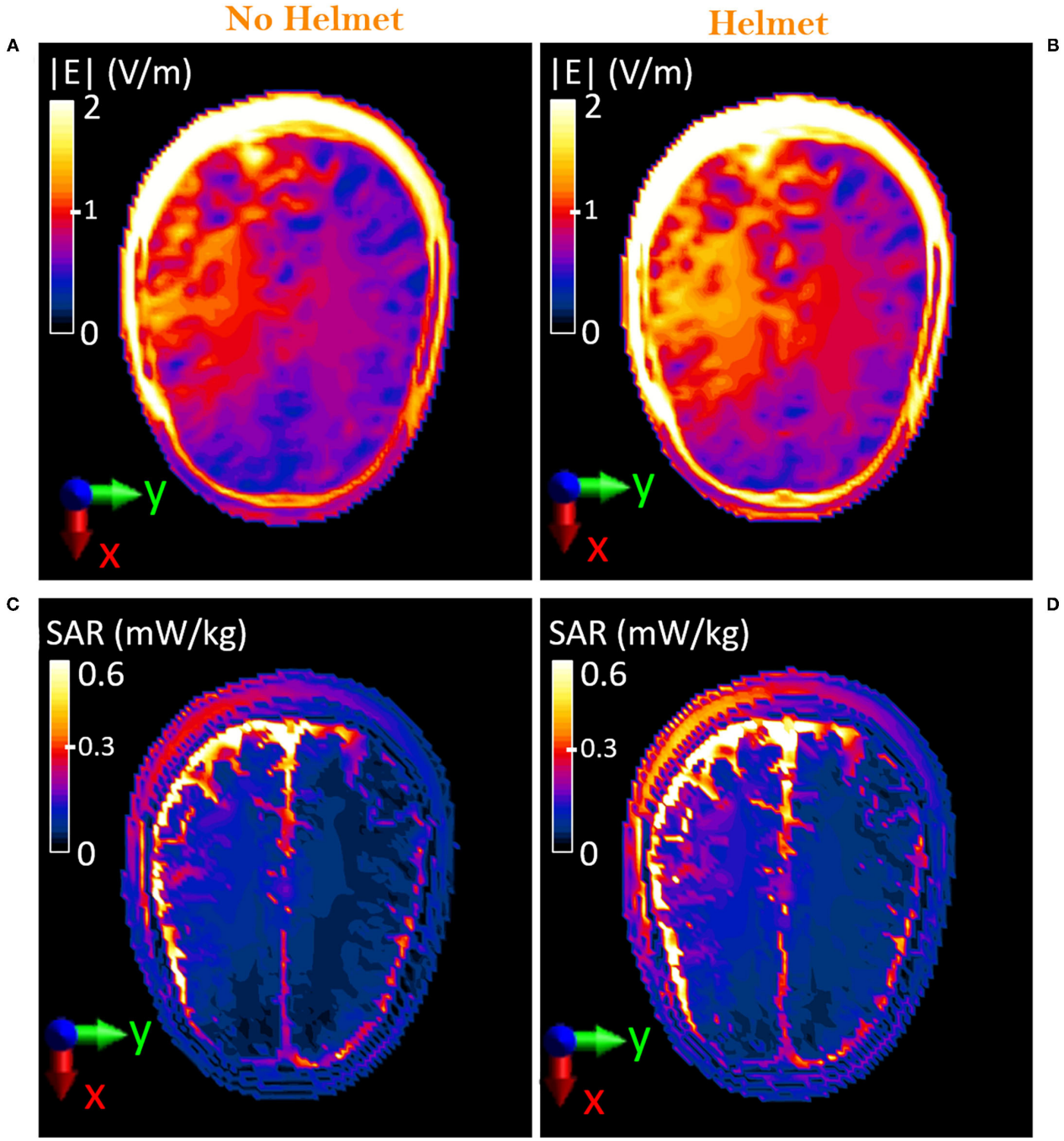

FIGURE 6 | Comparison on the axial plane, XY, between unequipped and equipped military operator, (XY plane): **(A,B)** Distribution of the E-field induced inside the head of the virtual body model Duke at 70 cm from the manhole. **(C,D)** Distribution of the local SAR induced inside the head of the virtual body model Duke at 70 cm from the manhole.

V/m were induced inside the cerebral tissues and lead to a local SAR below 0.6 mW/kg (**Figure 6C**). To ensure compliance with the guidelines, the whole-body averaged SAR (SAR_{wb}) and the peak SAR averaged over 10 g of tissue (SAR_{10Avg}) in the head were computed and resulted to be 0.2 and 3.2 mW/kg, respectively. These values were well below the limits reported in the guidelines, as shown in **Table 2**. A different version of scenario b, with the operator's body placed towards the edge of the manhole and the arm bent over the turret (i.e., scenario b1), was investigated as well, and results can be found in the **Supplementary Material**.

TABLE 2 | Comparison between the estimated SAR values in the three exposure scenarios that include the operator model and guidelines limits.

	Estimated value			Guidelines limit (6, 7, 9)
	Scenario b: vehicle with operator	*Scenario c:* vehicle with operator and helmet	*Scenario d:* vehicle with operator, helmet and cabled headset	
SAR_{wb}	0.20×10^{-3} W/kg	0.21×10^{-3} W/kg	0.21×10^{-3} W/kg	0.4 W/kg
SAR_{10Avg}	3.2×10^{-3} W/kg	3.7×10^{-3} W/kg	13.97×10^{-3} W/kg	10 W/kg

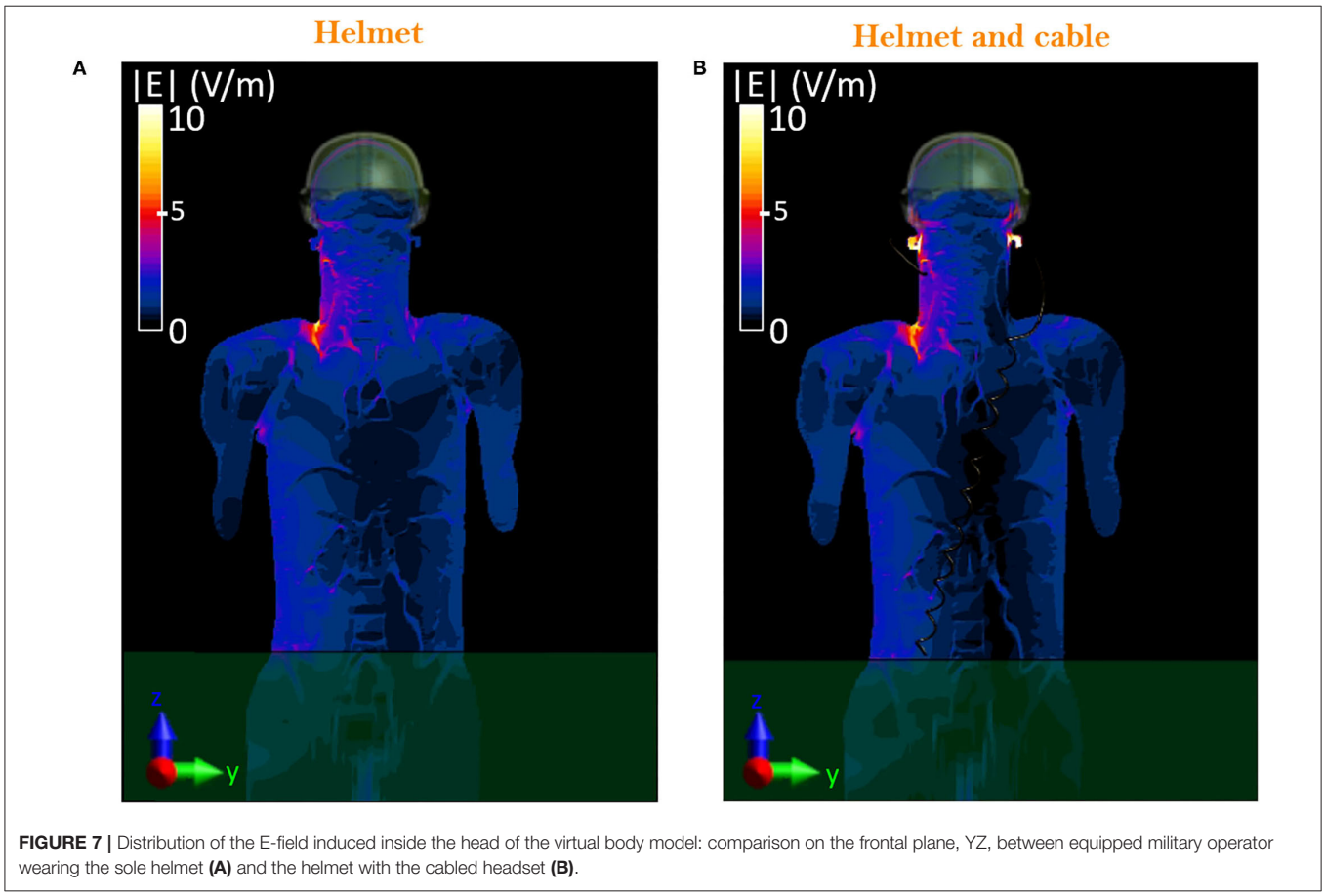

FIGURE 7 | Distribution of the E-field induced inside the head of the virtual body model: comparison on the frontal plane, YZ, between equipped military operator wearing the sole helmet **(A)** and the helmet with the cabled headset **(B)**.

Exposure Scenario *c*: Operator Equipped With the Protective Helmet

The presence of the protective helmet slightly influences the E-field that was induced inside the body of the Duke model. Particularly, changes would be mainly expected at the level of the head, where the helmet is located. **Figures 6A,B** show a comparison of the E-field distribution over the axial (XY) plane at the forehead (70 cm above the manhole) in the case of Duke without and with the protective helmet, respectively. The helmet causes a 10% increment in the induced E-field levels. Nevertheless, values were kept below 3.1 V/m in the cutaneous tissues and below 1.9 V/m in the cerebral tissues, such as the gray and the white matter. As for exposure scenario b, the induced SAR levels were investigated. Local SAR on the forehead plane is shown in **Figures 6C,D**. When the helmet is introduced, an increment of the SAR levels with respect to the levels obtained in the absence of the helmet is visible. The maximum local SAR, estimated as the 99.9th percentile of the SAR distribution inside the head (20), increases from 2.9 mW/kg (in **Figure 6C**) to 4.5 mW/kg (in **Figure 6D**). To evaluate compliance with the guidelines, the computed peak SAR averaged on 10 g of head tissues is 3.7 mW/kg, that is, 15% higher than the value that would be induced without the helmet but still well below the 10 W/kg limit. Conversely, the SAR_{wb} remains unchanged (**Table 2**).

Exposure Scenario *d*: Operator Equipped With the Protective Helmet and Cabled Headset

Figure 7 shows the induced E-field inside the whole-body Duke model in the two cases of the operator wearing the sole protective

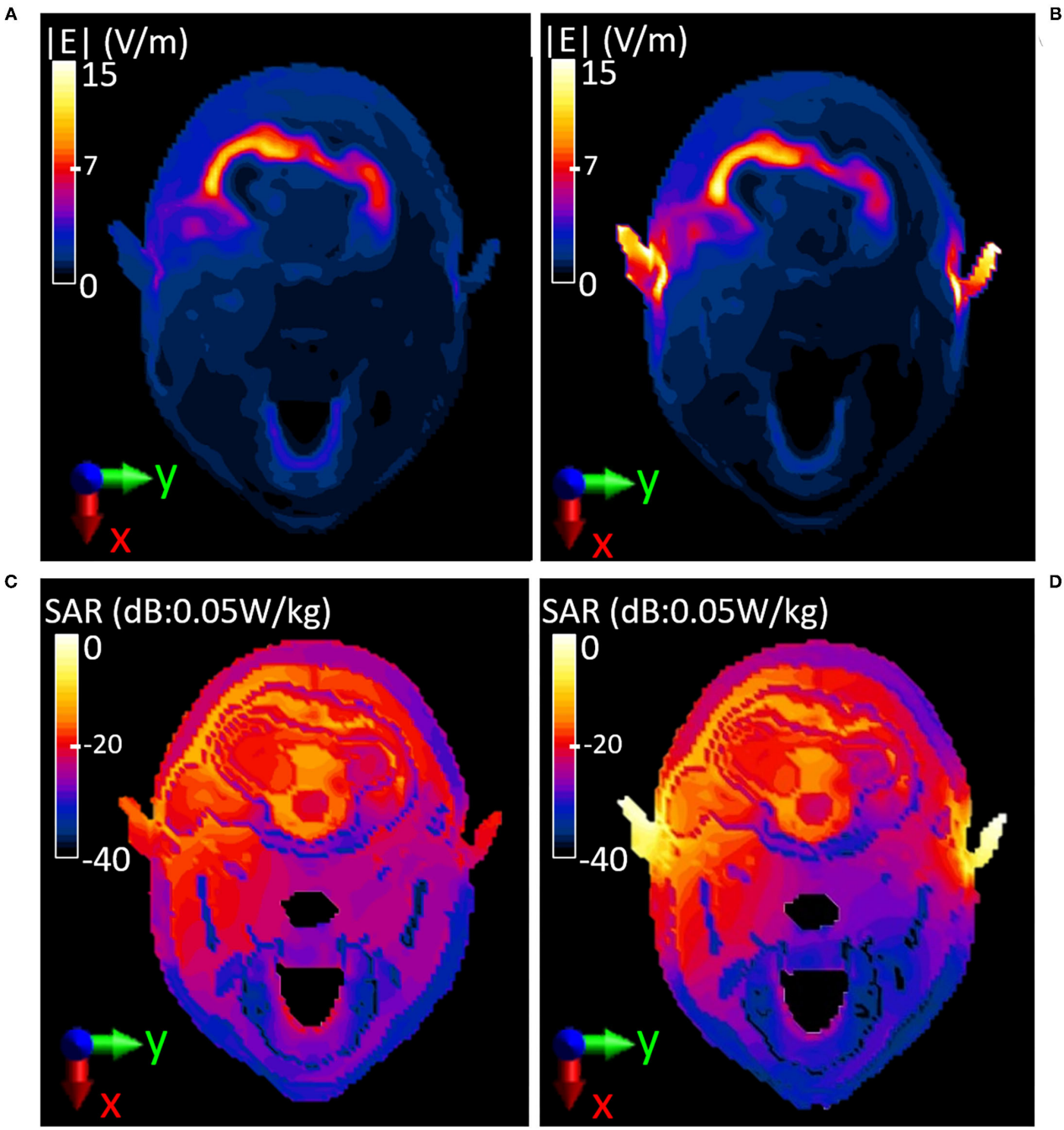

FIGURE 8 | Comparison on the axial plane, XY, between equipped military operator wearing the sole helmet and the helmet with the cabled headset. Distribution of the E-field induced inside the head of the virtual body model Duke at 65 cm from the manhole **(A,B)**. Distribution of the local SAR induced inside the head of the virtual body model Duke at 65 cm from the manhole **(C,D)**. Color bar for SAR is reported in logarithmic scale, considering 0.05 W/kg as the reference value (i.e., 0 dB = 0.05 W/kg).

helmet (**Figure 7A**) and the protective helmet with the cabled headset (**Figure 7B**). When in the presence of the cable, the induced E-field is below 3 V/m everywhere except for the areas of the ears where the presence of the cable causes a peak of 49.8 V/m. Since the cable runs from left to right behind the neck, the effect of the connected headset can be seen at the level of the nape as well (i.e., 65 cm above the manhole), as shown comparing **Figure 8A** with **Figure 8B**, where the peak intensity, again estimated as the 99.9th percentile, increases from 12.9 to 15.1 V/m. Nevertheless, despite the

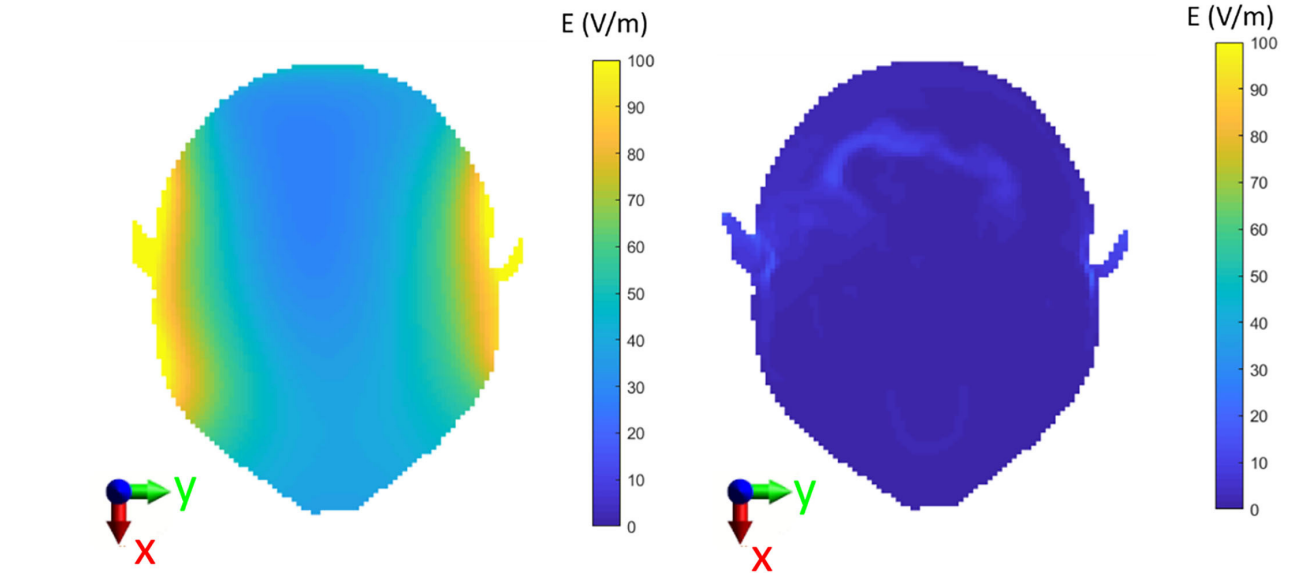

FIGURE 9 | Comparison on the axial plane, XY, between **(A)** the E-field radiated in the space surrounded by the helmet in absence of human head and **(B)** the E-field induced inside the head with the operator wearing the helmet at 65 cm from the manhole.

cable is close to the area of the chest and abdomen, the E-field induced in those areas is not influenced by its presence. In **Figures 8C,D**, the local induced SAR is shown for the two cases. The main difference is again on the ears, where the local SAR increases from 1.5 mW/kg (**Figure 8C**) to 40 mW/kg (**Figure 8D**), whereas the SAR_{wb} remains unchanged (**Table 2**). To investigate whether the hotspot on the ears would cause a non-compliance with the BRs, the peak head SAR_{10Avg} was computed and resulted equal to 13.97 mW/kg, well below the recommended 10 W/kg (**Table 2**). To correlate these results with the corresponding RLs that could be found in air, *exposure scenario d* was investigated in the absence of the Duke model. Results were compared with those obtained in the presence of the head inside the the helmet and were analyzed over the plane at 65 cm from the manhole (**Figure 9**). When considering the connected cable without the presence of the head, the mean value inside the helmet space is 46.7 V/m, whereas the peak value reaches 132 V/m. Higher intensity values are focused in correspondence of the right and left headset (**Figure 9A**), which means that the cable acts as a receiving antenna, which concentrates the E-field lines along its length. When in the presence of the head tissues (**Figure 9B**), the induced E-field was up to 49.8 V/m, with a mean value of 2 V/m.

DISCUSSION AND CONCLUSIONS

In this study, a realistic military scenario was simulated considering a highly detailed virtual human body model standing partially outside a vehicle. The vehicle was modeled as a low complexity replica of a real one. The RF antenna was modeled as a monopole placed on the roof of the vehicle. Numerical simulations were performed at 16 MHz, which is the central frequency of the working range 2–30 MHz, and considering an input power of 25 W. Four different conditions were investigated. The E-field levels in the free space without the human body were evaluated first (*scenario a*). Following, the exposure scenario in the presence of the operator was simulated (*scenario b*), and the level of detail in the exposure scenario was progressively increased by adding the protective helmet (*scenario c*) and a pair of cabled headsets (*scenario d*). In *scenario a*, it was estimated that areas above the manhole were mostly compliant with the limits at 16 MHz (i.e., 61 V/m rms or 86.3 V/m magnitude) (9), except for a small area where the local E-field intensity reached 127 V/m. To assess whether such intensity values would induce SAR and E-field values inside the body that exceed the BRs, the presence of the military operator, partially standing outside the vehicle, through a manhole, in close proximity to the radiating monopole, was considered. As a first step, the unequipped operator was modeled (*scenario b)* similarly to what was done in other dosimetric studies (3, 21). The induced E-field inside the body was estimated to be up to 12 V/m, leading to SAR_{wb} and a peak SAR_{10Avg} in the order of 10^{-3} mW/kg, well below the limits of 0.4 and 10 W/kg, respectively (6, 7, 9), thus finding that noncompliant E-field induced compliant SAR_{wb} and peak SAR_{10Avg}, as also found by Alcaras and colleagues in 2017, under similar exposure condition (21). To take into account a more realistic scenario, the equipment usually worn by the personnel was modeled. Specifically, a protective helmet with a cabled headset was added to the FDTD simulations, to investigate whether these elements could be detrimental due to a possible direct coupling with the antenna. Such modeling details were

progressively added, by running two sets of simulations, one with the sole helmet and one with the helmet plus the cabled headset. To the best of our knowledge, this aspect has never been considered in the previous dosimetric studies.

When the man is modeled with the protective helmet alone (*scenario c*), the induced E-field inside the head is 10% higher than the one obtained in case b (i.e., man without helmet) but always below 3.1 V/m and inducing a peak head SAR_{10Avg} of 3.7 mW/kg. When the cabled headset is included in the simulation (*scenario d*), a local increase of the E-field and induced SAR at the level of ears is observed, although with values still well below the guideline's limits. The presence of the helmet and the cabled headset was investigated in the absence of the operator model, as well, for a better understanding of the hotspot occurring at the level of the ears. The local increase of the E-field was found in the area surrounding the right and left elements of the headset. This allowed to conclude that such local increase of the E-field is caused by the induction of currents inside the cable, which, in turns, act focusing the EM field, rather than being an effect of the ears' shape and dielectric properties. Nevertheless, SAR and E-field values that were induced inside the body in such condition remained well below the BR's limits, with a peak head SAR_{10Avg} of 14 mW/kg. With these findings, giving the linear regime of the problem studied, even when considering the worst-case exposure scenario (scenario d), the respect of the BRs is still guaranteed even if the antenna is fed in more extreme conditions, such as 125 W (2). For instance, under these circumstances, the peak SAR_{10Avg} would be 69.85 mW/kg, still below the ICNIRP limit of 10 W/kg. In conclusion, a computational model that represents a good compromise between accuracy and efficiency was herein proposed to perform dosimetric evaluation for safety assessment of the exposure of military crew in high-power near-field conditions in the HF range. A realistic exposure scenario was simulated, in which the radiated electric field reached values that could be above the guidelines RLs and that coupled with the instrumentation, such as wearable communication systems. Nevertheless, it was shown that the E-field and SAR that were induced inside the operator's body located in the proximity of the radiating antenna would still respect the guideline limits for occupational exposure at the selected frequency.

DATA AVAILABILITY STATEMENT

The original contributions presented in the study are included in the article/**Supplementary Material**, further inquiries can be directed to the corresponding author/s.

AUTHOR CONTRIBUTIONS

MB and TC contributed in project administration. MB, MCav, FA, and ML supervised the work. MCo, MB, MCav, FA, and ML performed conceptualization, methodology, investigation, and wrote the original draft. MCo carried out formal analysis. MM, RP, TC, DF, AD, MCap, GP, and EM provided the resources, involved in reviewing, and editing. All authors contributed to the article and approved the submitted version.

ACKNOWLEDGMENTS

Authors want to thank Simona D'Agostino, for the support in the collection of all the meaningful guidelines of interest for military operator's health protection to EM fields exposure, and ZMT Zurich MedTech ADG, for providing licenses of the simulation software Sim4Life.

SUPPLEMENTARY MATERIAL

The Supplementary Material for this article can be found online at: https://www.frontiersin.org/articles/10.3389/fpubh.2021.794564/full#supplementary-material

REFERENCES

1. Garrido D, Ignatenko M, Filipovic DS. Computational study of electromagnetic exposure of military personnel in a humvee. In: *2014 United States National Committee of URSI National Radio Science Meeting*. Boulder, CO: USNC-URSI NRSM. (2014). doi: 10.1109/USNC-URSI-NRSM.2014.6928134
2. Guellab A, Wu Q. Modeling and EMC simulation of vehicular radio transmission antenna. In: *Proceedings of the 2016 IEEE International Conference on Electronic Information and Communication Technology (ICEICT) 2016*. Harbin: IEEE (2017). p. 436–8. doi: 10.1109/ICEICT.2016.7879734
3. Guellab A, Wu Q. Modeling human body using four-pole debye model in piecewise linear recursive convolution FDTD method for the SAR calculation in the case of vehicular antenna. *Int J Antennas Propag.* (2018) 2018:1–9. doi: 10.1155/2018/2969237
4. Sobiech J, Kieliszek J, Puta R, Bartczak D, Stankiewicz W. Occupational exposure to electromagnetic fields in the polish armed forces. *Int J Occup Med Environ Health.* (2017) 30:565–77. doi: 10.13075/ijomeh.1896.00696
5. Bit-Babik G, Faraone A. Standardization of SAR simulation techniques for RF exposure compliance in and around vehicles. In: *2013 7th European Conference Antennas Propagation, EuCAP 2013*. Gothenburg (2013). p. 1984–6.
6. International Commission on Non-Ionizing Radiation Protection (ICNIRP). Guidelines for limiting exposure to electromagnetic fields (100 kHz to 300 GHz). *Health Phys.* (2020) 118:483–524. doi: 10.1097/HP.0000000000001210
7. PC95.1-2345 - Standard for Military Workplaces – Force Health Protection Regarding Personnel Exposure to Electric, Magnetic, and Electromagnetic Fields, 0 Hz to 300 GHz. In *IEEE Std C95.1- 2345*. New York, NY: IEEE. (2014) p. 1–69.
8. International Commission on Non-Ionizing Radiation Protection. Guidelines for limiting exposure to time-varying electric and magnetic fields (1 Hz to 100 kHz). *Health Phys.* (2010) 99:818–36. doi: 10.1097/HP.0b013e3181f06c86
9. European Union. *Directive No. 2013/35/EU, of 26 June 2013, On The Minimum Health And Safety Requirements Regarding The Exposure Of Workers To The Risks Arising From Physical Agents (Electromagnetic Fields). Off J Eur Union.* (2013) L179:1–21. Available online at: http://eur-lex.europa.eu/legal-content/EN/TXT/PDF/?uri=CELEX:32013L0035&from=PT
10. Modenese A, Gobba F. Occupational exposure to electromagnetic fields and health surveillance according to the european directive 2013/35/eu. *Int J Environ Res Public Health.* (2021) 18:1–12. doi: 10.3390/ijerph18041730
11. *Evaluation and control of personnel exposure to radio frequency fields - 3 kHz to 300 GHz. STANAG 2345*. Edition 34 (2003).

12. Karpowicz J, Hietanen M, Gryz K. EU directive, ICNIRP guidelines and polish legislation on electromagnetic fields. *Int J Occup Saf Ergon.* (2006) 12:125–36. doi: 10.1080/10803548.2006.11076675
13. Ruddle AR. Computed SAR levels in vehicle occupants due to on-board transmissions at 900 MHz. In: *Loughborough Antennas Propagation Conference LAPC 2009 - Conf Proc.* Loughborough (2009). p. 137–40.
14. Rütschlin M, Tallini D. Simulation for antenna design and placement in vehicles. In: *IET Semin Dig.* Birmingham (2017). doi: 10.1049/ic.2017.0021
15. Garrido Lopez D, Ignatenko M, Filipovic DS. RF exposure inside and outside vehicles. In: *IEEE Antennas Propagation Society International Symposium.* Tennessee, TN: IEEE (2014). p. 607–8. doi: 10.1109/APS.2014.6904634
16. King RW. *Tables Of Antenna Characteristics.* 1st ed. Springer (1971). doi: 10.1007/978-1-4684-6081-0_1
17. Gosselin MC, Neufeld E, Moser H, Huber E, Farcito S, Gerber L, et al. Development of a new generation of high-resolution anatomical models for medical device evaluation: the virtual population 3.0. *Phys Med Biol.* (2014) 59:5287–303. doi: 10.1088/0031-9155/59/18/5287
18. Hasgall PA, Di Gennaro F, Baumgartner C, Neufeld E, Lloyd B, Gosselin MC, et al. *IT'IS Database for thermal and electromagnetic parameters of biological tissues, Version 4.0.* (2018). doi: 10.13099/VIP21000-04-0
19. Yee KS, Chen JS. The finite-difference time-domain (FDTD) and the finite-volume time-domain (FVTD) methods in solving Maxwell's equations. *IEEE Trans Antennas Propag.* (1997) 45:354–63. doi: 10.1109/8.558651
20. Soldati M, Laakso I. Computational errors of the induced electric field in voxelized and tetrahedral anatomical head models exposed to spatially uniform and localized magnetic fields. *Phys Med Biol.* (2020) 65:015001. doi: 10.1088/1361-6560/ab5dfb
21. Alcaras A, Frere J. Thermal risks due to land vehicle radioelectric exposure: results of thales research and study for military purpose. In: *2017 International Symposium on Electromagnetic Compatibility.* Angers: EMC Eur 2017. (2017). doi: 10.1109/EMCEurope.2017.8094719

Conflict of Interest: MM, RP, and TC are employees at Larimart S.p.A. DF, AD, MCap, GP, and EM are employees at CEPOLISPE. Larimart and Cepolispe provided information about vehicle and antenna dimensions. This work was carried out in the frame of the HEPROSYS project funded by Lariamrt S.p.A.

The remaining authors declare that the research was conducted in the absence of any commercial or financial relationships that could be construed as a potential conflict of interest.

frontiers in Public Health

BRIEF RESEARCH REPORT
published: 14 February 2022
doi: 10.3389/fpubh.2022.795414

Monte Carlo Simulation of Clothed Skin Exposure to Electromagnetic Field With Oblique Incidence Angles at 60 GHz

Kun Li[1]* *and Kensuke Sasaki*[2]

[1] Faculty of Engineering and Design, Kagawa University, Takamatsu, Japan, [2] Radio Research Institute, National Institute of Information and Communications Technology, Koganei, Japan

This study presents an investigation of clothed human skin exposure to obliquely incident electromagnetic waves at 60 GHz. We clarified the combined impacts of the cloth material, incidence angle, and polarization on the assessment of transmittance and absorbed power density (*APD*) at the skin surface. A Monte Carlo simulation was conducted considering the thickness variation of the cloth material and skin tissue. For the case of transverse magnetic^{TM} wave exposure, the transmittance increases with increasing incident angle up to the maximum transmittance angle in the range from 60 to 80°, which is known as the Brewster effects, regardless of textile materials and air gap between cloth and skin. The air gap results in a periodic fluctuation of the *APD*, where the variation is almost within 1 dB when the incident power density is constant and the incident angle is smaller than 40°. Our results also show that as the air gap increases to 2.5 mm, i.e., half-wavelength at 60 GHz in the air, the *APD* within the skin surface covered by typical cloth materials increases up to 40% compared with that of bare skin. Although the use of several cloth materials may increase the transmittance and *APD* in oblique incidence scenarios, all the results of the *APD* do not exceed the basic restriction for local exposure, demonstrating that the current guidelines for human exposure to electromagnetic fields are appropriate for preventing the excessive exposure at 60 GHz considering the impacts of oblique incidence angles and cloth materials.

Keywords: electromagnetic fields, millimeter wave, human skin, cloth effect, absorbed power density, exposure guideline

OPEN ACCESS

Edited by:
Theodoros Samaras, Aristotle University of Thessaloniki, Greece

Reviewed by:
Robert G. Olsen, Washington State University, United States
Esra Neufeld, ETH Zurich, Switzerland

***Correspondence:**
Kun Li
li.kun@kagawa-u.ac.jp

Specialty section:
This article was submitted to Radiation and Health, a section of the journal Frontiers in Public Health

Received: *15 October 2021*
Accepted: *07 January 2022*
Published: *14 February 2022*

Citation:
Li K and Sasaki K (2022) Monte Carlo Simulation of Clothed Skin Exposure to Electromagnetic Field With Oblique Incidence Angles at 60 GHz. Front. Public Health 10:795414. doi: 10.3389/fpubh.2022.795414

INTRODUCTION

In the upcoming beyond 5G/6G wireless communication system, millimeter-wave (MMW) devices have received considerable attention owing to the potentially high data rate transmission and a large amount of available bandwidth (1, 2). The increasing demand for MMW radio frequency (RF) transmitters operated in the human vicinity, such as mobile phones, tablet terminals, and Wi-Fi systems, has raised public concerns about human exposure to electromagnetic fields (EMFs) (3–7). The International Commission on Non-Ionizing Radiation Protection (ICNIRP) guideline (8) and the Institute of Electrical and Electronics Engineers (IEEE) International Commission on Electromagnetic Safety (ICES) (IEEE Standard C95.1) (9) have recommended the absorbed power density (*APD*) or epithelial power density, respectively, as a new metric for the basic restriction (BR) or dosimetric reference limit (DRL) to protect against the adverse health effects associated with superficial heating for local

exposures at frequencies from 6 to 300 GHz. The absorbed or epithelial power densities crossing a unit area in the direction normal to the body interface represents the total power deposited in the biological tissues, which was derived from an operational health effect threshold in terms of the temperature rise divided with the reduction factors employed in the RF exposure guidelines and standards (8, 9). According to the BR/DRL, exposure limits of incident power density (*IPD*) used as reference level (RL) (8) or exposure reference levels (ERLs) (9) were derived. For local exposures at a frequency from 6 to 300 GHz, the *IPD* should not exceed $275{f_G}^{-0.177}$ and $55{f_G}^{-0.177}$ (W/m^2) (f_G: frequency in GHz) for occupational exposure/restricted environments and general public exposure/unrestricted environments, respectively (8, 9).

Recent dosimetric studies to electromagnetic field exposure at MMW bands mainly aim to clarify the relationship between different definitions of power densities and temperature rise at skin surface including both plane wave incidence and practical RF sources (10–27). The first concern in investigating these subjects is the consideration of oblique radio wave incidence in general human exposure scenarios, especially referred to as beam steering technology, employed in 5G wireless systems. The incident angle dependence of transmittance, *APD*, and skin temperature elevation has been studied for plane-wave exposures (12–14) where the difference for transverse electric (TE) and transverse magnetic (TM) plane waves injection such as Brewster' angle effect was clarified. He et al. (24) and Nakae et al. (25) reported the research results of exposures to oblique incidence electromagnetic fields from phased array antennas at 28 GHz, i.e., the FR2 (MMW) frequency band assigned in Japan and some other countries. Considering the extension to other MMW bands, a new working group 5 under Subcommittee 6 of IEEE ICES TC95 was established to clarify these aspects, where the effect of the incidence angle on the spatial-average power densities and resultant temperature elevation using both computational and thermographic measurement approaches were reported (26, 27). It was found that the normal incidence scenario is generally the worst-case for surface temperature rise when bare skin is directly illuminated by an electromagnetic field.

Another important topic is the consideration of cloth effects for more realistic human exposure conditions. During the use of MMW wireless device approaching a human body wearing clothes made of different textile materials, the difference compared with bare skin should be clarified for accurate dosimetry. Several studies have investigated the cloth impacts on the variation of electromagnetic power deposition at MMW (3, 28–32). Through the analysis of the power penetration, it is well-known that the cloth material acts as an impedance transformer and may increase the power absorption in the clothed skin. In addition, the impact of a textile layer in the contact or proximity of skin on the power transmission coefficient, *APD* and temperature rise at 26 and 60 GHz has been reported in the literature (31). The literature (31) firstly gives a detailed evaluation of power absorption and thermal dosimetry under plane wave normal incidence conditions considering the influence of the textile material and air gap spacing. They clarified that the presence of an air gap between the cloth and the skin modifies the electromagnetic power deposition, which may result in a temperature rise variation from −11.1 to 20.9% compared to the bare skin at 60 GHz. However, the evaluation of power deposition at oblique incidence has not been investigated sufficiently. Considering a general exposure environment, it is essential to assess the clothed skin dosimetry for cases of not only normal incidence but also oblique incidence. The transmittance and *APD* may be significantly different from those of bare skin, which will be determined as the combined outcome of cloth materials, incident angles, polarization components, and air gap spacing.

In this study, we aim to analyze the electromagnetic field exposure of a clothed human skin tissue with an obliquely incident plane wave at 60 GHz. Following previous work, dosimetric studies were conducted by a theoretical analysis using the biological-tissue parameters employed by (15, 33). Variations of the transmittance and the *APD* were evaluated considering the dispersion of cloth and skin tissue thickness by Monte Carlo simulation. The effects of the air gap between the cloth and the skin were examined considering various textile materials, incidence angles, and polarization.

METHOD AND MODEL

Figure 1 illustrates a two-dimensional analytical model composed of cloth material, air gap space, and a conventional multi-layer human skin tissue. The skin model consists of the epidermis, dermis, subcutaneous fat, and muscle used to represent the skin tissue in the abdomen (15). Six textile materials used for typical cloth manufacturing were employed, which are cotton (M1), wool (M2), linen (M3), leatherette (M4), polyester fiber (M5), and latex mattress (M6), respectively. An oblique incident plane wave injected from the air to the surface of the cloth material layer with an angle of θ_0 is assumed. Two polarization components of the incident waves are considered individually, defined as TE and TM waves, whose electric-field vectors are perpendicular and parallel to the incident plane (*yz*-plane), respectively. The incident power density of 26.6 W/m^2, i.e., the reference level for local exposure of the general public at 60 GHz, as indicated in ICNIRP 2020 (8) and IEEE C95.1 2019 (9). The incident power density is defined at the plane whose normal is parallel to the wave-number vector. The *APD* crossing a unit area at $z = z_3$ in the air gap to skin boundary in the direction normal to the interface (14, 17, 18), is given by,

$$\boldsymbol{APD} = \frac{1}{2}\mathcal{R}\left\{\left(\boldsymbol{E}(z) \times \boldsymbol{H}^*(z)\right) \bullet \boldsymbol{n}\right\}\Big|_{z=z_3} \quad (1)$$

where $\boldsymbol{E}$ and $\boldsymbol{H}^*$ denote the electric field phasor and the complex conjugate of the magnetic field phasor, respectively. **Table 1** listed the parameters of cloth materials and skin tissues in the Monte Carlo simulation. For consistency with the results obtained by (14), the dielectric properties of multi-layer skin tissue reported by (15, 33) were used. The mean values and standard deviations of various tissue thicknesses of the abdomen [see Table 2 in (15)] were used, which was measured by (34, 35)

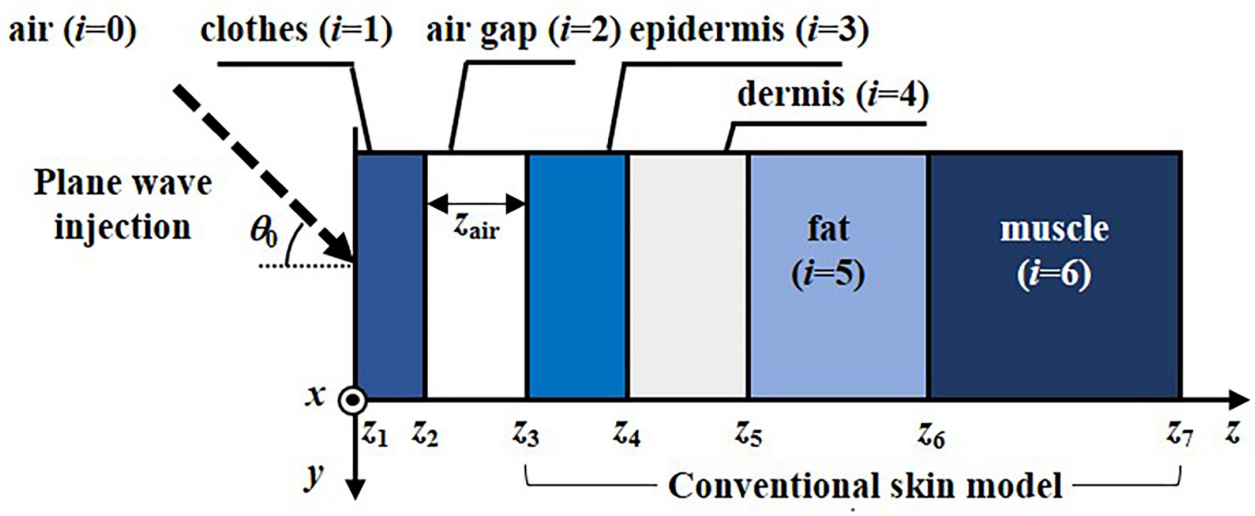

FIGURE 1 | Two-dimensional clothed skin model composed of various cloth material ($i = 1$), air gap layer ($i = 2$), epidermis ($i = 3$), dermis ($i = 4$), fat ($i = 5$), and muscle ($i = 6$) exposed to an obliquely incident plane wave.

TABLE 1 | Dielectric constants and thickness of cloth materials and skin tissues (mean ± standard deviation) used in Monte Carlo simulation.

Model	Layer	Thickness (mm) (mean ± std)	Relative complex permittivity ($\varepsilon_r = \varepsilon_r' - j\varepsilon_r''$)
Cloth	Cotton (M1)	0.2 ± 0.02	2.0 – *j*0.04
	Wool (M2)	2.0 ± 0.02	1.22 – *j*0.036
	Linen (M3)	0.98 ± 0.1	1.25 – *j*0.102
	Leatherette (M4)	0.91 ± 0.007	2.16 – *j*0.021
	Polyester Fiber (M5)	0.79 ± 0.194	1.22 – *j*0.003
	Latex Mattress (M6)	11.34 ± 0.241	1.11 – *j*0.009
Skin	Epidermis	0.0794 ± 0.0339	8.5 – *j*9.9
	Dermis	1.25 ± 0.26	10.4 – *j*11.9
	Fat	14.3 ± 7.5	5.7 – *j*4.7
	Muscle	14.4 ± 3.5	10.7 – *j*13.9

using a sufficient number of samples considering the individual differences in gender and age. In addition, we employed the relative complex permittivities and thicknesses of six different types of cloth materials based on the published data in (31, 36). The Monte Carlo simulation was conducted based on the statistical data on cloth material and skin tissue thickness using normally distributed random numbers generated by Matlab R2021a (14). The number of iterations was set to 10^4 for each oblique incidence angle and air gap spacing.

RESULTS

Transmittance and Absorbed Power Density at Skin Surface

Figures 2A,B show the transmittance as functions of incident wave angle (θ_0) and air gap spacing (z_{air}) when the skin is covered by cloth materials. **Figure 2A** shows the results for TE waves, whereas **Figure 2B** shows those for the TM waves. The mean value of transmittance at the skin surface is defined as,

$$T = 1 - |\gamma_2(\theta_2)|^2 \tag{2}$$

where γ_2 denotes the reflection coefficient from the skin surface to the air gap. θ_2 indicates the incident wave angle from the air gap layer to the skin surface, which equals θ_0 in the air on the basis of Snell's law.

In **Figure 2A**, the transmittance of the TE waves in each cloth material decrease with increasing incident wave angle. For the incident angle θ_0 smaller than 40°, most of the mean transmittance are shown below 0.5. When the cloth material of M4 is used, a relatively obvious fluctuation with the variation of air gap spacing is observed in this range of incident angles. Moreover, when the air gap is larger than 2.5 mm and the incident angle θ_0 is higher than 70°, a significant increase of transmittance over 0.9 is observed. This is different from the general characteristics of the TE waves incidence on bare skin. The reason may be attributed to the function of the impedance transformer of the cloth material (M4) affected by its dielectric property and thickness, which may result in a complicated phase reversal phenomenon with the increase in the air gap spacing.

On the other hand, the TM waves show increased transmittance with increasing θ_0 up to the maximum transmittance angle, which is known as the Brewster effect. In **Figure 2B**, for each cloth material, the maximum transmittance angle for the TM waves varies from about 60 to 80° regardless of the variation of air gap spacing. This fact corresponds well with that of bare skin at 60 GHz (14), indicating that the cloth material and air gap do not significantly affect the transmittance at the skin surface when the clothed skin is exposed to TM

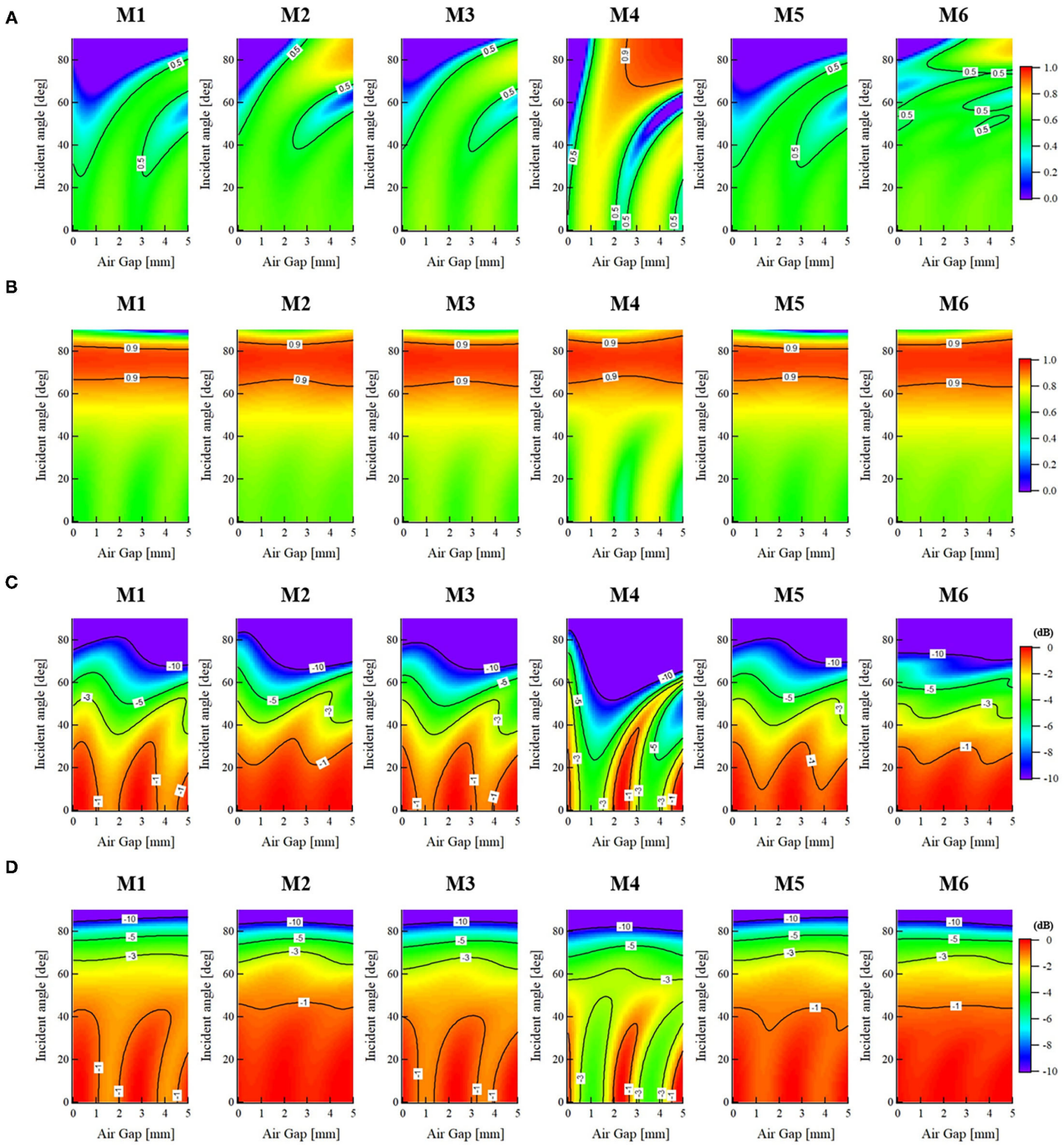

FIGURE 2 | Mean values of transmittance and absorbed power density at skin surface as functions of oblique incidence angles θ_0 and air gap spacing z_{air} when the skin model is covered by various types of cloth materials at 60 GHz, **(A)** Transmittance (TE wave), **(B)** Transmittance (TM wave), **(C)** *APD* (TE wave), and **(D)** *APD* (TM wave).

waves injection. In addition, similar to the behavior of TE waves, the dynamic variation using the cloth material of M4 at small incidence angles is relatively larger compared with other textile materials.

Figures 2C,D indicate the *APD* normalized to the maximum value as functions of incident wave angle (θ_0) and air gap spacing (z_{air}) considering the cloth effects. The contour lines in the figures show the difference from the maximum mean value of the *APD* at the skin surface. **Figure 2C** shows the results for TE waves, whereas **Figure 2D** shows those for TM waves. The mean value of *APD* within the skin surface is obtained by **Equation 1**.

In **Figure 2C**, the *APD* of the TE waves in each cloth material decrease with increasing incident wave angle. For the incident angle θ_0 smaller than 40°, an oscillatory behavior as the increase

of air gap spacing is observed. Especially when the cloth material of M4 is used, a significant fluctuation with a reduced period is shown compared with other cloth materials. This indicates that the variation of an air gap between the cloth and skin can decrease or increase the electromagnetic field power deposition in the skin tissues, as reported in (31). However, the variation normalized to the maximum mean value of *APD* is within −1 dB when $\theta_0 < 40^\circ$. With increasing the incident wave angle, the dynamic range from a peak to the valley is reduced, where the degradation of *APD* is almost below −5 and −10 dB, respectively, when θ_0 is <60 and 80°. Among all the textile materials, the relative standard deviation of the *APD* is within 6.9, 9.7, and 26.5% when the oblique incidence angle is smaller than 40, 60, and 80°, respectively.

For the TM waves, as shown in **Figure 2D**, the *APD* for all the cases of cloth materials also decreases with increasing incident wave angle, indicating that the normal incidence is also the worst-case exposure condition even for a clothed skin when an air gap spacing is determined. For the incident angle $\theta_0 < 40^\circ$, an oscillatory behavior as the increase of air gap can be observed only in the cloth materials of M1, M3, and M4. For those using M2, M5, and M6, the dynamic behavior is relatively small. Similar to the TE waves, a severe fluctuation with a reduced period is shown when the cloth material of M4 is used compared with other cloth materials. The variation normalized to the maximum mean value of *APD* is also within −1 dB when $\theta_0 < 40^\circ$. With the increase of θ_0, both the entire level and the fluctuation of the *APD* obviously reduce. Particularly, for TM wave incidence at $\theta_0 > 60^\circ$, the *APD* within the skin surface shows an almost flat profile with the increase of air gap, indicating that the increase of oblique incidence angle will reduce the variation of the *APD* due to the air gap effects. Moreover, the relative standard deviation of the *APD* is within 5.9, 5.1, and 7.6% when the incidence angle is smaller than 40, 60, and 80°, respectively. Thus, it was found that the contribution of the variation in cloth and skin thickness to the *APD* is not significant.

Comparison of Transmittance and Absorbed Power Density With Bare Skin

Figure 3 shows the comparison results of transmittance and *APD* for the cases between the clothed and bare skin. **Figures 3A,B** indicate the ratio of mean transmittance with cloth ($T_{\text{with cloth}}$) to that of bare skin without cloth ($T_{\text{bare skin}}$) when the air gap spacing (z_{air}) is set to 0.5 and 2.5 mm, respectively. **Figures 3C,D** indicate the ratio of mean *APD* with cloth ($APD_{\text{with cloth}}$) to that of bare skin ($APD_{\text{bare skin}}$) when the z_{air} is set to 0.5 and 2.5 mm, respectively. The error bars denote the standard deviations of the *APD* by the Monte Carlo simulation, which also implies the variation of *APD* due to the change of the thickness of cloth and skin tissue.

In **Figure 3A**, when $z_{\text{air}} = 0.5$ mm, which equals 0.1λ at 60 GHz (λ: free space wavelength), the results of $T_{\text{with cloth}}$ and $T_{\text{bare skin}}$ are almost comparable with each other. The maximum ratio of $T_{\text{with cloth}}$ to $T_{\text{bare skin}}$ of 1.3 occurs when the clothed skin with textile material of M6 is exposed by a TE wave with an incidence angle of 60°. For cases of other materials, the corresponding ratio, i.e., TE wave injection at $\theta_0 = 60^\circ$, reduces to <1.0. When z_{air} increases to 2.5 mm, which equals 0.5λ at 60 GHz, all the results do not exceed 1.0 obviously except for the cases of TE wave injection at $\theta_0 = 60^\circ$, as shown in **Figure 3B**. In that case, the maximum ratio of $T_{\text{with cloth}}$ to $T_{\text{bare skin}}$ exceeds 2.3 when the cloth material of M4 is used. In addition, the relative standard deviations for cases of cloth materials are below 28.2 and 14.7%, respectively, when z_{air} is 0.1 and 0.5 mm.

In **Figure 3C**, when $z_{\text{air}} = 0.5$ mm, most of the results of the $APD_{\text{with cloth}}$ show equivalent levels or below those of the $APD_{\text{bare skin}}$. Different from the relationship of transmittance shown in **Figure 3A**, the maximum ratio of $APD_{\text{with cloth}}$ to $APD_{\text{bare skin}}$ of 1.3 occurs when the clothed skin with textile materials of M1 and M5 is exposed by TE waves when $\theta_0 = 60^\circ$. In contrast, when z_{air} increases to 2.5 mm, all the ratios of $APD_{\text{with cloth}}$ to $APD_{\text{bare skin}}$ significantly degrades to <0.8 when TE waves incident at $\theta_0 = 60^\circ$. Instead of this, the maximum ratio of 1.4 occurs at normal incidence when M4 material is used. In addition to the above, other results show that there is no significant difference of the *APD* between the clothed and bare skin when exposed to oblique incidence plane waves at 60 GHz. Moreover, the relative standard deviations for all the cases of cloth materials are within 9.5 and 10.9%, respectively, when z_{air} is 0.1 and 0.5λ at 60 GHz, indicating that the effects caused by the variation of cloth thickness to the *APD* is marginal.

DISCUSSION AND CONCLUSION

This study briefly investigated the EMF exposures of a clothed skin model with an obliquely incident plane wave at 60 GHz. As an extension work of the previous study (14), this work mainly aimed to clarify the combined impacts of the cloth material, incidence angle, and polarization on the assessment transmittance as well as *APD* specified as the BR in ICNIRP guideline for human exposure to EMF. Our results show that for most cloth materials, the variations of oblique incident angle and air gap between cloth and skin may result in a significant fluctuation but a relatively small level of transmittance of the TE wave except for using the cloth material of leatherette (M4). For TM wave incidence, the maximum transmittance increases with increasing incident angle up to 0.9 in the range from 60 to 80°, which is known as the Brewster effect. Although periodic changes are observed at lower incident angles, it can be considered that the transmittance of the TM wave will not be obviously affected by the cloth material and the air gap.

On the other hand, with the increase of air gap spacing between cloth and skin surface, an oscillatory behavior with a peak to valley variation of the *APD* for both the TE and TM waves were observed. This indicates that the existence of an air gap between the cloth and skin can increase or decrease the *APD* at the skin surface (31), where the dielectric properties and thickness of cloth materials under various incident angles and polarizations will affect the role of the impedance transformer. However, the variation normalized to the maximum mean value of *APD* is only within −1 dB when $\theta_0 < 40^\circ$. On the basis of the

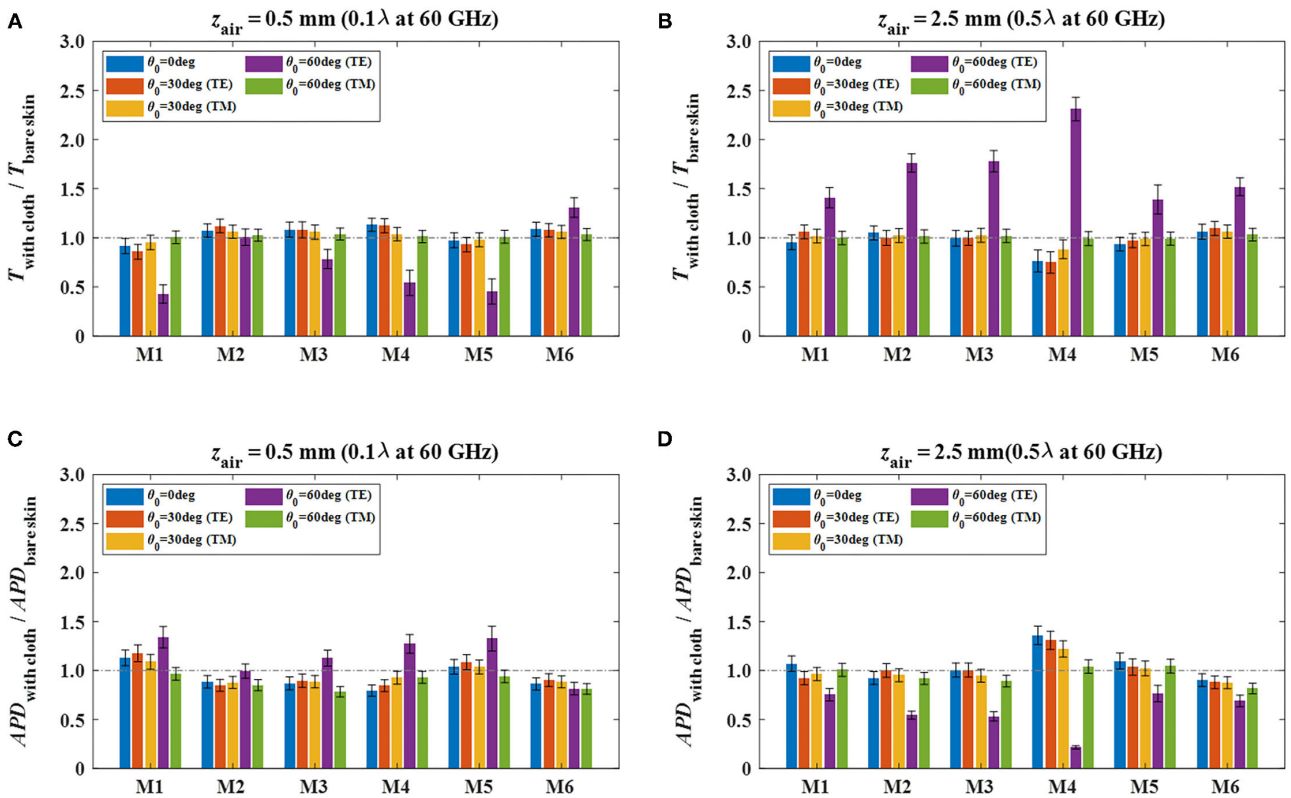

FIGURE 3 | Ratios of transmittance and absorbed power density at skin surface with various cloth materials to those of bare skin at different air gap spacing, **(A)** $T_{with\ cloth}/T_{bare\ skin}$ (z_{air} = 0.5 mm), **(B)** $T_{with\ cloth}/T_{bare\ skin}$ (z_{air} = 2.5 mm), **(C)** $APD_{with\ cloth}/APD_{bare\ skin}$ (z_{air} = 0.5 mm), and **(D)** $APD_{with\ cloth}/APD_{bare\ skin}$ (z_{air} = 2.5 mm).

reduction factor of 2 (about 3 dB) used for deriving the BR from the operational health effect threshold in local exposure above 6 GHz in the ICNIRP guidelines (8), an absolute difference <1 dB is sufficiently small considering the uncertainty of the evaluation. With increasing the incident angle of θ_0, the entire level and the fluctuation of the *APD* degrade obviously for both the TE and TM waves. The fact indicates that the normal incidence is the worst-case exposure condition for a clothed skin once the air gap between the cloth and skin is determined. In comparison to the bare skin, the use of various cloth materials under various oblique incidence exposure conditions generally increases the *APD* at the skin surface up to about 40%. In addition, the relative combined standard deviations for all the cases of cloth materials are within 9.5 and 10.9%, respectively, when z_{air} is 0.1 and 0.5λ at 60 GHz, indicating that the contribution to the *APD* caused by the cloth thickness variation is not significant. Furthermore, all the results of the *APD* do not exceed the BR for local exposure of 20 W/m^2 when the *IPD* is set to 26.6 W/m^2, i.e., the reference level for local exposure of the general public at 60 GHz, demonstrating that under the considered conditions, the current guidelines are appropriate for preventing the excessive exposure at millimeter-wave bands including the combined effects of cloth materials, air gap, oblique incidence angle, and polarization. The findings of this study are useful for understanding the appropriate use of BR in practical MMW exposure scenarios.

DATA AVAILABILITY STATEMENT

The original contributions presented in the study are included in the article/supplementary material, further inquiries can be directed to the corresponding author/s.

AUTHOR CONTRIBUTIONS

KL designed and performed all the simulations, analyzed the data, and wrote the paper. KS provided original data of skin model and dielectric properties and reviewed the manuscript. All authors have read and approved the manuscript.

FUNDING

This work was partly supported by the Ministry of Internal Affairs and Communications of Japan Grant Number JPMI10001.

REFERENCES

1. Rappaport TS, Sun S, Mayzus R, Zhao H, Azar Y, Wang K, et al. Wave mobile communications for 5G cellular: it will work! *IEEE Access.* (2013) 1:335–49. doi: 10.1109/ACCESS.2013.2260813
2. Rappaport TS, Xing Y, Kanhere O, Ju S, Madanayake A, Mandal S, et al. Wireless communications and applications above 100 GHz: opportunities and challenges for 6G and beyond. *IEEE Access.* (2019) 7:78729–57. doi: 10.1109/ACCESS.2019.2921522
3. Zhadobov M, Chahat N, Sauleau R, Quement CL, Drean Y. Millimeter L-wave interactions with the human body: state of knowledge and recent advances. *Int Microwave J Wireless Technolog.* (2011) 3:237–47. doi: 10.1017/S1759078711000122
4. Wu T, Rappaport TS, Collins CM. Safe for generations to come: considerations of safety for millimeter waves in wireless communications. *IEEE Microwave Mag.* (2015) 16:65–84. doi: 10.1109/MMM.2014.2377587
5. Guraliuc AR, Zhadobov M, Sauleau R, Marnat L, Dussopt L. Near-field user exposure in forthcoming 5G scenarios in the 60 GHz band. *IEEE Trans Antennas Propag.* (2017) 65:6606–15. doi: 10.1109/TAP.2017.2754473
6. Ziskin MC, Alekseev SI, Foster KR, Balzano Q. Tissue models for RF exposure evaluation at frequencies above 6 GHz. *Bioelectromagnetics.* (2018) 39:173–89. doi: 10.1002/bem.22110
7. Hirata A, Funahashi D, Kodera S. Setting exposure guidelines and product safety standards for radio-frequency exposure at frequencies above 6 GHz: brief review. *Ann Telecommun.* (2019) 74:17–24. doi: 10.1007/s12243-018-0683-y
8. ICNIRP. Guidelines for limiting exposure to time-varying electric, magnetic and electromagnetic fields (100 kHz to 300 GHz). *Health Phys.* (2020) 118:483–524. doi: 10.1097/HP.0000000000001210
9. IEEE. *IEEE Standard for Safety Levels with Respect to Human Exposure to Radio Frequency Electromagnetic Fields, 0 Hz to 300 GHz.* New York, NY: Standard IEEE C95.1-2019. (2019).
10. Christ A, Samaras T, Neufeld E, Kuster RF. N-induced temperature increase in a stratified model of the skin for plane-wave exposure at 6–100 GHz. *Radiat Prot Dosim.* (2020) 188:350–60. doi: 10.1093/rpd/ncz293
11. Christ A, Samaras T, Neufeld E, Kuster N. Transmission coefficient of power density into skin tissue between 6 and 300 GHz. *Radiat Prot Dosim.* (2020) 192:113–8. doi: 10.1093/rpd/ncaa179
12. Samaras T, Kuster N. Theoretical evaluation of the power transmitted to the body as a function of angle of incidence and polarization at frequencies> 6 GHz and its relevance for standardization. *Bioelectromagnetics.* (2019) 40:136–9. doi: 10.1002/bem.22170
13. Christ A, Samaras T, Neufeld E, Kuster N. Limitations of incident power density as a proxy for induced electromagnetic fields. *Bioelectromagnetics.* (2020) 41:348–59. doi: 10.1002/bem.22268
14. Li K, Sasaki K, Watanabe S, Shirai H. Relationship between power density and surface temperature elevation for human skin exposure to electromagnetic waves with oblique incidence angle from 6 GHz to 1 THz. *Phys Med Biol.* (2019) 64:065016. doi: 10.1088/1361-6560/ab057a
15. Sasaki K, Mizuno M, Wake K, Watanabe Monte S. Carlo simulations of skin exposure to electromagnetic field from 10 GHz to 1 THz. *Phys Med Biol.* (2017) 62:6993–7010. doi: 10.1088/1361-6560/aa81fc
16. Kanezaki A, Hirata A, Watanabe S, Shirai H. Parameter variation effects on temperature elevation in a steady-state, one-dimensional thermal model for millimeter wave exposure of one-and three-layer human tissue. *Phys Med Biol.* (2010) 55:4647–59. doi: 10.1088/0031-9155/55/16/003
17. Funahashi D, Hirata A, Kodera S, Foster KR. Area-averaged transmitted power density at skin surface as metric to estimate surface temperature elevation. *IEEE Access.* (2018) 6:77665–74. doi: 10.1109/ACCESS.2018.2883733
18. Diao Y, Rashed EA, Hirata A. Assessment of absorbed power density and temperature rise for nonplanar body model under electromagnetic exposure above 6 GHz. *Phys Med Biol.* (2020) 65:224001. doi: 10.1088/1361-6560/abbdb7
19. Li K, Sasaki K, Wake K, Onishi T, Watanabe S. Quantitative comparison of power densities related to electromagnetic near-field exposures with safety guidelines from 6 to 100 GHz. *IEEE Access.* (2021) 9:115801–12. doi: 10.1109/ACCESS.2021.3105608
20. Carrasco E, Colombi D, Foster KR, Ziskin MC, Balzano Q. Exposure assessment of portable wireless devices above 6 GHz. *Radiat Prot Dosim.* (2019) 183:489–96. doi: 10.1093/rpd/ncy177
21. Hashimoto Y, Hirata A, Morimoto R, Aonuma S, Laakso I, Jokela K, et al. On the averaging area for incident power density for human exposure limits at frequencies over 6 GHz. *Phys Med Biol.* (2017) 62:3124–38. doi: 10.1088/1361-6560/aa5f21
22. Hirata A, Kodera S, Sasaki K, Gomez J-T, Laakso I, Wood A, et al. Human exposure to radiofrequency energy above 6 GHz: review of computational dosimetry studies. *Phys Med Biol.* (2021) 66:08TR01. doi: 10.1088/1361-6560/abf1b7
23. Hirata A, Diao Y, Onishi T, Sasaki K, Ahn S, Colombi D, et al. Assessment of human exposure to electromagnetic fields: review and future directions. *IEEE Trans Electromagn Compat.* (2021) 63:1619–30. doi: 10.1109/TEMC.2021.3109249
24. He W, Xu B, Gustafsson M, Ying Z, He S. RF compliance study of temperature elevation in human head model around 28 GHz for 5G user equipment application: simulation analysis. *IEEE Access.* (2018) 6:830–8. doi: 10.1109/ACCESS.2017.2776145
25. Nakae T, Funahashi D, Higashiyama J, Onishi T, Hirata A. Skin temperature elevation for incident power densities from dipole arrays at 28 Ghz. *IEEE Access.* (2020) 8:26863–71. doi: 10.1109/ACCESS.2020.2970219
26. Li K, Diao Y, Sasaki K, Prokop A, Poljak D, Doric V, et al. Intercomparison of calculated incident power density and temperature rise for exposure from different antennas at 10–90 GHz. *IEEE Access.* (2021) 9:151654–66. doi: 10.1109/ACCESS.2021.3126738
27. Diao Y, Li K, Sasaki K, Sachiko K, Laakso I, Hajj WE, et al. Effect of incidence angle on the incident power density definition to correlate skin temperature rise for millimeter wave exposures. *IEEE Trans Electromagn Compat.* (2021) 63:1709–16. doi: 10.1109/TEMC.2021.3098594
28. Guraliuc AR, Zhadobov M, Valerio G, Sauleau R. Enhancement of on-body propagation at 60 GHz using electro textiles. *IEEE Antennas Wireless Propag Lett.* (2014) 13:603–6. doi: 10.1109/LAWP.2014.2313019
29. Guraliuc AR, Zhadobov M, Valerio G, Chahat N, Sauleau R. Effect of textile on the propagation along the body at 60 GHz. *IEEE Trans Antennas Propag.* (2014) 62:1489–94. doi: 10.1109/TAP.2013.2295425
30. Gandhi O, Riazi A. Absorption of millimeter waves by human beings and its biological implications. *IEEE Trans Microwave Theory Tech.* (1986) 34:228–35. doi: 10.1109/TMTT.1986.1133316
31. Sacco G, Pisa S, Zhadobov M. Impact of textile on electromagnetic power and heating in near-surface tissues at 26 GHz and 60 GHz. *IEEE J Electromagnet RF Microwav Med Biol.* (2021) 5:262–8. doi: 10.1109/JERM.2020.3042390
32. Sacco G, Nikolayev D, Sauleau R, Zhadobov M. Antenna/human body coupling in 5G millimeter-wave bands: do age and clothing matter? *IEEE Microwaves J.* (2021) 1:593–600. doi: 10.1109/JMW.2021.3063256
33. Sasaki K, Wake K, Watanabe S. Measurement of the dielectric properties of the epidermis and dermis at frequencies from 05 GHz to 110 GHz. *Phys Med Biol.* (2014) 59:4739–47. doi: 10.1088/0031-9155/59/16/4739
34. Lee Y, Hwang K. Skin thickness of Korean adults. *Surg Radiol Anat.* (2002) 24:183–9. doi: 10.1007/s00276-002-0034-5
35. Ishida Y, Carroll FJ, Pollock LM, Graves EJ, Leggett HS. Reliability of B-mode ultrasound for the measurement of body fat and muscle thickness. *Am Hum J Biol.* (1992) 4:511–20. doi: 10.1002/ajhb.1310040410
36. Luo J, Shao Y, Liao X, Liu J, Zhang J. Complex permittivity estimation for cloths based on QPSO method over (40 to 50) GHz. *IEEE Trans Antennas Propag.* (2021) 69:600–5. doi: 10.1109/TAP.2020.3005032

Conflict of Interest: The authors declare that the research was conducted in the absence of any commercial or financial relationships that could be construed as a potential conflict ofinterest.

frontiers in Public Health

ORIGINAL RESEARCH
published: 11 March 2022
doi: 10.3389/fpubh.2021.794167

Genetic Algorithm for TMS Coil Position Optimization in Stroke Treatment

Shujie Lu[1†], *Haoyu Jiang*[2†], *Chengwei Li*[1†], *Baoyu Hong*[1], *Pu Zhang*[1*] *and Wenli Liu*[1*]

[1] *Center for Medical Metrology, National Institute of Metrology, Beijing, China,* [2] *China Academy of Telecommunications Technology, Beijing, China*

Transcranial magnetic stimulation (TMS), a non-invasive technique to stimulate human brain, has been widely used in stroke treatment for its capability of regulating synaptic plasticity and promoting cortical functional reconstruction. As shown in previous studies, the high electric field (E-field) intensity around the lesion helps in the recovery of brain function, thus the spatial location and angle of coil truly matter for the significant correlation with therapeutic effect of TMS. But, the error caused by coil placement in current clinical setting is still non-negligible and a more precise coil positioning method needs to be proposed. In this study, two kinds of real brain stroke models of ischemic stroke and hemorrhagic stroke were established by inserting relative lesions into three human head models. A coil position optimization algorithm, based on the genetic algorithm (GA), was developed to search the spatial location and rotation angle of the coil in four 4 × 4 cm search domains around the lesion. It maximized the average intensity of the E-field in the voxel of interest (VOI). In this way, maximum 17.48% higher E-field intensity than that of clinical TMS stimulation was obtained. Besides, our method also shows the potential to avoid unnecessary exposure to the non-target regions. The proposed algorithm was verified to provide an optimal position after nine iterations and displayed good robustness for coil location optimization between different stroke models. To conclude, the optimized spatial location and rotation angle of the coil for TMS stroke treatment could be obtained through our algorithm, reducing the intensity and duration of human electromagnetic exposure and presenting a significant therapeutic potential of TMS for stroke.

Keywords: TMS, stroke, voxel of interest, genetic algorithm, coil position optimization

OPEN ACCESS

Edited by:
Tongning Wu,
China Academy of Information and Communications Technology, China

Reviewed by:
Weimin Wang,
Peking University, China
Hui Xiong,
Tianjin Polytechnic University, China

***Correspondence:**
Pu Zhang
zhangpu@nim.ac.cn
Wenli Liu
liuwl@nim.ac.cn

[†] These authors have contributed equally to this work and share first authorship

Specialty section:
This article was submitted to Radiation and Health, a section of the journal Frontiers in Public Health

Received: *13 October 2021*
Accepted: *30 December 2021*
Published: *11 March 2022*

Citation:
Lu S, Jiang H, Li C, Hong B, Zhang P and Liu W (2022) Genetic Algorithm for TMS Coil Position Optimization in Stroke Treatment. Front. Public Health 9:794167. doi: 10.3389/fpubh.2021.794167

INTRODUCTION

Stroke is a prevalent disease worldwide and has caused a heavy burden on the healthcare system (1–3). As a serious life-threatening disease, which is common in middle-aged and elderly people, stroke can cause sequelae such as hemiplegia and aphasia (4, 5). Strokes, which cutoff the blood supply to parts of the brain, are categorized as ischemic stroke and hemorrhagic stroke. Ischemic stroke is caused by a sudden reduction in blood perfusion or complete interruption of blood flow to the local brain tissue. Hemorrhagic stroke is caused by cerebral hemorrhage or subarachnoid hemorrhage (6). The cortical branches of the middle cerebral artery (MCA) extend to the functional areas of the cerebral cortex and provide 80% of the blood supply to the brain (7). Stroke in the main branches of the MCA can cause severe physical injury to the body.

Transcranial magnetic stimulation (TMS) is an effective and non-invasive neuromodulation and therapy technique, which gained popularity in scientific research and clinical applications (8). Transcranial magnetic stimulation device generates an electric current in coil by the discharge of capacitor, which will activate pulsed magnetic field in space. This magnetic field passes through the skin and other tissues to generate an eddy current electric field (E-field) in the intracranial tissue, consequently stimulating the targeted brain area and affecting neural activity (9, 10). TMS can accelerate the cortical blood supply to the targeted brain areas, effectively enhance synaptic plasticity and regulate excitability of nerve cells as well as release of neurotransmitters in short and long terms, thus enhance the stimulated network interaction (11–16). These above characteristics are of great significance for stroke rehabilitation.

During stroke rehabilitation, the existence of viable neurons at stimulation area of TMS highly contributes to the therapeutic effect. For small stroke lesions, functional recovery depends on the recruitment of peripheral or residual neurons (17). Murata et al. reported that the plasticity of neural activity, functional connectivity in the premotor cortex, and the remaining tissue near the lesion contribute to the functional recovery of induced motor defects following damage to the primary motor cortex. Therefore, direct promotion of affected brain area excitability could be more beneficial to poststroke recovery than inhibition of unaffected brain area excitability (18, 19) and the higher E-field intensity is, the more efficient therapy is. According to the International Federation of Clinical Neurophysiology, the scalp spot where the targeted muscle reaches the peak motor evoked potential is defined as a "hot spot," which is widely used in clinical practice for TMS stimulation (13, 20, 21). However, the "hot spot" definition is only a rough trade-off under the existing conditions without considering the angle of coil. In addition, since every individual has different cortex structures and the cortex folds of different brain areas of specific person are not the same, there is a high chance that the potential optimal stimulus "hot spot" remains undetected. Therefore, the targeted region may not acquire significant activation under specific TMS frequency and intensity, whereas the cortical and subcortical distant brain areas are activated from time to time (22, 23).

The therapeutic effect of TMS depends on the coil position, stimulation frequency, current intensity, etc. A set of accurate coil location and rotation angle can provide the most potent stimulation to the targeted brain area, while minimizing the impact on unrelated brain areas, which is crucial to an enhanced therapeutic effect (24, 25). However, coil placement by TMS operators is often accompanied by a deviation of 2 cm (26), which may affect the treatment efficiency through the change of the E-field distribution in target region. Therefore, it is necessary to study a more accurate clinical quantitative treatment scheme and a stimulus dose plan for the safe and precise TMS treatment (27). From what has been discussed above, the primary aim is to stimulate a more precise "hot spot" to acquire the E-field as high as possible for a stronger stimulation effect, which is truly helpful for activating neurons around the lesion. Some studies established comprehensive brain atlas of stimulation sites for quick operations to improve TMS stimulation accuracy (28, 29), whereas others used several heuristic algorithms, such as the fast computational auxiliary dipole method (ADM) (30) and particle swarm optimization (PSO) (31, 32), to regulate the position or current configuration of the coil to improve the overall E-field in the voxel of interest (VOI); thus, achieving optimal neural regulation. However, both these coil location optimization algorithms are based on a healthy brain. It is unknown if the algorithms are robust in the brain area with local conductivity changes, which mean that the coil position optimization of TMS stimulation near the lesion needs further study.

In this study, a method for TMS coil positioning is suggested, which will help clinician to find the optimal stimulus spot and get the E-field intensity near the lesion as high as possible for a better therapeutic effect. The optimization algorithm is based on the precision digital human head model with a stroke module inserted to simulate the two most common clinical MCA strokes (ischemic stroke and hemorrhagic stroke). Compared with other TMS coil position optimization algorithms for healthy human head models, the advantages of our method are a broader search domain, more coil positioning patterns, and a higher calculation efficiency. Further, the E-field intensity of the VOI is kept high and in the meantime, the intensity of the non-target region is under control to void any unnecessary exposure due to the constant emission energy. This method will have a great significance in clinical stroke rehabilitation during TMS treatment. The introduction of the optimization algorithm into TMS can effectively improve the stimulation efficiency of the treatment, reduce human electromagnetic exposure, and alleviate the concern of the public about electromagnetic exposure.

MATERIALS AND METHODS

Numerical Models

This study was based on three digital human head models (**Figure 1**) obtained from the Chinese Visible Human (CVH) project and the Virtual Family Project (33, 34). The two Chinese human head models included those of a 35-year-old male (CVH male) and a 22-year-old female (CVH female). The male and female models had resolutions of $1.0 \times 1.0 \times 1.0$ and $0.5 \times 0.5 \times 0.5$ mm, respectively. The third head model was that of a 34-year-old male Duke, with a resolution of $0.5 \times 0.5 \times 0.5$ mm. The models contained more than 40 tissues, such as skin, skull, and fat, covering 20 to 35-year-old males and females belonging to the yellow and white races.

The MCA disease is an important cause of stroke in humans (35). The central artery is the significant one of the MCA cortical branches (36). If this vessel suddenly ruptures or embolizes, some brain areas would suffer from pathological changes due to the lack of nutrients, resulting in temporary or permanent loss of brain function. To simulate the intracranial physiological state caused by stroke, a part of the central artery, thrombus, and the lesion (2×2 cm) with the four VOIs (3×3 cm) nearby were added to the cortex (**Figure 2**). The average diameters of the blood vessel and thrombus were both 1.9 mm (37, 38). The ischemic stroke and hemorrhagic stroke models were established by adjusting the tissue electromagnetic parameters of the lesion. When an ischemic stroke occurred

FIGURE 1 | Numerical head model.

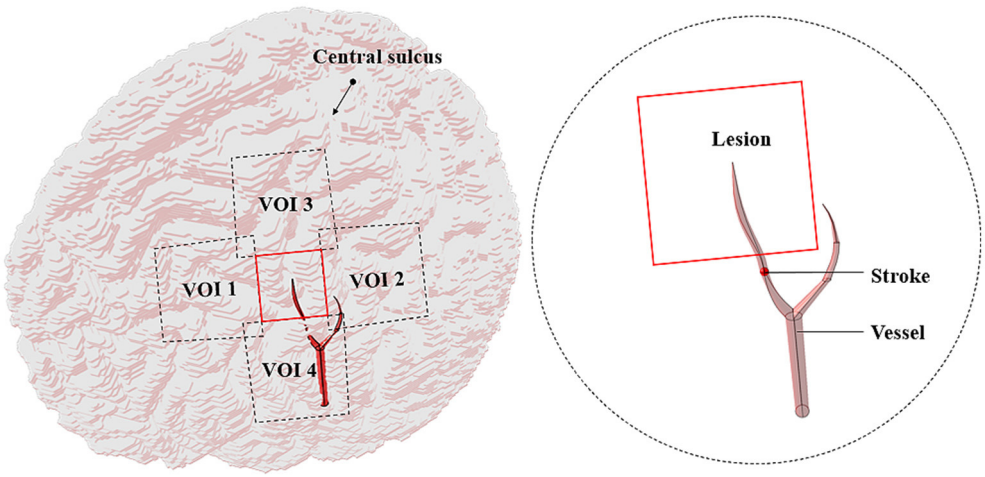

FIGURE 2 | Stroke model (a part of vessels with stroke only).

due to blocking the cerebrovascular, the affected gray matter (GM) conductivity decreased by 10–14% (39). In addition, the complex dielectric constant value decreased by 10% (40). When a hemorrhagic stroke occurred, blood infiltrated the cortical tissue and completely replaced brain tissue, such that the GM conductivity of the lesions was the same as that of blood (41). **Table 1** shows the tissues and all the electromagnetic parameters of models.

There exist numerous gyrus structures and specific cortical curvatures; thus, the lesions and the VOIs in different models have different thicknesses. The average thickness of lesions in the models ranged from 0.48 to 1.22 mm and that of the VOIs ranged from 1.74 to 4.67 mm (**Table 2**).

Numerical Simulation for the Induced E-Field

Transcranial magnetic stimulation was used to stimulate the area near the lesion to facilitate the function of residual neurons. A higher average value of the E-field intensity in the VOI resulted in a better stimulus effect. In TMS treatment of stroke, an eight-figure coil is often placed in a tangent position to the scalp and the handle of the coil is tilted to the rear of the midline at an angle of 45° (21, 42). At this time, the handle of the coil is perpendicular to the central sulcus and the induced current is perpendicular to the central sulcus, such that the induced E-field is significantly enhanced (43).

In the simulation, every model was divided into 1.0 × 1.0 × 1.0 mm voxels. Single-turn eight-figure coil with two wings of 70 mm diameter with currents in the opposite direction and no thickness was used as an excitation source (44). The frequency and intensity of the abstract harmonic current were 2.24 kHz and 1,000 A, respectively.

The magnetic vector A was introduced into the process of solving electromagnetic fields to calculate the induced magnetic field of the line current in the space using the Biot–Savart law.

$$A = \frac{\mu}{4\pi} \int_V \frac{J(x')dV}{r} \tag{1}$$

TABLE 1 | Electromagnetic parameters of tissues (f = 2,240 Hz).

Tissue	Conductivity (S/m)	Relative permittivity
Skin	2.00E-04	1.14E+03
Cortical bone	2.03E-02	1.56E+03
Cancellous bone	8.19E-02	6.19E+03
Cerebrospinal fluid	2.00E+00	1.09E+02
Gray matter	1.04E-01	8.56E+04
White matter	6.42E-02	3.71E+04
Cerebellum	1.24E-01	8.59E+04
Hypophysis	5.26E-01	3.07E+04
Hypothalamus	1.04E-01	8.56E+04
Hippocampus	1.04E-01	8.56E+04
Fat	4.23E-02	7.47E+03
Pineal gland	5.26E-01	3.07E+04
Intervertebral discs	8.30E-01	6.07E+01
Spinal cord	3.02E-02	6.12E+04
Dura	5.01E-01	3.00E+03
Red bone marrow	1.02E-01	2.73E+03
Muscle	3.31E-01	1.44E+05
Cornea	4.25E-01	9.04E+04
Lens cortex	3.31E-01	4.71E+04
Nucleus	2.00E-01	9.91E+02
Iris	3.31E-01	1.44E+05
Sclera	5.07E-01	3.15E+04
Vitreous body	1.50E+00	9.90E+01
Retina	1.04E-01	8.56E+04
Aqueous humor	2.00E+00	1.09E+02
Lacrimal apparatus	2.00E+00	1.09E+02
Salivary gland	6.70E-01	9.16E+01
Respiratory tract	0.00E+00	1.00E+00
Tongue	2.76E-01	3.22E+04
Teeth	2.03E-02	1.56E+03
Nerve	3.02E-02	6.12E+04
Cartilage	1.75E-01	1.27E+04
Lymph node	5.90E-01	9.48E+01
Blood and stroke	7.00E-01	5.26E+03
Ischemic lesion	9.11E-02	7.71E+04
Hemorrhagic lesion	5.00E-01	5.26E+03

TABLE 2 | Average thickness of the voxel of interests (VOIs) and lesions in stroke model (mm).

Model	VOI 1	VOI 2	VOI 3	VOI 4	Lesion
The CVH female	1.74	1.85	2.16	1.75	0.48
The CVH male	4.11	4.59	3.23	2.63	1.22
Duke	4.67	3.62	3.10	4.56	1.21

The average thickness is determined by the ratio of volume (V) to projected area (S) (thickness = V/S).

Where, $\mu = \mu_0$ is the magnetic permeability, r is the distance between the source element x' and the model element x, and the source current is $J(x')$.

Combining Maxwell's equations, the current continuity equation derived from linear media gives:

$$\nabla \times \frac{1}{\mu} \nabla \times A = \omega^2 \tilde{\varepsilon} A - j\omega\tilde{\varepsilon} \nabla\phi + J_0 \quad (2)$$

Where, $\tilde{\varepsilon}$ is the complex permittivity, ω is the angular frequency, J_0 is the source current, and the scalar potential is ϕ.

Thereby, the E-field intensity can be obtained in each voxel:

$$E = -j\omega\mathbf{A} - \nabla\phi = -j\omega A - \frac{\omega^2\tilde{\varepsilon}A + J_0 - \nabla \times \frac{1}{\mu}\nabla \times A}{j\omega\tilde{\varepsilon}} \quad (3)$$

Genetic Algorithm

In the genetic algorithm (GA), a group of solutions (individuals) is obtained through several generations of evolution. In every generation, each individual codes in a specific way and the fitness function is used to evaluate its adaptability. Based on the principle of "survival of the fittest," individuals with poor performance are eliminated and those individuals with excellent performance are selected to enter the next generation. The individuals are recombined under the influence of gene crossover and gene mutation to form a new genotype (45). Both the theory and experiment verify the robustness of the GA in a complex search space (46).

In order to identify the best position of the coil, the population of each generation consisted of 10 individuals and the genotype of an individual was determined by six bits of binary coding of their position P_i ($x_i, y_i, z_i, and\ \varphi_i$). The steps of x_i and y_i were both 1 mm and then z_i could be calculated according to the placement of the coil relative to the scalp. The step of the rotation angle φ_i was 2.8125°. It should be also mentioned that the x_i, y_i, z_i, and φ_i were all in float format as a result of data code and decode process and were simplified to two decimal places further. The 24 bits of binary code could cover all the genotypes of individuals in the search domain. Each genotype corresponded to one phenotype (spatial location and rotation angle of the coil). The search domain covered $x \in [-20 + x_0,\ x_0 + 20]$, $y \in [-20 + y_0,\ y_0 + 20]$, where x_0 and y_0 are the central coordinates of the VOI. In each generation, individuals were involved in 0–1 mutation and randomized crossovers. The fitness value of each coil position was evaluated by the fitness function (the average E-field intensity in the VOI) (47). A higher average value of the E-field intensity in the VOI resulted in a better fitness value. Finally, natural selection was performed according to the fitness values; individuals with the worst fitness values were eliminated and those individuals with excellent fitness values were copied as offspring according to the probability. The number of iterations was set to 9. The algorithm idea was as follows:

Begin:

T ← 0; //T: Number of iterations
Initialize Pop(T); //Initial population
Fitness E(x, y, z, ϕ); //Survival of the fittest
While (**not** terminating number of iterations) **do**:

Crossover operation to Pop(T);
Mutation operation to Pop(T);

T ← T + 1;
End
Output: Optimal fitness E(x, y, z, ϕ) and corresponding parameters (x, y, z, ϕ)

End

Following the idea of the GA, we wrote an algorithm to search the coil location and angle in the VOIs. The optimization algorithm controlled Sim4Life version 6.0 (ZMT Zurich MedTech AG, Zürich, Switzerland, UK) for the E-field distribution, solving the stimulation at random spots in the coil search domain. The optimal position of the coil with the peak VOI average E-field intensity was obtained to improve the effectiveness of magnetic stimulation during the treatment of stroke. The 2.5 GHz Intel I7–11700F 16-core processor was used for the calculation and the time of each simulation iteration was set to 2–3 min. The resolution was 1.0 × 1.0 × 1.0 mm and the convergence tolerance difference was 1.00E-08.

Quantitative Evaluation Parameters of the E-Field

In this study, we selected the P_{ref} ($x_{ref}, y_{ref}, z_{ref}$, *and* φ_{ref}) pointing out 1 cm from the lateral normal of the scalp above the center of the VOI as the clinical reference stimulation spot (**Figure 3**).

For comparing the E-field of the VOI with stimulation spot located in P_{ref} and P_{opti}, the percentage improvement in the E-field intensity in the VOI ($E_{improved}$), spatial distance optimization $(d_{changed})$, and rotation angle optimization ($\varphi_{changed}$) of coil was used as quantitative indexes to evaluate the optimization degree of the coil. A larger value of the index resulted in a greater optimization effect.

$$E_{improved} = \frac{(E_{opti} - E_{ref})}{E_{ref}} \times 100\% \quad (4)$$

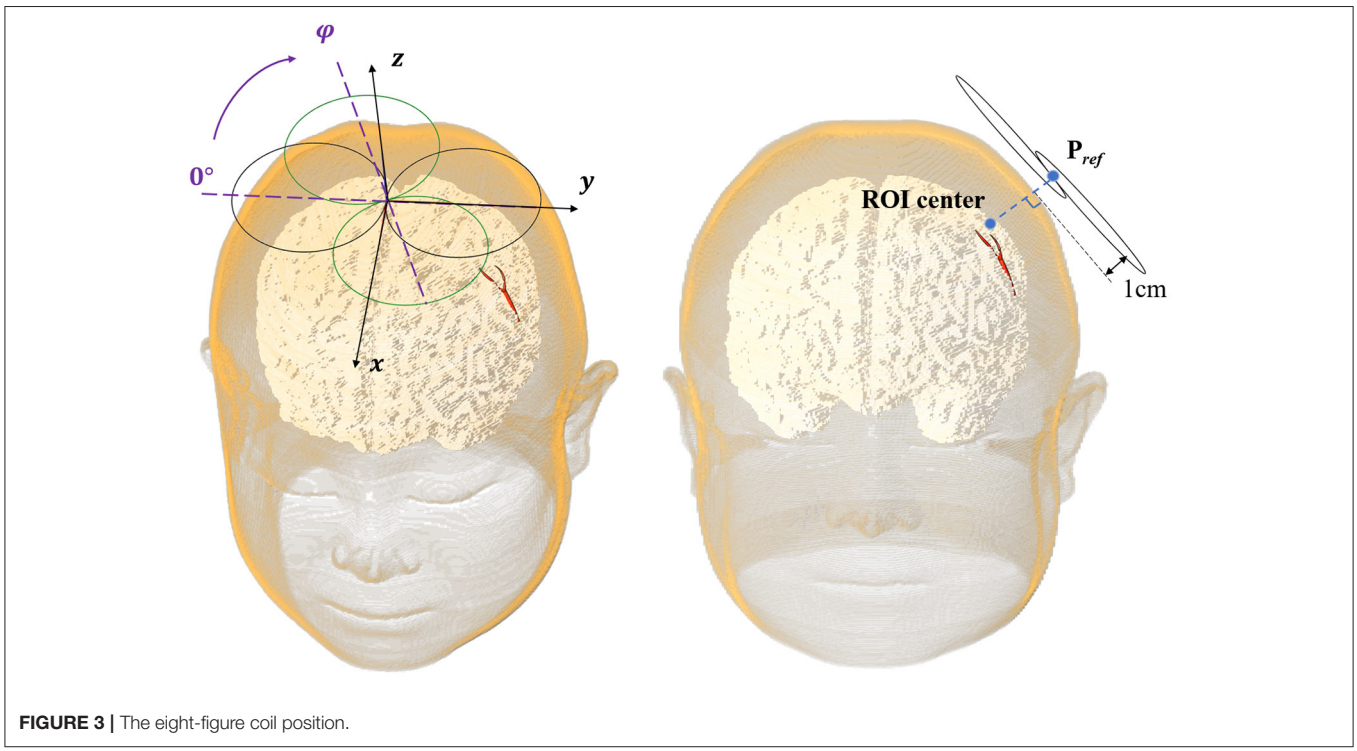

FIGURE 3 | The eight-figure coil position.

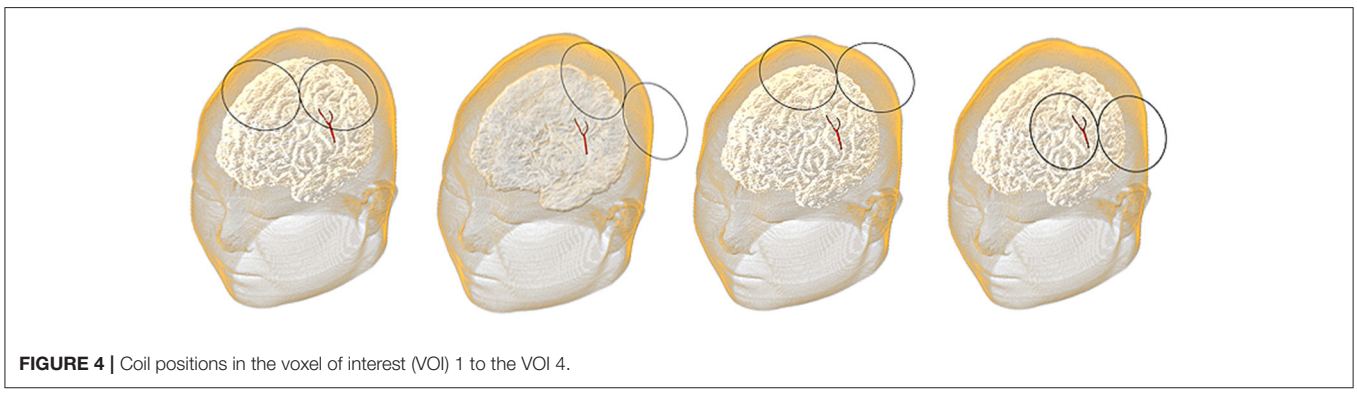

FIGURE 4 | Coil positions in the voxel of interest (VOI) 1 to the VOI 4.

$E_{improved}$ reflects the relative improvement as a percentage of the E-field intensity during the coil positioning in comparison with the simulation at a reference spot. The larger the value, the higher the efficiency of the algorithm.

$$d_{changed} = \sqrt{(x_{opti} - x_{ref})^2 + (y_{opti} - y_{ref})^2 + (z_{opti} - z_{ref})^2} \quad (5)$$

$$\varphi_{changed} = |\varphi_{opti} - \varphi_{ref}| \quad (6)$$

$d_{changed}$ means Euclidean space distance between the optimal spot and the reference spot and the $\varphi_{changed}$ is the difference between the angle of coil at the optimal spot and the reference spot. A large value of both means a different position.

For slight injury stroke lesions (<10 cm^3) (48), a specific frequency stimulation is often operated on the affected hemispheres to maximize the activation of the undamaged brain functional connections and enhance the plasticity of the affected cortex; thus, accelerating functional recovery (49, 50).

TABLE 3 | Optimization results of the electric fields (E-fields).

Model	P_{ref}	P_{opti}	E_{ref} (V/m)	E_{opti} (V/m)	$E_{improved}$ (%)	$d_{changed}$ (mm)	$\varphi_{changed}$ (°)
Ischemic stroke							
The CVH female							
VOI 1	(15.00, 40.00, 92.00, 45.00)	(19.00, 42.00, 90.00, 120.00)	1.75	1.92	9.59	4.90	75.00
VOI 2	(–37.00, 70.00, 77.00, 45.00)	(–41.00, 74.00, 70.00, 67.10)	1.50	1.55	3.34	9.00	22.10
VOI 3	(–22.00, 43.00, 97.00, 45.00)	(–20.00, 26.00, 105.0, 41.40)	1.57	1.81	15.32	18.00	3.60
VOI 4	(4.00, 77.00, 62.00, 45.00)	(12.00, 71.00, 67.00, 41.40)	1.78	1.85	3.82	11.18	3.60
Mean	/	/	1.65 ± 0.12	1.78 ± 0.14	8.02 ± 4.88	10.77 ± 4.74	26.08 ± 29.24
The CVH male							
VOI 1	(–36.50, 17.50, 60.50, 45.00)	(–46.50, 22.50, 55.50, 0.00)	1.89	2.57	16.99	12.20	45.00
VOI 2	(–70.50, –16.50, 47.50, 45.00)	(–73.50, –18.50, 46.50, 71.40)	2.50	2.67	6.82	3.70	26.40
VOI 3	(–37.50, –18.50, 65.50, 45.00)	(–34.50, –11.50, 66.50, 34.00)	2.20	2.36	7.19	7.70	11.00
VOI 4	(–81.50, 15.50, 27.50, 45.00)	(–77.50, 17.50, 30.50, 34.30)	2.50	2.77	10.89	33.38	10.70
Mean	/	/	2.27 ± 0.25	2.59 ± 0.15	10.47 ± 4.09	14.24 ± 11.45	23.28 ± 14.06
Duke							
VOI 1	(67.87, –32.95, 31.43, 45.00)	(66.88, –41.93, 26.44, 54.30)	2.05	2.22	8.13	10.30	9.30
VOI 2	(76.86, 16.97, 35.42, 45.00)	(78.85, 20.96, 33.42, 125.70)	2.71	2.80	3.60	4.90	80.70
VOI 3	(53.90, –5.99, 58.37, 45.00)	(67.87, –6.99, 43.40, 157.10)	2.08	2.19	5.21	20.50	67.90
VOI 4	(82.85, –12.98, 11.47, 45.00)	(81.85, –15.97, 12.47, 5.70)	2.32	2.39	3.10	3.30	39.30
Mean	/	/	2.29 ± 0.26	2.40 ± 0.24	5.01 ± 1.96	9.75 ± 6.73	49.30 ± 27.53
Hemorrhagic stroke							
The CVH female							
VOI 1	(15.00, 40.00, 92.00, 45.00)	(21.00, 40.00, 91.00, 172.90)	1.78	1.89	6.01	6.08	52.10
VOI 2	(–37.00, 70.00, 77.00, 45.00)	(–25.00, 58.00, 87.00, 137.10)	1.51	1.55	2.93	19.70	87.90
VOI 3	(–22.00, 43.00, 97.00, 45.00)	(–19.00, 27.00, 105.00, 47.10)	1.56	1.63	5.02	18.14	2.14
VOI 4	(4.00, 77.00, 62.00, 45.00)	(10.00, 69.00, 69.00, 47.10)	1.78	1.84	3.46	12.21	2.14
Mean	/	/	1.66 ± 0.12	1.73 ± 0.14	4.36 ± 1.23	14.03 ± 5.37	36.07 ± 36.21
The CVH male							
VOI 1	(–36.50, 17.50, 60.50, 45.00)	(–41.50, 26.50, 55.50, 174.30)	2.35	2.77	17.48	11.45	50.70
VOI 2	(–70.50, –16.50, 47.50, 45.00)	(–74.50, –11.50, 45.50, 65.71)	2.58	2.69	4.20	6.71	20.71
VOI 3	(–37.50, –18.50, 65.50, 45.00)	(–44.50, –22.50, 62.50, 11.43)	2.07	2.17	5.19	39.84	33.57
VOI 4	(–81.50, 15.50, 27.50, 45.00)	(–77.50, 17.50, 30.50, 17.14)	2.52	2.80	11.31	5.39	27.86
Mean	/	/	2.38 ± 0.20	2.61 ± 0.25	9.54 ± 5.33	15.84 ± 14.03	33.21 ± 11.08
Duke							
VOI 1	(67.87, –32.95, 31.43, 45.00)	(54.90, –44.93, 44.40, 20.00)	2.08	2.20	5.43	21.91	25.00
VOI 2	(76.86, 16.97, 35.42, 45.00)	(70.87, 22.96, 44.40, 120.00)	2.80	3.04	8.71	12.34	75.00
VOI 3	(53.90, –5.99, 58.37, 45.00)	(44.92, –6.99, 64.35, 177.10)	2.12	2.32	9.55	10.84	47.90
VOI 4	(82.85, –12.98, 11.47, 45.00)	(85.85, –12.98, –6.49, 11.43)	2.32	2.43	4.48	18.21	33.57
Mean	/	/	2.33 ± 0.29	2.50 ± 0.32	7.04 ± 2.13	15.83 ± 4.46	45.37 ± 18.96

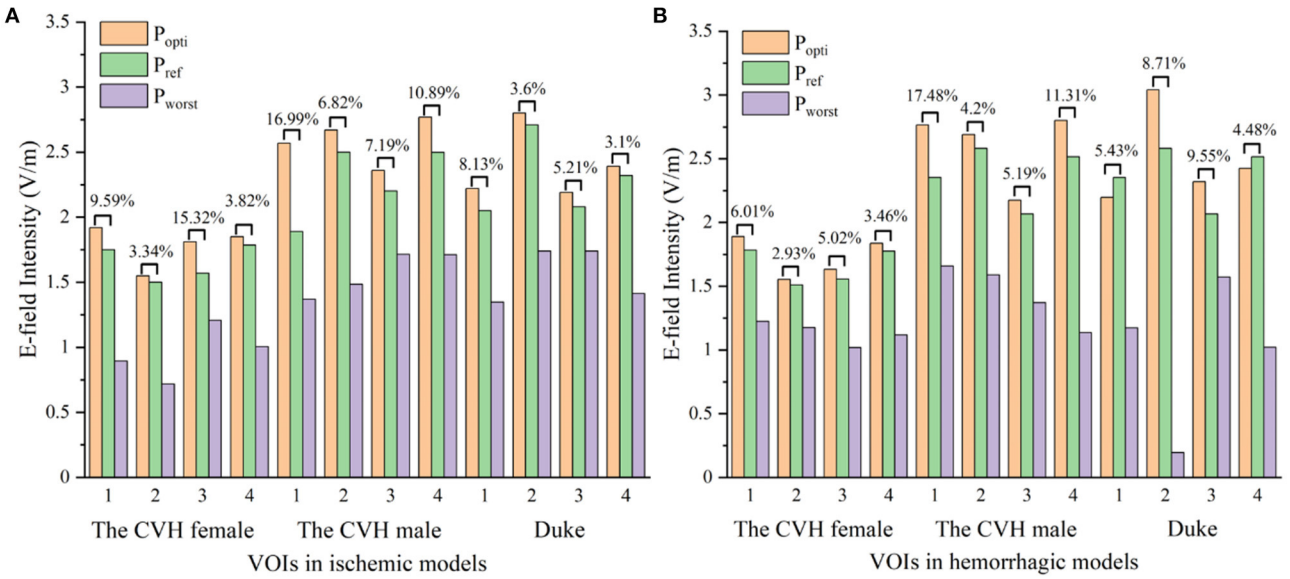

FIGURE 5 | The electric fields (E-fields) at different stimulus spots in ischemic **(A)** and hemorrhagic **(B)** stroke models (P_{opti}, P_{worst}: coil stimulation spot in the search domain, where the VOI average E-field reached the peak and trough; P_{ref}: clinical coil reference stimulation spot).

In this study, the lesion area (2 × 2 cm) was surrounded by four 3 × 3 cm stimulation VOIs (**Figure 2**). Each VOI corresponded to a search domain (4 × 4 cm) for optimizing the coil position (31). The center of the search domain overlapped with the center of the corresponding VOI. The search domain covered all the VOIs and a part of the lesion and each VOI intersected with adjacent edges of the lesion and the other VOIs.

The position of the coil was determined by the spatial location ($x, y, and\ z$) of the coil center and its rotation angle φ around the z-axis (**Figure 3**). The coil plane was always kept parallel to the scalp. The position can be described as $P\ (x, y, z, and\ \varphi)$ and the optimal coil position P_{opti} ($x_{opti}, y_{opti}, z_{opti}, and\ \varphi_{opti}$) contributed to the maximum average E-field intensity in VOI. **Figure 4** shows the coil positions in the VOI 1 to VOI 4.

RESULTS

Optimization Results of the E-Field

The E-fields in the VOIs of the ischemic stroke and hemorrhagic stroke models were optimized. Compared with the reference spot, the E-field optimization results are shown in **Table 3**.

As can be seen from **Table 3** and **Figure 5**, compared with P_{ref}, the overall induced E-field in the VOI with the coil at P_{opti} significantly improved. The E-field improvement was lower in the Duke stroke model. The average E-field improvements in the VOIs ranged from 5.01 to 10.47% for ischemic stroke models and from 4.36 to 9.54% for hemorrhagic stroke models. There were about 66.7% of the VOIs that showed significant improvement in the E-field intensity ($E_{improved}$ over 5%). During coil position optimization, the maximum spatial location change was 39.84 mm and the maximum rotation angle change was 87.9°.

To visually present the E-field enhancement in the VOIs, the distribution of the E-field in GM at two different stimulating positions (P_{opti} and P_{ref}) in two stroke models was studied.

Figure 6 shows that all the focus centers of the eight-figure coil were in the VOIs and the average E-field intensity and the whole uniformity of the VOI were greatly improved after optimization of the coil position. The distribution of the E-field in the VOIs of the ischemic stroke model was consistent with that of the hemorrhagic stroke model. Furthermore, the improvement of the E-field intensity in the VOIs of the ischemic stroke model was higher.

The optimization iteration process showed that the E-field values were no longer updated after the seventh generation (**Figure 7**), implying that the algorithm converged effectively at the ninth generation. Therefore, an iteration number of 9 was selected to ensure the optimal position parameters in the coil search domain and each optimization of the model took 4.5–5.71 h.

Validation of the Algorithm

To analyze the robustness of the algorithm, the CVH female (ischemic)-VOI 1 was selected to repeat the optimization process five times. The $\Delta E_{improve}$ below 1% was regarded as the no E-field improvement. The results are shown in **Table 4**.

The distribution of E_{opti} obtained using five repeated experiments was concentrated with a small fluctuation (SD = 0.01 V/m), indicating that our optimization algorithm could find the optimal position of the coil after nine iterations and exerted a stable improvement effect on the E-field of the VOI.

To verify the effectiveness of the algorithm in searching the optimal coil position in the search domain, a 6 × 6 mm ergodic search domain covering both the P_{ref} and P_{opti} was set. In the

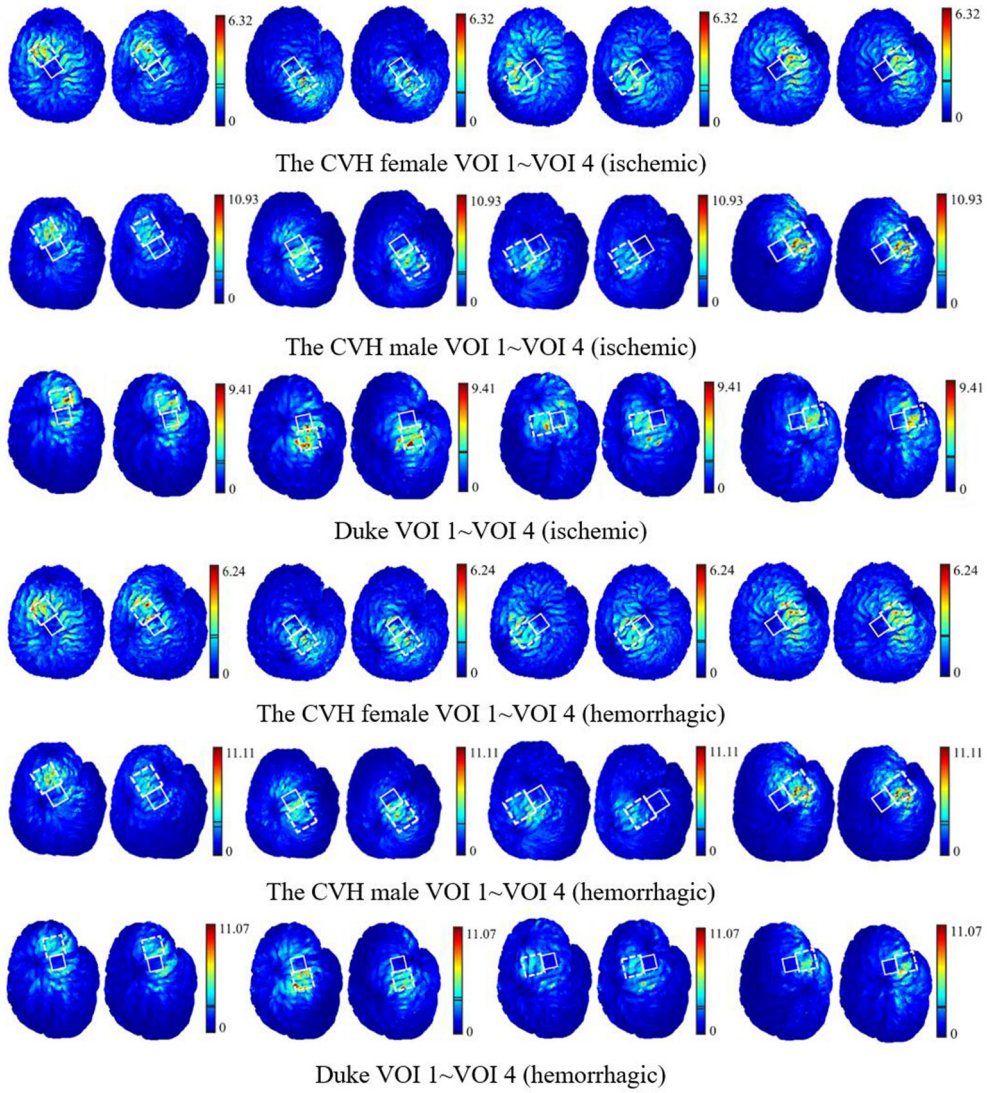

FIGURE 6 | The E-field distribution of the VOIs with the coil at P_{opti} (left) and P_{ref} (right) [unit: V/m; the two lines in the linear color bar represent the average E-field intensity induced by P_{opti} (upper) and P_{ref} (lower)].

search domain, the distance steps in the *x*-, *y*-, and *z*-directions were set as 1 mm and each space point was set with 11 rotation angles (the rotation angle step was 11.25° and could cover 45°). The average E-field intensities in the VOIs under all the coil positions were calculated and compared with P_{opti}.

There are many coil positions that contribute to the higher average E-field intensity than the reference position (1.50 V/m) in the whole search domain for the same VOI (**Figure 8**). It can be concluded that the reference position is not very likely to be the optimal one due to the diversified structure of local cortical folds. The average E-field intensity in the VOI can reach the maximum value (1.92 V/m) when the coil stimulates at the optimal position given by the algorithm and this also confirms the accuracy of our algorithm.

DISCUSSION

Several differences exist in the structure of the local gyri among models and locations and, thus, the intensity and distribution of the induced E-field of the coil position in the different VOIs vary. For a better therapeutic effect, the E-field intensity in the VOI needs to be improved maximally. It is necessary to optimize the spatial location and angle of the coil for specific stimulation areas because there is no fixed paradigm for it.

The average E-field intensity in the VOIs of the CVH female was lower than that of others (**Table 3**), which was attributed to the specificity of the gyrus structure. The deeper and wider sulcus of the CVH female leads to greater filling of the cerebrospinal fluid (CSF) near the GM. As a result, the electromagnetic field

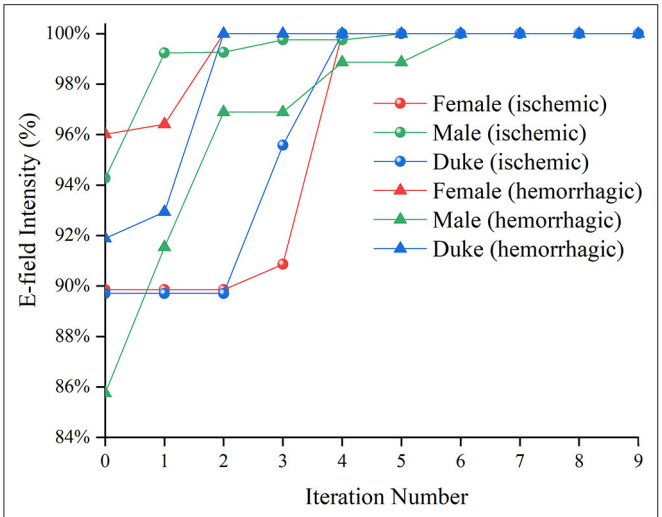

FIGURE 7 | The average E-field intensity in the Chinese Visible Human (CVH) female (ischemic)-VOI 1 in every iteration.

TABLE 4 | Algorithm repeatability verification.

Test	E_{ref} (V/M)	E_{opti} (V/M)	$E_{improve}$ (%)
1	1.75	1.92	9.59
2	1.75	1.92	9.30
3	1.75	1.93	9.93
4	1.75	1.93	10.27
5	1.75	1.91	8.96
Mean ± SD	1.75 ± 0.00	1.92 ± 0.01	9.61 ± 0.46

travels a longer distance through the CSF, resulting in more energy attenuation. Therefore, the induced E-field intensity in the VOIs of female was lower than other models. The lesion in the CVH female was thinner than in others, i.e., more residual GM voxels were classified as the VOIs below the thin lesion (four edges of the lesion had about 2 mm intersection with each VOI). The presence of these GM voxels closer to the stimulation coil below the lesion resulted in an enhanced E-field. Therefore, the stimulation intensity can be appropriately reduced in the treatment of lesions with a light injury.

Figure 6 shows that when the coil was at P_{opti}, the E-field distribution gradient in the VOI was significantly different due to the coil position and gyrus structure difference. The VOI E-field average of ischemic and hemorrhagic stroke models can be maximally improved by 16.99 and 17.48%, respectively, due to the optimization of the coil position (**Figure 5**). Although in a few models, the peak E-field of the VOI was higher when the coil was at P_{ref}. A greater effect on the average value of the induced E-field and the field uniformity of the VOI was observed when the coil was at P_{opti}, which could maximally activate the residual nerve around the lesion and improve the efficiency of stroke treatment. In addition, because the cerebral cortex has numerous folds, the optimal coil stimulation position, where the maximum overall E-field intensity in the VOIs could be acquired, tended to deviate

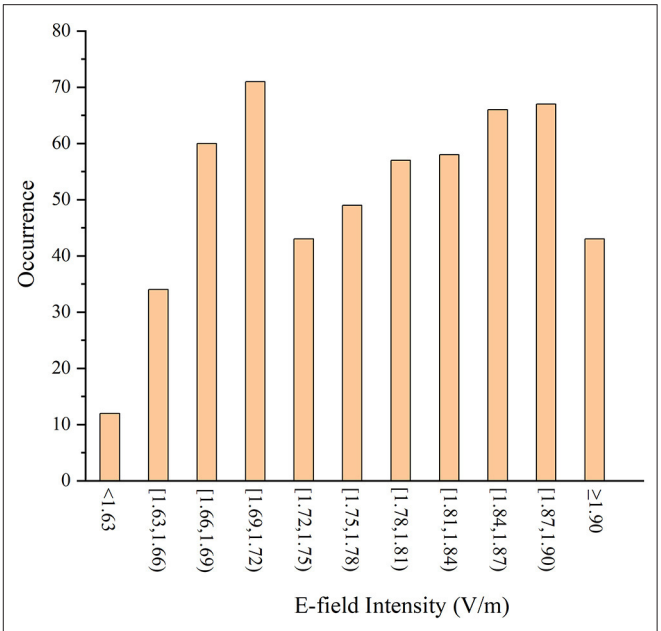

FIGURE 8 | The average E-field intensity of the VOIs in different stimulus spots.

directly over the VOI center (**Table 3**; **Figure 6**). When the scalp edge curve was steep, the distance optimization value increased significantly such as $d_{changed}$ in the CVH female-VOI 3, the CVH male-VOI 1, and the Duke-VOI 1. The distance change fell within 20–30 mm, which was equivalent to the lesion size.

Previous study showed that induced currents pass perpendicularly through the local gyri to cause at least a 51% increase in the E-field (51), which means the coil at P_{ref} with 45° can cause the induced current to pass vertically into the central sulcus. Therefore, P_{ref} is generally considered as a good stimulus spot in the search domain (**Table 3**; **Figure 5**). However, gyri in the VOIs such as the VOI 1 and the VOI 2, which had a little distance from the central sulcus, were mostly not parallel with the central sulcus. Therefore, the eight-figure coil with a 45° angle could not let the currents be vertical to the CSF-GM boundary and resulted in the poor E-field improvement under stimulation of the coil at P_{ref}. In addition, the optimization effect of the algorithm was obvious. Even for the VOI 3 and the VOI 4, which were closer to the central sulcus, the optimal stimulus angle was not 45° such as P_{ref}. On average, the angle optimization was 35.55° and the coil angle optimization was up to 87.90° in the CVH female (hemorrhagic)-VOI 2. In conclusion, for the specificity of gyri, the clinical stimulation mode is insufficient to ensure that the overall intracranial microcurrent is vertically passed through the local gyri. To obtain safer and more effective treatment conditions, it is necessary to regulate the location and angle of the coil according to various cortical gyrus structures for different patients and different targeted areas in the clinics.

The coil position under the guidance of the optimization algorithm proposed in this study was optimal after nine iterations and exhibited excellent performance in five repeated experiments (**Table 4**). In addition, after position optimization, the average

E-field and the distribution uniformity in the VOIs greatly improved. The optimization algorithm improved the E-field by 7.83 and 6.98% on average in the VOIs of the ischemic and hemorrhagic stroke models, respectively. The optimization algorithm improved the E-field up to 16.99% maximally for the ischemic stroke models and 17.48% maximally for the hemorrhagic stroke models. Furthermore, the enumeration method proved that the algorithm provided a global optimal coil position in the search domain (**Figure 8**).

This study result shows a significant improvement of the average E-field in the VOIs by the quantified coil positioning method, which reduces the positioning error caused by manual operation. By adopting GA, the electromagnetic response induced by pulse stimulus is maximized, the efficiency of magnetic stimulation can be improved, and the unexpected induced E-field in non-targeted brain area would also be reduced. As a result, this optimization process reduces the electromagnetic exposure time of patients and shortens the period of treatment to reduce the probability of the occurrence of complications. In addition, the efficacy of TMS is related to the gyrus structure of different brain regions between different patients. Yet, the proposed algorithm can be used to solve this problem by designing the clinical TMS stroke therapeutic schedule individually. The variable of the two stroke models can be abstracted as the electrical conductivity of the lesion. Therefore, our coil position optimization algorithm is robust in different diseases, with electrical conductivity changes in the local brain tissue, such as brain tumor treatment.

CONCLUSION

Although the death rate of stroke is decreasing, its incidence has been continuously increasing worldwide and is higher in the younger population than in the elderly (1). To improve the efficiency of stroke rehabilitation treatment and provide patients with a more accurate and safe magnetic stimulation treatment in clinics, the ischemic stroke models and the hemorrhagic stroke models of the CVH female, the CVH male, and Duke were established. GA was applied to regulate the optimal coil location and rotation angle in a 4×4 cm search domain around the lesion, in which the rotation angle can be involved by the automatic search of coil spatial location within millimeter accuracy. Finally, the coil position is given in every VOI.

The proposed algorithm can be used to guide TMS coil positioning in clinical settings to achieve a more accurate TMS treatment. Contributing to the applied algorithm, the output energy of TMS can be freely dependent on clinicians to improve TMS stimulation efficiency and the dose of unnecessary region can be well-controlled; thus, the risk of electromagnetic exposure as well as the incidence of complications such as epilepsy can be lower, which is of great significance to public health and safety. Besides, benefitting from the robustness and repeatability of the algorithm in different races and strokes, our method can also be used in the plan of treatment for people of different races. This study gives a more accurate clinical quantitative treatment scheme and a proper stimulus dose plan for a safe and precise TMS treatment, which shows great prospect in stroke rehabilitation treatment. Furthermore, the proposed algorithm is also expected to be applied to TMS treatment of brain tumors in the future.

DATA AVAILABILITY STATEMENT

The original contributions presented in the study are included in the article/supplementary material, further inquiries can be directed to the corresponding author/s.

AUTHOR CONTRIBUTIONS

SL designed the model and realized all the three-dimensional (3D) models in this manuscript. HJ designed the algorithm to realize the optimized position search near the lesion. CL participated in the design of the model and the verification of location optimization and analyzed data. BH took part in the design of GA and the verification of data. PZ and WL provided ideas for the algorithm selection, model building, and electromagnetic field calculation and gave detailed guidance in the process of writing this manuscript. All the authors have read and agreed to the published version of the manuscript.

FUNDING

This study was supported by the Science and Technology Project of State Administration for Market Regulation (2021MK152 and 2020MK149) and the Basic Scientific Research Funds of the National Institute of Metrology (China) (32-AKYZD2014–2).

REFERENCES

1. Hankey GJ. Stroke. *Lancet.* (2017) 389:641–54. doi: 10.1016/S0140-6736(16)30962-X
2. Mohamed Fuad Z, Mahadzir H, Syed Zakaria SZ, Mohamed Ibrahim N. Frequency of cognitive impairment among malaysian elderly patients following first ischaemic stroke-a case control study. *Front Publ Health.* (2020) 8:577940. doi: 10.3389/fpubh.2020.577940
3. Lobo EH, Frolich A, Rasmussen LJ, Livingston PM, Grundy J, Abdelrazek M, et al. Understanding the methodological issues and solutions in the research design of stroke caregiving technology. *Front Publ Health.* (2021) 9:647249. doi: 10.3389/fpubh.2021.647249
4. Stroke. *Health A to Z.* (2019). Available online at: https://www.nhs.uk/conditions/stroke/ (accessed September 6, 2021).
5. Feigin VL, Lawes CM, Bennett DA, Anderson CS. Stroke epidemiology: a review of population-based studies of incidence, prevalence, andcase-fatality in the late 20th century. *Lancet Neurol.* (2003) 2:43–53. doi: 10.1016/s1474-4422(03)00266-7
6. Clay MT, Ferree TC. Weighted regularization in electrical impedance tomography with applications to acute cerebral stroke. *IEEE Trans Biomed Imaging.* (2002) 21:629–37. doi: 10.1109/TMI.2002.800572
7. Pai SB, Varma RG, Kulkarni RN. Microsurgical anatomy of the middle cerebral artery. *J Neurol.* (2005) 53:186–90. doi: 10.4103/0028-3886.16406

8. Najib U, Horvath JC. Transcranial magnetic stimulation (TMS) safety considerations and recommendations. In: Rotenberg A, editor. *Transcranial Magnetic Stimulation*. New York; Heidelberg; Dordrecht; London: Springer (2014) 15–30. doi: 10.1007/978-1-4939-0879-0_2
9. Zhang S, Yin T, Liu Z, Li Y, Jin J, Ma R. Experimental study to improve the focalization of a figure-eight coil of rTMS by using a highly conductive and highly permeable medium. *IEEE Trans Neural Syst Rehabil Eng.* (2013) 21:364–9. doi: 10.1109/TNSRE.2012.2194723
10. Najib U, Bashir S, Edwards D, Rotenberg A, Pascual-Leone A. Transcranial brain stimulation: clinical applications and future directions. *Neurosurg Clin N Am.* (2011) 22:233–51. doi: 10.1016/j.nec.2011.01.002
11. Ren J, Li H, Palaniyappan L, Liu H, Wang J, Li C, et al. Repetitive transcranial magnetic stimulation versus electroconvulsive therapy for major depression: a systematic review and meta-analysis. *Prog Neuro Psychopharmacol Biol Psychiatry.* (2014) 51:181–9. doi: 10.1016/j.pnpbp.2014.02.004
12. Khedr EM, Ahmed MA, Fathy N, Rothwell JC. Therapeutic trial of repetitive transcranial magnetic stimulation after acute ischemic stroke. *Neurology.* (2005) 65:466–8. doi: 10.1212/01.wnl.0000173067.84247.36
13. Kim YH, You SH, Ko MH, Park JW, Lee KH, Jang SH, et al. Repetitive transcranial magnetic stimulation-induced corticomotor excitability and associated motor skill acquisition in chronic stroke. *Stroke.* (2006) 37:1471–6. doi: 10.1161/01.STR.0000221233.55497.51
14. Summers JJ, Kagerer FA, Garry MI, Hiraga CY, Loftus A, Cauraugh JH. Bilateral and unilateral movement training on upper limb function in chronic stroke patients: a TMS study. *J Neurol Sci.* (2007) 252:76–82. doi: 10.1016/j.jns.2006.10.011
15. Miniussi C, Rossini PM. Transcranial magnetic stimulation in cognitive rehabilitation. *Neuropsychol Rehabil.* (2011) 21:579–601. doi: 10.1080/09602011.2011.562689
16. Wassermann EM. Risk and safety of repetitive transcranial magnetic stimulation: report and suggested guidelines from the International Workshop on the Safety of Repetitive Transcranial Magnetic Stimulation. *Electroencephalogr Clin Neurophysiol.* (1997) 108:1–16. doi: 10.1016/s0168-5597(97)00096-8
17. Ayach S, Farhat WH, Zouari HG, Hosseini H, Mylius V, Lefaucheur J-P. Stroke rehabilitation using non-invasive cortical stimulation: motor deficit. *Expert Rev Neurother.* (2012) 12:949–72. doi: 10.1586/ern.12.83
18. McDonnell MN, Stinear CM, TMS. measures of motor cortex function after stroke: a meta-analysis. *Brain Stimul.* (2017) 10:721–34. doi: 10.1016/j.brs.2017.03.008
19. van Assche M, Dirren E, Bourgeois A, Kleinschmidt A, Richiardi J, Carrera E. Periinfarct rewiring supports recovery after primary motor cortex stroke. *J Cereb Blood Flow Metab.* (2021) 41:2174–84. doi: 10.1177/0271678X211002968
20. Khedr EM, Etraby AE, Hemeda M, Nasef AM, Razek AA. Long-term effect of repetitive transcranial magnetic stimulation on motor function recovery after acute ischemic stroke. *Acta Neurol Scand.* (2010) 121:30–7. doi: 10.1111/j.1600-0404.2009.01195.x
21. Chang WH, Kim YH, Yoo WK, Goo KH, Park CH, Kim ST, et al. rTMS with motor training modulates cortico-basal ganglia-thalamocortical circuits in stroke patients. *Restor Neurol Neurosci.* (2012) 30:179–89. doi: 10.3233/RNN-2012-110162
22. Bestmann S, Baudewig J, Siebner HR, Rothwell JC, Frahm J. BOLD MRI responses to repetitive TMS over human dorsal premotor cortex. *Neuroimage.* (2005) 28:22–9. doi: 10.1016/j.neuroimage.2005.05.027
23. Bestmann S, Baudewig J, Siebner HR, Rothwell JC, Frahm J. Functional MRI of the immediate impact of transcranial magnetic stimulation on cortical and subcortical motor circuits. *Eur J Neurosci.* (2004) 19:1950–62. doi: 10.1111/j.1460-9568.2004.03277.x
24. Thielscher A, Wichmann FA. Determining the cortical target of transcranial magnetic stimulation. *Neuroimage.* (2009) 47:1319–30. doi: 10.1016/j.neuroimage.2009.04.021
25. Meincke J, Hewitt M, Liebetanz D. P101 impact of coil rotation on TMS threshold. *Clin Neurophysiol.* (2017) 128:e61. doi: 10.1016/j.clinph.2016.10.225
26. Gomez LJ, Yücel AC, Hernandez-Garcia L, Taylor SF, Michielssen E. Uncertainty quantification in transcranial magnetic stimulation via high-dimensional model representation. *IEEE Trans Biomed Eng.* (2015) 62:361–72. doi: 10.1109/TBME.2014.2353993
27. Opitz A, Windhoff M, Heidemann RM, Turner R, Thielscher A. How the brain tissue shapes the electric field induced by transcranial magnetic stimulation. *Neuroimage.* (2011) 58:849–59. doi: 10.1016/j.neuroimage.2011.06.069
28. Duecker F, Frost MA, de Graaf TA, Graewe B, Jacobs C, Goebel R, et al. The cortex-based alignment approach to TMS coil positioning. *J Cogn Neurosci.* (2014) 26:2321–9. doi: 10.1162/jocn_a_00635
29. Gomez-Tames J, Hamasaka A, Laakso I, Hirata A, Ugawa Y. Atlas of optimal coil orientation and position for TMS: a computational study. *Brain Stimul.* (2018) 11:839–48. doi: 10.1016/j.brs.2018.04.011
30. Gomez LJ, Dannhauer M, Peterchev AV. Fast computational optimization of TMS coil placement for individualized electric field targeting. *Neuroimage.* (2021) 228:117696. doi: 10.1016/j.neuroimage.2020.117696
31. Li C, Liu C, Yang L, He L, Wu T. Particle swarm optimization for positioning the coil of transcranial magnetic stimulation. *Biomed Res Int.* (2019) 2019:9461018. doi: 10.1155/2019/9461018
32. Xiong H, Qiu, B, Liu, J. An improved multi-swarm particle swarm optimizer for optimizing the electric field distribution of multichannel transcranial magnetic stimulation. *Artif Intell Med*. (2020) 104:101790. doi: 10.1016/j.artmed.2020.101790
33. Wu T, Tan L, Shao Q, Zhang C, Zhao C, Li Y, et al. Chinese adult anatomical models and the application in evaluation of RF exposures. *Phys Med Biol.* (2011) 56:2075. doi: 10.1088/0031-9155/56/7/011
34. Christ A, Kainz W, Hahn EG, Honegger K, Zefferer M, Neufeld E, et al. The virtual family—development of surface-based anatomical models of two adults and two children for dosimetric simulations. *Phys. Med. Biol.* (2010) 55:N23. doi: 10.1088/0031-9155/55/2/N01
35. Xu W, Li M, Gaoa S, Nia J, Zhou L, Yao M, et al. *In vivo* high-resolution MR imaging of symptomatic and asymptomatic middle cerebral artery atherosclerotic stenosis. *Atherosclerosis.* (2010) 212:507-11. doi: 10.1016/j.atherosclerosis.2010.06.035
36. Ugur HC, Kahilogullari G, Coscarella E, Unlu A, Tekdemir I, Morcos JJ, et al. Arterial vascularization of primary motor cortex (precentral gyrus). *Surg Neurol.* (2005) 64(Suppl 2):S2:48–S2:52. doi: 10.1016/j.surneu.2005.07.049
37. Röther J, Schwartz A, Wentz K. U, Rautenberg W, Hennerici M. Middle cerebral artery stenoses: assessment by magnetic resonance angiography and transcranial doppler ultrasound. *Cerebrovasc Dis.* (1994) 4:273–9. doi: 10.1159/000108494
38. Tseng S, Li X. An observation of arterial system of Chinese brains. *Acta Anat Sin.* (1965) 8:259–81.
39. Kim HJ, Oh TI, Kim YT, Lee BI, Woo EJ, Seo JK, et al. *In vivo* electrical conductivity imaging of a canine brain using a 3 T MREIT system. *Physiol Meas.* (2008) 29:1145–55. doi: 10.1088/0967-3334/29/10/001
40. Pichot C, Kanfoud IE, Aliferis a, Migliaccio C, Dolean V, Bonazzoli M, et al. Investigation of measurement errors in microwave imaging system for brain stroke monitoring. *Progress In Electromagnetics Research Symposium (PIERS).* Saint Petersburg (2017) 1–4.
41. Gao N, Zhu SA, He B. Use of 3-D magnetic resonance electrical impedance tomography in detecting human cerebral stroke: a simulation study. *J Zhejiang Univ Sci B.* (2005) 6:438–45. doi: 10.1631/jzus.2005.B0438
42. Tscherpel C, Dern S, Hensel L, Ziemann U, Fink GR, Grefkes C. Brain responsivity provides an individual readout for motor recovery after stroke. *Brain.* (2020) 143:1873–88. doi: 10.1093/brain/awaa127
43. Thielscher A, Opitz A, Windhoff M. Impact of the gyral geometry on the electric field induced by transcranial magnetic stimulation. *Neuroimage.* (2011) 54:234–43. doi: 10.1016/j.neuroimage.2010.07.061
44. Ruoli J, Jansen BH, Sheth BR Ji C. Dynamic multi-channel TMS with reconfigurable coil. *IEEE Trans Neural Syst Rehabil Eng.* (2013) 21:370–5. doi: 10.1109/TNSRE.2012.2226914
45. Sriniva M and Patnaik L.M. Adaptive probabilities of crossover and mutation in genetic algorithms. *IEEE Trans Syst Man Cybern.* (1994) 24:656–67. doi: 10.1109/21.286385

46. Gen M. and Lin L. *Genetic Algorithms: Wiley Encyclopedia of Computer Science and Engineering.* (2008). doi: 10.1002/9780470050118.ecse169
47. HODGKIN AL HUXLEY AF, A. quantitative description of membrane current and its application to conduction and excitation in nerve. *J Physiol.* (1952) 117:500–44. doi: 10.1113/jphysiol.1952.sp004764
48. Reimann M, Niehaus L, Lehmann R. Kernspintomographische untersuchung der hämorrhagischen transformation ischämischer posteriorinfarkte. *Neuroradiologie.* (2000) 172:675–9. doi: 10.1055/s-2000-7170
49. Di Lazzaro V, Pilato F, Dileone M, Profice P, Capone F, Ranieri F, et al. Modulating cortical excitability in acute stroke: a repetitive TMS study. *Clin Neurophysiol.* (2008) 119:715–23. doi: 10.1016/j.clinph.2007.11.049
50. Richards LG, Stewart KC, Woodbury ML, Senesac C, Cauraugh JH. Movement-dependent stroke recovery: a systematic review and meta-analysis of TMS and fMRI evidence. *Neuropsychologia.* (2008) 46:3–11. doi: 10.1016/j.neuropsychologia.2007.08.013
51. McCann H, Pisano G, Beltrachini L. Variation in reported human head tissue electrical conductivity values. *Brain Topography.* (2019) 3:825–58. doi: 10.1101/511006

Conflict of Interest: HJ was employed by China Academy of Telecommunications Technology.

The remaining authors declare that the research was conducted in the absence of any commercial or financial relationships that could be construed as a potential conflict of interest.

Advantages of publishing in Frontiers

OPEN ACCESS
Articles are free to read for greatest visibility and readership

FAST PUBLICATION
Around 90 days from submission to decision

HIGH QUALITY PEER-REVIEW
Rigorous, collaborative, and constructive peer-review

TRANSPARENT PEER-REVIEW
Editors and reviewers acknowledged by name on published articles

Frontiers
Avenue du Tribunal-Fédéral 34
1005 Lausanne | Switzerland

Visit us: www.frontiersin.org
Contact us: frontiersin.org/about/contact

REPRODUCIBILITY OF RESEARCH
Support open data and methods to enhance research reproducibility

DIGITAL PUBLISHING
Articles designed for optimal readership across devices

FOLLOW US
@frontiersin

IMPACT METRICS
Advanced article metrics track visibility across digital media

EXTENSIVE PROMOTION
Marketing and promotion of impactful research

LOOP RESEARCH NETWORK
Our network increases your article's readership